

Dust Shells around Oxygen–Rich Miras and Long–Period Variables

von

M. Sc. Kyung Sook Jeong
aus Seoul Korea

Vom Fachbereich 04 (Physik)
der Technischen Universität Berlin
zur Erlangung des akademischen Grades

Doktor der Naturwissenschaften (Dr. rer. nat.)

genehmigte Dissertation

Berlin 2000

D 83

Promotionsausschuß:

Vorsitzender: Prof. Dr. P. Zimmermann

Berichter: Prof. Dr. E. Sedlmayr

Prof. Dr. H. P. Röser

Tag der mündlichen Prüfung: 7. 4. 2000

To my parents

*Die Straße gleitet fort und fort,
Weg von der Tür, wo sie begann,
Weit überland, von Ort zu Ort,
Ich folge ihr, so gut ich kann.
Ihr lauf ich raschen Fußes nach,
Bis sie sich groß und breit verflucht
Mit Weg und Wagnis tausendfach.
Und wohin dann ? Ich weiß es nicht.
Tolkien Der Herr der Ringe.*

Zusammenfassung

Zirkumstellare Hüllen kühler pulsierender Sterne späten Typs sind die bedeutenden Objekte, die durch das Ausströmen von Materie in Form komplexer Moleküle und Staubteilchen das interstellare Medium anreichern. Im Gegensatz zu kohlenstoffreichen Sternen, in deren Hüllen sich hauptsächlich amorphe, kohlenstoffhaltige Festkörperpartikel bilden, ist praktisch der gesamte Kohlenstoff in *sauerstoffreichen* Sternen im chemisch inaktiven CO Molekül gebunden. Daher können sich die Staubteilchen in diesen Sternen nur aus dem verbleibenden Sauerstoff und dem weniger häufigen Elementen wie Fe, Si, Mg, S, Al, Ca und Ti bilden. Dies führt zu einer *heterogenen* chemischen Zusammensetzung der Staubteilchen.

Zur Beschreibung eines Nukleationsprozesses, d.h. dem Gas-Festkörperübergang zur Bildung der ersten Oberfläche, werden Informationen über die thermodynamischen Eigenschaften von Clustern, wie die Gibb'sche freie Bildungsenergie, benötigt. Die erforderlichen Daten für die in Frage kommenden Kondensate (z. B. TiO_2) im kühlen Ausstrom sauerstoffreicher zirkumstellarer Hüllen sind größtenteils nicht vorhanden. Um die thermodynamischen Eigenschaften des in diesen Objekten favorisierten Nukleationskeims, TiO_2 , berechnen zu können, sind Geometrie-Optimierungsrechnungen der elektronischen Strukturen der Cluster im Rahmen der Dichtefunktionaltheorie durchgeführt worden. Die so berechneten Gibb'schen freien Bildungsenergien zeigen eine gute Übereinstimmung mit den Werten, die im Rahmen der klassischen Nukleationstheorie bisher anhand der Oberflächenspannung des Festkörpers approximiert wurden. Dieses Resultat rechtfertigt die weitere Anwendung von klassischer Nukleationstheorie bei der Berechnung von Nukleationsraten für die Kondensate, um den primären Nukleationskeim zu bestimmen.

In dieser Arbeit wird gezeigt, daß Titanoxide eine relevante Nukleationsrate bei den höheren, in der Staubbildungszone sauerstoffreicher Rote Riesen vorherrschenden Temperaturen von ca. 1000 K aufweisen. Dabei sind, aufgrund der höheren Moleküldichten im Gas, die Nukleationsraten von TiO_2 wesentlich effizienter als die von TiO . Durch Akkretion verschiedener Wachstumsspezies auf den TiO_2 -Keim – entsprechend ihre Stabilitätsgrenzen in den Hüllen sauerstoffreicher Objekte – kommt es zur Entstehung eines *heterogenen* Staubteilchenmantels.

Bilden sich die Staubteilchen bereits in den inneren Bereichen der zirkumstellaren Hülle, üben sie, aufgrund der hohen Leuchtkraft des Sterns und dem daraus resultierenden Strahlungsdruck, einen starken Einfluß auf die hydrodynamische Struktur der Hülle selbst aus. Daher ist eine konsistente Beschreibung der staubbildenden zirkumstellaren Hüllen und damit die Lösung des nichtlinear gekoppelten Systems bestehend aus Hydrodynamik, Thermodynamik, Strahlungstransport, Chemie und die Staubbildung unerlässlich.

In dieser Arbeit werden die ersten konsistenten Rechnungen sauerstoffreicher Staubbüllen von Miras und Langperiodisch Veränderlichen durchgeführt. Diese Modelle sind eindeutig durch die stellaren Parameter Leuchtkraft L_* , Mass M_* , Stern-temperatur T_* , die Elementhäufigkeiten ε_i sowie die Pulsationseigenschaften des

zentralen Sterns, d.h. die Pulsationsamplitude Δu_p und die Pulsationsperiode P , bestimmt. Das hier im Vordergrund stehende Model ($L_* = 2 \cdot 10^4 L_\odot$, $T_* = 2000$ K, $M_* = 1 M_\odot$, $\Delta u_p = 5 \text{ kms}^{-1}$, $P = 300$ d und solare Häufigkeiten) zeigt eine Massenverlustrate von $\dot{M} \approx 6 \cdot 10^{-5} M_\odot \text{yr}^{-1}$ und eine Endgeschwindigkeit von $v_\infty \approx 16 \text{ kms}^{-1}$, welche gut mit den beobachteten Werten übereinstimmen.

Im Allgemeinen wird gezeigt, daß der Strahlungsdruck auf Staub auch in *sauerstoffreichen* zirkumstellaren Hüllen die Ursache für starke Massenverluste und damit für den Sternenwind sein kann. Die Wirkung des Staubes wird durch die Pulsation unterstützt, die eine Levitation der Atmosphäre verursacht und somit günstigere Bedingungen für die Staubbildung schafft. Staub ist von großer Bedeutung in *sauerstoffreichen* zirkumstellaren Hüllen, wo er starke Stoßwellen induzieren kann und die Struktur der zirkumstellaren Hüllen dominierend bestimmt. Die staubinduzierten Stöße führen zu einer Schalen-Struktur der zirkumstellaren Hüllen in der räumlichen Verteilung der Staubteilchen einen inhomogenen Charakter aufweist.

Abstract

Circumstellar dust shells around cool pulsating late type stars are the major sources for the replenishment of the interstellar medium with processed material, in particular in the form of complex molecules and of dust particles. In contrast to the carbon-rich situation, where mainly *homogeneous* amorphous carbon grains and also PAHs are formed, almost all carbon is locked up in the chemically inert CO molecule in an *oxygen-rich* gas. Therefore, grains can only be formed from molecules containing the remaining oxygen and those less abundant elements (Fe, Si, Mg, S, Al, and Ti) Hence, a *heterogeneous* composition of the emerging dust component has to be expected in this case.

Nucleation, the onset of the dust formation, requires the information about the cluster size distribution, which can be calculated from the Gibbs free energy of formation. Often it is the case that the data needed are not available for the condensates. In order to calculate the thermochemical properties, e.g. Gibbs free energy of formation for TiO_2 clusters, the geometric optimisation of the electronic structures has been performed in the quantum mechanical calculations based on the density functional theory. The Gibbs free energies of $(\text{TiO}_2)_n$ clusters resulting from the quantum mechanical density functional theory are in good agreement with those values derived by approximation in terms of the surface energy of the solid bulk, which is considered in the nucleation theory. Therefore, it is appropriate to further use the modified nucleation theory for calculating the homogeneous nucleation rates of the high temperature condensates.

Among the considered primary condensates Fe, SiO, TiO and TiO_2 , only the titanium oxides show efficient nucleation rates at temperatures above 1000 K, where TiO_2 nucleation is by far more efficient than TiO due to its higher gas phase concentration. The TiO_2 nuclei grow by accretion of those molecular species which can form stable condensates under the thermodynamic conditions prevailing in the circumstellar environment. The result is a *heterogeneous* grain mantle composition.

The consistent description of a dust forming circumstellar shell constitutes a non-linearly coupled problem comprising hydrodynamics, thermodynamics, chemistry, dust formation, growth and evaporation, and the radiative transfer. Therefore, a simultaneous solution of the complete system, including the dust formation, is indispensable for the reliable description of a circumstellar dust shell.

The first consistent model calculations for *oxygen-rich* circumstellar shells around Miras and long-period variables including dust formation have been performed. The solution of the equation system is completely determined by the 4 fundamental stellar parameters L_* , M_* , T_* , and ε_i and the additional 2 pulsation parameters Δu_p and P . The model studied in this work with $L_* = 2 \cdot 10^4 L_\odot$, $T_* = 2000 \text{ K}$, $M_* = 1 M_\odot$, $\Delta u_p = 5 \text{ kms}^{-1}$, $P = 300 \text{ d}$, and solar metallicity produces a mass loss rate of $\dot{M} \approx 6 \cdot 10^{-5} M_\odot \text{ yr}^{-1}$ and an outflow velocity of $v_\infty \approx 16 \text{ kms}^{-1}$ which show a good agreement with the observation.

Dust plays the key role in the determination of the structure of also the *oxygen-*

rich circumstellar shells by driving the wind through the radiation pressure on dust as it has been shown in case of the carbon-rich circumstellar shells. Due to the periodic formation of the dust layers, the radial dust distribution reveals inhomogeneous characteristics.

The non-linear effect due to the strong coupling of the whole systems of hydrodynamics, thermodynamics, radiative transfer, chemistry, and the dust formation reflects the multiperiodicity such that the radial structure of circumstellar dust shells repeats in the time scale of βP with the pulsation period P and integer β . In the time variation of the mass loss rates, this multiperiodicity is also reflected, involving with the different timescales, e.g. the duration time of the successive two layers of the shell.

Contents

Table of contents	v
List of Figures	vii
List of Tables	x
1 Introduction	1
1.1 In the evolutionary track	1
1.2 Characteristics of AGB stars	3
1.2.1 Internal structure	4
1.2.2 Spectra	4
1.2.3 Dust shells	5
1.2.4 Period	6
1.3 Mass loss mechanisms for the cool giant stars	6
1.4 The aim and structure of this work	9
2 Basic Equations	11
2.1 Hydrodynamic equations	11
2.2 Gas phase chemistry	13
2.3 Dust Formation	15
2.3.1 Nucleation	16
2.3.2 Growth and destruction of the dust grains	17
2.3.3 Chemical composition of the dust grains	18
2.4 The moment equations	19
2.5 Radiative transfer	20
2.6 Boundary conditions	21
3 Clusters	23
3.1 Overview	23
3.2 Previous investigations on titanium oxides	24
3.3 The electronic structure of Ti_xO_y Clusters	25
3.3.1 Density Functional Theory	26
3.3.2 Computational Aspects	28

3.4	Results and Discussions	29
3.4.1	Equilibrium geometries	29
3.4.2	Energetics	31
3.4.3	Vibrational Analysis	38
3.5	The Partition functions	43
3.6	Calculation of the thermochemical functions	46
3.7	The distribution of clusters	50
4	On the nucleation seeds	55
5	Dust formation in a gas element	63
5.1	The thermodynamic conditions	63
5.2	Condensation and evaporation of oxides	65
5.2.1	Dust formation on the TiO_2 nuclei	65
5.2.2	Dust formation on the Fe nuclei	75
5.2.3	concluding remarks	81
6	Dynamic Models of O-rich CDS around LPVs	85
6.1	Initial Hydrostatic Models	85
6.2	Comparison of Dynamic Model Calculations	88
6.2.1	The degree of Condensation f_{cond}	91
6.2.2	The Dust to Gas Ratio ρ_d/ρ_g	92
6.2.3	The Volume Fraction of Growth Species in Dust Grains	96
6.2.4	The Mass Loss Rate	96
6.3	Detailed Study: Model A	102
6.3.1	The radial structure	102
6.3.2	grain size distribution	110
6.3.3	Temporal variation of the mass loss rates	111
7	Summary and the outlook	115
A	Thermochemical properties of TiO and TiO_2	119
B	Thermochemical properties of Ti_xO_y	129
C	Harmonic wave number of Ti_xO_y	135
	Bibliography	141

List of Figures

3.1	Equilibrium geometries of the investigated Ti_xO_y systems	33
3.2	Binding energy per TiO_2 unit for $(\text{TiO}_2)_n$ $n=1-6$ clusters	36
3.3	First order energy difference $\Delta E(n)$ as a function of cluster size n . . .	36
3.4	Comparison of the atomisation energy D_0 and the bond energy D_b . .	37
3.5	Calculated IR spectra for $(\text{TiO})_n$ $n=1-3$ systems	40
3.6	Calculated IR spectra for Ti_xO_y systems	41
3.7	Calculated IR spectra for the $(\text{TiO}_2)_n$ $n=1-6$ systems	42
3.8	The logarithm of partial pressure of $(\text{TiO}_2)_n$ clusters at $P_{<H>} = 0.1 \text{ dyn cm}^{-2}$	49
3.9	Comparison between $\Delta_f G^o(N)/N$ values of TiO_2 clusters	53
4.1	Contour lines of the nucleation rate for different nucleating species in the p - T plane	59
4.2	Contour lines of the nucleation rate for different nucleating species in the ρ - T plane	60
5.1	The temporal variation of chemical composition of the gas for the dust free case	66
5.2	Heterogeneous growth on the seed material TiO_2	68
5.3	Stability hierarchy ($S = 1$) for some high temperature condensates in the p - T plane	68
5.4	Thermodynamical and dust quantities of dust with TiO_2 nuclei. . . .	70
5.5	Supersaturation ratio of TiO_2	72
5.6	Chemical composition of the dust grains with TiO_2 nuclei	73
5.7	The dust properties as a function of temperature for dust with TiO_2 nuclei	74
5.8	Thermodynamical and dust quantities for dust with Fe nuclei	76
5.9	Supersaturation ratio of Fe dust	78
5.10	Chemical composition of the dust grains with Fe nuclei as a function of time	79
5.11	The dust properties as a function of temperature for dust with Fe nuclei	80
5.12	The size distribution for TiO_2 nuclei and for Fe nuclei	81
6.1	Initial hydrostatic models	87

6.2	Radial structure of models with $\Delta u_p = 5 \text{ km s}^{-1}$	89
6.3	Radial structure of models with $\Delta u_p = 10 \text{ km s}^{-1}$	90
6.4	Radial structure of degree of condensation for models with $\Delta u_p = 10 \text{ km s}^{-1}$	93
6.5	Radial structure of degree of condensation for models with $\Delta u_p = 5 \text{ km s}^{-1}$	94
6.6	Radial structure of dust to gas ratio ρ_d/ρ_g for models with $\Delta u_p = 5 \text{ km s}^{-1}$	95
6.7	Radial structure of dust to gas ratio ρ_d/ρ_g for models with $\Delta u_p = 10 \text{ km s}^{-1}$	95
6.8	Radial structure of the volume fraction of the growth species in dust grains for model A	97
6.9	Radial structure of the volume fraction of the growth species in dust grains for model E	98
6.10	Radial structure of the volume fraction of the growth species in dust grains for model D	99
6.11	Radial structure of the local mass loss rates for models with $\Delta u_p = 5 \text{ km s}^{-1}$	100
6.12	Radial structure of the local mass loss rates for models with $\Delta u_p = 10 \text{ km s}^{-1}$	101
6.13	Radial structure of Model A at $t = (123 + \beta)P$ with $\beta = 12$	104
6.14	Radial structure of Model A at the different phase	106
6.15	Radial structure of Model A at the different phase	107
6.16	The radial structure of Model A with different optical constant of dust grains	109
6.17	Degree of condensation in a rdial structure of Model A	110
6.18	Temporal variation of $\langle \dot{M} \rangle$ of Model A	111
6.19	Temporal variation of $\langle \dot{M} \rangle$ of Model B	112
6.20	Temporal variation of $\langle \dot{M} \rangle$ of Model C	113

List of Tables

1.1	The period distribution of LPVs according to the spectral type	6
2.1	the abundances of the elements	14
2.2	The partial pressure \bar{p}_j^o of the element j	15
3.1	Comparison of the calculated equilibrium geometries and the previous works	30
3.2	Equilibrium geometric parameters of the investigated Ti_xO_y systems .	32
3.3	DFT/B3P86 energies	34
3.4	The binding energies $D_0(n)$ for $(\text{TiO})_n$ $n = 1-3$ and $(\text{TiO}_2)_n$ $n = 1-6$ clusters	34
3.5	Comparison of the computed harmonic wave numbers $\tilde{\nu}_k$ with the experimental value	39
5.1	Growth species and their chemical properties	67
6.1	The input parameters for the initial hydrostatic models	86
6.2	The resulting wind properties from the extended models	102
6.3	The resulting wind properties with different optical porperties of dust grains	109
A.1	The calculated thermochemical properties of TiO molecule.	120
A.2	The calculated thermochemical properties of $(\text{TiO})_2$ molecule.	121
A.3	The calculated thermochemical properties of $(\text{TiO})_3$ molecule.	122
A.4	The calculated thermochemical properties of TiO_2	123
A.5	The calculated thermochemical properties of $(\text{TiO}_2)_2$	124
A.6	The calculated thermochemical properties of $(\text{TiO}_2)_3$	125
A.7	The calculated thermochemical properties of $(\text{TiO}_2)_4$	126
A.8	The calculated thermochemical properties of $(\text{TiO}_2)_5$	127
A.9	The calculated thermochemical properties of $(\text{TiO}_2)_6$	128
B.1	The calculated thermochemical properties of TiO_3 molecule.	130
B.2	The calculated thermochemical properties of Ti_2O molecule.	131
B.3	The calculated thermochemical properties of Ti_2O_3 molecule.	132
B.4	The calculated thermochemical properties of Ti_3O_4 molecule.	133

B.5	The calculated thermochemical properties of Ti_3O_5 molecule.	134
C.1	the calculated harmonic wave number $\tilde{\nu}_k$ [cm^{-1}], wavelength λ [μm], and absorption coefficient A_k [$10^{-8}\text{cm}^2\text{s}^{-1}$] of TiO_3 and of Ti_2O with the label k	135
C.2	The calculated harmonic wave number $\tilde{\nu}_k$ [cm^{-1}], the wavelength λ [μm], and the absorption coefficient A_k [$10^{-8}\text{cm}^2\text{s}^{-1}$] of $(\text{TiO})_n$ $n=1-3$ with the label k	136
C.3	vibrational wave number $\tilde{\nu}_k$ [cm^{-1}], wavelength λ [μm], and absorption coefficient A_k [$10^{-8}\text{cm}^2\text{s}^{-1}$] of Ti_2O_3 , Ti_3O_4 , and Ti_3O_5 with the label k	137
C.4	vibrational wave number $\tilde{\nu}_k$ [cm^{-1}], wavelength λ [μm], and absorption coefficient A_k [$10^{-8}\text{cm}^2\text{s}^{-1}$] of TiO_2 , $(\text{TiO}_2)_2$, and $(\text{TiO}_2)_3$ with label k	138
C.5	vibrational wave number $\tilde{\nu}_k$ [cm^{-1}], wavelength λ [μm], and absorption coefficient A_k [$10^{-8}\text{cm}^2\text{s}^{-1}$] of $(\text{TiO}_2)_4$ and of $(\text{TiO}_2)_5$ with label k	139
C.6	vibrational wave number $\tilde{\nu}_k$ [cm^{-1}], wavelength λ [μm], and absorption coefficient A_k [$10^{-8}\text{cm}^2\text{s}^{-1}$] of $(\text{TiO}_2)_6$ with label k	140

Chapter 1

Introduction

Highly evolved intermediate mass stars generally are surrounded by the expanding circumstellar dust shells (CDS). These dust shells are characterized by low expanding velocities ($5 \text{ km s}^{-1} \leq V_{\infty} \leq 40 \text{ km s}^{-1}$) and high mass loss rates ($\approx 10^{-7} \text{ M}_{\odot} \text{ yr}^{-1} \leq \dot{M} \leq 10^{-4} \text{ M}_{\odot} \text{ yr}^{-1}$). The material lost during the Asymptotic Giant Branch (AGB) phase, enriched with nuclear processed material, complex molecules, and solid dust particles, is recycled to the interstellar medium. About 90 % of the total dust mass returned to the interstellar medium is produced by stars evolving along the AGB (Gehrz 1989). AGB stars, therefore, are major sources of freshly processed matter and consequently, plays a key role for the chemical evolution of the interstellar medium.

1.1 In the evolutionary track

The evolutionary model calculations reveal that Miras and LPVs are considered as highly evolved objects of about one solar mass on the Asymptotic Giant Branch (AGB) in the Hertzsprung–Russell diagram (HR diagram), a quite common stellar evolutionary stage of the low mass and intermediate mass star (e.g. review in Iben and Renzini 1983). Their shells lose considerable amount of matter and this causes an severe influence on the evolutionary track of the star itself.

The stars of low mass ($1 \text{ M}_{\odot} \leq M \leq 2 \text{ M}_{\odot}$) and of intermediate mass ($2 \text{ M}_{\odot} < M \leq 8 \text{ M}_{\odot}$), after leaving the main sequence, are thought to evolve to the AGB on which they evolve along the Hayashi line towards higher luminosities until they end up as Planetary Nebulae (PN) leaving the central object as a white dwarf. Massive stars ($M > 8 \text{ M}_{\odot}$), on the contrary, don't evolve hereafter to Mira stars. Due to the difference in mass, the evolution of these objects differs shortly after the main sequence proceeds.

After the exhaustion of hydrogen in the core, the stars of intermediate mass ignite He-burning under non degenerate conditions and evolve nearly horizontally in the HR-diagram from the main sequence directly to the red giant region, performing

loops towards the hotter region of the HR–diagram and back to the red giants, while undergoing central helium burning. Low mass stars, on the other hand, develop a degenerate He–core, after hydrogen exhaustion on the main sequence and subsequent H–shell burning, and climb the Red Giant Branch (RGB) along the Hayashi line. The increase of the H–shell burning leads to the luminosity increase on the RGB, which is necessary to balance the gravity of the increasing degenerate He–core. At the end of the RGB phase, where low mass stars have reached luminosities of $3 \cdot 10^8 L_{\odot}$, the He–burning in the core (helium core flash) is ignited. This causes the lift of the degeneracy and the luminosity drops to values about $1.8 \cdot 10^3 L_{\odot}$.

Due to the high luminosities during the RGB phase, the stars already lose substantial amount of mass, which decisively influences their evolution. The helium core flash, however, shifts these stars from the red giant region.

After the central helium is exhausted, the stars of low and intermediate mass exhibit the qualitatively similar evolutionary track. They switch again to shell burning and extensive He–burning shell causes the stars to expand, cooling the outer regions which extinguishes the outer H–burning shell. Their luminosities increase again up to $10^4 L_{\odot}$, where the temperature remains almost constant, < 3000 K and they reach asymptotically the red giant region: Early Asymptotic Giant Branch (E–AGB) phase.

The stars on this evolutionary phase consist of a degenerate increasing core of carbon and oxygen, a He–burning shell, and a hydrogen rich envelope. At the end of the E–AGB phase, the outwards moving He–burning shell reaches the outer H–envelope. At temperatures above 10^8 K due to He–burning, the H–shell is ignited again. Due to its small geometric extension, the helium shell becomes thermally unstable, since an expansion of the shell proceeds isobaric and leads to an increase of the shell temperature: Helium shell flashes or thermal pulses (TP). This instability occurs under non–degenerate conditions and rather periodically in time scales of 10^4 yr. This second stage of AGB evolution is, therefore, called TP–AGB phase.

This thermal pulse phase could theoretically continue until the core mass exceeds the critical value ($1.1 M_{\odot}$) for core–carbon ignition, but this limits in practice the number of thermal pulses and prevents the star from becoming a supernova.

Another important mechanism during the phase of shell flash is the third dredge–up process. During the TP–AGB phase, two convective zones are present: The inner convective zone within the inter shell region mixes processed material from the He–shell upwards close to the H–burning shell the outer convective zone extends from the stellar surface down during a flash maximum, even beyond the H–burning shell. By the third dredge–up process, newly processed material is distributed over the whole outer envelope up to the stellar surface after each thermal pulse and the outer layers become enriched mainly in carbon but also in a variety of neutron–rich isotopes, e.g. the *s*–process elements like Tc.

When the central object has reached about $3 \cdot 10^4$ K its ultraviolet radiation is able to ionize the expanded shell. Due to recombination effects of the emitted radiation of the shell, it becomes visible as a planetary nebulae (PN). Finally, the

H-burning of the central star ceases and the luminosity steeply decreases. The temperature, which so far has reached values as high as $1.5 \cdot 10^5$ K, decreases and the object cools down to white dwarf. Although the lifetime on the tip of AGB rather is relatively short, $10^4 \sim 10^5$ yr, the mass loss process of Miras and LPVs is of extreme importance, since the following post-AGB evolution is strongly determined by their stellar structure on the AGB (Weidemann and Schönberner 1990, Vassiliadis and Wood 1993) and since most of the stars on the main sequence have masses less than $6 M_{\odot}$ and reach the evolutionary phase on the AGB.

The investigation on the final stage the evolution from the main sequence to PN phase is still suffering, since the no consistent treatment of mass loss process has been given and therefore, theoretical calculations have been given only qualitatively, omitting many details. This contaminated with a lot of free parameters, which make quantitative statements rather uncertain.

The mass loss rates occurring during AGB evolution are so high, that they have a significant impact on the evolution of the central star. In order to describe the high mass loss rates which is required for the remnant cores of AGB evolutions, a fit formula is usually used like the so called Reimers formula. This formula gives a fit to the observed mass loss rates of RGB stars with the parameter $\eta = 0.4$. In order to account for the super wind mass loss in evolutionary calculations for PN (Renzini 1981), the parameter η in the Reimers formula is ad hoc switched to different values needed during different evolutionary stages with the constant, that the final core masses after termination of the AGB phase match the observed masses of white dwarfs (e.g. Schönberner 1983, Boothroyd and Sackmann 1988b).

Fit formulae have been given by Dominik *et al.* (1990) for the stationary dust driven wind problem and by Arndt *et al.* (1996) for the dynamic wind problem for the carbon-rich AGB stars, which describes the dependence of the mass loss rate on the basic stellar parameters. These formulae are capable of explaining the observed high mass loss rates without introducing artificial fit parameters, especially in case of the presence of the a pulsating dust-driven super wind (Schröder *et al.* 1999). The mass loss rates occurring during AGB evolution are so high, that they have a significant impact on the evolution of the central star, especially on the final phase of AGB.

1.2 Characteristics of AGB stars

According to their evolutionary status, AGB stars are characterized by low surface temperatures, $T_{*} \leq 3000$ K, high luminosities up to several $10^4 L_{\odot}$, and by a peculiar chemical composition and they are largely geometrically extended (Habing 1996). The atmospheres of these giant stars provide favourable thermodynamic conditions for the formation of complex molecules, due to the low temperatures and simultaneously high densities.

The photospheric temperatures are too high ($T_{*} \approx 2000$ K), the formation of

the solid particles must occur in the expanding circumstellar shells. The observed correlation between the infrared excess and the mass loss rates indicates that the dust plays a decisive role by generating the massive outflows (Veen and Rugers 1989). The dust grains absorb effectively the radiative momentum which is transmitted to the surrounding gas via frictional coupling. This causes the acceleration of the material and drive a mass outflow, a *wind*. The terminal outflow velocities of AGB stars range from $\sim 10 \text{ km s}^{-1}$ up to 45 km s^{-1} (Knapp and Morris 1985, Jura 1986a, Zuckermann *et al.* 1986, Barnbaum *et al.* 1991). The mass loss rates of AGB stars are between $10^{-8} \text{ M}_{\odot} \text{ yr}^{-1}$ and $10^{-4} \text{ M}_{\odot} \text{ yr}^{-1}$ (Olofsson *et al.* 1993).

Dusty AGB stars are also known as pulsating variable stars with typical periods between 100 and 1000 d (Jura 1986b, Habing 1990, Habing 1996). The radial pulsation of these stars generate strong shock waves which propagates through the atmosphere and the circumstellar shell. The dissipation of the shock wave energy and momentum can contribute to the mass loss mechanism of these stars.

1.2.1 Internal structure

Through the 3α process, the core of an AGB star consists of about 80 % ^{16}O and 20 % ^{12}C . On the top of the helium burning shell exits the processed material by H-burning, contains primarily He with enhancement of ^{14}N resulting from the CNO cycle. Outside the H-burning shell the envelope has a main sequence chemical composition, modified by the abundance changes due to the first and second dredge-up phases through the convective zone. During the third dredge-up, the pulses can reach a luminosity up to $10^7 L_{\odot}$ from the He-burning. The deposition of this energy causes a convective zone to form at base of the He-burning zone. The temperatures exceeds $3 \cdot 10^8 \text{ K}$ at the bottom of the convective zone and this leads reactions like $^{22}\text{N}(\alpha, n)^{25}\text{Mg}$ forming free neutrons. The *s*-process elements can be then formed by the capture of these neutrons by ^{56}Fe (Iben and Renzini 1983, Gallino *et al.* 1990).

1.2.2 Spectra

According to the photospheric carbon to oxygen ratio C/O, the stars can be classified as M stars ($\text{C/O} < 1$), S stars ($\text{C/O} \approx 1$) and C stars ($\text{C/O} > 1$). The CO molecule already forms at high temperatures in the stellar photosphere and is chemically inert due to the large bond energy of about 11 eV. Therefore, CO molecules block the respective less abundant element and thus plays a key role for the molecular composition of the atmospheric gas, even under non-equilibrium conditions (Beck *et al.* 1992). Consequently, the spectra of M stars are dominated by the lines of oxygen bearing molecules e.g. the metal oxides SiO and TiO, and H_2O , whereas in C stars atmospheres the carbon bearing molecules like CH, C_2 , C_2H_2 and HCN prevail (Hoffmeister *et al.* 1984, Olofsson 1988, Gustafsson 1989).

S and C stars must have been enriched with carbon during their evolution and this carbon enrichment can be achieved especially by the third dredge-up. The

experience of the third dredge-up can be deduced from the presence of *s*-process elements in their photosphere. The most convincing indicator for recent mixing is provided by the detection of technetium lines in their spectra (Little *et al.* 1987). 75% of the C stars show Tc in their spectra and the presence of Tc clearly indicates very recent production of this element.

A simultaneous increase of the C/O ratio and of the abundance of *s*-process elements imply an evolutionary sequence starting from oxygen-rich giants via S stars towards the luminous C-stars (Little *et al.* 1987).

1.2.3 Dust shells

A common feature of AGB stars is the presence of expanding circumstellar dust shells accompanied by considerable mass loss (Deutsch 1956). Observations in the infrared spectral region revealed a continuous excess emission and also broad emission feature around $10\ \mu\text{m}$ in M type giants (Woolf and Ney 1969, Gillette *et al.* 1971) and a feature around the $11\ \mu\text{m}$ in the spectra of C-type giants (Treffers and Cohen 1974). These features could not be attributed to chromospheric emission and were concluded to be of circumstellar origin (Woolf and Ney 1969). The formation of the features can be explained as a result of the interaction of photons with the vibration modes of certain active molecular groups contained in solid particles.

The identification of these features implies the presence of silicate compounds, e.g. Mg_2SiO_4 in the circumstellar shells of M stars (Gilman 1969, Gillets *et al.* 1971) and of carbon compounds like amorphous or graphite carbon in C-stars (Treffers and Cohen 1974).

Based on the photometric observation in the mid-infrared range of $10 - 20\ \mu$ by Le Bertre (1993), Le Sidaner and Le Bertre (1993, 1996) showed the correlation between the circumstellar shell optical depth for oxygen-rich objects and the colour indices, e.g. $[\text{K}-12\ \mu\text{m}]$, in terms of circumstellar dust shell radiative transfer model.

The interferometric observation at $11\ \mu\text{m}$ indicate that the inner radius of the dust shell varies with the phase of the stellar luminosity (Danchi *et al.* 1994). This study shows two different classes of stars. One class has inner radii of their dust shells close to their photospheres (3-5 stellar radii) at the higher temperature ($\sim 1200\ \text{K}$) and the other has dust shells with substantially larger inner radii and very little dust close to the stars, which indicates sporadic production of dust with episodes of substantial production typically separated by a few decades.

Recent ISO observations reveal variety of the dust features (e.g. Waters and Molster 1999) and the mineralogy of the oxygen-rich circumstellar dust. For stars with high mass loss rates and for post-AGB stars, a very rich structure of narrow solid state emission bands, which can be identified with crystalline silicates, both olivines $\text{Mg}_{2(1-x)}\text{Fe}_{2x}\text{SiO}_4$ and pyroxenes $(\text{Mg}_{1-x}\text{Fe}_x\text{SiO}_3)$ (Waters *et al.* 1996, Molster *et al.* 1998).

1.2.4 Period

Most of the dusty AGB stars are known to be pulsating variable stars (Jura 1986b and Habing 1990, Habing 1996) having typical periods between 100 d and 1000 d (Beyers 1965). The frequency distribution of the period of the Mira stars are given according to the spectral types in Tab 1.1 (Hoffmeister *et al.* 1984).

Table 1.1: The period distribution according to the spectral type.

period [d]	M	C	S
101–200	100	–	–
201–300	320	6	11
301–400	297	19	25
401–500	90	24	11
501–600	16	4	–
601–700	3	–	–

1.3 Mass loss mechanisms for the cool giant stars

High masses loss rates can be considered, from the observed facts, to have the strong connection with the formation of dust occurs during the late evolutionary phases of low and intermediate mass stars.

In contrast to the fast massive winds of hot luminous stars driven by radiation pressure on the ultraviolet lines of abundant atomic ions (Castor *et al.* 1975, Pauldrach *et al.* 1986), no generally accepted mechanism exists for driving the cool massive winds of low gravity stars. Depending on the evolutionary status, different mechanism might be involved, but in most cases a self consistent description of the mechanisms, which could account for both, the observed high mass loss rates and the low terminal velocities is still lacking (review of Holzer and MacGregor 1985, Lafon and Beruyer 1991).

- the dissipation of energy and momentum of different kinds of waves propagating through the atmosphere
 - non compressive Alfvén waves: in this case, no heating of the atmosphere by energy dissipation are able to extend the atmosphere and to lift the material out of the stellar gravitational field. Most of the energy flux is, however, transferred to the gas in the outer, supersonic region of the wind and hence undamped Alfvén waves are able to produce high mass loss rates, but the resulting too high terminal wind velocities in comparison

to the observations (Holzer and MacGregor 1985). Since the calculated terminal wind velocities are very sensitive to the adopted value of the damping length, its values are confirmed to a rather small range in order to produce the observed velocities. It is however unclear, which physical mechanism could lead to such a fine tuning of the damping length.

- Considering the effect of small amplitude sound waves on isothermal atmospheres ($T = T_* = 3000$ K), Pijpers and Hearn (1989) have investigated the driving mechanism by the acoustic waves, prescribing the damping length as a parameter and their calculations exhibits the well agreement of the mass loss rates and the terminal velocities with the observed values. Generally, these winds accelerate slowly over a long distance (Hearn 1990) and the transition from subsonic to supersonic motion occurs outside of $10R_*$. However, dust forms much closer to the photosphere (e.g. Danchi *et al.* 1990, Danchi *et al.* 1994). The additional action of radiation pressure on dust would then not only lead to higher terminal velocities, but also to considerably higher mass loss rates and thus would completely dominate the wind structure. Wind generation by sound waves, therefore seems unlikely to be a primary mechanism in dusty AGB stars.
- Since most AGB stars with high mass loss rates are also known to be long period variables, the effects of shock waves alone as a driving mechanism for late type stellar outflows have been investigated e.g. by Wood (1979) in the isothermal limit case as well as in the adiabatic case. In the isothermal case, no continuous outflow is produced and only a small amount of material is occasionally ejected. The mass loss rates produced by these models are of the order of $10^{-12}M_\odot\text{yr}^{-1}$ and therefore, pure isothermal shocks seems to be not the mechanism causing the observed much higher values. In the adiabatic models,

Wood's calculations were considerably improved by Bowen (1988), considering a time dependent post-shock relaxation of the gas by means of a parameterized cooling function. This approach results in rather low outflow velocities which becomes smaller than the escape velocity at $20R_*$. This leads to the rather small mass loss rates of $\dot{M} = 10^{-9}M_\odot\text{yr}^{-1}$). A further result is the formation of a kind of chromosphere, i.e. an extended region between $3R_*$ and $10R_*$ with an enhanced gas temperature of $T_g = 8000$ K. From these results it is obvious that shock waves alone cannot be responsible for the observed winds of AGB stars.

- radiation pressure on dust and/or molecules: levitation of the atmosphere by wave dissipation and effective acceleration of the material by radiation pressure on dust grains.

- radiation pressure on molecules: Although radiation pressure on molecules alone cannot account the outflow, it considerably reduces the effective gravitational acceleration in the atmosphere to lift the material out of the gravitational field and induces high densities at low temperatures which favour effective dust condensation (Jørgensen and Johnson 1992).
- The observation indicates that most dust enshrouded AGB stars are LPVs or Miras (Jura 1986, Habing 1990). Therefore, a two step mechanism has been proposed as being responsible for the mass loss of LPVs (Jones *et al.* 1981), levitation of the atmosphere by dissipation of shock waves and subsequent acceleration of the material by radiation pressure on dust grains. In order to explain the observed mass loss rates ($\dot{M} \geq 10^{-7} M_{\odot} \text{yr}^{-1}$) of AGB stars, Wood (1979) has introduced parameterized expression to account for the effects of dust acceleration. This approach has been improved by Bowen (1988) with regard to the hydrodynamical calculations. However, on both cases, the process of dust formation has been considered in detail and, thus, important coupling between the dust complex and the atmospheric structure have not been taken into account.

Observations indicate that in many dust forming shells the ratio between the momentum flux of the material and the momentum flux of the radiation field is of the order of unity (Jura 1986a) and proportional to the UV optical depth of the dust component in the circumstellar shell (Knapp 1986). This result confirms that radiation pressure on dust grains at least accelerates the wind to its terminal velocity. On the theoretical side, detailed calculations of the hydrodynamic structure of stationary circumstellar dust shells have been performed by several authors (Salpeter 1974, Lucy 1976, Menietti and Fix 1978, Tielens 1983, Beruyser and Frisch 1983, Kozasa *et al.* 1984, Gail and Sedlmayr 1985, Gail and Sedlmayr 1986, 1987). Each of these works emphasizes different aspects of dust forming winds. The common conclusion is that radiation pressure on dust alone is in fact capable of driving an outflow exhibiting the observed high mass loss rates of the star, which implies a minimum luminosity (cf. Gail and Sedlmayr 1987a, Dominik *et al.* 1990). Therefore, dust driven winds are only possible during the late phases of AGB evolution.

A major improvement in the time dependent has been achieved by Fleischer *et al.* (1991,1992) and Höffner *et al.* (1994) for carbon rich cases. In these calculations, the coupled system describing time dependent hydrodynamics, thermodynamics, chemistry and dust formation, growth and evaporation is solved simultaneously. The detailed treatment of the dust complex and of the interaction between dust and the atmospheric structure leads to surprising new dynamic effects, which decisively influence both the resulting shell structure (Fleischer *et al.* (1991,1992) as well as the optical appearance of these models (Winters *et al.* 1993, 1994, 1995, 1996).

1.4 The aim and structure of this work

The aim of this work is to describe the expanding circumstellar dust shells around *oxygen-rich* Miras and LPVs. The CDS around Miras and LPVs is a nonlinear dynamical system, oh which local physics and the global structure are strongly coupled in the interaction among the hydrodynamics, thermodynamics, radiative transfer, chemistry, and dust formation. In order to describe these physical processes of pulsation and dust formation in circumstellar shells, all of physical subsystems have to be treated simultaneous due to their strong coupling.

Even the modelling of a classical stellar atmosphere involves the simultaneous solution of a coupled equation system of hydrodynamic, thermodynamic and chemical structure of atmospheres, the consideration of the formation of solid particles in stellar atmosphere implies a considerable further increase in the complexity of the problem to be solved: a physical description of the phase transition from gas phase and the solid state is required for those chemical species, which possesses a stable solid phase under the circumstellar conditions. Once solid particles have formed in the circumstellar environment, they cause immense influence on the structure of the dust forming atmosphere itself. Therefore, the existence of dust in a system leads to a strong, nonlinear coupling among the different physical subsystems and consequently influence the local and global structure of the circumstellar shell itself.

In contrast to the carbon-rich case, where the chemistry are well informed through the combustion chemistry, inorganic chemistry is still suffering from the lack of the available data for the dust formation process. A possible way to solve this kind of problem is the theoretical calculations e.g. done by in this work based on the quantum mechanical calculations.

Since most of the Miras and LPVs are *oxygen-rich*, the physical understanding of the circumstellar shell around these stars leads us to achieve the more precise description about the whole class of these stars.

This aim shall be approached by the work presented in this thesis in the following way:

Chapter 2 consist of two parts: the physical problem describing a dust forming circumstellar shell and the basic equations constituting the coupled system, which needs to be solved, are discussed. The ingredients necessary for a consistent modelling of such systems are summarized and their mutual interrelations are considered.

Chapter 3 contains the overview about the previous work on the cluster calculations which could serve as the primary condensates in *oxygen-rich* circumstellar shells. The quantum mechanical calculation for the geometry optimisation based on the density functional theory has been represented to get the Gibbs free energy of the TiO_2 clusters via the partition functions. A comparison has been carried out between the calculated Gibbs free energy based on the

density functional theory and the Gibbs free energy derived from the modified nucleation theory adopting the surface energy.

Chapter 4 discussed on the nucleation seeds in the *oxygen-rich* circumstellar shells in the frame of the *homogeneous nucleation* theory, in order to determine the most primary nucleation seed in the circumstellar shells around Miras and LPVs.

Chapter 5 demonstrates the heterogeneous growth on the different nucleation seeds in the gas element prevailing the inner region of the wind. The change of the dust composition on the different nuclei is discussed.

Chapter 6 gives the first results of the *oxygen-rich* circumstellar dust shells around Miras and LPVs and demonstrates the non-linear effect and the complex structure of the dust forming circumstellar shells. Dust is the component that determines the dynamics and structure of the circumstellar shell.

Chapter 7 contains the summary of the main results of this work and the further investigations starting from the results of this present work.

Appendix A contains thermochemical properties of TiO and TiO₂ clusters.

Appendix B contains thermochemical properties of the desultory molecules Ti_xO_y.

Appendix C contains the calculated harmonic wave number in the ground state of Ti_xO_y molecules.

Chapter 2

Basic Equations

2.1 Hydrodynamic equations

In order to investigate dust formation, growth, and evaporation in a volume element of gas under time dependent conditions, the Lagrangian formulation of hydrodynamics is chosen here for the model calculations. Contrary to the Eulerian field description, the paths of an ensemble of small fluid elements are treated individually in the Lagrangian (e.g. Chorin and Marsden 1979).

The radial position R of a certain fluid parcel is described as a function of the Lagrangian variable r , such that at an instant of time t_1 we have $R = R(r, t_1)$, and $r = R(r, t_0)$, which denotes the initial or so called reference configuration. The time development along the path of the fluid is governed by the equation

$$\frac{\partial R}{\partial t} = u \quad (2.1)$$

with the fluid velocity u .

The continuity equation usually is expressed in the Lagrangian form as

$$\frac{D\rho}{Dt} + \rho \nabla \cdot \mathbf{u} = 0 \quad (2.2)$$

where ρ denotes the mass density and D/Dt denotes the material derivate, which is related to the spatial derivative $\partial/\partial t$ via $\frac{D}{Dt}(\cdot) = \frac{\partial}{\partial t}(\cdot) + u\nabla(\cdot)$. In case of the stationary situation $\partial/\partial t = 0$, the mass loss rate \dot{M} can be specified by the integration of the equation of continuity as $\dot{M}(r) = 4\pi\rho r^2 v(r)$.

The equation of motion in Lagrangian is

$$\frac{Du}{Dt} = -\frac{1}{\rho}\nabla p_g + f \quad (2.3)$$

where f and p_g denote an external force and thermal pressure of gas, respectively.

The external forces acting on a fluid element are gravitational deceleration and acceleration due to radiation pressure:

$$f = -\frac{GM}{R^2} + \frac{4\pi}{c} \frac{\chi_H}{\rho} H \quad (2.4)$$

where χ_H denotes the flux weighted mean of the mass extinction coefficient, G the gravitational constant, c the speed of light, and H the Eddington flux. The mass contained in the region under consideration is small compared to the mass of the star we assume $M = M_*$. If the circumstellar shell contains comparatively large mass to the mass of center, this has to be considered and $M = M_* + M_s(r)$ with the mass contained in the circumstellar shells $M_s(r)$ within the radial distance r from the central star.

In the radiative equilibrium the conservation of the radiative flux H can be expressed as $4\pi H = L_*/4\pi r^2$ and hence the external force f can be expressed as follows

$$f = -\frac{GM_*}{R^2}(1 - \alpha) \quad (2.5)$$

with the radiative acceleration α in unit of gravitational acceleration

$$\alpha = \frac{L_*}{4\pi c G M_*} \chi_H \quad (2.6)$$

$$\chi_H = \frac{\int_0^\infty \chi_\nu^{tot} H_\nu d\nu}{\int_0^\infty H_\nu d\nu}. \quad (2.7)$$

The equation of state of a system, the gas pressure p_g can be calculated by ideal gas law

$$pV = \frac{kT_g}{\mu m_H} \quad (2.8)$$

The quantity k is the Boltzmann constant, m_H is the mass of the hydrogen atom and T_g is the gas temperature. A constant molecular weight $\mu = 1.26$ is taken for the calculations.

The system of equation is completed by the gas energy equation

$$\frac{\partial U}{\partial t} = -p \frac{\partial V}{\partial t} + Q \quad (2.9)$$

where U and Q denote the internal energy per unit mass, and the net heating rate, respectively. The quantity Q is the net energy gain of the gas per unit mass and unit time by absorption of radiative energy and by collision with dust grains.

In most parts of this work we deal only with isothermal processes, in the sense that T_g equals the local radiative equilibrium temperature T_{eq} at very instant of time throughout the atmosphere. Thus we treat shocks in the isothermal limit case, i.e. cooling behind the shock fronts is assumed to take place instantaneously. The inclusion of cooling functions is a subject of further important investigations (Gauger *et al.* 1993, Woitke 1997).

2.2 Gas phase chemistry

For the dust formation, it is of course essential to know the chemical composition of the gas phase, i.e. the concentration of all relevant atoms and molecules. The general way of calculating the chemical composition is the solution of the the system of rate equations for all chemically relevant species: Atoms, molecules, ions, and electrons (Goeres *et al.* 1988, Beck *et al.* 1992). However, the solution of this non linear stiff set of equation requires a considerable amount of computing effort. Furthermore, enormous problems are associated with the input data needed for the calculation of the reaction rates which are often uncertain, if at all available.

Chemical equilibrium is, therefore, assumed and the concentrations of species in gas phase become independent of time. The concentration of the species in gas is functions of temperature T , density $n_{<H>}$, and the chemical abundances ε_j of the element j only.

Let E^j denote the element j and let $\overset{\circ}{p}_j$ be the partial pressure of the element E^j in the equilibrium. Then the partial pressure of a molecules $\overset{\circ}{p}_{M_l}$ with the chemical formula $E_{\nu_{l,1}}^1 E_{\nu_{l,2}}^2 \cdots E_{\nu_{l,J}}^J$ is given by

$$\overset{\circ}{p}_{M_l} = k_{M_l} \prod_{j=1}^J \left(\overset{\circ}{p}_j \right)^{\nu_{l,j}} \quad (2.10)$$

where

$$k_{M_l} = \exp\left\{-\frac{\Delta G_l}{kT}\right\} \quad (2.11)$$

is the so called dissociation constant given by the difference of ΔG_l of the Gibbs energy between the molecule and its constituents and k_{M_l} is a function of the temperature alone.

In a closed system, the total number of atoms of every elements is conserved and can be expressed by

Table 2.1: the abundances of the elements given in logarithm (Allen 1974).

He	O	C	N	Fe	Si	Mg	S	Al	Ti
-1.00	-3.18	-3.48	-4.04	-4.40	-4.48	-4.58	-4.80	-5.39	-6.87

$$\sum_{l=1}^L \nu_{l,j} \overset{\circ}{p}_{M_l} = \sum_{l=1}^L \nu_{l,j} k_{M_l} \prod_{j=1}^J \left(\overset{\circ}{p}_j \right)^{\nu_{l,j}} = \varepsilon_j n_{<H>} kT \quad (2.12)$$

where ε_j is the abundance of the element E^j relative to hydrogen.

Gail and Sedlmayr (1987a) discussed an equilibrium chemistry consisting of the elements H, C, N, O, Si, Mg, Al, S, and Fe which are the most abundant elements in typical mixtures in astrophysics (Allen 1974). Only the noble gases He and Ar have been neglected since they are chemically inactive.

Due to the extraordinary strong bond in the CO molecule (11.2eV), it is one of the first molecules formed after which it cannot be easily destroyed. The one of the exceptions is the destruction by UV photons from the interstellar UV radiation field in the outer optically thin regions of the envelope. This has important consequences for the chemistry. In oxygen stars, where oxygen is more abundant than carbon, almost all carbon is contained in the chemically inert CO molecule. Since the same is true for nitrogen through blocking itself by being bound in the N₂ molecule, the remaining oxygen is by far the most abundant element after hydrogen. Therefore, the chemistry in M stars is dominated by water vapour and oxides of less abundant elements like Mg, Si, Al, Fe, and Ti. The molecules considered in this work and the hierarchy of the dissociation equilibrium are given in Tab. 2.2.

Oxygen is essentially present in atomic form at higher temperatures and H₂O at lower temperatures. The OH and O₂ molecule play only minor roles. Silicon is present as SiO at higher temperatures and SiS molecule becomes important as much silicon as there is sulphur present. Magnesium is present in atomic form almost in the complete temperature range and at around 600 K, MgOH becomes present. Iron also is in atomic form almost in the complete temperature range, but at lower temperatures, the amount of Fe(OH)₂ becomes larger than the atomic Fe. Most of Ti is atomic at higher temperatures above 2000 K, but at the lower temperatures TiO and TiO₂ compete, whereas TiO₂ becomes dominated in the gas phase with decreasing temperatures.

A simple equilibrium chemistry may be applied only to model calculations, if the expected deviation from this equilibrium have no crucial consequences for the results. Large non-equilibrium effects in red giants have to be expected, if either a rapid expansion of the medium leads to a frozen chemistry or if UV radiation stronger than that of the usual photospheric radiation field, i.e. the interstellar

Table 2.2: The partial pressure $\overset{\circ}{p}_j$ of the element j and the constituents contributing to the dissociation equilibrium.

$\overset{\circ}{p}_j$	constituents
$\overset{\circ}{p}_H$	H H ₂
$\overset{\circ}{p}_N$	N N ₂
$\overset{\circ}{p}_O$	O OH H ₂ O
$\overset{\circ}{p}_{Si}, \overset{\circ}{p}_S$	Si SiH SiO S H ₂ S HS SO SiS
$\overset{\circ}{p}_{Mg}$	Mg MgH MgO MgOH MgS
$\overset{\circ}{p}_{Fe}$	Fe FeO Fe(OH) ₂
$\overset{\circ}{p}_{Al}$	Al AlOH AlO ₂ H Al ₂ O
$\overset{\circ}{p}_{Ti}$	Ti TiO TiO ₂

UV radiation field or radiation originating from a chromosphere, are present (Beck *et al.* 1992). It is well known that late type giants later than about M5 do not have active chromosphere. Therefore, the UV radiation is only the photospheric field in the inner region of the envelope. Since the stars considered in this work are characterised by effective dust formation, the interstellar UV radiation field will be effectively absorbed in the outer regions of the envelope and will not affect the inner regions, where dust formation takes place.

2.3 Dust Formation

The formation of solid particles from the gas phase is generally a results of chemical reactions leading from a single atoms via small and subsequently larger molecules to macroscopic solid particles. Though the formation of solids is, in principle, a continuous process from atoms to macroscopic particles, it can be generally divided into two parts: Nucleation and growth.

Nucleation: Many competing reactions leading to the formation and dissociation of molecules which can be the candidates for a subsequent growth to macroscopic particles. The formation rate for these large molecules serving as condensation nuclei will be called the *nucleation rate* J_* . This process occur in the *molecular* domain.

Growth/evaporation : the reactions between *macroscopic* dust particles and molecules from the gas phase let describe in some degree more simple than the molecule – molecule reactions, since the properties of macroscopic particles become less dependent on the size of the particle. With a given chemical composition of the grain, the properties of the surfaces do not vary with the grain size. Every unit area on the grain has some reactive sites where reactions with gas molecules can

occur. Therefore, The reaction rates become proportional to the surface area of the grain. This allows the treatment of processes concerning dust by appropriate moment methods as they have used in the literature (e.g. Fix 1969, Draine and Salpeter 1977, Gail and Sedlmayr 1988)

2.3.1 Nucleation

One of the most critical problems in calculating the dust formation is the determination of the nucleation rate, since the nucleation rate is an extremely steep function of the conditions in the gas, especially the gas temperature. The usual *Ansatz* is to consider the most effective chain of reactions from atoms to macroscopic particles and to calculate the flux of clusters through the chain. The production rate of particles in this critical size is the nucleation rate J_* (Gail *et al.* 1984, Gail and Sedlmayr 1988).

The nucleation rate J_* is given by the result of the classical nucleation theory for the stationary nucleation

$$J_* = \tau_{gr}^{-1}(1, N_*) \overset{\circ}{f}(N_*) Z(N_*) \quad (2.13)$$

τ_{gr} is the growth rate of the critical cluster N_* and defined as follows

$$\frac{1}{\tau} = \sum_{i=1}^I i A_1 v_{th}(i) \alpha(i) f(i, t) \left\{ 1 - \frac{1}{S^i} \frac{1}{b^i} \alpha_*(i) \right\} \quad (2.14)$$

$$+ \sum_{i=1}^I i A_1 \sum_{m=1}^{M_i} u_{th}(i, m) \alpha_m^c(i) n_{i,m} \left\{ 1 - \frac{1}{S^i} \frac{1}{b_{i,m}^c} \alpha_*^c(i, m) \right\}. \quad (2.15)$$

with the generalised departure coefficient $b_i, b_{i,m}^c$ due to the thermodynamical and chemical non-equilibrium between the solid and gas phase and the non-TE effect α_*, α_*^c due to the different temperatures and the chemical reactions.

$Z(N_*)$ is the Zel'dovich factor and $f(N_*)$ is the particle density of the critical cluster given by

$$Z = \left(\frac{1}{2\pi} \frac{\partial^2 f(N)}{\partial N^2} \Big|_{N_*} \right) f(N_*) = f(1) \exp \left\{ N_* \ln(S) - \theta_\infty N_*^{2/3} \right\} \quad (2.16)$$

with supersaturation ratio S of nucleating species and the surface energy of cluster θ .

Since the net rate does not depend on the grain radius a , the change of a is the same for all dust particle, independent of their size. The fact that a is a uniquely determined function of t let the independent variable t substitute by a (Gauger *et al.* 1990). Therefore, the actual value of the size distribution function $f(a, t)$ with the

grain radius a during an evaporation phase is given by the value of the function $g = \frac{d}{\xi_A^d} J_* \tau(t)$ for the actual maximum particle radius, i.e. $g(a_{max})|_{a_{max}(t)}$. ξ_A^d is the geometric constant (see in 2.30, 2.32). Then the destruction rate is determined by

$$J_{ev}(N, t) = \frac{1}{\tau d} g(a_{max})|_{a_{max}(t)}$$

2.3.2 Growth and destruction of the dust grains

The dust particles are subject to various processes that alter their size and composition. The different processes are involved in the dust formation: Reaction of the dust grain with a molecule, in which the molecule sticks on the grains, and its reverse reaction as a spontaneous evaporation of the molecule from the grain. Another type of reaction is sputtering effect of molecules on the grains. One sort of molecules sticks on to the grain, while another molecules eventually that belonged to the grain before the reaction, are returned into the gas phase.

With the size distribution of the dust particles $f(V, t)$, the frequency of reaction per unit volume can be written in the general form of $R_i = f(V, t) dV \cdot \omega_i A(V)$ where $A(V)$ is the surface of a grain with volume V and ω_i denotes the reaction frequency per unit surface area and can be written

$$\omega_i = n_i v_i \alpha_i \quad (2.17)$$

where n_i is the number density of the molecules in the gas phase and v_i is the relative velocity between the grain and the molecule. For a spherical dust grain at rest in a gas with kinetic temperature T , $v_i^2 = kT/(2\pi m_i)$ with Boltzmann constant k and the mass of the molecules m_i . α is the number of reactions divided by the number of collisions and therefore is called the reaction probability or the sticking probability. α_i may depend on the properties of the molecule and the interaction energy of the collision as well as on the grain temperature and the chemical composition of the grain surface.

Since the reactions may occur in both directions one may define a net reaction frequency by

$$\omega_i = \omega_i - \omega_{r(i)} = \omega_i(1 - S_i^{-1}). \quad (2.18)$$

S_i is the generalised supersaturation ratio defined by

$$S_i = \frac{\omega_i}{\omega_{r(i)}} = \frac{p(1)}{p_v}, \quad (2.19)$$

where $p(1)$ is the partial pressure of the condensing species in the gas phase and p_v is the vapor saturation pressure with respect to the dust temperature.

In the case of compounds with a definite stoichiometric composition, the equilibrium densities of the molecules involved in the gas phase can be calculated as follows (Dominik 1992). Consider a solid particle $E_{s_1}^1 E_{s_2}^2 \cdots E_{s_J}^J$ consisting of a number of J of chemical elements denoted by E^j . The $s_j, j = 1, \dots, J$ are the stoichiometric coefficient of the solid. From thermodynamics the equilibrium between atoms in the gas and the solid may be expressed by

$$\prod_{j=1}^J p_{E^j}^{s_j} = (p^o)^{\sum_j s_j} \cdot \exp \left\{ \frac{\Delta G_s - \sum_{j=1}^J s_j \Delta G(E^j)}{kT} \right\} \quad (2.20)$$

where ΔG_s is the Gibbs energy of the solid state per monomer and $\Delta G(E^j)$ is the Gibbs energy for the atoms in the gas phase, both Gibbs energies taken relative to their reference states. $p_{E^j}^o, j = 1, \dots, J$ are the equilibrium pressures of the atoms in the gas phase.

By incorporation of this Milne relation, the growth velocity of the dust grains can be then written by

$$\chi = \xi_A^d \sum_{i=1}^I \omega_i V_i = \xi_A^d \sum_i \omega_i (1 - S_i^{-1}) V_i. \quad (2.21)$$

The generalised supersaturation ratio S_i indicates the direction of the net effect of a forward and backward of reactions. If $S_i > 1$, χ becomes larger than zero and the reaction leads to the grain growth and if $S_i = 1$, the reaction is balanced and is in case of the thermodynamic equilibrium. If $S_i < 1$, the reaction occur reverse and by the evaporation of the respective species the dust particles are destructed.

It is possible that not all S_i are either greater or less than unity. In this case, different competing processes take place on the surface of the dust grains and the net effect (determined by the value of χ) cannot be seen from a single supersaturation ratio alone (Gauger *et al.* 1990).

The maximum radius of the dust grain can be derived from the growth velocity χ as follows

$$a_{max} = a_l + \frac{\xi_A^d}{d} \int_{t_i}^t \chi(t') dt' \quad (2.22)$$

where t_i is the time of onset of dust formation, when the particle size exceeds the macroscopic size a_l .

2.3.3 Chemical composition of the dust grains

If reactions on all grains proceed in the same way, the grains have the same chemical composition at their surface. This composition is determined by the composition

of the actually condensing material from gas phase. The number of a condensing species m_ℓ per unit time and on a unit surface of the grains is given by $\sum_{m_\ell=1}^M \omega_{m_\ell}$. The change in the abundance of an element i due to the growth by condensing species on the dust grains can be, therefore, written by

$$\dot{\epsilon}_i = -\frac{\xi_A^d}{n_{<H>}} \sum_{i=1}^M \nu_{m_\ell, i} \omega_{m_\ell} L_{j-1} \quad (2.23)$$

where $\nu_{m_\ell, i}$ is the stoichiometric number of atom i contained in the condensing species m_ℓ . From this quantity, the depletion of elements from the gas phase, which is called the degree of condensation can be calculated for the element i , $f_c^i = \int dt' \dot{\epsilon}_i$.

2.4 The moment equations

The moment equation with a size distribution function $f(V, t)$ of the dust grains with volume V at time t are defined as follows (Gail *et al.* 1984, Gail and Sedlmayr 1988, Dominik *et al.* 1993)

$$L_j(t) = \int_{V_l}^{\infty} f(V, t) V^{j/d} dV \quad (2.24)$$

$$\frac{d}{dt} L_0 = J_l \quad (2.25)$$

$$\frac{d}{dt} L_j = J_l^{j/d} V_l + \frac{j}{d} \chi L_{j-1} \quad j = 1, 2, 3 \quad (2.26)$$

Here d indicates the geometry of the dust particle, V_l is the lower boundary of the dust volume where the particles are considered to be macroscopic, usually about 10^2 to 10^3 atoms, and χ is the growth velocity of the dust grains. The moments have units $[\text{cm}^j]$ and are closely related to the averages of the powers of the particle radius with respect to the size distribution. Generally, the moment equations are normalised by the total number density of hydrogen $n_{<H>}$.

J_l is particles flux into the cluster through the boundary value of volume V_l . If the process associated with a positive change in volume V_l are dominant in the region around V_l , J_l can be regarded as the nucleation rate J_* and this can be calculated by means of a microscopic theory. If on the other hand the processes associated with a negative change in volume are dominant, one needs to know the value of $f(V, t)$ in the interval $(V_l, V_l + |V_i|)$. Due to the condition $V_l \gg |V_i|$, one may assume that $f(V, t)$ is only varying slowly in this small interval and may approximate $f(V_l + V_i, t)$ by $f(V, t)$. Hence, the only information one needs to know for the calculation of J_l in this case is the value of the size distribution at the lower boundary (Gauger *et al.* 1990, Dominik 1992).

For spherical grains with $d = 3$, the total number of grains n_d per cm^3 , the mean grain radius, the mean grains surface $\langle A \rangle$, and the mean grain volume $\langle V \rangle$ can be calculated from the moment equation as follows

$$n_d = L_0 \quad (2.27)$$

$$\langle a \rangle = \xi_a^d V^{\frac{1}{d}} = \xi_a^d \frac{L_1}{L_0} \quad (2.28)$$

$$\langle A \rangle = \xi_A^d V^{\frac{d-1}{d}} = \xi_A^d \frac{L_2}{L_0}$$

$$\langle V \rangle = \frac{L_3}{L_0}.$$

ξ_a^d and ξ_A^d are constants depending on the geometry of the grains. For $d = 2$ these values are

$$\xi_a^d = \sqrt{\frac{1}{\pi}} \quad (2.29)$$

$$\xi_A^d = \sqrt{4\pi} \cdot 2a_{reactive} \quad (2.30)$$

where $a_{reactive}$ is the width of the reactive ring at the edge of the circular grain and for spherical grains with $d = 3$ these geometric constants are

$$\xi_a^d = \sqrt[3]{\frac{3}{4\pi}} \quad (2.31)$$

$$\xi_A^d = \sqrt[3]{36\pi}. \quad (2.32)$$

2.5 Radiative transfer

Radiative transfer equation describes the interaction between photons and the material in the atmospheres and is generally derived from the Boltzmann equation of the particle transport in kinetic theory (e.g. Mihalas 1978). Since the typical time scale of transport coefficients variation is longer compared to the light travel time through the circumstellar shells (e.g. Winters 1994), the radiative transfer equation is considered as stationary here for the calculations.

The radiative transfer problem is solved in grey approximation by the method of Unno and Kondo (1976,1977). With the separation angle $\mu' = \cos \theta$ and the calculated from

$$\frac{\partial \mu'}{\partial r} = \frac{\rho \chi_H}{4} + \frac{3\mu'}{r} - \frac{5}{4} \rho \chi_H \mu'^2 - 3 \frac{\mu'^3}{r},$$

the temperature structure can be derived as follows

$$T_{eq}^4 = \frac{\kappa_J}{\kappa_P} \frac{\pi}{\sigma} \frac{L_*}{8\pi^2} \left\{ \frac{1}{1 + \mu'(R_{out})R_{out}^2} + \frac{\mu'(R_{out})}{R_{out}^2} - \frac{\mu'}{r^2} + \frac{3}{2} \int_r^{R_{out}} \left(\frac{\rho\chi_H}{r'^2} + \frac{2\mu'}{r'^2} \right) \right\}.$$

In case of $R_{out} \rightarrow \infty$ and $\mu' = \mu_* = \sqrt{1 - (R_*/r)^2}$, the Lucy approximation can be derived from the equation of T_{eq} (Lucy 1971, 1976).

For the solution of the radiative transfer problem in the approximation, the *flux mean* of the absorption coefficient is required. For the calculation of this mean the Eddington flux of the radiation field has to be known (which is only the case if the radiative transfer is explicitly solved). The mean mass absorption coefficient κ_H is the sum of the dust opacity κ_d and the gas opacity κ_g . The gas opacity is assumed to be constant, $\kappa_g = 2 \cdot 10^{-4} \text{g}^{-1} \text{cm}^{-2}$, based on the Rosseland mean opacity (Alexander *et al.* 1983, Bowen 1988).

The absorption coefficient for the dust generally can be calculated from the Mie theory. In the calculations presented here the *small particle limit* of the Mie theory has been used which is applicable if the particle radii are small compared to the wavelength of the light divided by 2π . If this condition is valid, the absorption cross section of the particle is proportional to its volume.

Since the total volume occupied by grains per unit gas volume is given by L_3 , the absorption coefficient may be written as

$$\kappa_{abs}(\lambda) = \frac{6\pi}{\lambda} L_3 \text{Im} \left\{ \frac{m^2 - 1}{m^2 + 2} \right\} \quad (2.33)$$

(Wickramasinghe 1972). The scattering coefficient in this approximation always is small compared to the absorption coefficient and may be neglected. For the dust opacity, the optical constants are taken for astronomical silicates by Draine and Lee (1984) which is tabulated in Draine (1985) for the calculations in this work.

The optical constants of grains depend not only on the dust material, but also on the microscopic structure of the particles. The recent observations (e.g Waters *et al.* 1999) imply the presence of amorphous and crystalline of oxides in the circumstellar envelopes. Considering the grain structure in case of the crystalline, however, requires intense investigation on the optical properties.

2.6 Boundary conditions

The coupled equation systems describing the circumstellar shells require the initial values and the boundary conditions as follows

$$R_{inner} = R_0 + \Delta u \frac{P}{2\pi} \sin \left(\frac{2\pi}{P} t \right) \quad (2.34)$$

From the 2.1, the velocity at the inner boundary u_{inner} varies

$$u_{inner} = \Delta u \frac{P}{2\pi} \cos\left(\frac{2\pi}{P}t\right) \quad (2.35)$$

The velocity amplitude Δu simulates the interior pulsation of the star with the pulsation period P . At every period $t=nP$, the inner boundary locates at its initial position R_0 moving outward with the velocity Δu . This instant of time is defined as the zero phase of the pulsation cycle as the beginning of the hydrodynamic cycle. The radiative flux at the inner boundary R_0 is assumed to be constant.

Chapter 3

Clusters

3.1 Overview

In an oxygen-rich circumstellar environment the formation of seed nuclei for subsequent growth of dust grains is not possible by nucleation of abundant gas phase species bearing the abundant dust forming element like Si, Fe, and Mg (Gail & Sedlmayr 1998). The onset of dust formation would occur in this case at a temperature significantly lower than derived from IR emission from circumstellar dust shells (Danchi *et al.* 1994). Therefore, dust formation is triggered by the formation of cluster from molecules bearing less abundant element like Al and Ti: Al has a slightly lower abundance than Si, Fe, and Mg and the Al-bearing compounds have high stability due to their high bond energy. Titanium compounds have exceptional high bond energies and the solid titanium compounds favor condensation at high temperatures despite the lower abundance of Ti.

The formation of small clusters is the first step of the condensation process from the vapor and this process can be described quantitatively, if the Gibbs free energy of formation $\Delta_f G^\circ(N)$ of the clusters is known. Several calculations exist for thermodynamic properties of those clusters which can be considered as the primary condensation seed.

For $(\text{MgO})_n$ clusters ($n=1-16$), Köhler *et al.* (1997) calculated the thermodynamic properties using a semi-empirical interaction potential. The magnesium oxide solid is assumed to be a pure ionic compound formed from Mg^{2+} cations and O^{2-} anions, respectively. The crystal structure of the solid is of the NaCl lattice type. The properties of such ionic crystals can well be described by the classical Born–Mayr potential model, as is well known from solid state physics (Martin 1983). Since the dissociation energy of the MgO molecule has been considerably revised to lower values, it is unlikely that MgO is an important species for the circumstellar dust formation problem.

Iron is one of the most abundant elements having a stable condensate. From this criterion of abundance, clustering of iron atoms is considered to initiate the

dust formation process (Gail & Sedlmayr 1986). Following the general concept for MgO, John (1995) has calculated the nucleation rate for iron clusters up to $n=19$. In this case, the particle–particle interaction can not be described by the Born–Mayr potential model, but the bond energy of clusters is available from experimental values. The bond energy for Fe_2 and Fe_3 is small and the equilibrium abundances of clusters with such a small dissociation energy is low at the relevant temperature (> 1000 K), in the dust forming zone. Since the growth chain has to pass through the clusters Fe_2 and Fe_3 during the nucleation process, the nucleation of iron atoms can be effective only well below 1000 K.

The thermodynamic properties of molecular Al_2O_3 that is expected to be the first condensation species in oxygen–rich circumstellar environments (Kozasa & Hasegawa 1987, Sedlmayr 1989, Tielens 1990, Ohnaka *et al.* 1989, Begemann *et al.* 1997, Nittler *et al.* 1997, Kozasa *et al.* 1999) are presented in Patzer *et al.* (1999) for seven different geometric isomers, for which the molecular data of Al_2O_3 are obtained from *ab initio* calculations (Chang *et al.* 1998) with Møller–Plesset second order perturbation theory and 6-31G(d) basis set (Rassolov *et al.* 1998). The numerical expenditure prevents the applications of this quantum mechanical *ab initio* method to clusters of larger size. Chemical equilibrium calculations show that the local concentration of the nominal molecule, Al_2O_3 , almost vanishes in the relevant temperature range (Patzer *et al.* 1999) due to the low stability, although the supersaturation ratio of this molecule is of considerable value due to the small vapor pressure. This indicates that the *homogeneous* nucleation of Al_2O_3 is inefficient. the other nucleation of Al_2O_3 could occur *heterogeneous*, but this is unlikely as well, since the stability of the contributing Al_xO_y clusters to the heterogeneous nucleation is low.

The TiO molecule forms at rather high temperatures in the atmospheres of K and M stars due to its high bond energy of about 6.87 eV (Huber & Herzberg 1979). The stability limits of titanium oxides occur in a pressure–temperature region where the titanium in the gas phase is nearly completely bound in the TiO_2 molecule which may condense into a solid of the same stoichiometric composition (see also Gail & Sedlmayr 1998). An serial uptake of TiO_2 molecule would be the kinetically most simple process to form the seeds which serve later as the nuclei for the heterogeneous growth. Hence, the investigation about the cluster formation of TiO_2 is the first step to explore whether this process triggers the observed dust formation of M stars.

3.2 Previous investigations on titanium oxides

Regarding gas phase species, there is extensive literature on the isolated TiO molecule which is both spectroscopically (Merer 1984, Barnes *et al.* 1997, Loock *et al.* 1998) and theoretically (Bauschlicher *et al.* 1983, Dolg *et al.* 1987, Bakalbassis *et al.* 1996) well understood. Less has been reported about the TiO_2 molecule for which a few available electronic structure calculations (Ramana & Phillips 1988, Bergström

et al. 1996, Rosi *et al.* 1998) and experimental studies (Kaufman *et al.* 1967, McIntyre *et al.* 1971, Chertihin & Andrews 1995) show that the molecule is bent (C_{2v}) with angle $110^\circ \pm 15$ and has a singlet ground state. Mass spectroscopic studies of gaseous reaction equilibria involving TiO and TiO_2 gave a dissociation energy of 13.18 ± 0.12 eV for the dioxide (Huber and Herzberg 1976) and infrared spectroscopy of TiO_2 trapped in a neon matrix at 4 K gave the stretching frequencies $934.8\text{ cm}^{-1}(\nu_3)$ and $962.0\text{ cm}^{-1}(\nu_1)$ (McIntyre *et al.* 1971). A weak emission system of TiO_2 at 5295 \AA leading to the ground state was also observed in a neon matrix. This emission could arise from either a bent-bent or linear-bent electronic transition.

Although bulk and surface properties of titanium dioxide in solid phases have been amply studied due to their importance in technology (Henrich and Cox 1994, Hagfeldt *et al.* 1992), studies on gas phase titanium oxide clusters have been rather scarce. Only recently interest has been growing in small isolated titanium-oxygen systems Ti_xO_y and clusters thereof, all of which disclose an amazingly rich structural diversity of strongly bound neutral, charge, and spin states (Yu & Freas 1990, Wu & Wang 1997) and there has been quite some interest in TiO_2 nanoparticles (Saraf *et al.* 1998). On the theoretical side there is a small number of articles on isolated Ti_xO_y systems employing various different levels of electronic structure theory (Hagfeldt *et al.* 1992, 1993, 1994; Albaret *et al.* 1999; Tsipis and Tsipis 1999). Experimentally, there have been two reports on the cation mass distributions of the Ti_xO_y^+ clusters (Yu & Freas 1990, Guo *et al.* 1992) employing an empirical ionic pair potential model and one report about the electronic structure of titanium dioxide cluster ($n=1-4$) using anion photo-electron spectroscopy (Wu & Wang 1997). A mass spectroscopic investigation of the vapor at high temperatures between 2000 K and 2500 K has been carried out for gaseous Ti_2O_3 and Ti_2O_4 by Balducci *et al.* (1985). There is no spectroscopic or structural information on any higher Ti_xO_y clusters other than TiO and TiO_2 from the laboratory works.

Inspired by the results of Yu & Freas, Hagfeldt *et al.* (1993,1994) performed HF/STO-4G* study on the structure and energy levels of $(\text{TiO}_2)_n$ clusters for $n=1-3$ and the recent DFT/LSDA was calculated by Albaret *et al.* (1999) for the same size of $(\text{TiO}_2)_n$ clusters. In order to understand the chemical and physical properties of bulk TiO_2 , Hagfeldt *et al.* (1992) carried out calculations of the density of states for the small $(\text{TiO}_2)_n$ clusters $n=1,3,6,9$ and 14 by means of the semi-empirical intermediate neglect of differential overlap (INDO) method.

3.3 The electronic structure of Ti_xO_y Clusters

Clusters of titanium oxides could play an important role in dust formation processes from the gas phase in circumstellar shells of oxygen-rich stars (Gail & Sedlmayr 1998, Jeong *et al.* 1999a, Jeong *et al.* 1999b). For a study of this kind of processes information about thermodynamic and energetic properties of the gas phase species is required. Unfortunately often these data cannot be found in the literature for

the relevant molecular species. In this case, theoretical computation is the only possibility to obtain at least some estimates of the desired quantities. Performing density functional theory (DFT) calculations were carried out for the electronic structure of Ti_xO_y clusters and the partition functions and the thermochemical properties, e.g. the Gibbs free energy of formation, were derived to calculate the nucleation rate .

3.3.1 Density Functional Theory

A major impact on electronic structure calculations is done through the density functional theory, where emphasis has been put in particular on ground state properties of solids. This theory has also been widely applied to the computation of excitation energies where its basis is less founded than for ground state calculations. It provides a scheme for calculating these properties and avoids the problem of calculating the ground state wave function (e.g. Fulde 1993, Parr & Yang 1989). The density functional approach expresses ground state properties, such as total energies and equilibrium positions in terms of the electronic density $\rho(r)$.

Thomas and Fermi (March 1975) had attempted to formulate such an approach in the 1920s in terms of a variational method for determining the electron density $\rho(r)$ in the ground state of an inhomogeneous system such as an atom. The ground state energy E is expressed in terms of $\rho(r)$ and minimized. The crucial assumption of the Thomas–Fermi method is the form of the functional chosen to express the energy in terms of the density.

$$E[\rho] = \int d^3r V(\mathbf{r})\rho(\mathbf{r}) + \frac{e^2}{2} \int d^3r \int d^3r' \frac{\rho(\mathbf{r})\rho(\mathbf{r}')}{|\mathbf{r} - \mathbf{r}'|} + \frac{3}{10m}(3\pi^2)^{2/3} \int d^3r \rho^{5/3}(\mathbf{r}). \quad (3.1)$$

The first term represents the energy of an electron density $\rho(\mathbf{r})$ in an external electrostatic potential $V(\mathbf{r})$ and the second term is the Coulomb repulsion energy of a classical charge distribution $\rho(\mathbf{r})$. The third term represents the kinetic energy of the electronic charge distribution, and is obtained through the corresponding functional for the homogeneous electron gas, by assuming that these relations also hold for an inhomogeneous system, which is a reasonable approximation only as long as $\rho(\mathbf{r})$ varies sufficiently slowly.

The ground state density $\rho(\mathbf{r})$ can be derived by varying $E[\rho]$, under the condition that the total electron number density remains constant. Introducing a chemical potential μ and the effective potential $V_c(\mathbf{r}) = e^2 \int d^3r' \rho(\mathbf{r}')/|\mathbf{r} - \mathbf{r}'|$, the density $\rho(\mathbf{r})$ is written as

$$\rho(\mathbf{r}) = \frac{(2m)^{3/2}}{3\pi^2} [\mu - V(\mathbf{r}) - V_c(\mathbf{r})]^{3/2}. \quad (3.2)$$

Although the kinetic energy is treated with crude approximation and the exchange and correlations due to the interaction between electrons are neglected, this method contains the important ingredients of the density functional theory.

Recent developments of density functional theory are based on two theorems by Hohenberg and Kohn (Hohenberg & Kohn 1964, Kohn 1965, Perdew 1986). First, the ground state energy E of a many-electron system in the presence of an external potential $V(\mathbf{r})$ is a functional of the electron density $\rho(\mathbf{r})$ and can be written as

$$E[\rho] = \int d^3r V(\mathbf{r})\rho(\mathbf{r}) + F[\rho]. \quad (3.3)$$

$F[\rho]$ is here an unknown, but universal functional of the density $\rho(\mathbf{r})$ only, and does not depend on $V(\mathbf{r})$. The second theorem is that $E[\rho]$ is minimized by the ground state density. The functional $F[\rho]$ is divided into three parts:

$$F[\rho] = \frac{e^2}{2} \int d^3r d^3r' \frac{\rho(\mathbf{r})\rho(\mathbf{r}')}{|\mathbf{r} - \mathbf{r}'|} + T_0[\rho] + E_{xc}[\rho]. \quad (3.4)$$

The first term describes the Coulomb repulsion of the electrons and $T_0[\rho]$ is the kinetic energy of a system of noninteracting electrons. $E_{xc}[\rho]$ is usually called the exchange and correlation energy. Here it should be noted that $T_0[\rho]$ is not the true kinetic energy of the system, which would be hard to calculate due to the many body effects, but the kinetic energy of a fictitious noninteracting system with the ground state density $\rho(\mathbf{r})$.

In order for $E[\rho]$ to be minimized, the density must satisfy the variational equation

$$\int d^3r \delta\rho(\mathbf{r}) \left\{ V(\mathbf{r}) + e^2 \int d^3r' \frac{\rho(\mathbf{r}')}{|\mathbf{r} - \mathbf{r}'|} + \frac{\delta T_0[\rho]}{\delta\rho(\mathbf{r})} + \frac{\delta E_{xc}[\rho]}{\delta\rho(\mathbf{r})} \right\} = 0 \quad (3.5)$$

The variation $\delta\rho(\mathbf{r})$ is subject to the subsidiary condition $\int d^3r \delta\rho(\mathbf{r}) = 0$ in order for the total electron number to be conserved. The important observation is Eqn. 3.5 is precisely the same as for a noninteracting electron system in which the electrons move in an effective external potential

$$V_{eff}(\mathbf{r}) = V(\mathbf{r}) + e^2 \int d^3r' \frac{\rho(\mathbf{r}')}{|\mathbf{r} - \mathbf{r}'|} + v_{xc}(\mathbf{r}) \quad (3.6)$$

with an exchange–correlation potential $v_{xc}(\mathbf{r}) = \delta E_{xc}[\rho]/\delta\rho(\mathbf{r})$. In practice it is sometimes difficult to determine the functional derivative even when $E_{xc}[\rho]$ is known. The equivalence to a noninteracting electron system has become possible, due to the way the kinetic energy $T_0[\rho]$ has been extracted. This implies that $\rho(\mathbf{r})$ can be obtained if first Schrödinger equation of the form

$$\left(-\frac{1}{2m}\nabla^2 + V_{eff}(\mathbf{r})\right) \chi_\mu(\mathbf{r}) = \varepsilon_\mu \chi_\mu(\mathbf{r}) \quad (3.7)$$

A common is in order on the physical significance of the eigenvalues ε_μ of Eqn. 3.7 and is taken usually

$$2 \sum_{\mu}^{N/2} \varepsilon_\mu = T_0[\rho] + \int d^3r V_{eff}(\mathbf{r}) \rho(\mathbf{r}) \quad (3.8)$$

From Eqs. 3.1 and 3.4 the total energy is given by

$$E[\rho] = 2 \sum_{\mu}^{N/2} \varepsilon_\mu - \frac{e^2}{2} \int d^3r d^3r' \frac{\rho(\mathbf{r})\rho(\mathbf{r}')}{|\mathbf{r} - \mathbf{r}'|} + E_{xc}[\rho] - \int d^3r v_{xc}(\mathbf{r}) \rho(\mathbf{r}) \quad (3.9)$$

Here v_{xc} is the exchange correlation potential and has been defined by $v_{xc}(\mathbf{r}) = \delta E_{xc}[\rho] / \delta \rho(\mathbf{r})$ and the complexity of the real many-body problem is contained in the unknown exchange correlation potential. The real eigenvalue ε_μ does not describe electronic excitation energies, but it is generally understood to be complex quantities due to the finite lifetimes of the excitations.

3.3.2 Computational Aspects

For all computations the Gaussian94 systems was used (Frisch *et al.* 1994). The chosen basis set is of standard all electron split valence 6-31G(d) type (Rassolov *et al.* 1998). Preliminary test calculations revealed that for the systems under consideration it is auspicious to employ a gradient corrected hybrid exchange correlation functional within the density functional theory (DFT) approach. Compared to other choices, it turned out that the B3P86 functional (Becke 1993, Perdew 1986) was the most appropriate commensurate with the crucial quantity of the energy of atomisation. We therefore can support a remark by Gill (1996) that the P86 functional is at times more advantageous yielding systematically better predictions than e.g. the later developed PW91 functional. We conjecture that this might hold especially true for transition metal oxide systems, although there are only a few publications comparing different functionals with respect to this kind of species (Berström *et al.* 1996, Rosi *et al.* 1998, Tsipis & Tsipis 1998).

At the chosen level of electronic structure theory viz. DFT/B3P86/6-31G(d), which is a compromise between desired accuracy and computational cost, all geometric structures were fully optimized starting from configurations that were determined at a smaller basis level (STO-3G) beforehand.

The energies of atomisation were computed according to

$$D_{at} = \left(\sum_{j=atom} n_j E_{tot}(j) \right) - E_{tot}(molecule) \quad (3.10)$$

where n_j is the number of the atoms j contained in the molecule and the experimentally observable quantity then is

$$D_0 = D_{at} - E_{zp} \quad (3.11)$$

where E_{zp} is the zero point vibrational energy.

In the frequency calculations the vibrational wave numbers $\tilde{\nu}_k$ were computed in the harmonic approximation. The integrated absorption coefficients A_k for strictly harmonic motion are then given by

$$A_k = \int_{\nu} \epsilon_k(\nu) d\nu = \frac{\pi}{3c} \left| \left(\frac{\partial \vec{\mu}}{\partial Q_k} \right)_0 \right|^2 \quad (3.12)$$

where c is the speed of light, $\vec{\mu}$ the electric dipole moment, and Q_k the normal coordinate of the k -th vibrational mode. The linear absorption coefficient ϵ is macroscopically defined by the intensity relation

$$dI(\nu) = -\epsilon(\nu) n_0 I(\nu) dl \quad (3.13)$$

where n_0 is the number density of the particles in $[\text{cm}^{-3}]$.

3.4 Results and Discussions

The equilibrium structures of all investigated Ti_xO_y systems are depicted in Fig. 3.1. Their geometric, energetic, and vibrational properties will be subsequently discussed. It should be noted that for every system only one low energy isomer was explicitly treated, because the specific focus will be on those local minima that follow a particular structural building principle. The discussion involves comparison of our findings with previous studies which deal with the determination of stable isomers of various Ti_xO_y clusters and which were essentially of threefold nature: First of all a force field approach employing an empirical ionic pair potential model by Yu and Freas (1990). Secondly, inspired by the results of Yu and Freas an *ab initio* HF/STO-4G* study by Hagfeldt *et al.* and finally the recent DFT/LSDA approach by Albaret *et al.* (1999).

Tab. 3.1 grossly summarises the comparative structures. Geometric and energetic data of this work are given in Tab. 3.2 - 3.4.

3.4.1 Equilibrium geometries

(TiO)_n n=1-3: The calculated interatomic distance of the monomer TiO is 1.57 Å, cf. the experimental value of 1.62 Å [36]. The optimised structure of dimer (TiO)₂

Table 3.1: Comparison of the calculated equilibrium geometries and assigned point groups discussed in previous studies and the present work.

Molecule	Yu & Freas	Hagfeldt <i>et al.</i>	Albaret <i>et al.</i>	This Work
(TiO ₂) ₂	D_{2h} C_1	C_{2h} C_{3v}	C_{2v} C_{3v}	C_{2v}
(TiO ₂) ₃	D_{2d} C_s	C_s	C_s S_4	C_{2h}
(TiO ₂) ₄	C_s			C_{2h}
Ti ₂ O ₃	C_{2v}	C_s		C_s
TiO ₃			C_s	C_s

is a lozenge (D_{2h}) with an edge length of 1.78 Å and an angle $\theta_{\text{OTiO}} = 94^\circ$. The trimer (TiO)₃ is of C_{2v} symmetry. Its two quadrangular units share one side which is the longest of all usually unequal Ti–O distances. In general, the Ti–O distances in the (TiO)_n systems increase as the number of the atoms in the clusters is growing.

(TiO₂)_n n=1-6: the monomer TiO₂ has a bent C_{2v} structure. Its computed interatomic distance and angle are 1.62 Å and 110.4°, respectively. These are in good agreement with the experimentally determined values of 1.62 ± 0.08 Å and $110^\circ \pm 15^\circ$ (McIntyre *et al.* 1971).

For the dimer (TiO₂)₂, only one structure of C_{2h} symmetry could be located in contrast to the studies by Hagfeldt *et al.* (1993) and by Albaret *et al.* (1999) who report another pyramidal C_{3v} species. It has two pendant oxygen atoms bound to a rhombic unit similar to the one in (TiO)₂. The other isomeric structure of C_{3v} symmetry found by Hagfeldt *et al.* (1993) could only be reproduced by a geometry optimisation with a smaller basis set (STO-3G). Employing the larger standard 6-31G(d) basis, the DFT/B3P86 geometry optimisation reveals a transgression of this C_{3v} structure to the C_{2h} species. This means that the C_{3v} configuration could not be located at a higher level of theory in contrast to the previous investigations (Yu & Freas 1990, Hagfeldt *et al.* 1993, Albaret *et al.* 1999a,1999b).

The calculated equilibrium structure of the trimer (TiO₂)₃ is of C_2 symmetry. Its main characteristic are two kite-shaped perpendicularly oriented Ti₂O₂ units sharing a Ti atom as vertex. The optimised configuration of the tetramer (TiO₂)₄ belongs to the C_{2h} point group and is composed of a central parallelogram-shaped Ti₂O₂ unit perpendicularly linked to two kite-shaped Ti₂O₂ units at two ends having each a common Ti atom as a vertex. The number of these central parallelogram-shaped Ti₂O₂ units increases linearly as (n–3) with the size n of the (TiO₂)_n systems. This could reflect a possible structural building principle of one sort of (TiO₂)_n isomers, in general. Furthermore, it can be noted that the interatomic Ti–O distances remain little affected as the size of the molecules grows.

The non-stoichiometric molecules, TiO₃, Ti₂O, Ti₂O₃, Ti₃O₄, and Ti₃O₅:

The optimised equilibrium structure of TiO_3 is of C_s symmetry. The two interatomic distances are 1.81 Å and 1.6 Å. The interatomic O–O distance is 1.46 Å. The angle between the two longer 1.81 Å distances is 66°. Ti_2O is bent (C_{2v}) with an angle of 95°.

In Ti_2O_3 , Ti_3O_4 , and Ti_3O_5 , the Ti–O distances are all different. Their calculated equilibrium structures all belong to the C_s point group. Ti_2O_3 has a kite-shaped Ti_2O_2 unit which is characterised by the distances of 1.74 Å and 1.90 Å. The length of the pendant oxygen to this kite-shaped unit is 1.61 Å. The two oxygen deficient systems Ti_3O_4 and Ti_3O_5 (with respect to $(\text{TiO}_2)_3$) also exhibit those typical basic kite-shaped building units. In Ti_3O_4 there are two of such that are geometrically identical, whereas in Ti_3O_5 they are differing due to the presence of a pendant oxygen atom at one end.

From the results described above the following rough rules can be concluded: *For $(\text{TiO})_n$ and the non-stoichiometric molecules, the interatomic distances and angles are essentially determined by the total number of the atoms, whereas these quantities are little affected by the increasing cluster size for the $(\text{TiO}_2)_n$ series. The interatomic distance of the pendant oxygen remains constant, 1.60 Å, independent of the total number of atoms in all Ti_xO_y molecules.*

There seems to be a basic building principle for one kind of stable $(\text{TiO}_2)_n$ isomers which consists of several central parallelogram-shaped Ti_2O_2 units linked to two kite-shaped Ti_2O_2 units all having a common Ti atom as a vertex and all being perpendicularly oriented to each other. *For the $(\text{TiO})_n$ clusters, the basic building block is rhombic, whereas the non-stoichiometric molecules have two different kite-shaped Ti_2O_2 units in their geometric structures.* These building principles are illustrated in Fig. 3.1.

3.4.2 Energetics

The total electronic energy E_{tot} , the atomisation energy D_{at} and the zero point energy D_{zp} for all investigated Ti_xO_y molecules are given in Tab. 3.4.

The calculated dissociation energy D_0 of the monomer TiO is 6.56 eV which is comparable to the experimental value of 6.87 eV (Huber & Heryberg 1979). The atomisation energy D_0 of TiO_2 is 13.79 eV which is 0.73 eV larger than the value from experiment (13.06 eV) (Balducci *et al.* 1985a). $(\text{TiO}_2)_2$ has a D_0 of 32.93 eV, compared to the experimental value 31.27 eV (Balducci *et al.* 1985a), whereas the D_0 of Ti_2O_3 is 25.34 eV and deviates by 1.38 eV from the mean experimental value (Balducci *et al.* 1985b).

The bond strength of the pendant Ti–O unit, E_{pend} , was directly calculated from the differences of the dissociation energies of the involved molecules. A significant energy of 7.6 eV was evaluated for the dissociation of the pendant oxygen off $(\text{TiO}_2)_2$ and Ti_2O_3 , Ti_3O_5 and Ti_3O_4 , as well as $(\text{TiO}_2)_3$ and Ti_3O_5 as follows:

Table 3.2: Equilibrium geometric parameters of the investigated Ti_xO_y systems. (Interatomic distances r_{ij} in [\AA] and angles θ_{ijk} in [deg]: the geometric meaning of these parameters can be inferred from Fig. 3.1).

Clusters	Symmetry	r_{ij}	θ_{ijk}
TiO	$C_{\infty v}$	$r_{12} = 1.57$	
(TiO) ₂	D_{2h}	$r_{14} = 1.78$	$\theta_{314} = 86$
(TiO) ₃	C_{2v}	$r_{16} = 1.71$	$\theta_{162} = 99$
		$r_{14} = 1.84$	$\theta_{142} = 91$
		$r_{26} = 1.92$	$\theta_{426} = 80$
		$r_{24} = 2.02$	$\theta_{416} = 90$
TiO ₂	C_{2v}	$r_{12} = 1.62$	$\theta_{213} = 110.4$
(TiO ₂) ₂	C_{2h}	$r_{13} = 1.84$	$\theta_{314} = 85.5$
		$r_{15} = 1.61$	$\theta_{215} = 123$
(TiO ₂) ₃	C_2	$r_{34} = 1.84$	$\theta_{435} = 85$
		$r_{24} = 1.81$	$\theta_{524} = 86$
		$r_{18} = 1.60$	$\theta_{239} = 122$
(TiO ₂) ₄	C_{2h}	$r_{45} = r_{28} = 1.84$	$\theta_{546} = 84$
		$r_{35} = r_{27} = 1.81$	$\theta_{536} = 86, \theta_{738} = 85$
		$r_{412} = 1.60$	$\theta_{3412} = 122$
(TiO ₂) ₅	C_2	$r_{56} = r_{39} = r_{210} = 1.84$	$\theta_{657} = 84, \theta_{647} = 86$
		$r_{46} = r_{38} = r_{211} = 1.81$	$\theta_{849} = 85$
		$r_{515} = 1.60$	$\theta_{4515} = 122$
(TiO ₂) ₆	C_{2h}	$r_{67} = r_{410} = r_{311} = 1.84$	$\theta_{768} = 84, \theta_{758} = 86$
		$r_{57} = r_{49} = r_{312} = 1.81$	$\theta_{9510} = 85$
		$r_{618} = 1.60$	$\theta_{5618} = 122$
TiO ₃	C_s	$r_{12} = 1.81$	$\theta_{123} = 66$
		$r_{14} = 1.60$	$\theta_{214} = 117$
		$r_{23} = 1.46$	$\theta_{314} = 117$
Ti ₂ O	C_{2v}	$r_{13} = 1.76$	$\theta_{132} = 95$
Ti ₂ O ₃	C_s	$r_{13} = 1.88$	$\theta_{423} = 92$
		$r_{23} = 1.74$	$\theta_{314} = 84$
		$r_{15} = 1.60$	$\theta_{215} = 125$
Ti ₃ O ₄	C_s	$r_{34} = 1.90$	$\theta_{425} = 84$
		$r_{24} = 1.83$	$\theta_{435} = 88$
Ti ₃ O ₅	C_s	$r_{16} = r_{24} = 1.84$	$\theta_{716} = \theta_{425} = 84$
		$r_{26} = 1.81$	$\theta_{435} = 88$
		$r_{34} = 1.77$	$\theta_{627} = 86$
		$r_{18} = 1.60$	$\theta_{218} = 120$

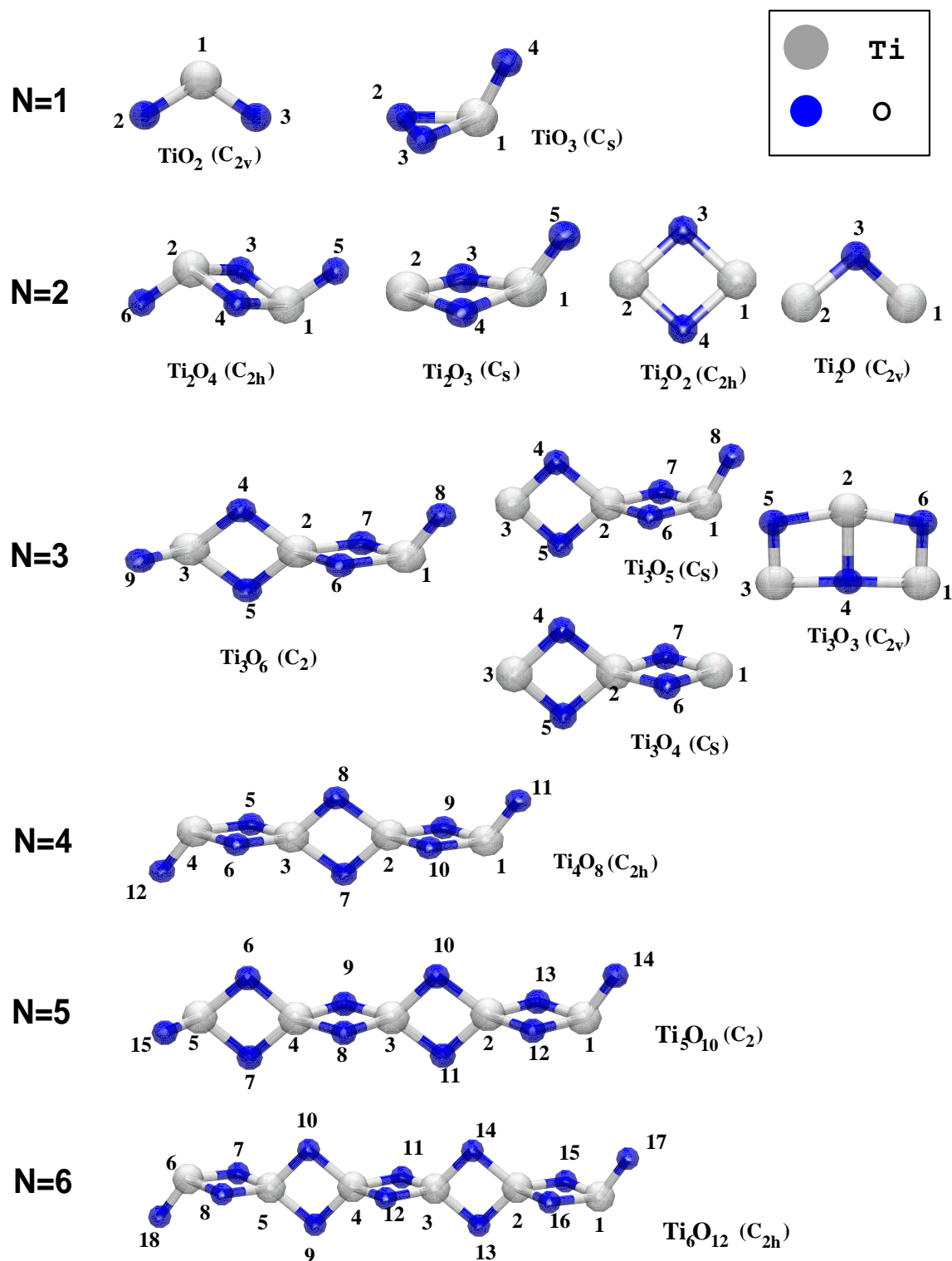
Figure 3.1: Equilibrium geometries of the investigated Ti_xO_y systems.

Table 3.3: DFT/B3P86 energies. E_{tot} is the total electronic energy, D_{at} the atomisation energy with respect to seperated atomic reference states ($E_{tot}[\text{Ti}(^3\text{F})] = -849.715898$, $E_{tot}[\text{O}(^3\text{P})] = -75.194538$ hartree) and E_{zp} the zero point vibrational energy. [1] Huber and Herzberg 1979, [2] Balducci *et al.* 1985a, [3] Balducci *et al.* 1985b

Molecule	Symmetry	$E_{tot}[\text{hartree}]$	E_{zp} [eV]	D_{at} [eV]	D_0 [eV]	D_0^{exp} [eV]
TiO	$C_{\infty v}$	-925.154025	0.07	6.63	6.56	6.87 ¹
(TiO) ₂	D_{2h}	-1850.465540	0.22	17.54	17.32	
(TiO) ₃	C_{2v}	-2775.747794	0.32	27.66	27.34	
TiO ₂	C_{2v}	-1000.617166	0.15	13.94	13.79	13.06 ² 31.27 \pm 0.68 ³
(TiO ₂) ₂	C_{2h}	-2001.435293	0.41	33.34	32.93	
(TiO ₂) ₃	C_2	-3002.234273	0.65	52.23	51.58	
(TiO ₂) ₄	C_{2h}	-4003.036837	0.88	71.21	70.33	
(TiO ₂) ₅	C_2	-5003.837876	1.13	90.15	89.02	
(TiO ₂) ₆	C_{2h}	-6004.635471	1.34	108.99	107.65	
TiO ₃	C_s	-1075.932025	0.24	17.21	16.97	23.96 \pm 0.58 ³
Ti ₂ O	C_{2v}	-1774.917037	0.11	7.91	7.80	
Ti ₂ O ₃	C_s	-1925.957241	0.29	25.63	25.34	
Ti ₃ O ₄	C_s	-2851.279220	0.44	36.83	36.39	
Ti ₃ O ₅	C_s	-2926.756543	0.54	44.52	43.98	

Table 3.4: The total binding energy $D_0(n)$ for (TiO)_n n=1-3 and (TiO₂)_n n=1-6 clusters, the binding energy per unit monomer $D_0(n)/n$, the binding energy per atom $D_0(n)/(x+y)$ and the energy gain $\Delta E(n)$ obtained by adding a monomer.

Clusters	$D_0(n)$ [eV]	$D_0(n)/n$ [eV]	$\Delta E(n)$ [eV]	$D_0(n)/(x+y)$ [eV]
TiO	6.6	6.6	6.6	3.3
(TiO) ₂	17.3	8.7	10.8	4.3
(TiO) ₃	27.3	9.1	10.0	4.4
TiO ₂	13.8	13.8	13.8	4.6
(TiO ₂) ₂	32.9	16.5	19.2	5.5
(TiO ₂) ₃	51.6	17.2	18.6	5.7
(TiO ₂) ₄	70.3	17.6	18.8	5.9
(TiO ₂) ₅	89.0	17.8	18.7	5.9
(TiO ₂) ₆	107.7	17.9	18.6	6.0

$$\begin{aligned}
E_{pend} &= D_0[(\text{TiO}_2)_2] - D_0[\text{Ti}_2\text{O}_3] = D_0[\text{Ti}_3\text{O}_5] - D_0[\text{Ti}_3\text{O}_4] \\
&= D_0[(\text{TiO}_2)_3] - D_0[\text{Ti}_3\text{O}_5]
\end{aligned}$$

The bond strength of the Ti–O unit in a ring-like environment, $E_{ring} = D_0/n_{ring}$, where n_{ring} is the number of Ti–O units in rings, was calculated from the atomisation energy of Ti_2O_2 and Ti_3O_4 . This quantity is 4.3 eV for Ti_2O_2 and 4.6 eV for Ti_3O_4 . In the case of the $(\text{TiO}_2)_n$ series and the non-stoichiometric systems, the bond strength of the Ti–O unit in a ring is calculated with $E_{pend} = 7.6$ eV the as follows:

$$E_{ring} = \frac{D_0(\text{molecule}) - 7.6 \text{ eV} \cdot n_{pend}}{n_{ring}}$$

where n_{pend} is the number of pendant Ti–O units. For the $(\text{TiO}_2)_n$ molecules with $n \geq 3$, the bond strength of the Ti–O unit in a ring is 4.6 eV, but it tends to decrease in the case of $n < 3$ from 4.6 eV to 4.3 eV.

From these two different kind of bond strengths of Ti–O units the bond energy of each molecule was calculated according to $D_b = E_{ring} \cdot n_{ring} + E_{pend} \cdot n_{pend}$ with $E_{ring} = 4.55 \pm 0.05$ eV and $E_{pend} = 7.6 \pm 0.5$ eV. The comparison between the DFT/B3P86 atomisation and the bond energy determined from the bond strengths of pendant and ring-like Ti–O units shows an excellent agreement as shown in Fig. 3.4.

In order to get an idea about the stability of the $(\text{TiO})_n$ and $(\text{TiO}_2)_n$ series of clusters, the atomisation energies of molecules per unit monomer are calculated from the atomisation energy and the zero point energy. The respective values are given in Tab. 3.4 and are illustrated in Fig. 3.2. The binding energy per TiO_2 unit in Fig. 3.2 shows a monotonous increase as a function of TiO_2 units. This growth is large, 2.7 eV, in the case of $n=1$ and $n=2$, whereas the clusters with $n>2$ exhibit a rather smooth rise of less than 0.7 eV in their binding energy.

The energy gained by adding a single monomer of TiO to $(\text{TiO})_n$ and of TiO_2 to $(\text{TiO}_2)_n$ is determined as follows

$$\Delta E(n) = D_0(n) - D_0(n-1) \quad n \geq 2.$$

In Fig. 3.3 the energy gain $\Delta E(n)$ is plotted as a function of n . Note that the energy gain in adding a TiO_2 unit to clusters abruptly changes from $n=1$ to $n=2$ and remains essentially constant for larger n . Except for this noticeable increase, the first order energy difference $\Delta E(n)$ shows no further conspicuous peaks.

These tendencies in the binding energies and the energy gain $\Delta E(n)$ show the same behaviour in the case of $(\text{TiO})_n$ molecules as can be seen in Tab. 3.4. Especially for the TiO_2 clusters, this tendency in the binding energies could be well supported by the recent investigation on the growth dynamics of the neutral titanium clusters through the very specific cluster growth pathways of the uptake of TiO_2 units (Foltin *et al.* 1999).

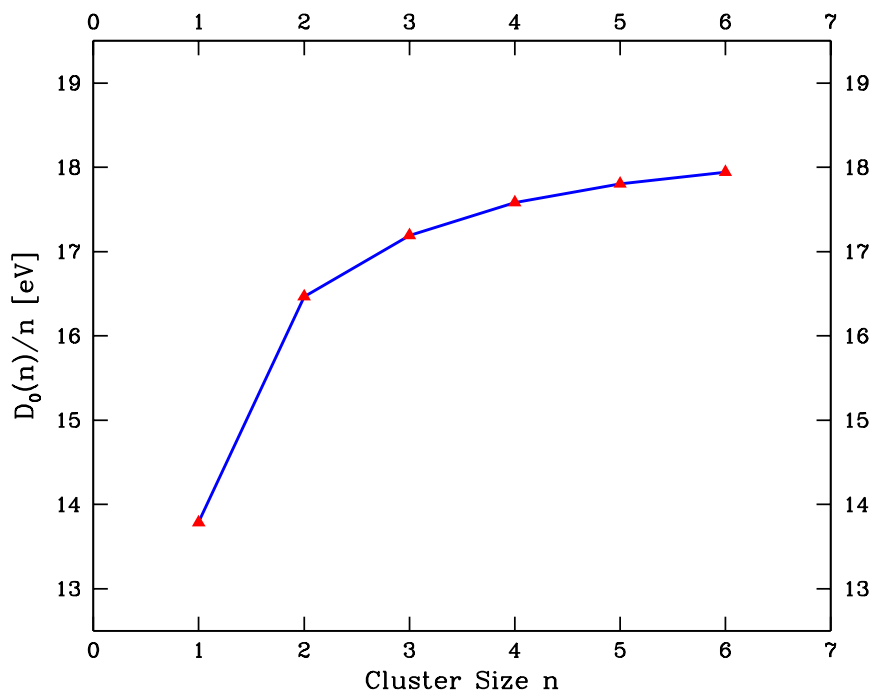


Figure 3.2: Binding energy per TiO_2 unit, $D_0(n)/n$, for $(\text{TiO}_2)_n$ $n=1-6$ clusters as a function of cluster size n .

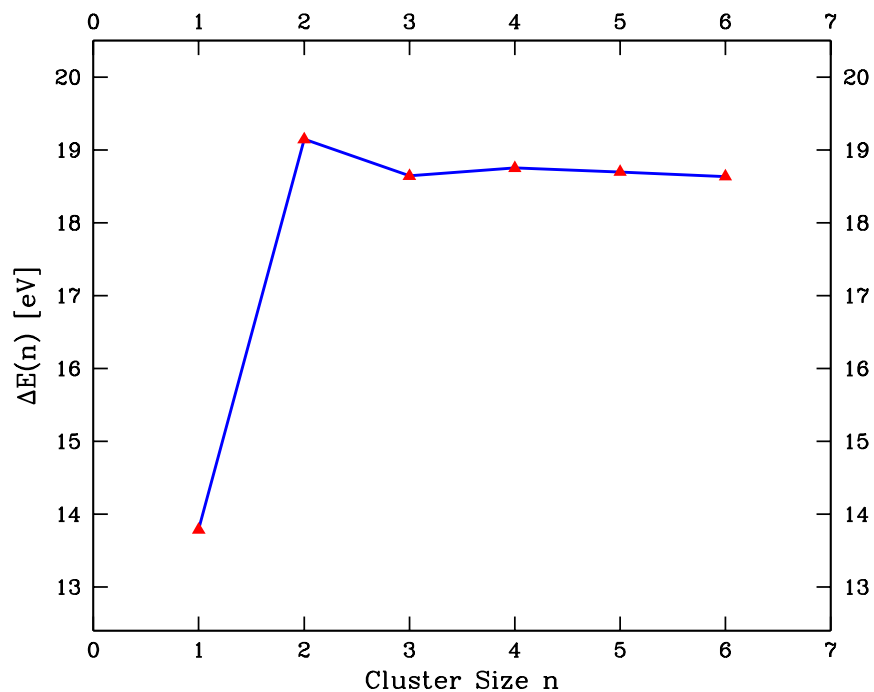


Figure 3.3: First order energy difference $\Delta E(n)$ as a function of cluster size n .

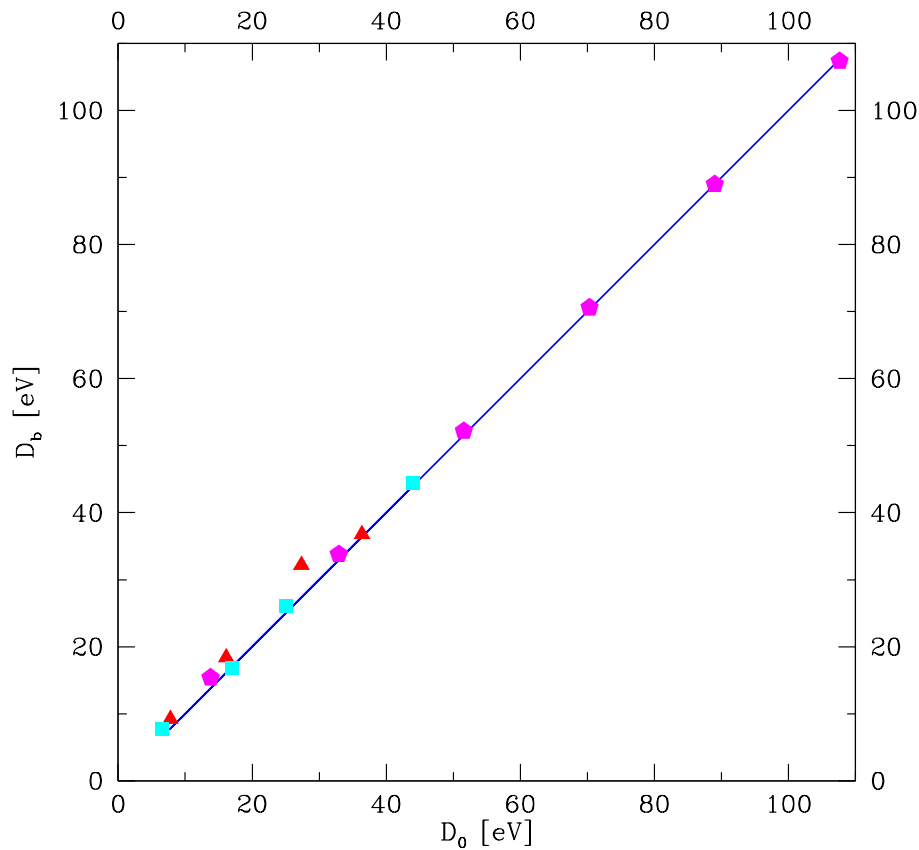


Figure 3.4: Comparison of the atomisation energy D_0 and the bond energy D_b calculated using the two types of Ti–O units. Different polygons represent this relationship for pendant Ti–O units. Triangles: $n_{pend} = 0$ for Ti_2O , $(TiO)_2$, $(TiO)_3$, and Ti_3O_4 . Squares: $n_{pend} = 1$ for TiO , TiO_3 , Ti_2O_3 , and Ti_3O_5 . Pentangles: $n_{pend} = 2$ for $(TiO_2)_n$ $n = 1 - 6$. The solid line delineates an idealisation for any Ti_xO_y following the specific building principle.

3.4.3 Vibrational Analysis

The calculated harmonic wave numbers of the symmetric stretch vibrations are $1152\text{ cm}^{-1}(\sigma_g)$ for TiO and $1088\text{ cm}^{-1}(a_1)$ for TiO_2 which are in reasonable agreement with the experimentally determined IR-active fundamental vibration of TiO at $988\text{ cm}^{-1}(\sigma_g)$ (Chertihin & Andrews 1995) and TiO_2 at $962\text{ cm}^{-1}(\nu_1)$ (McIntyre *et al.* 1971). The asymmetric stretch vibration of TiO_2 is observed at $934.8\text{ cm}^{-1}(\nu_3)$ (McIntyre *et al.* 1971), whereas the calculation on TiO_2 gives a wave number of $1044\text{ cm}^{-1}(a_2)$. The symmetric bending vibration of TiO_2 is predicted to be observable at $355\text{ cm}^{-1}(a_1)$.

The calculated IR spectra of TiO and TiO_2 are schematically presented in Fig. 3.5 and in Fig. 3.7 together with the IR spectra of the higher homologues $(\text{TiO})_n$ $n=2,3$, and $(\text{TiO}_2)_n$ $n=2-6$. One interesting fact to be recognised is that the wave number of the vibration with the greatest IR intensity is shifted to lower wave numbers with increasing n , i.e. in case of $(\text{TiO})_n$ $n=1-3$ to a wave number of 750 cm^{-1} and for $(\text{TiO}_2)_n$ $n=1-6$, to a wave number of 650 cm^{-1} . The other fact to be noticed is that there is another set of intense IR-active vibrations present in the range from 1044 cm^{-1} to 1111 cm^{-1} due to the presence of pendant Ti–O units in the molecules $(\text{TiO}_2)_n$ $n=1-6$. A corresponding IR-active vibration in the series $(\text{TiO})_n$ $n=1-3$, is only present for the monomer TiO . *Noteworthy for the series of $(\text{TiO}_2)_n$ compounds is that the calculated intensities of the most prominent IR-active vibrations show a strong positive correlation with the cluster size n .*

In the calculated IR spectra of the non-stoichiometric molecules, the intense IR-active vibrations are present at 693 cm^{-1} for Ti_2O and 695 cm^{-1} for Ti_3O_4 and around 1100 cm^{-1} for the molecules TiO_3 , Ti_2O_3 and Ti_3O_5 as shown in Fig. 3.6. The presence of the band around 1100 cm^{-1} is characteristic for a pendant Ti–O unit in these molecules.

The calculated wave numbers are about 15 % higher than the experimental data, which is expected in view of the known efficiencies of the harmonic approximation and of DFT methods in general for the description of molecular vibrations (Perdew 1986, Becke 1993, Gill 1996). In order to take care of this discrepancy and to compare with the experimental values, a scale factor of 0.86 was introduced as given in Tab. 3.5.

Chertihin & Andrews (1995) assigned IR-active vibrations of matrix isolated species to the molecules TiO , TiO_2 , TiO_3 , Ti_2O_2 and Ti_2O_3 . The assignments were based on oxygen isotopic splittings and shifts of the corresponding IR-active vibrations at 10 K. The observed IR band at 987.8 cm^{-1} was assigned to the isotopomer $^{48}\text{Ti}^{16}\text{O}$, and the bands at 946.9 cm^{-1} and 917.1 cm^{-1} were identified as ν_1 and ν_3 vibrations of $^{48}\text{Ti}^{16}\text{O}_2$.

The observed vibrations at 972.1 cm^{-1} and 790.2 cm^{-1} were assigned to the species OTiOO and TiO_3 . This assignment is in reasonable accordance with the calculated prominent harmonic wave number at 1103 cm^{-1} (scaled: 949 cm^{-1}), but is not supported with the wave number at 974 cm^{-1} (scaled: 837 cm^{-1}) by

Table 3.5: Comparison of the computed harmonic wave numbers $\tilde{\nu}_k$ with the experimentally observed IR bands by Chertihin & Andrews (1995) at the corresponding assignments.

Chertihin and Andrews		This work		
$\tilde{\nu}_k$ [cm ⁻¹]	assign.	$\tilde{\nu}_k$ [cm ⁻¹]	$\tilde{\nu}_k^{scaled}$ [cm ⁻¹]	assign.
987.8	TiO	1151.9	990	TiO
972.1	OTiOO	1103.5	949	TiO ₃
956.8	Ti ₂ O ₃	1099.9	945	Ti ₂ O ₃
946.9	TiO ₂ (ν_1)	1088.4	936	TiO ₂
917.1	TiO ₂ (ν_3)	1044.1	898	TiO ₂
866.0	Ti _x O _y			
842.4	Ti _x O _y			
790.2	TiO ₃	973.6	837	TiO ₃
753.5	Ti ₂ O ₃	789.3	679	Ti ₂ O ₃
736.5	Ti ₂ O	692.9	596	Ti ₂ O
704.2	Ti ₂ O ₂	764.4	657	(TiO) ₂
695.9	Ti _x O _y			
680.1	Ti ₂ O ₂	730.2	628	(TiO) ₂
625.0	Ti _x O _y	695.4	597	Ti ₃ O ₄

the frequency calculations for a non-planar TiO₃ molecule of C_s symmetry. The assignments of the observed IR-active vibration at 736.5 cm⁻¹ to the molecule Ti₂O and the bands at 704.2 cm⁻¹ and 680.1 cm⁻¹ to the species Ti₂O₂ are not supported by the results of the frequency calculations which predict the intense b₂ band of Ti₂O to be observable at 693 cm⁻¹ (scaled: 596 cm⁻¹), and the b_u vibrations of Ti₂O₂ to be present at 730 cm⁻¹ (scaled: 628 cm⁻¹) and 764 cm⁻¹ (scaled: 657 cm⁻¹).

Only the calculated wave number of 1099 cm⁻¹ (scaled: 945 cm⁻¹) supports the experimentally observed bands at 956.8 cm⁻¹ and 753.5 cm⁻¹ in case of the species Ti₂O₃. The other calculated IR-active band for Ti₂O₃ at 789 cm⁻¹ (scaled: 679 cm⁻¹) was assigned to Ti₂O₂. IR-active vibrations observed at 866 cm⁻¹, 842 cm⁻¹ and 625 cm⁻¹ were assigned to oxides of the general formula Ti_xO_y. According to the calculated wave numbers presented here, these bands are probably indicative for the formation of (TiO₂)_n molecules upon annealing of the matrix-isolated TiO₂ molecules.

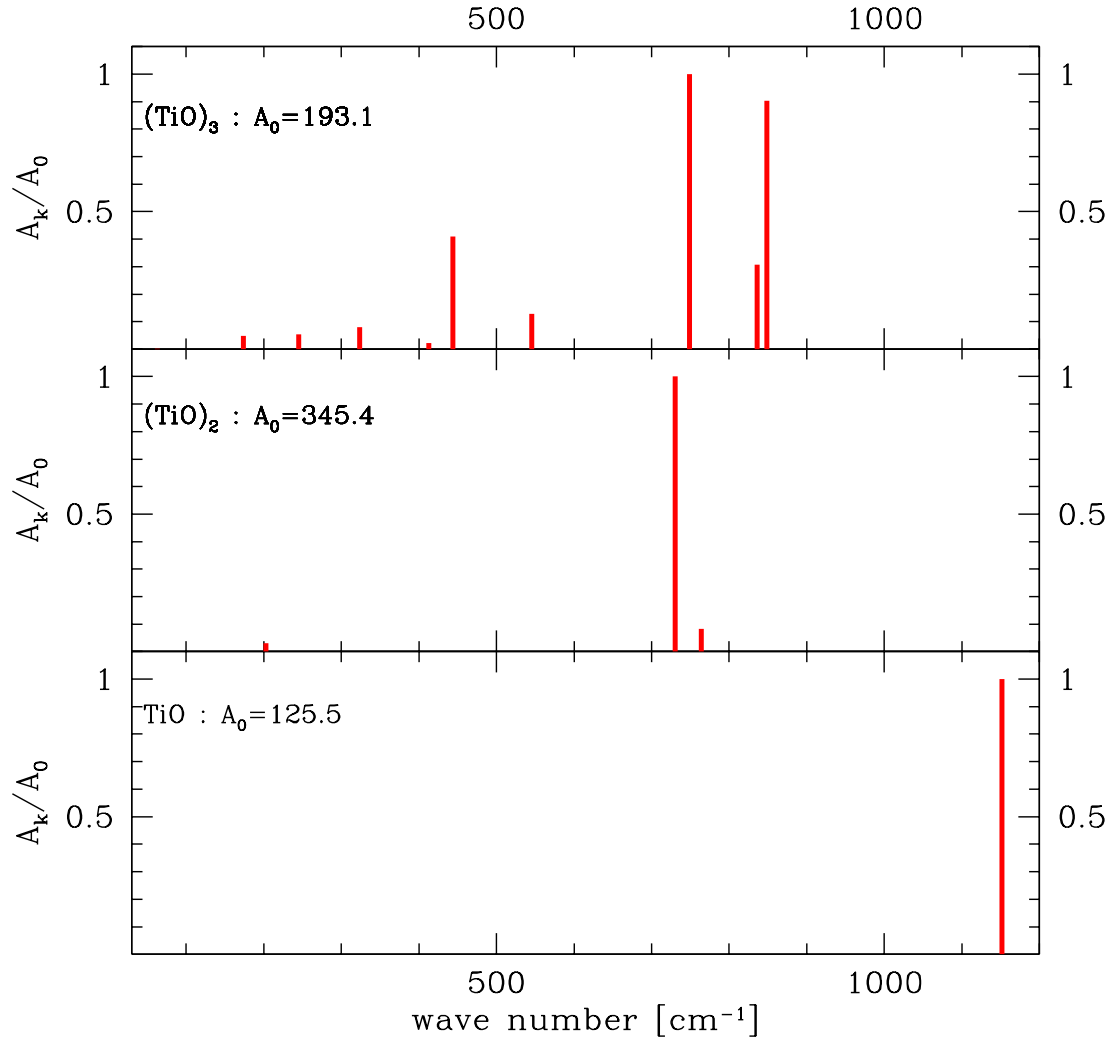


Figure 3.5: Calculated IR spectra in the 30–1200 $[\text{cm}^{-1}]$ range of wave numbers $\tilde{\nu}_k$ for $(\text{TiO})_n$ $n=1-3$ systems. A_0 is the maximum of the integrated absorption coefficients A_k in $[10^{-8}\text{cm}^2 \text{s}^{-1}]$.

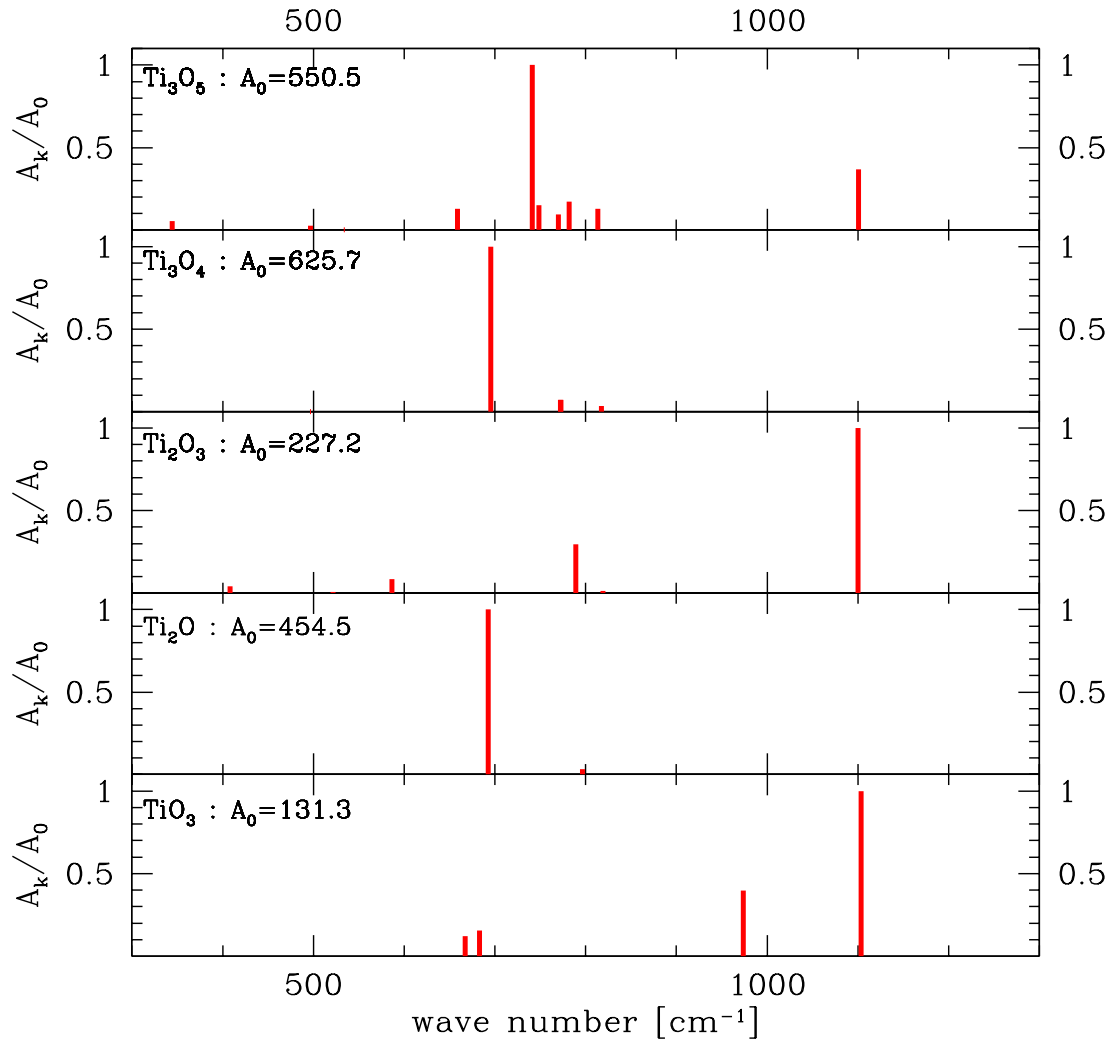


Figure 3.6: Calculated IR spectra in the 30–1200 $[\text{cm}^{-1}]$ range of wave numbers $\tilde{\nu}_k$ for the non-stoichiometric Ti_xO_y systems. A_0 is the maximum of the integrated absorption coefficients A_k in $[10^{-8}\text{cm}^2 \text{s}^{-1}]$.

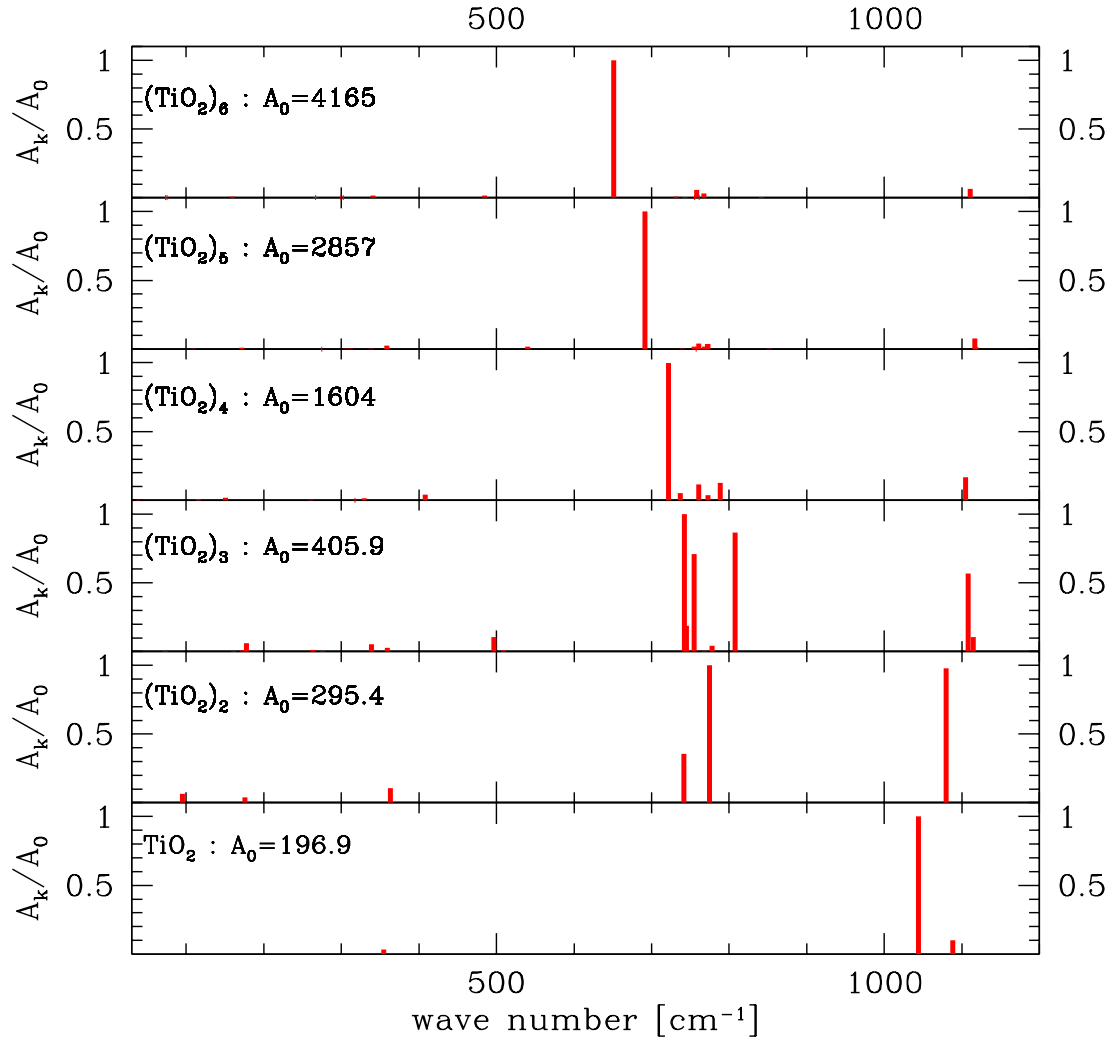


Figure 3.7: Calculated IR spectra in the 30–1200 $[\text{cm}^{-1}]$ range of wave numbers $\tilde{\nu}_k$ for the $(\text{TiO}_2)_n$ $n=1-6$ systems. A_0 is the maximum of the integrated absorption coefficients A_k in $[10^{-8}\text{cm}^2 \text{s}^{-1}]$.

3.5 The Partition functions

On the basis of the results obtained by the DFT calculations, the partition functions are calculated in order to calculate the thermochemical properties, e.g. Gibbs free energy of formation. From these values the distribution of the TiO_2 clusters in the gas phase and the nucleation rate of TiO_2 can be calculated. The thermochemical properties are calculated in the following section and the respective values calculated are given in Appendix.

The system partition function $Q(N, V, T)$ of N independent, indistinguishable atoms or molecules can be written with the molar partition function $q(V, T)$ as following

$$Q(N, V, T) = \frac{[q(V, T)]^N}{N!} \quad (3.14)$$

where N is the number of the particle, V the volume, T the temperature of a system. The molecular partition function can be written as

$$q(V, T) = \sum_j e^{-\beta \varepsilon_j} \quad \beta = \frac{1}{k_B T} \quad (3.15)$$

where k_B is the Boltzmann factor. Regarding molecules as rigid rotator harmonic oscillator, we can write the total energy of a molecule as the sum of its translational, rotational, vibrational, and electronic energies:

$$\varepsilon_j = \varepsilon^{trans} + \varepsilon^{rot} + \varepsilon^{vib} + \varepsilon^{elec} \quad (3.16)$$

Except for the translational degree of freedom, the degrees of freedom are not totally independent of each other, for example, the coupling between rotation and vibration. Generally, this simple addition of degrees of freedom is sufficient for calculating the total energy of a molecule and the separation between the motions of the nucleus and the electron can be justified for example by the Born–Oppenheimer approximation. From Eqs. 3.15 and 3.16, the molecular partition function can be written as

$$q(V, T) = q_{el} \cdot q_{tr} \cdot q_{rot} \cdot q_{vib} \quad (3.17)$$

The translational energy states $\varepsilon_{n_x n_y n_z}$ of a particle with mass m in a volume $V = a^3$ is

$$\varepsilon_{n_x n_y n_z} = \frac{h^2}{8ma^2} (n_x^2 + n_y^2 + n_z^2) \quad n_x, n_y, n_z = 1, 2, 3, \dots \quad (3.18)$$

where h is the Planck constant and n_x, n_y, n_z are the quantum numbers. From Eqn. 3.18 the translational partition function q_{trans} is written as

$$q_{trans}(V, T) = \left(\frac{2\pi m k_B T}{h^2} \right)^{3/2} V = \left(\frac{2\pi m}{\beta h^2} \right)^{3/2} V \quad (3.19)$$

The zero of the electronic energy is generally taken to be separated atoms at rest in their ground electronic states. The depth of the ground electronic state potential well is denoted by D_e , the difference in energy between the minimum of the potential energy and the dissociated atoms and hence the energy of the ground electronic state is $\varepsilon_1 = -D_e$. The electronic partition function q_{el} is

$$q_{el}(T) = \sum_i g_i \exp \{-\beta \varepsilon_i\} = g_1 \exp \{\beta D_e\} + g_2 \exp \{-\beta \varepsilon_2\} + \dots \quad (3.20)$$

where g_i is the degeneracy and ε_i the energy of the i -th electronic level. In the harmonic oscillator approximation

$$D_e = D_0 + \frac{1}{2} h\nu. \quad (3.21)$$

If we measure the vibrational energy levels relative to the minimum of the inter-nuclear potential well, the vibrational energies ε_v are given by

$$\varepsilon_v = \left(v + \frac{1}{2}\right) h\nu \quad v = 0, 1, 2, \dots \quad \text{with} \quad \nu = \frac{1}{2\pi} \sqrt{\frac{k}{\mu}} \quad (3.22)$$

where k is the force constant of the molecule and μ is the reduced mass. The vibrational partition function can be written from Eq. 3.22 as following

$$q_{vib}(T) = \sum_v \exp \{-\beta \varepsilon_v\} = \sum_{v=0}^{\infty} \exp \left\{ -\beta \left(v + \frac{1}{2} \right) h\nu \right\}. \quad (3.23)$$

Using the geometric series

$$\sum_{n=0}^{\infty} x^n = \frac{1}{1-x} \quad x = \exp \{-\beta h\nu\} < 1,$$

the vibrational partition function q_{vib} can be written as

$$q_{vib}(T) = \prod_i \frac{\exp \{-\beta h\nu_i/2\}}{1 - \exp \{-\beta h\nu_i\}}. \quad (3.24)$$

The rotational energy levels ε_J of a rigid rotator are given by

$$\varepsilon_J = \frac{h^2 J(J+1)}{8\pi^2 I} \quad J = 0, 1, 2, \dots \quad (3.25)$$

where $I = \sum_{j=1}^n m_j r_j^2$ is the moment of inertia of the rotator with distance r_j and mass m_j of the j th nucleus from the center of the molecule. Each energy level has a degeneracy of $g_J = (2J+1)^2$. We can write the rotational partition function of a rigid rotator as

$$q_{rot}(T) = \sum_{J=0}^{\infty} (2J+1)^2 \exp \left\{ -\frac{\beta h^2 J(J+1)}{8\pi^2 I} \right\}. \quad (3.26)$$

Introducing three characteristic rotational temperatures in terms of the three principal moments of inertia I_A, I_B , and I_C according to the rotational temperatures $\Theta_{rot,j} = \frac{h^2}{8\pi^2 I_j k_B}$, the sum can be converted into an integral for $\Theta_{rot} \ll T$

$$q_{rot}(T) = \frac{1}{\sigma} \int_0^{\infty} (2J+1)^2 \exp \left\{ -\frac{\Theta_{rot} J(J+1)}{T} \right\} dJ. \quad (3.27)$$

The symmetry number σ is the correction for the repeated count of indistinguishable configurations.

The rotational partition function q_{rot} is represented by the rotational temperatures

$$q_{rot}(T) = \frac{\pi^{1/2}}{\sigma} \left(\frac{T^3}{\Theta_{rot,A} \Theta_{rot,B} \Theta_{rot,C}} \right)^{1/2}. \quad (3.28)$$

In the case of linear molecules, the principle moments of inertia coincide and hence the rotational partition for a linear molecule is written as

$$q_{rot} = \frac{1}{\sigma h c B \beta} \quad (3.29)$$

with rotational constant $B = h/8\pi^2 c I$. For nonlinear molecules, the rotational partition function is

$$q_{rot} = \frac{\pi^{1/2}}{\sigma} \left(\frac{1}{h c \beta} \right)^{3/2} \left(\frac{1}{ABC} \right)^{1/2} \quad (3.30)$$

with the rotational constants A,B,C.

From the respective degrees of freedom in Eqs. 3.19, 3.20, 3.23, and 3.28, the molecular partition function of a polyatomic molecule can be written as following

$$q(V, T) = \left(\frac{2\pi m}{\beta h^2} \right)^{3/2} V \frac{1}{\sigma} \left(\frac{\pi^{1/2}}{hc\beta} \right)^{3/2} \left(\frac{\pi}{ABC} \right)^{1/2} \prod_i \frac{e^{-\beta h\nu_i/2}}{1 - e^{-\beta h\nu_i}} \left(\sum_i g_i e^{-\beta \varepsilon_i} \right) \quad (3.31)$$

3.6 Calculation of the thermochemical functions

For calculating the thermochemical functions, the third law method is here applied. The third law method is based on the knowledge of the absolute entropy of the reactants and products. It allows the calculation of the reaction enthalpy at a temperature and pressure, when the change in the Gibbs energy of formation for the reaction is known. The Gibbs energy function used here is defined as $[G^\circ(T) - H^\circ(298.15K)]/T$ and is calculated from the relation

$$S^\circ(T) = -\frac{G^\circ(T) - H^\circ(T)}{T} \quad (3.32)$$

$$= -\frac{G^\circ(T) - H^\circ(298.15K)}{T} + \frac{H^\circ(T) - H^\circ(298.15K)}{T}. \quad (3.33)$$

and the Gibbs energy of formation is given

$$\frac{G^\circ(T) - H^\circ(298.15K)}{T} = -S^\circ(T) + \frac{H^\circ(T) - H^\circ(298.15K)}{T} \quad (3.34)$$

From the definition, the change of the Gibbs energy of a reaction can be written as

$$\frac{\Delta G^\circ(T)}{T} = \frac{G^\circ(T) - H^\circ(298.15K)}{T} + \frac{\Delta H^\circ(298.15K)}{T} = -R \ln K_p \quad (3.35)$$

where R is the gas constant and K_p is the equilibrium constant of formation.

To calculate the enthalpy of formation at temperatures different from 298.15 K requires the knowledge of the enthalpies of the reference elements.

$$\Delta_f H^\circ(T) = \Delta_f H^\circ(298.15K) + [H^\circ(T) - H^\circ(298.15K)]_{compound} \quad (3.36)$$

$$- \sum [H^\circ(T) - H^\circ(298.15K)]_{elements}. \quad (3.37)$$

The Gibbs energy of formation is readily calculated from the enthalpy of formation when the entropies of the elements are known. Then,

$$\Delta_f G^\circ(T) = \Delta_f H^\circ(T) - TS^\circ(T)_{\text{compound}} - \sum S^\circ(T)_{\text{elements}} \quad (3.38)$$

As a first step to calculate the thermochemical functions and the formation functions, the thermodynamic internal energy of a system of independent molecules is calculated as follows. From the thermodynamic internal energy, the entropy of a system can be calculated. The internal energy of a system is given by

$$U(T) - U(0) = - \left(\frac{\partial \ln Q(N, V, T)}{\partial \beta} \right)_V = -N \left(\frac{\partial \ln q(V, T)}{\partial \beta} \right)_V \quad (3.39)$$

$$= -N \left[\frac{1}{q_{tr}} \frac{\partial q_{tr}}{\partial \beta} + \frac{1}{q_{rot}} \frac{\partial q_{rot}}{\partial \beta} + \frac{1}{q_{vib}} \frac{\partial q_{vib}}{\partial \beta} + \frac{1}{q_{elec}} \frac{\partial q_{elec}}{\partial \beta} \right]_V \quad (3.40)$$

From Eqs. (3.19), (3.28), and (3.23)

$$\frac{1}{q_{tr}} \frac{\partial q_{tr}}{\partial \beta} = -\frac{3}{2\beta} \quad (3.41)$$

$$\frac{1}{q_{rot}} \frac{\partial q_{rot}}{\partial \beta} = -\frac{3}{2\beta} \quad (3.42)$$

$$\frac{1}{q_{vib}} \frac{\partial q_{vib}}{\partial \beta} = \sum_i \frac{hc\tilde{\nu}_i}{1 - \exp\{hc\tilde{\nu}_i\beta\}} \quad (3.43)$$

where the vibrational wavenumber $\tilde{\nu}_i = \nu_i/c = h/8\pi^2 c I_i$. Therefore, the internal energy is described by

$$U(T) - U(0) = Nk \left(3T - \sum_i \frac{hc\tilde{\nu}_i/k}{1 - \exp\{hc\tilde{\nu}_i/kT\}} \right). \quad (3.44)$$

Boltzmann constant k is replaced by the gas constant $R = N_A k$ with Avogadro number N_A , if the energies in the Boltzmann distribution are replaced by the molar energies. The particle number N can be expressed by the amount of substance $n = N/N_A$. With the vibrational constants $a = hc/k$, the molar internal energy is given by

$$U_m(T) - U_m(0) = \frac{U(T) - U(0)}{n} = R \left(3T - \sum_i \frac{a\tilde{\nu}_i}{1 - \exp\{a\tilde{\nu}_i/T\}} \right). \quad (3.45)$$

Using the internal energy, the entropy of a system of independent molecules is expressed by

$$S = \frac{U(T) - U(0)}{T} + nR \left(\ln \frac{q}{N} + 1 \right) \quad (3.46)$$

and the molar entropy for the relation

$$S_m = \frac{S}{n} = \frac{U_m(T) - U_m(0)}{T} + R \left\{ \ln \frac{q_m}{N_A} + 1 \right\} \quad (3.47)$$

holds. The Gibbs energy function is given relative to the value at temperature $T=0$ K by

$$G(T) - G(0) = -nRT \ln \left(\frac{q}{N} \right) \quad (3.48)$$

Since $H_m(0) = G_m(0)$, the molar value of the Gibbs energy function is expressed by

$$- \frac{G_m(T) - H_m(0)}{T} = R \ln \left(\frac{q_m}{N_A} \right). \quad (3.49)$$

The molar enthalpy increment can be calculated from Eqs. 3.47 and 3.49 as follows

$$H_m(T) - H_m(0) = G_m(T) - H_m(0) + TS_m \quad (3.50)$$

$$= -RT \ln \left(\frac{q_m}{N_A} \right) + TS_m \quad (3.51)$$

The calculated heats of formation of the $(\text{TiO}_2)_n$ clusters at $T=0$ K have been obtained from the DFT atomization energies ΔH_{at} in conjunction with the standard experiment $\Delta_f H^\circ(0)$ values for the neutral atoms from Eq. (3.37):

$$\Delta_f H_{(\text{TiO}_2)_n}^\circ(0) = N \Delta_f H^\circ(0)(\text{Ti}, g) + 2N \Delta_f H^\circ(0)(\text{O}, g) - \Delta_{at} H_{(\text{TiO}_2)_n}. \quad (3.52)$$

These calculated thermodynamical properties of the $(\text{TiO}_2)_n$ clusters are listed in the Appendix. The tables contain the thermal functions: entropy S , enthalpy increments $H(T) - H(T_{ref})$, and Gibbs energy function $(G(T) - H(T_{ref}))/T$ and formation functions: enthalpy of formation $\Delta_f H^\circ(T)$ and Gibbs free energy of formation $\Delta_f G^\circ(T)$ with reference temperature T_{ref} , which is generally taken as the standard temperature, 298.15 K, in laboratory work.

Using these calculated thermodynamical functions, the concentration of $(\text{TiO}_2)_N$ clusters in the gas phase has been calculated in chemical equilibrium and the result

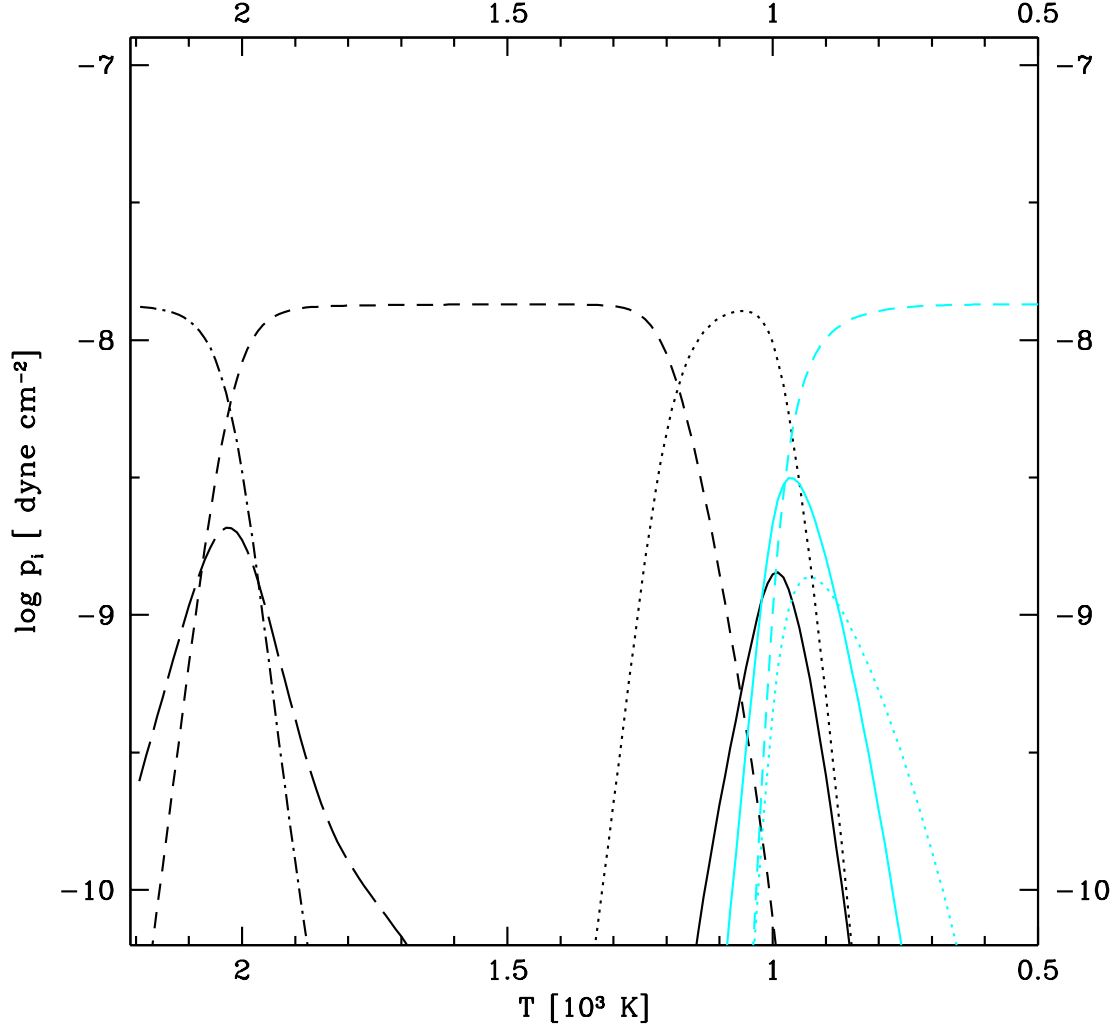


Figure 3.8: The logarithm of partial pressure of $(\text{TiO}_2)_n$ clusters at $P_{<H>} = 0.1 \text{ dyn cm}^{-2}$ and solar abundances. Depicted are Ti in dashed-dotted line, TiO in long dashed line, TiO_2 in dashed line, $(\text{TiO}_2)_2$ in dotted line, $(\text{TiO}_2)_3$ in black solid line, $(\text{TiO}_2)_4$ in blue solid line, $(\text{TiO}_2)_5$ in blue dotted line and $(\text{TiO}_2)_6$ in blue dashed line.

is depicted in Fig. 3.8 for $p_{<H>} = 0.1 \text{ dyn cm}^{-2}$ and temperatures between 500 K and 2200 K. Comparing the calculations by Tsuji (1973), this calculation shows the different concentration of TiO_2 . In Tsuji (1973), TiO is the most abundant molecule below about 2800 K for $P_{\text{gas}} = 10^3 \text{ dyn cm}^{-2}$ among the titanium bearing molecules and the concentration of TiO_2 is negligible small (4 order magnitude), whereas the concentration of TiO_2 in this calculation is larger than TiO below 2000 K (Helling 1999). Around 1200 K, where the nucleation can start in circumstellar shells, dimer of titanium dioxide becomes the most abundant in the gas phase. In the temperature range between 1000 K and 900 K there exist various $(\text{TiO}_2)_n$ clusters in the gas phase and the most stable cluster is $(\text{TiO}_2)_6$ in this temperature range.

3.7 The distribution of clusters

Let N be the number of monomers forming the clusters. With the assumption of sphericity, the radius of a cluster of size N is $r = r_0 N^{1/3}$, where r_0 is the hypothetical radius of a monomer and the surface area of a particle is $A_N = 4\pi r_0^2 N^{2/3}$. The equilibrium distribution of N -cluster can be given by a Boltzmann distribution in size

$$\overset{\circ}{f}(N) = \overset{\circ}{f}(1) \exp \left\{ \frac{\Delta G(N)}{RT} \right\} \quad (3.53)$$

where $\Delta G(N)$ is the Gibbs free energy change associated with the formation of the N -cluster from the vapor and $\overset{\circ}{f}(1)$ is the equilibrium density of the monomer. The values of $\Delta G(N)$ depends on the definition of the reference state and is related to the standard molar Gibbs free energy of formation of N -cluster $\Delta_f G^\circ(N)$ by

$$\Delta G(N) = \Delta_f G^\circ(N) - \Delta_f G^\circ(1) - (N-1)\Delta_f G_1^\circ(s) \quad (3.54)$$

where $\Delta_f G_1^\circ(s)$ is the Gibbs free energy of formation of a monomer in the solid state. $f(N_*)$ depends again exponentially on the Gibbs free energy of formation for the critical clusters N_* , which according to the classical nucleation theory is given by the difference between the energy required for the formation of the surface and the formation energy of the monomer in the critical clusters.

The classical nucleation theory refers to a constrained equilibrium state between the clusters and the supersaturation ratio S and temperature T existing in the real situation. Based on thermodynamical arguments, the Gibbs free energies of formation of the N clusters in this constrained equilibrium can be derived as

$$\frac{\Delta G(N)}{RT} = -N \ln(S) + \theta_\infty N^{\frac{2}{3}} \quad \theta_\infty = \frac{4\pi r_0^2 \sigma_\infty}{k_B T}. \quad (3.55)$$

N clusters are considered to be spherical droplets with a hypothetical monomer radius r_0 and σ_∞ denotes the surface tension of the macroscopic solid. The dependence of the surface energy on the size is neglected in the classical nucleation theory, but it must be considered for the small clusters.

Due to the definition of the equilibrium, the equilibrium particle density of the monomer $\overset{\circ}{f}(1)$ in this state is equal to the monomer particle density in the actual situation

$$\overset{\circ}{f}(N) = \overset{\circ}{f}(1) \exp \left\{ N \ln(S) - \theta_\infty N^{2/3} \right\} \quad (3.56)$$

for the cluster size distribution in the constrained equilibrium state. If this is inserted into $J_* = \tau_{gr}^{-1}(1, N_*) \overset{\circ}{f}(N_*) Z(N_*)$, the result of the classical nucleation theory for the stationary nucleation is recovered.

Despite the fact that the classical nucleation presupposes the thermal equilibrium between the clusters and the gas and chemical equilibrium in the gas phase, the classical expression of $\Delta G(N)$ has two shortcomings: the size dependence of the surface energies of the clusters is neglected and it does not yield the correct limit $\Delta G(N) \rightarrow 0$ for $N \rightarrow 1$.

A correction of the classical form of the Gibbs free energy change has been introduced by Draine and Salpeter (1977) in the limit of the bulk material for the surface energy

$$\overset{\circ}{f}(N) = \overset{\circ}{f}(1) \exp \left\{ (N-1) \ln(S) - \theta_N (N-1)^{2/3} \right\}. \quad (3.57)$$

Although the consistency correction for $\Delta G(N)$ in Eq. (3.57) is applied to both the bulk and surface term, only the classical surface term needs in fact to be corrected, if the LTE state of a saturated vapor is chosen as the reference equilibrium. In this state, $\overset{\circ}{f}(1)$ equals the particle density corresponding to the vapor saturation pressure p_{vap} and $\Delta G(N)$ consists of the surface contribution to the Gibbs free energy only.

With this reference the bulk contribution is a natural result of the derivation of J_* from the kinetic theory. For the equilibrium in the gas phase, one obtains

$$J_{*,1}^c(t) = \tau_{gr}^{-1}(1, N_*, t) f(1, t) Z(N_*) \exp \left\{ (N_* - 1) \ln(S) - \frac{\Delta \tilde{G}(N_*)}{RT_g} \right\}. \quad (3.58)$$

For large N, the quantity θ_N is determined by the surface contribution to the free energy $\Delta G(N)$. On the basis of classical thermodynamics, Draine (1979) and Gail *et al.* (1984) defined a size dependent θ_N , which leads to

$$\frac{\Delta\tilde{G}(N)}{RT} = \theta_\infty \frac{N-1}{(N-1)^{1/3} + N_f^{1/3}} \quad (3.59)$$

where N_f is a fit constant, essentially representing the particle size at which the surface energy is reduced to one half of the bulk value.

To consider the effect of the curvature on the surface energy for small clusters, available $\Delta_f G^\circ(N)$ values can be used to fix the quantities entering into the approximations for $\Delta G(N)$. For small N , the function θ_N is related to the dissociation constant K_p by

$$\theta_N(T) = -T \{ \ln K_p(N, T) + (N-1) \ln (p_{vap}) \} (N-1)^{-2/3} \quad (3.60)$$

$$\frac{\theta_N(T)}{T} (N-1)^{2/3} = -\frac{\Delta\tilde{G}(N)}{RT} = \ln K_p(N, T) + (N-1) \ln (p_{vap}) \quad (3.61)$$

$$\Delta\tilde{G}(N) = -RT \{ \ln K_p(N, T) + (N-1) \ln (p_{vap}) \}. \quad (3.62)$$

For large N , the standard linear regression method of Press *et al.* (1986) gives maximum likelihood estimates, which yields a surface energy of $\sigma_\infty = 521 \text{ erg cm}^{-2}$ for the classical expression for $\Delta G(N)$ and $\sigma_\infty = 618 \text{ erg cm}^{-2}$ for the modified expression for the Gibbs free energy change with $N_f = 0$. From these values σ_∞ is taken as 620 erg cm^{-2} .

To compare the description of cluster properties expressed in terms of $\Delta G(N)$ by means of Eq.(4.52) with data available, $\Delta_f G^\circ(N)/N$ of small clusters are calculated, for both the modified and for the classical approximation with the same value for $\sigma_\infty = 620 \text{ erg cm}^{-2}$. The obtained standard Gibbs free energies of formation of the N -clusters at $T = 1200 \text{ K}$ are depicted in Fig.3.9. The surface tension of TiO_2 measured in a function of the slab thickness is 730 erg cm^{-2} (Bates *et al.* 1997).

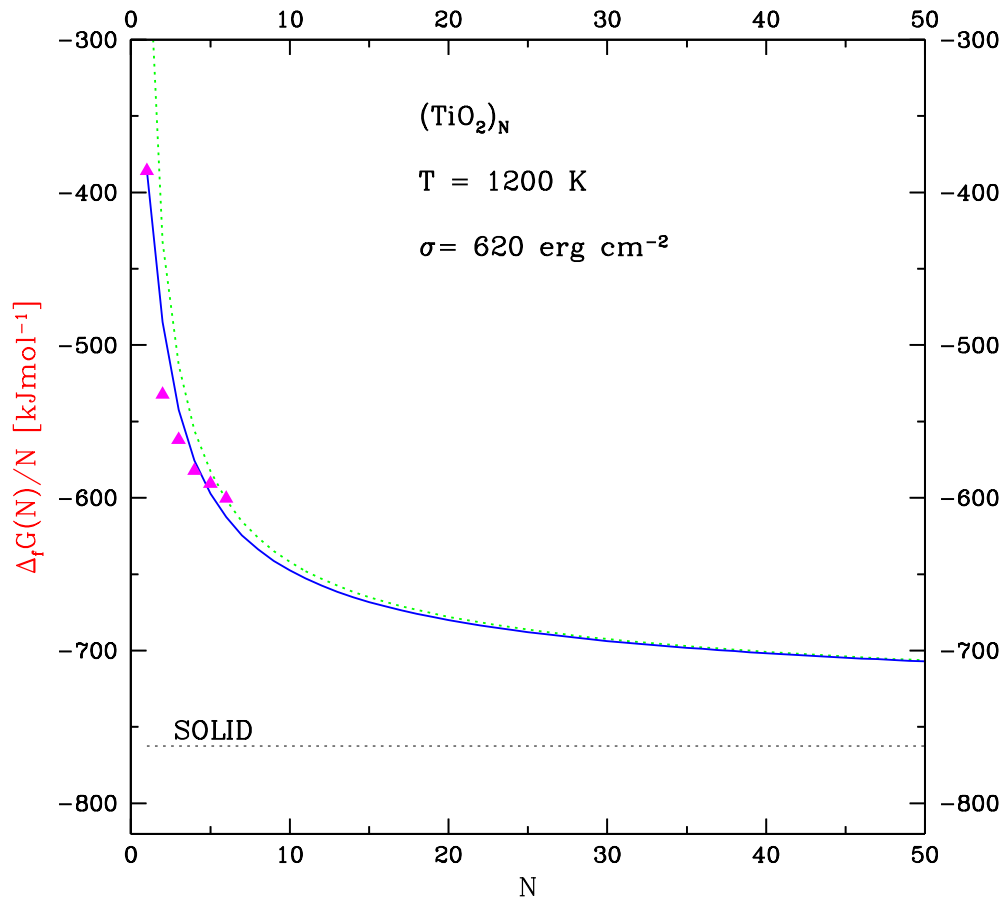


Figure 3.9: Comparison between $\Delta_f G^o(N)/N$ values of TiO_2 clusters. $\Delta_f G^o(N)/N$ of small clusters at 1200 K calculated by DFT are depicted in filled triangles for $N=1-6$ and calculated value in terms of $\Delta G(N)$ of modified expression with $\sigma_\infty = 620$ erg cm⁻² and with $N_f = 0$ depicted in blue solid line. The green dotted line is the value by the classical relation with $\sigma_\infty = 620$ erg cm⁻².

Ein Traum, ein Traum ist unser Leben hier,
wie Schatten auf den Wogen schweben und schwinden wir,
Und messen unsre trägen Tritte nach Raum und Zeit,
Und sind (und wissen's nicht) in Mitte der Ewigkeit.

Johann Gottfried Herder

Chapter 4

On the nucleation seeds

The process of grain formation can be seen as a diffusion process in the range of the grain size. Consequently, the classical equation describing this process is a diffusion equation, a partial differential equation second order in the cluster size and first order in time for the size distribution function (see Feder *et al.* 1966). Describing dust formation by this equation, requires to approximate the discrete size distribution function $f(N, t)$ which gives the number density of grains of size N at time t by a continuous function of grain size. The calculation of grain formation by this equation confronts two problems:

1. the continuous approximation becomes critical at very small grain sizes.
2. the solution of the partial differential equation requires a large computing effort especially if $f(N, t)$ is nonvanishing over an extremely broad size interval.

The problems with very small grain size can be avoided by a discrete theory in this range. Approximate analytical solutions of the Zel'dovich equation have been given by several works (e.g. Draine and Salpeter 1977, Yamamoto and Hasegawa 1977). They use Taylor expansions for the temperature as a function of time and the Gibbs free energy of formation of small clusters as a function of their size. These approximations can be used in situations in which the external conditions change independently of the dust formation in the temperature range of the most effective nucleation. However, these approximations might lead to large errors in environments, where the dust itself controls the time scales of the changes of temperature and other hydrodynamic and chemical parameters. Furthermore, these methods are not appropriate to describe the evaporation or destruction of dust grains, which could occur in variable stars.

A numerical treatment of dust formation was carried by Fix (1969) and later by Draine and Salpeter (1977). They used a kind of moment method where the evolution of the size distribution means being weighted by powers of the particle size was followed by the solution of a coupled set of ordinary differential equations. The moment equations given by Draine and Salpeter (1977) are formally the same as

given later by Gail and Sedlmayr (1988). Gail and Sedlmayr (1988) gave a complete discrete theory of the formation of homogeneous dust grains and derived the master equation by balancing the gains and losses of every particle size N , neglecting the destructive processes, e.g. the evaporation of monomers from the grains by thermal evaporation or sputtering processes. This discrete theory gives the exact expression for the nucleation rate for very small grain sizes. and allow for a detailed numerical treatment of dust formation with a minimum of computational effort. Gauger *et al.* (1990) investigated the evaporation process and showed that thermal evaporation as a destructive process can quite easily be incorporated into the moment equations, if the size distribution is known. Therefore, dust formation in variable situation can be treated in the same frame of the moment equation.

There are different attempts to describe the dust formation process in oxygen rich environments where the grains are composed of several chemical elements.

Gail and Sedlmayr (1986) have considered the formation of dust in M stars, especially considering the question of the primary condensates that are responsible for the formation of the grain nuclei. They discussed that the primary condensates should be MgS, SiO, Fe, and eventually MgO. The formation of the pure iron grains and pure magnesium oxide grains was considered. In the case of the silicate, the formation of MgSiO_3 was assumed as long as magnesium and iron were left in the gas phase. The moment method used by these authors is the basis for the work presented here.

Considering the formation of pure MgSiO_3 , Al_2O_3 , and CaTiO_3 , Kozasa and Hasegawa (1987) Sogawa and Kozasa (1999) define a generalized supersaturation ratio essentially by the quotient of the right and left hand side is Eq. 2.20 With that generalised supersaturation ratio, a key species which is the species with the smallest collision rate is determined by the equations of the classical nucleation of the growth velocity and this species triggers the growth process. Furthermore, they assume a constant monomer of the dust material determining the composition of the condensing material. However, the direct application of the classical nucleation theory to the formation of dust grains where the monomer does not exit in the gas phase which is true for almost all the condensates considered is at least controversial (Sedlmayr 1989b, Donn and Nuth 1985).

All physical conditions e.g. temperature and densities are assumed to either be independent or linear function of time. The equations of the nucleation, growth, and depletion are interpreted analytically. This is a good approximation only in systems where the dust formation itself has a negligible influence on the structure of the systems. In a situation like a dust driven wind where the whole hydrodynamic and thermodynamic structure is critically triggered by the dust formation, the equation cannot be solved in that way.

In the interesting work by Sharp and Huebner (1990), the equilibrium densities of all relevant molecules in the gas phase are calculated in chemical equilibrium, including the existence of a large variety of the solid compounds. All compounds are assumed to be in pure stoichiometric form and the equilibrium is calculated by

a global minimization of the Gibbs energy of the whole system. However, there are several reasons that these calculations cannot be applied to our situation:

- a complete equilibrium situation which is the limit for large time scales. It is, however, well known that the process of dust formation in the envelope of red giants is essentially a non equilibrium process occurring at temperatures lower than those to be expected from equilibrium situations.
- Only pure condensates are considered. In our case the condensates will certainly not be pure, but a mixture of varying composition.
- The equilibrium calculations give no information on the time dependent behaviour of the system and on number and size of the dust grains formed.

One of the most critical problems in calculating the dust formation is the determination of the nucleation rate, since the nucleation rate is an extremely steep function of the conditions in the gas, especially the gas temperature. The usual Ansatz is to consider the most effective chain of reactions leading from atoms to macroscopic particles and to calculate the flux of clusters through the chain. The production rate of particles in this critical size is the so called nucleation rate J_* .

If the chemical pathway for the nucleation process is known, the nucleation rate can be directly calculated from the solution of the corresponding rate equations (Gail and Sedlmayr 1988). The application of this theory depends, however, on the data required for the molecules involved in the reaction and on the reaction rates. The evaluation of relevant nucleation path way (Feder *et al.* 1966) is worked on Goeres (1992) for carbon chemistry, but the respective investigation on the oxygen-rich case is still lacking.

Since the reaction coefficients of the molecules often vary by orders of magnitude, there is generally one slowest reaction in the chain, *the bottle neck reaction*. The cluster produced by this reacting is called the critical cluster. Since this formation reaction is the slowest in the chain the next growth step is much faster and consequently the concentration of the critical cluster is always very small. If the chemical time scales in the system below the critical cluster are sufficiently small compared to the time scales in which the thermodynamic conditions in the gas change, one may assume that the chain molecules smaller than the critical cluster achieve their chemical equilibrium concentrations. The nucleation rate is then given essentially by the equilibrium value of the number density of the critical cluster multiplied by the net growth reaction rate for this cluster.

In order to calculate the nucleation rate this way it is necessary to know the equilibrium concentration of the chain molecules, which can be obtained from the thermodynamic functions of the molecules. Since it is usually impossible to get all the data required, in classical nucleation theory these thermodynamic functions are often calculated from the surface energy of the bulk material. This concept is able to describe the evaporation energy of molecules from large clusters, but for very

small clusters, the detailed investigation is still required, e.g. the thermodynamical properties of the clusters.

Basically, the formation of dust grains can be conceived as a two step process: **i)** formation of a **critical cluster** which serves as a condensation seed and **ii) growth** of these clusters to macroscopic dust grains by addition of suitable molecules. Step one, the formation of the critical cluster requires high supersaturation ratios ($S \gg 1$), whereas the growth process, i.e. condensation of the growth molecules on preexisting nucleation seeds proceeds already if $S > 1$ for the respective growth species.

In order to determine the most likely primary condensation seed, nucleation rates J_* were calculated for the candidates shown in Fig. 4.1 in a range of the $p-T$ plane, relevant for the inner region of a dust forming circumstellar shell. Contour plots of the resulting nucleation rates are shown in Fig. 4.1 for various seed nuclei, which were calculated from kinetic nucleation theory (see Patzer *et al.* 1998) assuming chemical equilibrium in the gas phase. Though this assumption of chemical equilibrium may be considered as highly unrealistic in pulsating situations, due to the large numerical expenditure, no consistent non-equilibrium chemical structure exists so far for Miras and LPVs.

Since Al_2O_3 is already stable at very high temperatures, it might be expected to be the first condensate in the cooling outflows of oxygen-rich stars (e.g. Kozasa and Sogawa 1999). However, using the thermodynamic functions resulting from quantum mechanical *ab initio* calculations for the structure of the Al_2O_3 molecule to calculate its equilibrium concentration shows, that this molecule is virtually not present in the gas phase (see Chang *et al.* 1998, Patzer *et al.* 1999). Therefore, homogeneous **nucleation** of molecular Al_2O_3 from the gas phase seems to be very unlikely in a circumstellar environment (see Fig. 4.2).

However, the analysis of meteorites reveals that corundum-bearing grains in fact are formed in the circumstellar shells of oxygen-rich AGB stars (e.g. Zinner 1998). The formation of solid Al_2O_3 in principle might proceed via chemical reactions like $\text{Al}_2\text{O} + 2\text{H}_2\text{O} \rightarrow \text{Al}_2\text{O}_3 + 2\text{H}_2\text{O}$ (e.g. Gail & Sedlmayr 1998) or $2\text{Al} + 3\text{H}_2\text{O} \rightarrow \text{Al}_2\text{O}_3 + 3\text{H}_2$ (Kozasa & Hasegawa 1987) which require a three body collision and a five body collision, respectively. Such a scheme seems to be realistic for the formation of corundum in a grain mantle, where the reaction partner can be adsorbed at the grain surface for a certain time. For the formation of an **isolated** $(\text{Al}_2\text{O}_3)_N$ cluster by this kind of chemical reactions, at least N (simultaneous) three body collisions in the gas phase are required, the effective occurrence of which is a delicate question of the involved time scales. In the following we therefore consider corundum only as a growth species and are left with SiO, Fe, TiO and TiO_2 for the nucleation process (see Fig. 4.1).

Although the SiO molecule is the most abundant candidate for nucleation in oxygen-rich circumstellar shells, its nucleation rate only peaks around 600 K, which is significantly lower than the typical temperatures at the inner edge of the dust shells as derived e.g. from infrared interferometry (Danchi *et al.* 1994). As can be

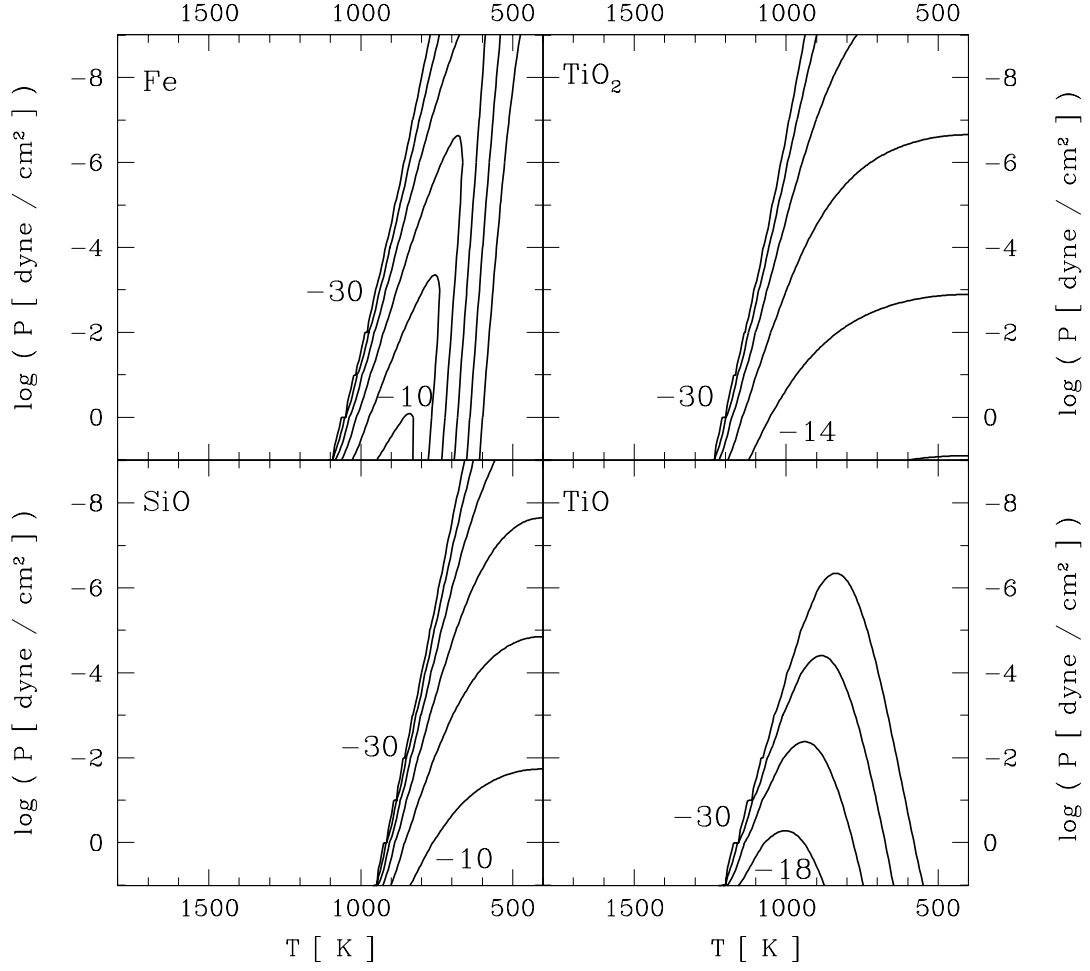


Figure 4.1: Contour lines of the nucleation rate for different nucleating species in the p-T plane. Contour levels are plotted in steps of $\Delta \log(J_*/n_{<H>}) = 4$.

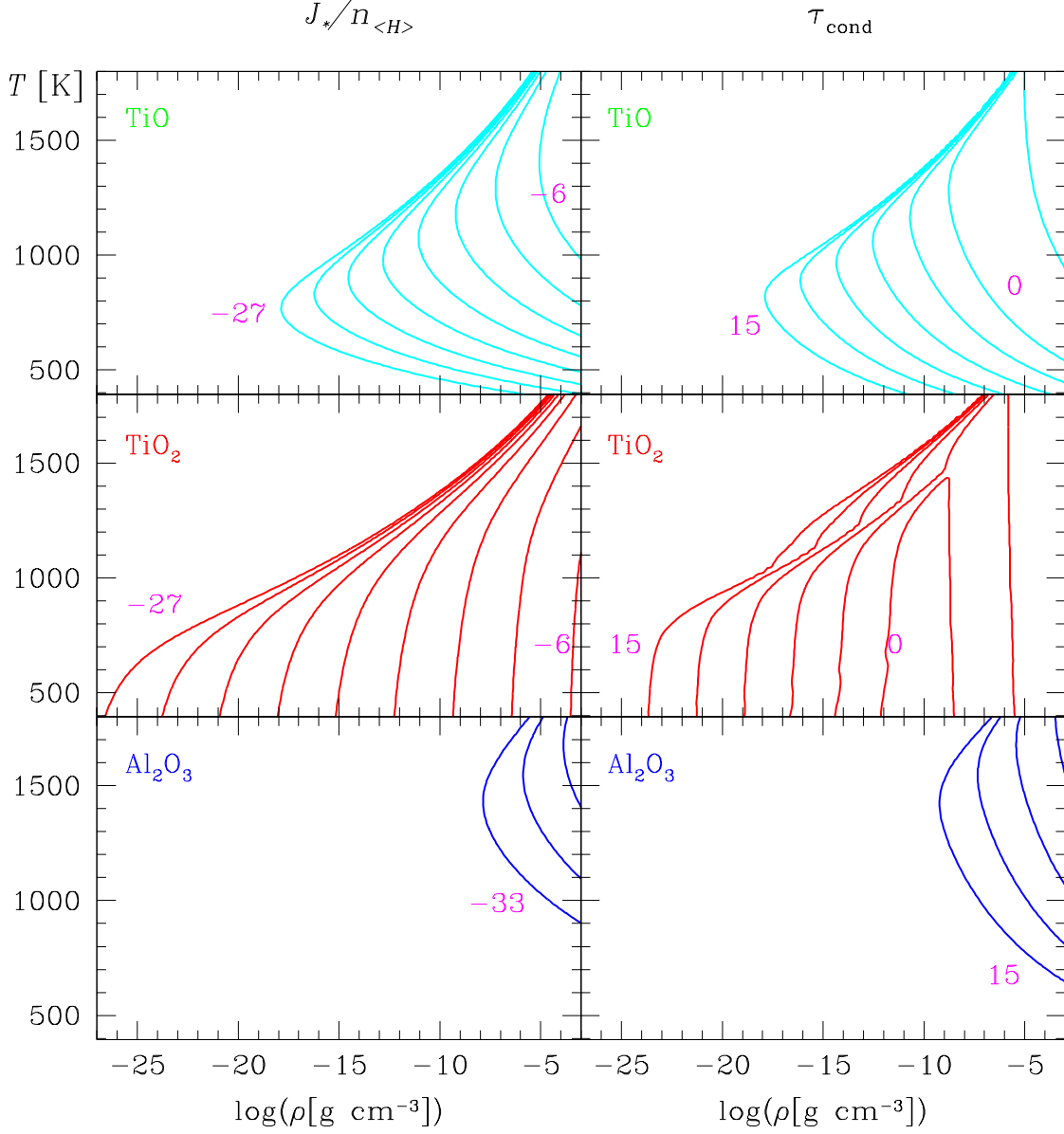


Figure 4.2: Contour lines of the nucleation rate for different nucleating species in the ρ - T plane. Contour levels are plotted in steps of $\Delta \log(J_*/n_{<H>}) = 3$. τ_{cond} is the time in [s] needed that the condensing material is contained 10 % in the dust grains.

seen from Fig. 4.1, also efficient Fe nucleation occurs only at temperatures well below 1000 K. Only the titanium oxides show relevant nucleation rates at temperatures above 1000 K where TiO_2 nucleation is by far more efficient, due to its higher molecular concentration in the relevant region of the $p-T$ plane (Gail and Sedlmayr 1998). An interesting investigation has been performed on the mineral species that could account for 13 μm emission feature in oxygen-rich AGB stars (Posch *et al.* 1999), in which the emissivity of rutile, TiO_2 is shown at 13.5 μm .

The formalism still leaves open the detailed structure of the crystal formed. It should be clear from the arguments above that the resulting solid compound will not have a definite stoichiometric composition. Descriptions of dust formation which claim such a composition have to be taken with care.

Two different ways can be considered which could lead to the realisation of the chemical composition above.

1. The different grain material might form rather pure patch on the grain from the core to the surface of the grains, so that a part of surface is partly covered by a species, another by the other species.
2. The grains show a completely amorphous structure. This should happen, if the colliding molecules are not able to migrate freely over the surface, but stick to the grain at the place of their impact.

This kind of study has been already discussed in Gail and Sedlmayr (1984) for the case of the pure carbon grains. The time scales for the growth of atom are compared to hopping time scales on the surface. These time scales let a criterium be derived, to decide whether the atoms reach an equilibrium position in the grain to form the most stable compound at the considered temperature or whether they stay approximately at the position where they impacted the grain.

Nun scheint es zwar natürlich, daß, so bald man den Boden der Erfahrung verlassen hat, man doch nicht mit Erkenntnissen, die man besitzt, ohne zu wissen woher, und auf dem Credit der Grundsätze, deren Ursprung man nicht kennt, sofort ein Gebäude errichten werde, ohne der Grundlage dessenselben durch sorgfältige Untersuchungen vorher versichert zu sein, daß man also vielmehr die Frage vorlängst werde aufgeworfen haben, wie denn der Verstand zu allen diesen Erkenntnissen a priori kommen könne, und welchen Umfang, Gültigkeit und Werth sie haben mögen.

Immanuel Kant Kritik der reinen Vernunft

Chapter 5

Dust formation in a gas element

In this chapter the moment equations (Eq. 2.25 and 2.26) are applied to the condensation and evaporation of dust under varying thermal conditions typical for the circumstellar shells of LPVs.

To focus the investigation on the condensation process, we neglect here the non-linear effects on the dust formation process which result from the fully coupled system including time-dependent hydrodynamics and radiative transfer. Instead, the concept of a gas element used already by Fix (1969) and Gauger *et al.* (1990) has been taken here. A single gas element is subjected to periodic variations of temperature and density in order to simulate the varying conditions encountered by the gas elements moving through the circumstellar shell of an oxygen-rich LPV. Although the assumed temporal changes are only a crude approximation, the fundamental process of condensation and evaporation of the dust and the characteristics of these processes under conditions typical for LPVs can be studied already in this way.

In oxygen-rich shells oxides are not only the primary condensates, but they also contribute to the heterogeneous growth of the grains.

5.1 The thermodynamic conditions

To simulate the temporal change of the thermodynamic conditions in a gas element in a pulsating atmosphere, the gas temperature is assumed to vary sinusoidally in time.

The gas temperature T_g at time t is given as

$$T_g(t) = \bar{T}_g + \Delta T_g \cos(2\pi \frac{t - t_0}{P}) \quad (5.1)$$

where \bar{T}_g is the mean gas temperature, ΔT_g is the amplitude of the temperature variation and P is the period of the oscillation.

A motivation for this attempt is the thermodynamic characteristics of a gas element moving in a Mira atmosphere, if the shocks are treated in the isothermal limit case: In this case, the gas temperatures before and after the shock front are taken as equal and are determined in equilibrium with the local radiation field. According to the model calculations of Bowen (1988), the trajectories of the elements below the dust formation region behave approximately ballistic and, after being pushed outwards, return to their starting point. Due to the outward motion of the gas elements, the temperature decreases at first, reaches a minimum value at maximum distance from the star and increases again with the inward movement of the gas elements.

For the variation of the mass density ρ in the element, its temporal change is assumed to proceed adiabatically with the temperature and is given as

$$\rho(t) = \bar{\rho} \left(\frac{T_g(t)}{\bar{T}_g} \right)^{1/(\gamma-1)} \quad (5.2)$$

where $\bar{\rho}$ is the mean density during the cycle and γ is the adiabatic exponent, i.e. the ratio of the specific heats at constant pressure and volume, respectively. For simplification, γ is assumed to be constant during the cycle.

For the calculation of dust condensation and evaporation, the following parameter values are chosen for the mean temperature \bar{T} , temperature amplitude ΔT , mean mass density $\bar{\rho}$, period P , and adiabatic exponent γ

$$\bar{T} = 700 \text{ K}$$

$$\bar{\rho} = 10^{-13} \text{ g cm}^{-3}$$

$$P = 2.6 \cdot 10^7 \text{ s} \approx 300 \text{ d}$$

$$\Delta T = 300 \text{ K}$$

$$\gamma = 5/3.$$

The dust formation sets in, when the supersaturation ratio is greater than the critical value S_c . Since the nucleation begins first at high supersaturation ratio, the value $S_c = 1000$ is assumed here.

The chemical composition of the gas is depicted for the dust free case in Fig. 5.1 for each chemical element considered here. At the higher temperature above 1400 K, the most of the elements are contained in the atoms. Most of the oxygen is contained in H_2O in the relevant region of temperature. Si and S are contained respectively in SiO and SiS , which are in competition with decreasing temperature. This is mainly due to the chemical shift from SiO to SiS at the lower temperature. Interesting is the situation for the Al-bearing molecules. In the relevant temperature range, AlOH

is the most dominant molecule except at the minimum of the temperature profile, where the most of the Al is contained in AlO_2H . At low temperatures, the most of Fe and Mg is bound in OH-bearing molecules, MgOH and $\text{Fe}(\text{OH})_2$. Ti is mainly bound in TiO_2 in the relevant temperature range, whereas the concentration of TiO in the gas decreases steeply below $T_g = 1400$ K.

The temporal development of the dust component is calculated by means of the moment equations given in Gauger *et al.* (1990) which include a description of dust evaporation.

From the growth rate for each condensible species $n_j = \xi_A \omega_j L_2$, the total number of the growth species contained in dust particles can be derived from

$$\dot{\varepsilon}_i = -\frac{\xi_A^d}{n_{<H>}} \sum_{i=1}^M \nu_{m_\ell, i} \omega_{m_\ell} L_{j-1} \quad (5.3)$$

ξ_A is a geometric constant, $(36\pi)^{1/3}$ and ω_j is the growth rate per unit area and per time unit of the species contributing to the growth.

As lower boundary for the size of the dust particles respected as macroscopic is assumed a value of $N_l = 1000$. The dust temperature T_d is taken as same as the gas temperature, $T_d = T_g$.

5.2 Condensation and evaporation of oxides

In this section, the condensation and evaporation of oxides is considered, which can appear as primary condensate in oxygen-rich shells. Since a purely homomolecular heterogeneous condensation exists in case of the oxides and it differs clearly in its characteristics relevant for the condensation from the carbon condensation.

The growth process considered in this calculation is described here according to the method of Dominik *et al.* (1993) and the growth material is listed in Table 5.1.

5.2.1 Dust formation on the TiO_2 nuclei

The TiO_2 seed nuclei grow by accretion of those molecular species, which can form a stable condensate under the thermodynamic conditions prevailing in the circumstellar environment. The respective monomer of these condensates does not necessarily have to exist in the gas phase, but may be formed by chemical reactions on the grain surface from the atoms and molecules present in the gas phase (see Fig. 5.2).

For example, Mg_2SiO_4 can be formed by addition of the atoms Mg, Si and O, and the molecules O_2 , MgO , SiO , SiO_2 , etc. Actual formation of such a solid compound requires that all the generalized supersaturation ratios of the contributing atomic and molecular species are larger than unity (Dominik *et al.* 1993). Their method is applied here to describe this heterogeneous growth process. Generally,

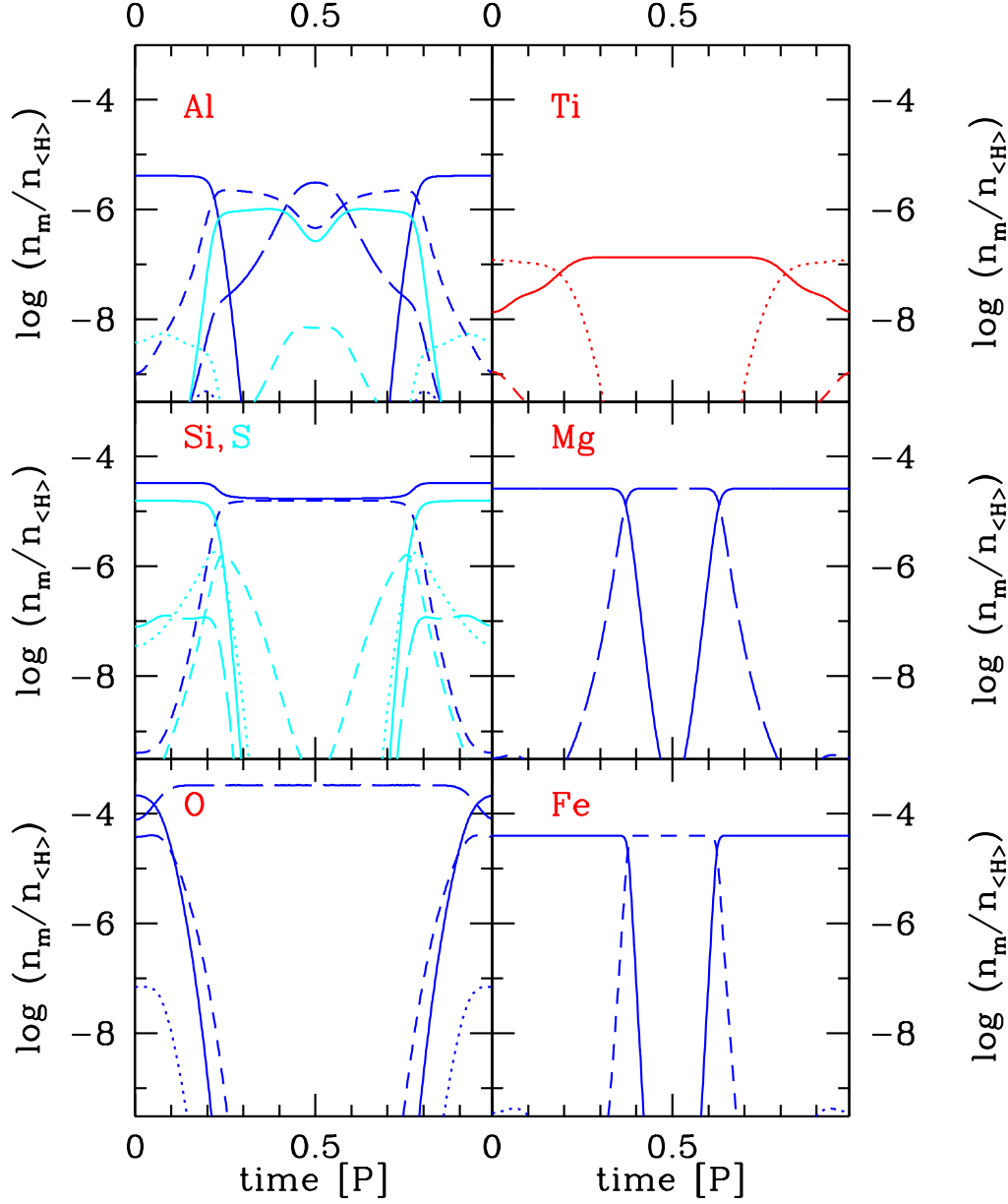


Figure 5.1: The temporal variation of chemical composition of the gas for the dust free case. **upper left diagram:** Aluminium compounds, Al blue solid line, AlOH blue dashed line, AlO₂H blue long dashed line, Al₂O light-blue solid line, AlO light-blue dotted line and Al₂O₂ light-blue dashed line. **middle left diagram:** Silicon and sulphur compounds, SiO blue solid line, SiS blue dashed line, S light-blue solid line, HS light-blue dotted line, H₂S light-blue dashed line and SO light-blue long dashed line. **lower left diagram:** Oxygen compounds, O solid line, O₂ dotted line, OH dashed line and H₂O blue long dashed line. **upper right diagram:** Titanium compounds, Ti dashed line, TiO dotted line and TiO₂ solid line. **middle right diagram:** Magnesium compounds, Mg solid and MgOH long dashed line. **lower right diagram:** Iron compounds, Fe solid line, FeO dotted line and Fe(OH)₂ dashed line.

Table 5.1: Growth species and their chemical properties. The species in the upper part of the table exist also in gas phase, whereas those in the lower part do not exist in gas the phase.

name	formula	mol.wt [a.u.]	density [gcm ⁻³]	melt. point [K]	boil.point [K]
iron	Fe	55.85	7.86	1808	3023
silicon monoxide	SiO	44.08	2.13	>1975	2153
periclase	MgO	40.30	3.58	3125	3878
wuestite	FeO	71.85	5.70	1642	
titanium oxide	TiO	63.85	4.93	1750	>3000
magnesium sulfide	MgS	56.37	2.84	>2273	
quartz	SiO ₂	60.08	2.64–2.66	1883	2503(2863)
rutile	TiO ₂	79.88	4.26	1839–1850	2500–3000
silicon sulfide	SiS ₂	92.21	2.02	s 1363	
hermatite	Fe ₂ O ₃	159.69	5.24	1838	
corundum	Al ₂ O ₃	101.96	3.97	2288	3253
aluminium sulfide	Al ₂ S ₃	150.14	2.02	1373	1773
magnesium sulfate	MgSO ₄	120.36	2.66	> 1397	
magnetite	Fe ₃ O ₄	231.54	5.18	1867	
cyanite	Al ₂ O ₃ · SiO ₂	162.05	3.25	1818	>1818
mullite	3Al ₂ O ₃ · 2SiO ₂	426.05	3.16	2193	
spinel	MgAl ₂ O ₄	142.27	3.60	2408	
clinoenstatite	MgSiO ₃	100.39	3.19	1830	
forsterite	Mg ₂ SiO ₄	140.69	3.21	2183	

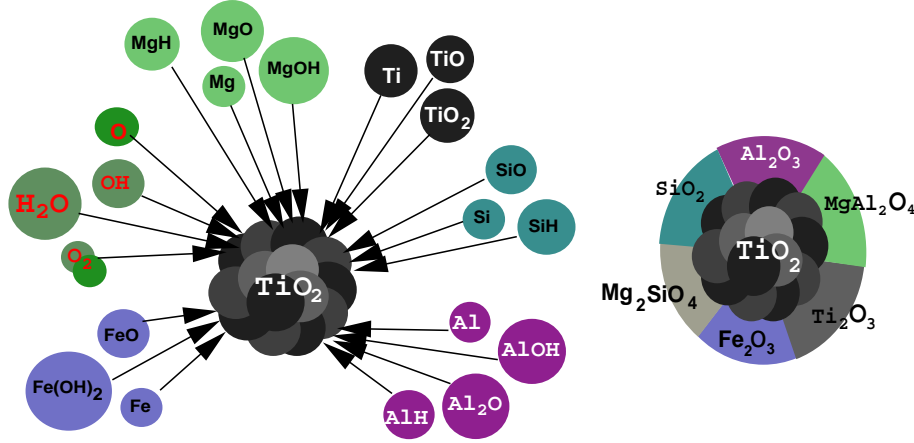


Figure 5.2: Heterogeneous growth on the seed material TiO_2 . **l.h.s.:** molecules contributing to grain growth **r.h.s.:** sketch of some compounds constituting the resulting grain mantle

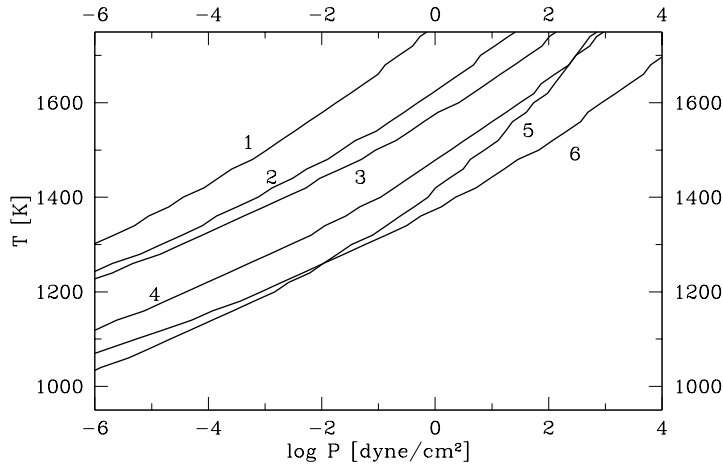


Figure 5.3: Stability hierarchy ($S = 1$) for some high temperature condensates in the p - T plane. 1: Al_2O_3 , 2: $\text{Al}_6\text{Si}_2\text{O}_{13}$, 3: Ti_2O_3 , 4: MgSiO_3 , 5: MgAl_2O_4 , 6: MgTiO_3

several compounds are simultaneously stable at a given pressure and temperature and there is a hierarchy of dust materials which successively become stable with decreasing temperature. The first condensing compounds are aluminum-bearing species like $\text{Al}_6\text{Si}_2\text{O}_{13}$, Al_2SiO_5 and Al_2O_3 , followed by Mg_2SiO_4 , MgSiO_3 , SiO_2 and by the iron oxides and MgO , while sulphur-bearing compounds like MgSO_4 and SiS_2 only become stable at temperatures around 600 K. This stability hierarchy (shown in Fig. 5.3) might depend on the total gas pressure (which affects the partial pressure of the contributing species in a non-linear way) as can be seen e.g. from the stability limit of MgAl_2O_4 depicted in Fig. 5.3 (see also Gail & Sedlmayr 1998).

According to the discussion in Chap. 4, TiO_2 is taken as the seed for homogeneous nucleation and the heterogeneous growth process is investigated in this section. The thermodynamical quantities, density and temperature and the dust properties nucleation rate J_* , evaporation rate J_{ev} (normalized to the total number density of H-atoms), the number of dust particles per H-atom $n_d/n_{<H>}$, and the mean grain radius $\langle r \rangle$ are shown in Fig. 5.4.

At $T = 1159$ K, where the supersaturation ratio reaches the critical value S_c , the nucleation rate of TiO_2 is still negligible in this time ($t = [0.2, 0.24]$ P) with $J_* = 2.9 \cdot 10^{-32} \text{s}^{-1}$ in comparison to the maximum of J_* . The nucleation rate increases rapidly with decreasing temperature and reaches a maximum value of $J_{*,max} = 1.1 \cdot 10^{-16} \text{s}^{-1}$ at a temperature of $T = 836$ K at time $t = 0.31$ P.

The nucleation rate of TiO_2 has its value in the wider range of time than Fe nucleation, due to the larger molecular concentration of TiO_2 with decreasing temperature.

Around $T = 700$ K, the evaporation rate shows a peak with a value of $|J_{ev}| = 5.8 \cdot 10^{-16} \text{s}^{-1}$ and this is due to the evaporation of the sulphur-bearing species from the dust grains. The evaporation occurs in the different thermodynamic conditions and have its maximum $|J_{ev,max}| = 2.4 \cdot 10^{-16} \text{s}^{-1}$ at $t = 0.8$ P and at $T = 1339$ K, which is larger than the maximum nucleation rate. At this temperature, the most species contained except Al- and Ti-bearing species become unstable and the number density $n_d/n_{<H>}$ of the dust grains falls rapidly down from $1.1 \cdot 10^{-10}$ to $2.8 \cdot 10^{-11}$. The number density of the dust grains is a factor of 10 less than for the iron condensation and this is mainly due to the less abundance of the nuclei material Ti. The evaporation of the mantle material of the dust grains continue up to around $T = 1650$ K. At this temperature, the seed TiO_2 is already unstable (see also the supersaturation ratio in Fig. 5.5) and hence the complete destruction of the dust grains occur simultaneously through the complete evaporation of the mantle material.

The mean grain radius is around $0.025 \mu\text{m}$ and relatively small at the beginning of condensation, but reaches $0.1 \mu\text{m}$ in a very short time span of less than 0.1 P. Its maximum is $1.3 \mu\text{m}$ at $t = 0.64$ P, just before the evaporation of sulphur bearing species begins. The decrease of the mean grain radius in the time span between 0.64 P and 0.76 P is due to the evaporation of the sulphur-bearing species, SiS_2 , MgS , and MgSO_4 . The released Si from SiS_2 enriches the abundance of Si in the gas and the Si-bearing species, for example MgSiO_3 , which are still stable at temperatures around 1200 K can grow further on the dust grains. This causes the growth of the dust grains, just before the evaporation reaches its maximum.

The temporal change of temperature T , density ρ , and supersaturation ratio S are depicted in Fig. 5.5 for a period. The supersaturation ratio is greater than unity at time $t = 0.2$ P at temperatures $T \leq 1300$ K. The critical supersaturation ratio $S_c = 1000$ is reached at $T = 1159$ K at $t = 0.24$ P. At that instant, the nucleation rate of TiO_2 is negligible, $J_* = 2.9 \cdot 10^{-32} \text{s}^{-1}$, in comparison with the maximum value of $J_* = 1.1 \cdot 10^{-16} \text{s}^{-1}$ at a temperature of $T = 836$ K ($t = 0.31$ P).

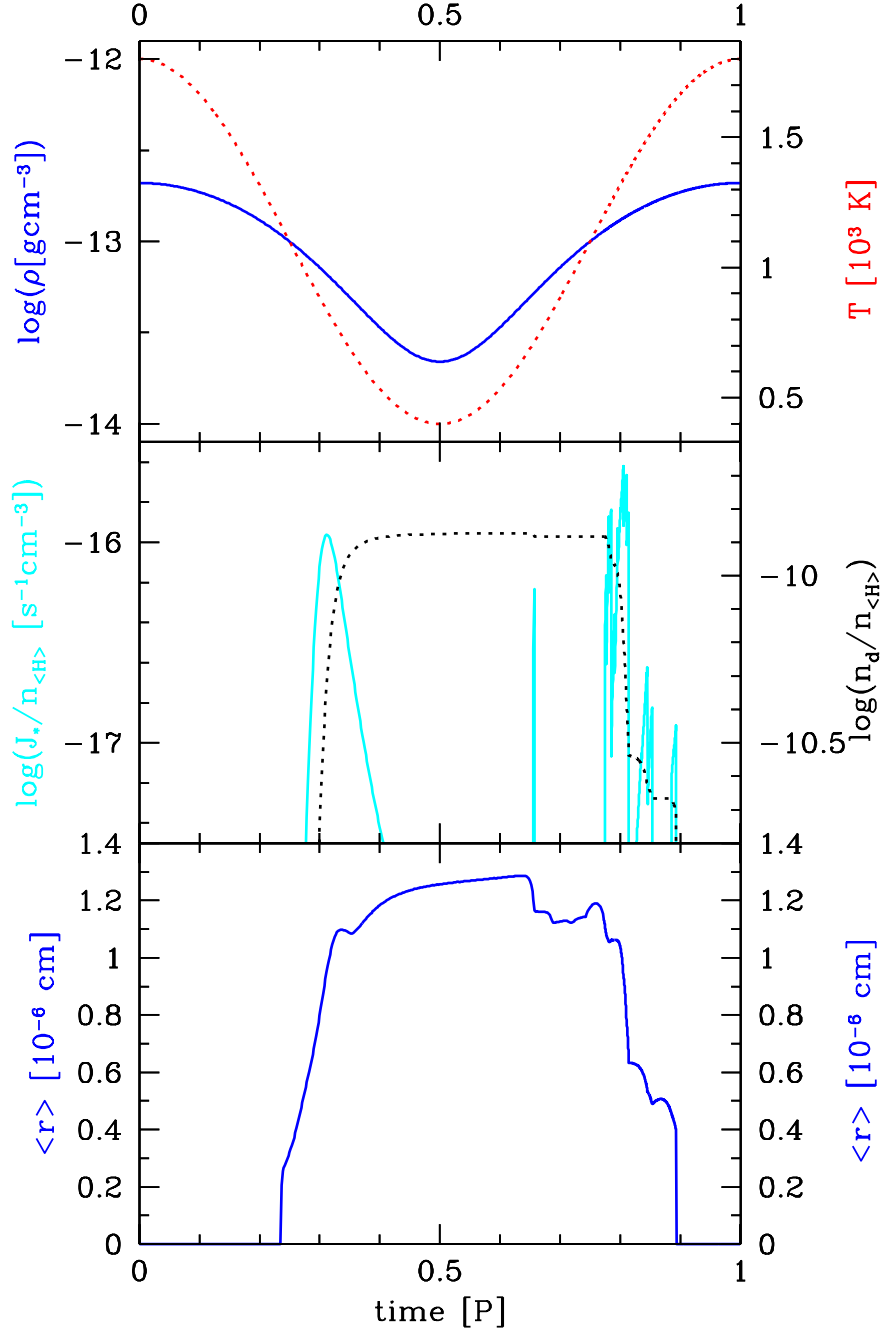


Figure 5.4: Thermodynamical and dust quantities of dust with TiO_2 nuclei. **upper diagram:** logarithm of the mass density ρ (full line, l.h.s. ordinate) and temperature T (dotted line, r.h.s. ordinate); **middle diagram:** logarithm of the nucleation and evaporation rate J_* and J_{ev} (full line, l.h.s. ordinate) and logarithm of the number of dust particles per H-atom $n_d/n_{<H>}$ (dotted line, r.h.s. ordinate); **lower diagram:** mean particle radius $\langle r \rangle$.

In the evaporation phase, around $t = 0.77$ P and $T = 1260$ K, the supersaturation ratio reaches again unity due to the rising vapor pressure with increasing temperature. The triangles on the decreasing temperature and the supersaturation ratio curves correspond the values for $S = 1, 10, 100, 1000$ at $t = 0.2, 0.22, 0.23, 0.25$ P. The values of the supersaturation ratio of TiO_2 is relatively larger than those of Fe in comparison.

The transition from the growth to the evaporation occurs at relatively high temperature of $T = 1150$ K, which is only 110 K below the nominal evaporation temperature of $T = 1260$ K, at which S is unity in the dust free gas. S decreases below unity and with further increasing temperature, S becomes negligible small and the evaporation process is accelerated.

The temporal variation of the chemical composition of the dust grains is shown in Fig. 5.6. Depicted are the number density of the elements contained in dust grains and the degree of condensation for each element.

In the degree of condensation, Ti is the first element to be contained in the dust grains as seed and serves as the further growth species in the mantle. Fe and Al reach a degree of condensation of 100 % even at the beginning of the growth phase, since they are bound in those of the most stable species like Al_2O_3 and Fe_2O_3 at the relatively higher temperature.

The degree of condensation of Ti and of Mg reaches almost 100 %, whereas silicon, sulphur, and oxygen are not completely depleted from gas phase. The degree of condensation of oxygen is about 35 % for most of time, shows an increase to the maximum value of 42 %, just before the evaporation rate has its maximum. This temporal change is also the same for silicon, which increases monotonically at first, but after the sulphur-bearing species SiS_2 , becomes unstable at around 650 K, and is returned back to gas. This enriches again the abundance of silicon in the gas and the silicon-bearing species, for example SiO and SiO_2 can be formed on the dust grains, which makes the degree of condensation increase. The most stable species, which still bound in the dust grains in the relatively high temperature are Al_2O_3 and titanium oxides.

During the evaporation phase, we can see the stability hierarchy of the elements very well. Sulphur is the first unstable element, followed by iron, which is given back to the gas at $T = 1250$ K. Most of the silicon and the magnesium is given back to gas more or less at the same temperature around $T = 1370$ K.

In Fig. 5.7 the degree of condensation and the number of the dust particles per H-atom as function of the temperature are presented, both for the formation and growth phase and for the evaporation phase. The growth phase continues after the temperature minimum still up to $T = 1250$ K.

For this reason f_c increases also after the minimum still. The temperature difference between the condensation temperature ($T = 836$ K at $J_{*,max}$) and the evaporation temperature ($T = 1339$ K at $J_{ev,max}$) is 503 K in case of the TiO_2 and can be

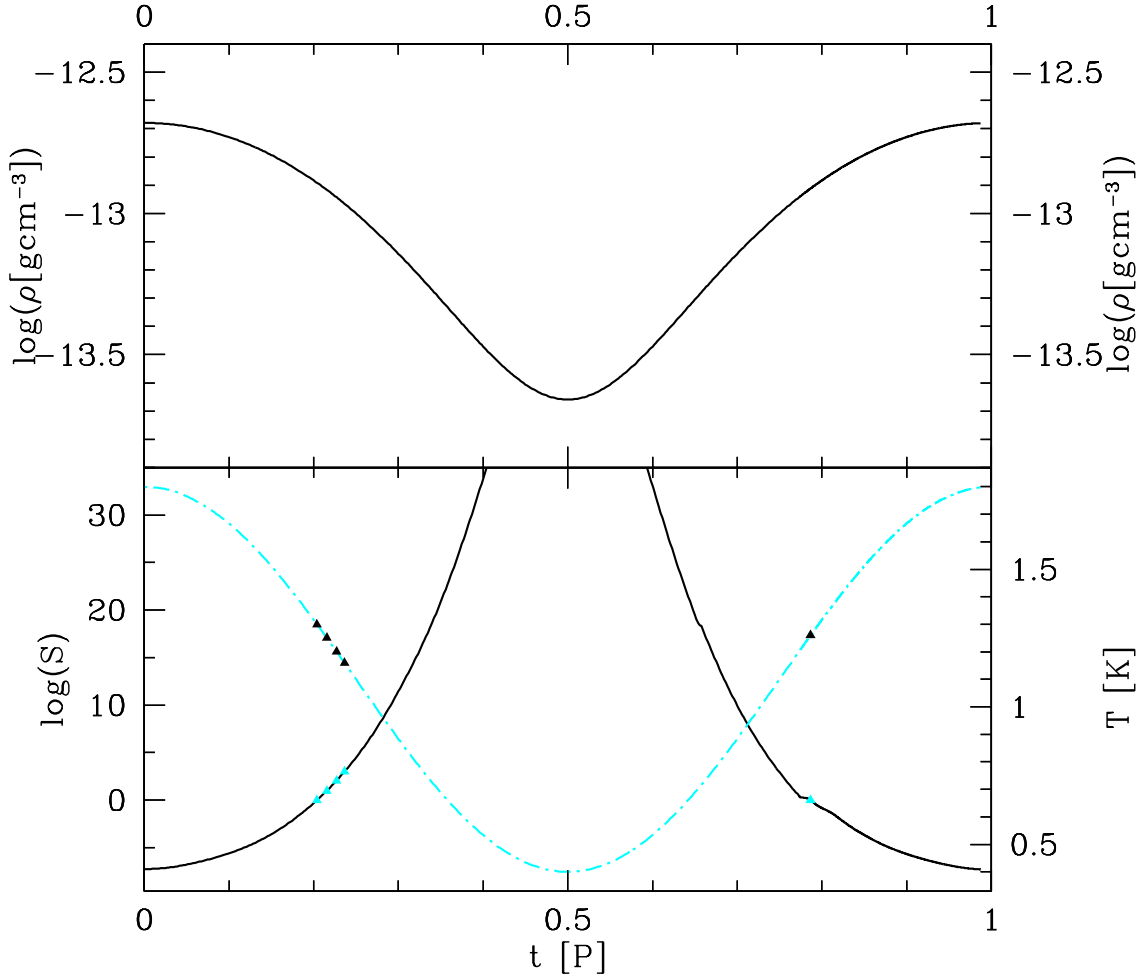


Figure 5.5: Supersaturation ratio of TiO_2 . In the upper diagram, the temporal variation of density is shown and in the lower diagram the temporal variation of temperature (dash-dot-line) and of the supersaturation ratio for TiO_2 are shown. The mass density and supersaturation ratio S are given on a logarithmic scale. The triangles before the temperature minimum correspond to $S = 1, 10, 100, 1000$ and the triangles after the temperature minimum refer to $S = 1$.

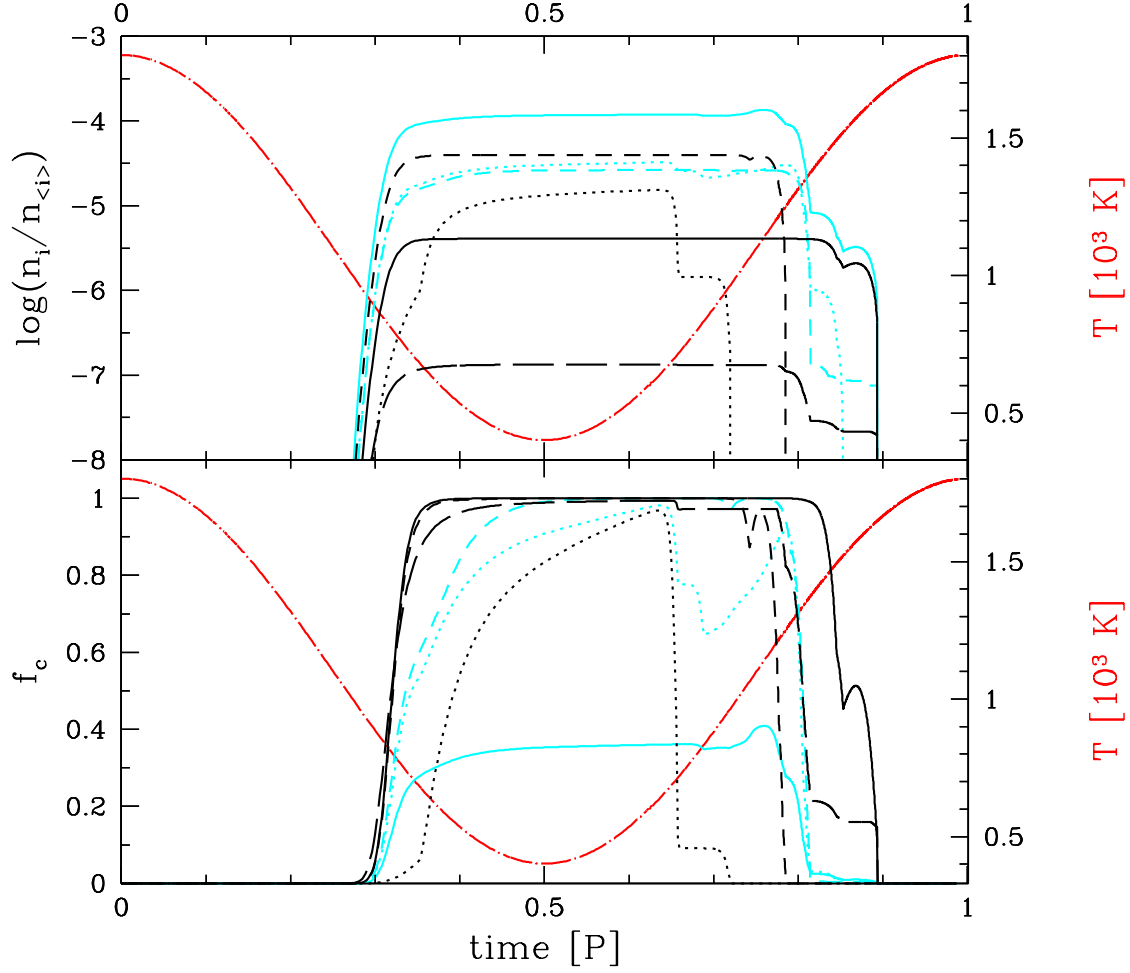


Figure 5.6: Chemical composition of the dust grains with TiO_2 nuclei as a function of time. light-blue full: O, light-blue dotted: Si, light-blue dashed: Mg, black full: Al, black dotted: S, black dashed: Fe. **upper diagram:** logarithm of the number of condensed element i per H-atom $n_i/n_{\langle\text{H}\rangle}$, **lower diagram:** Degree of condensation f_c of the considered elements.

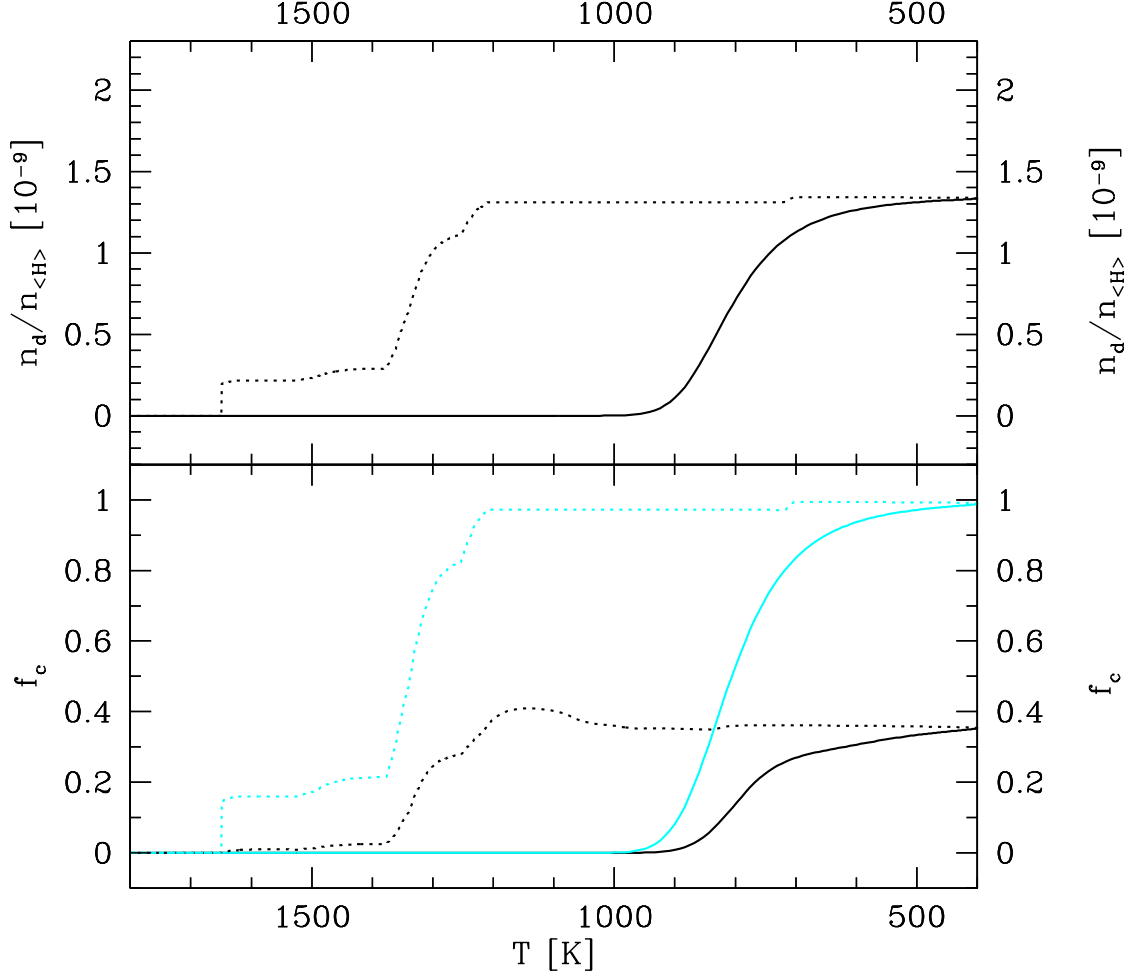


Figure 5.7: The dust properties as a function of temperature for dust with TiO_2 nuclei. The change of the degree of condensation f_c (lower diagram) and the number density of dust per H-atom $n_d/n_{<H>}$ for dust with TiO_2 nuclei in the formation phase (full lines) and the evaporation phase (dotted lines) as a function of temperature. The light-blue lines in the lower diagram represent the degree of condensation of Ti and the black lines indicate the degree of condensation of O.

clearly seen in Fig. 5.7, which shows the different paths of formation and evaporation of the dust grains.

5.2.2 Dust formation on the Fe nuclei

In Fig. 5.8 the thermodynamical quantities and dust properties for the dust grains with Fe nuclei are shown. The supersaturation ratio reaches its critical value S_c at $T = 924$ K, the nucleation rate of Fe is still negligible with $J_* = 5.5 \cdot 10^{-38} \text{s}^{-1}$ in comparison with the maximum value of J_* . The nucleation rate increases, however, with decreasing temperature rapidly and reaches a maximum value of $J_{*,max} = 3.4 \cdot 10^{-15} \text{s}^{-1}$ at $t = 0.35$ P and at $T = 687$ K. The nucleation rate of Fe has its value in a rather narrow range of time, but more larger nucleation rate than TiO_2 nucleation.

The evaporation rate shows a slightly larger than the nucleation rate and this occurs also in the narrow range of time and temperature. The evaporation occurs similar to the case of TiO_2 nuclei in the different thermodynamic conditions and has its maximum value $|J_{ev,max}| = 4.0 \cdot 10^{-15} \text{s}^{-1}$ at $T = 1347$ K ($t = 0.81$ P), which is slightly higher than for the case of TiO_2 . At this temperature, most species become unstable and the number density $n_d/n_{<H>}$ of the dust grains falls rapidly down from $1.3 \cdot 10^{-9}$ to $6.0 \cdot 10^{-10}$.

After the evaporation rate reaches its maximum, the most of the dust grains are destroyed and there remain only the dust grains with high temperature condensates in the mantle. The maximum number density of the dust grains is a factor of 10 larger than for the TiO_2 nucleation and this is mainly due to the difference of the abundance of the seed material. The evaporation of the mantle material of the dust grains continues up to around $T = 1638$ K, which is just slightly different from the destruction temperature for the TiO_2 nuclei.

At the beginning of condensation, the mean grain radius is around $0.018 \mu\text{m}$ and relatively small and reaches its maximum $0.068 \mu\text{m}$ at $t = 0.64$ P, in a time span of 0.1 P. The decrease of the mean grain radius in the time span between 0.64 P and 0.76 P is due to the evaporation of the sulphur-bearing species, SiS_2 , MgS and MgSO_4 as for the TiO_2 nuclei. The decrease of the mean grain radius is here not so significant as in the case of TiO_2 and this is mainly due to the larger number density of the dust grains, on which the evaporating sulphur-bearing species have been formed.

The temporal change of temperature T , density ρ , and supersaturation ratio S are depicted in Fig. 5.9. The supersaturation ratio is greater than unity at a temperature around $T = 1066$ K ($t = 0.26$ P). The critical supersaturation ratio $S_c = 1000$ is reached at $T = 924$ K ($t = 0.29$ P), the nucleation rate of Fe is negligible in this time with $J = 2.7 \cdot 10^{-41} \text{s}^{-1}$ in comparison with the maximum value $J_* = 3.4 \cdot 10^{-15} \text{s}^{-1}$ at $T = 687$ K ($t = 0.35$ P). The supersaturation ratio of Fe is significantly smaller than that of TiO_2 . The increase of the supersaturation ratio around $T = 600$ K becomes

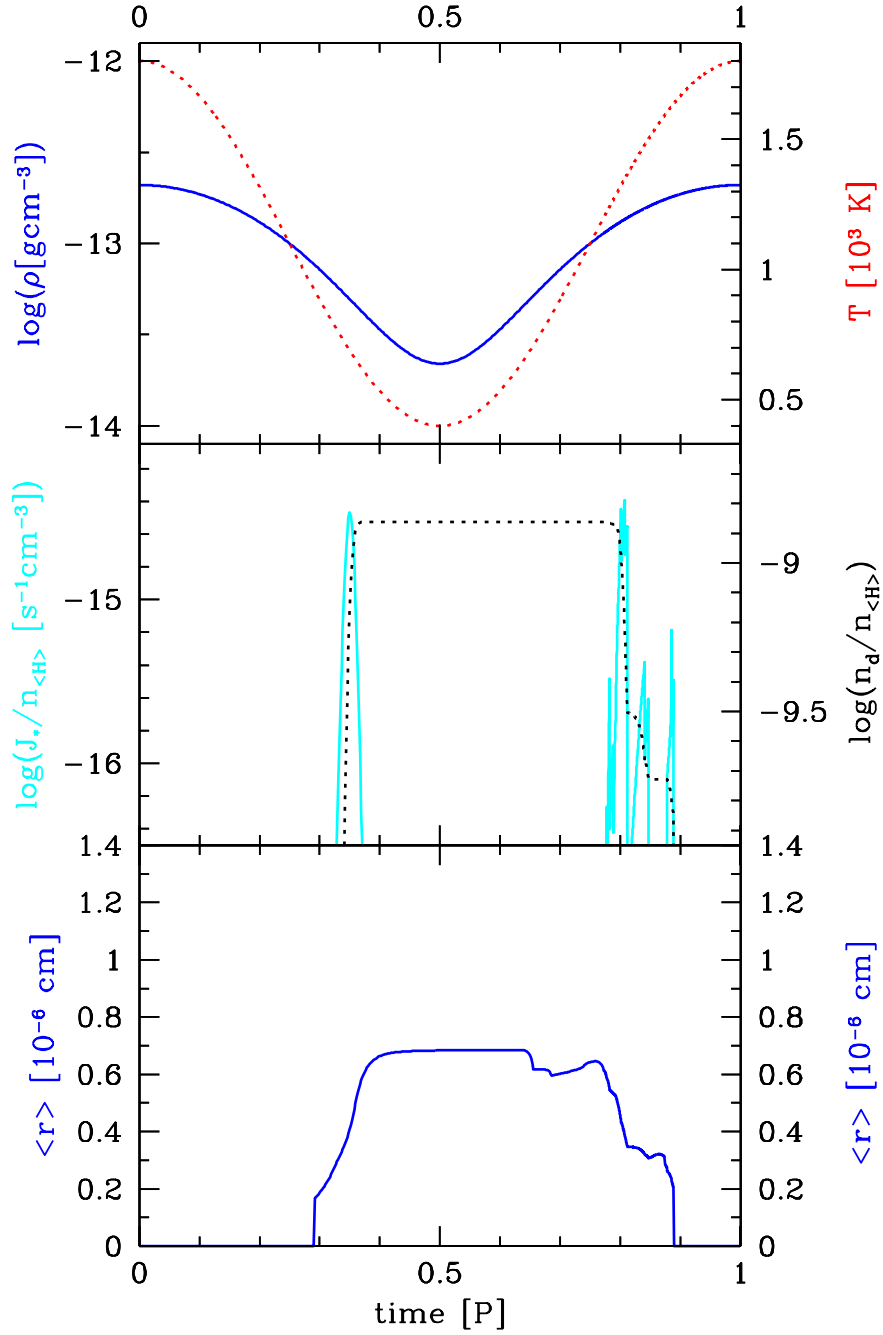


Figure 5.8: Thermodynamical and dust quantities for dust with Fe nuclei.

upper diagram: logarithm of the mass density ρ (full line, l.h.s. ordinate) and temperature T (dotted line, r.h.s. ordinate); **middle diagram:** logarithm of the nucleation and evaporation rate J_* and J_{ev} (full line, l.h.s. ordinate) and logarithm of the number of dust particles per H-atom $n_d/n_{<H>}$ (dotted line, r.h.s. ordinate); **lower diagram:** mean particle radius $\langle r \rangle$.

smaller than the above temperature and this is due to the chemical conditions in the gas phase. In this temperature range the most iron is bound in more complex and less stable molecule $\text{Fe}(\text{OH})_2$ which shows increase of concentration in the gas phase accordingly (Gail and Sedlmayr 1986, Gauger 1991).

After the evaporation of sulphur, iron in gas is enriched by the evaporation of iron nuclei. This leads the increase of supersaturation ratio shortly in time. The transition from growth to evaporation occurs at an relatively high temperature of $T = 1141$ K, which is 389 K above the nominal evaporation temperature of $T = 752$ K, at which S would be unity in the dust free gas. Hence, the Fe nuclei are shielded by the mantle and kept in stable phase.

The temporal variation of the chemical composition of the dust grains with Fe nuclei can be seen in Fig. 5.10 and the number density of the elements contained in the dust grains and the degree of condensation for each element are also depicted.

As can be seen for the degree of condensation, Fe is the first element to be contained in the dust grains as seed. For Fe and Al, the degree of condensation reaches unity even at the beginning of the growth phase, since they are bound in the most stable species Al_2O_3 and Fe_2O_3 already at these high temperatures. The degrees of condensation for Si and Mg show similar course to the course of the degree of condensation for Fe and reach their maximum value after the temperature minimum, whereas magnesium and sulphur are totally depleted from the gas phase. Oxygen is still not completely depleted, since the most oxygen is bound in H_2O .

The degree of condensation for oxygen is around 35 %, but reaches its maximum of 44 %, just before the evaporation rate has its maximum. This temporal change is also the same for silicon is due to the same reason, the chemical conditions and the following enrichment of each elements in the gas phase through the evaporation of sulphur-bearing species. The species contained still in the dust grains are Al-bearing species (Al_2O_3 , Al_2SiO_5 , $\text{Al}_6\text{Si}_2\text{O}_{13}$ and MgAl_2O_4). The stability hierarchy of the elements in the evaporation shows similar variation. Sulphur is the first unstable element, followed by the iron. Silicon and magnesium are given back to gas simultaneously around $T = 1370$ K and aluminium are still contained at higher temperature till 1638 K.

In Fig. 5.11 the degree of condensation and the number of the dust particles per H-atom are depicted as function of the temperature, for the formation and growth phase as well as for the evaporation phase.

Figure 5.12 depicts the size distribution of the dust particles at temperature minimum 400 K and time $t = 0.5$ P, both for TiO_2 nuclei and for Fe nuclei for comparison. Since the dust grains with TiO_2 nuclei have a lower number density than those with Fe nuclei, the size distribution for TiO_2 nuclei shows its maximum at larger radius of grains in comparison with the case for Fe nuclei. Both size distribution have a rather narrow range of grain radii. For TiO_2 nuclei, the size distribution has its maximum $f(a)/n_{<H>} = 4.5 \cdot 10^{-5} \text{cm}^{-1}$ at $a = 9.3 \cdot 10^{-6} \text{cm}$ and it covers a range of grain radii between $9.2 \cdot 10^{-6}$ and $9.8 \cdot 10^{-6} \text{cm}$. For Fe nuclei, the

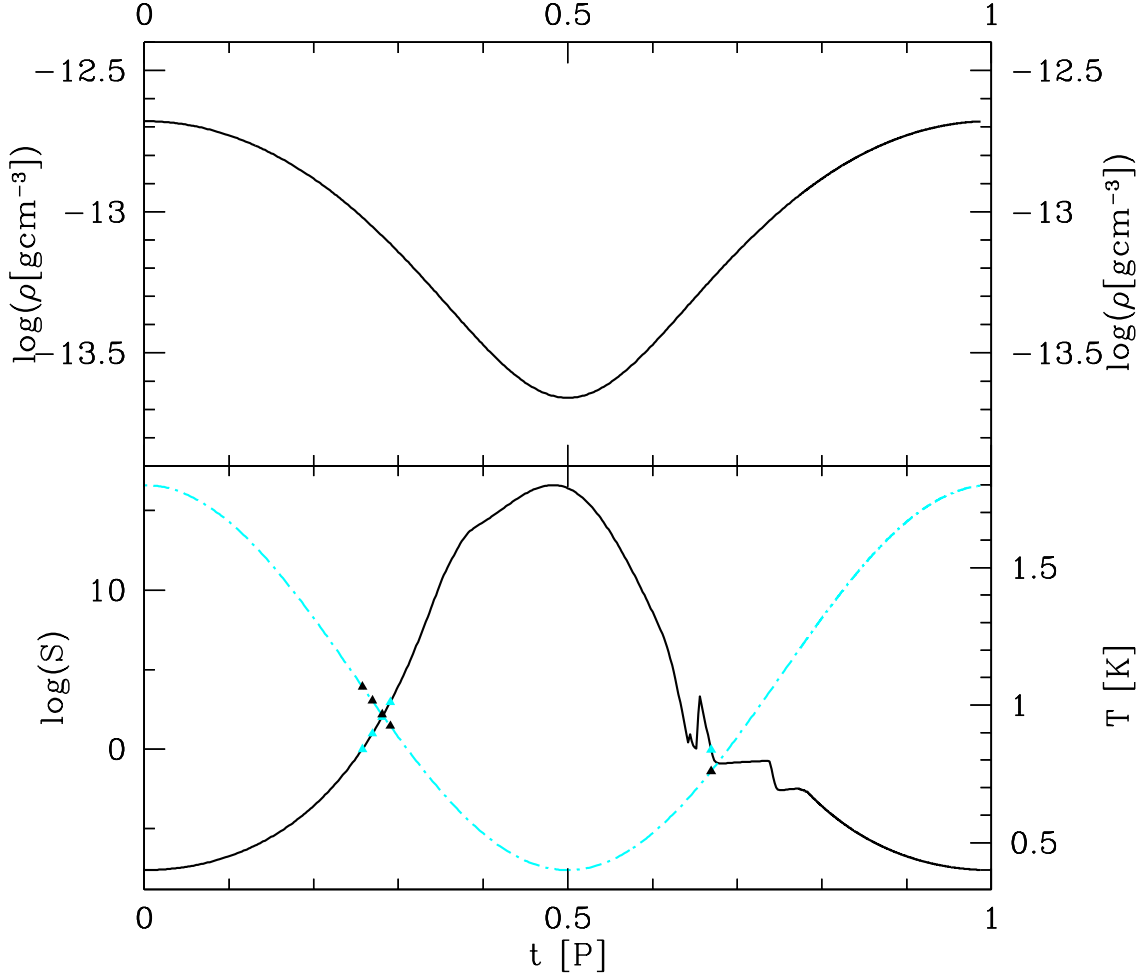


Figure 5.9: Supersaturation ratio of Fe dust.

The temporal variation of temperature (dash-dot-line), density, and of the supersaturation ratio for Fe dust are shown. The mass density and supersaturation ratio S are given on a logarithmic scale. The triangles correspond the respective values at $S = 1, 10, 100, 1000$.

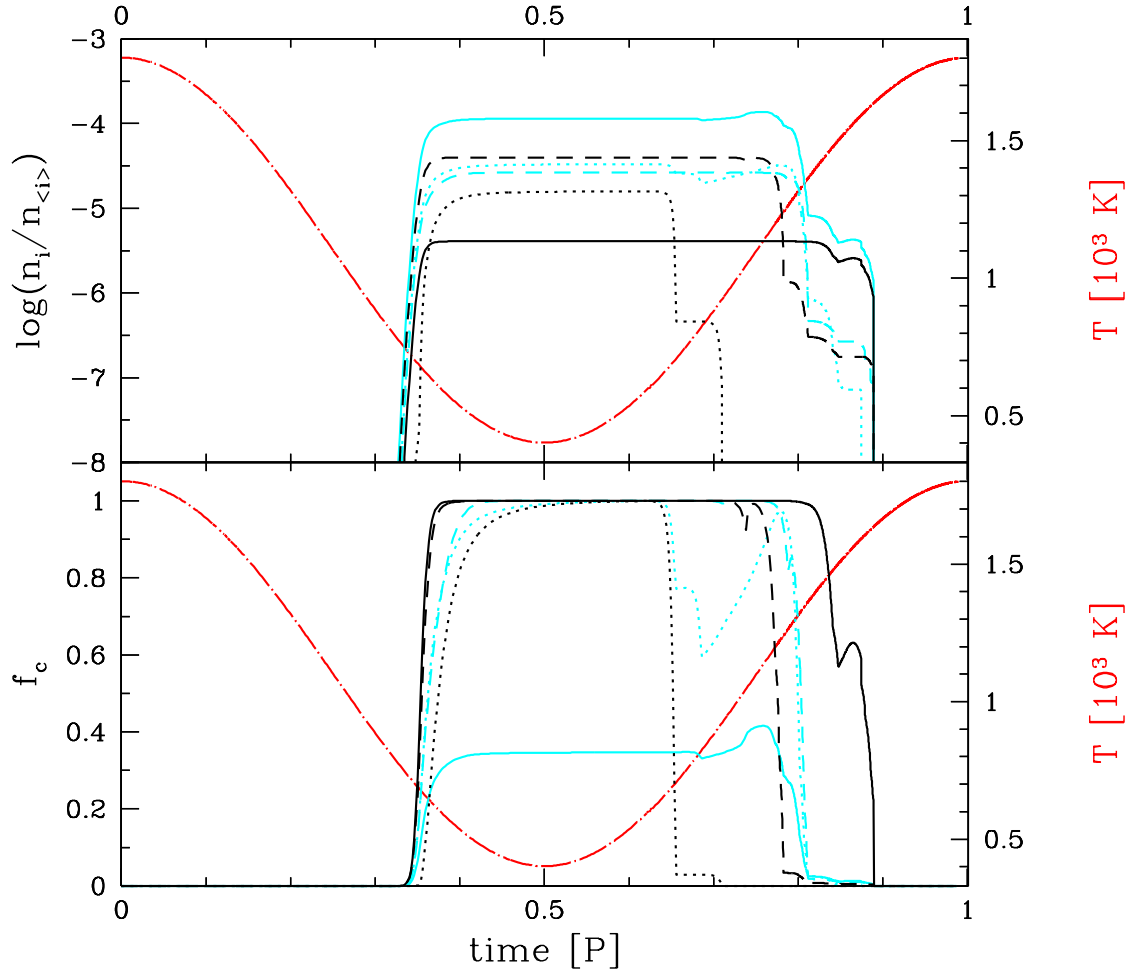


Figure 5.10: Chemical composition of the dust grains with Fe nuclei as a function of time. The longdashed–dotted lines are temperatures.

light–blue full: O, light–blue dotted: Si, light–blue dashed: Mg, black full: Al, black dotted: S, black dashed: Fe. **upper diagram:** logarithm of the number of condensed atoms of element i per H–atom $n_i/n_{<H>}$, **lower diagram:** Degree of condensation f_c of the considered elements.

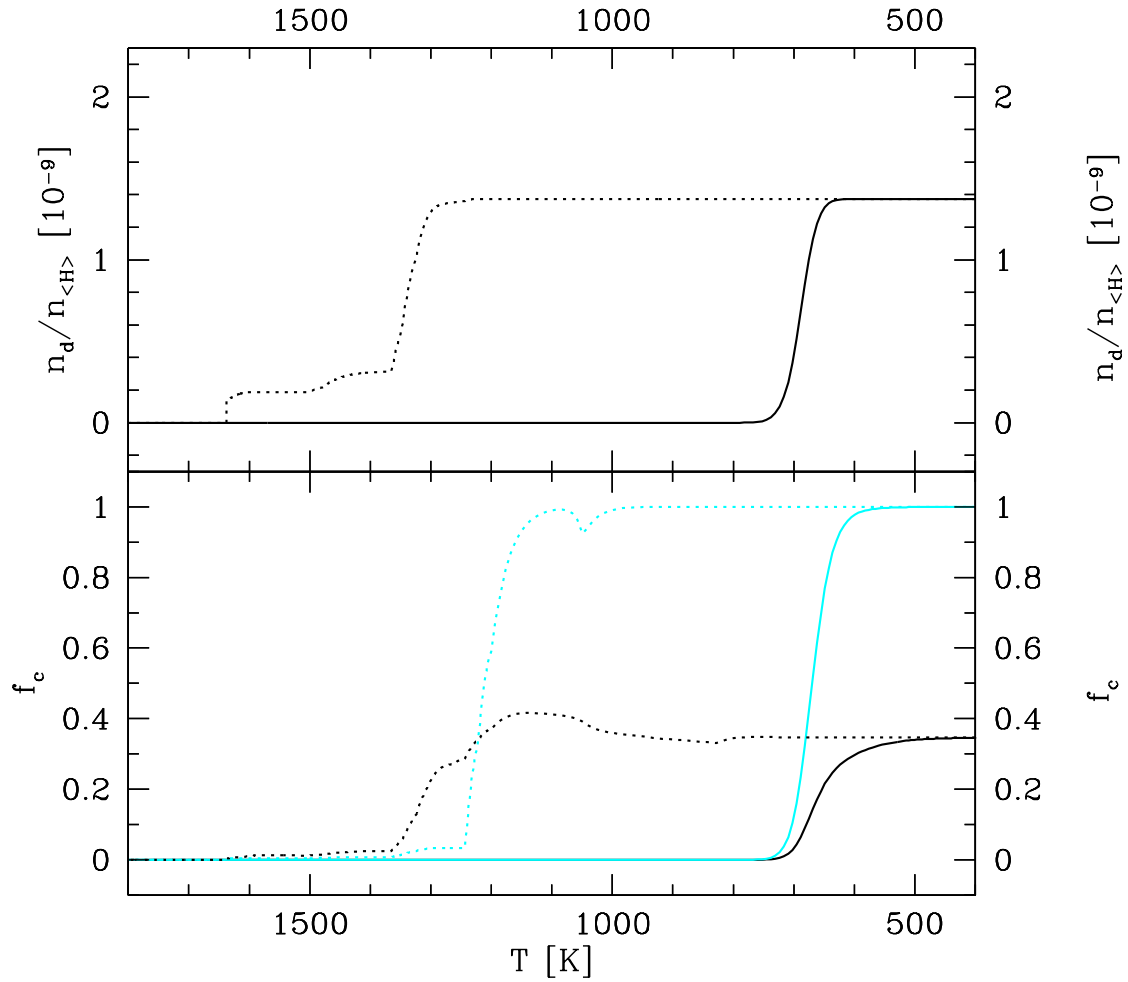


Figure 5.11: The dust properties as a function of temperature for dust with Fe nuclei. The change of the degree of condensation f_c (lower diagram) and the number density of dust per H-atom $n_d/n_{<H>}$ for Fe in the formation phase (full line) and the evaporation phase (dotted line) as a function of temperature. The light-blue lines in the lower diagram are the degree of condensation for element Fe and the black lines are the degree of condensation for element O in the respective phases.

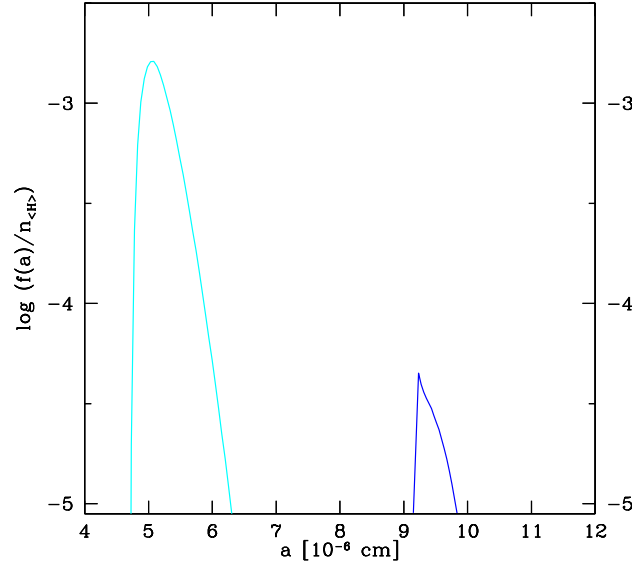


Figure 5.12: The size distribution for TiO_2 nuclei (blue) and for Fe nuclei (light-blue).

maximum $f(a)/n_{<H>} = 1.6 \cdot 10^{-3} \text{cm}^{-1}$ occurs at $a = 5.1 \cdot 10^{-6} \text{cm}$ and the distribution ranges from $a = 4.8 \cdot 10^{-6} \text{cm}$ to $a = 6.3 \cdot 10^{-6} \text{cm}$.

The asymmetry of distribution is mainly due to the different growth times before and after the nucleation maximum. Since the nuclei formed after the maximum grow more slowly than those before. The difference in radius between grains, whose formation instant of time corresponds to the change of nucleation, is distinctly smaller than after $J_{*,max}$ and the size distribution decreases rapidly at smaller radii of grains.

5.2.3 concluding remarks

If one conceives a gas element as a thermodynamic system, which reacts on a process forced from outside, this investigation can be interpreted as the two phase system to reach in equilibrium. If the change of the conditions forced from outside is quick enough in comparison to the relaxation time to the equilibrium, the system departs from the equilibrium, whereas the relaxation time diminishes, however, until the system approaches ultimately again the equilibrium, which is shown in this study as the transition between formation and evaporation.

The differences in the processes of nucleation, growth and evaporation lead back to the characteristics of the dust material and the different abundances of the nucleation material. The growth process in this investigation of a gas element shows essentially the same characteristics for the two cases with different nuclei, where the nucleation determines the dust properties in dependence of the thermodynamical properties of the nucleation material. The difference in the number density, which

is due to the different abundances of the nucleation species, leads to the different course of the dust properties. In case of the Fe nuclei, a larger number of dust particles forms and therefore, in comparison with the dust with TiO_2 nuclei, the mean grain radius is small by the slower growth. The evaporation occurs first at higher temperatures than the formation and proceeds comparatively more rapidly than the formation. The temperature difference between condensation and evaporation is approximately 500 K.

*HEAVEN'S NET CASTS WIDE.
THOUGH ITS MESHERS ARE COARSE, NOTHING SLIPS THROUGH.*

– LAO-TSU

Chapter 6

Dynamic Models of oxygen-rich CDS around LPVs

The highly evolved stars on the Asymptotic Giant Branch provide the peculiar physical conditions of cool extended atmospheres in which small solid particles, dust grains, are formed. Driven by the radiation pressure on these dust particles, massive outflows can develop with a substantial mass loss.

Through the consumption of elements into dust grains, dilution of the gas by the generation of an outflow, and by thermal heating, dust changes its environment and regulates the conditions of its own formation. Therefore, the dust formation in a circumstellar environment is an extremely coupled, self-regulating process.

Dynamic models for oxygen-rich CDS are presented in this chapter, which include a consistent treatment of the dust formation process according to the moment equation.

6.1 Initial Hydrostatic Models

To define the initial values for the time dependent dynamical model calculations, the initial structure has been calculated in terms of hydrostatic atmospheres.

The hydrostatic models are calculated in Lucy approximation (Lucy 1971, 1976) for the temperature determination. The gas opacity χ^g/ρ is taken as constant, $2 \cdot 10^{-4} \text{cm}^2 \text{g}^{-1}$ (Bowen 1988) and for the mean molecular weight we adopted $\mu = 1.26$. The innermost radial grid point is set at $R_{\text{inner},0} = 0.91 R_{*,0}$ and the number of grid point is 40.

The input parameters for the initial hydrostatic models are the four fundamental stellar parameters: stellar luminosity L_* , stellar mass M_* , effective temperature T_* , and over abundance $\varepsilon_C/\varepsilon_O$. Two additional pulsation parameters are also given for the following dynamic calculations: pulsation period P and velocity amplitude at the inner boundary Δu_p . The stellar radii $R_*(t_0)$ are calculated from the relation, $L_* = 4\pi R_*^2 \sigma T_*^4$. The input parameters for model calculations are listed in Table 6.1.

Table 6.1: The input parameters for the initial hydrostatic models.

model	M_*/M_\odot	T_* [K]	L_*/L_\odot	C/O	Δu_p [km s ⁻¹]	P [d]	$R_{*,0}/[R_\odot]$
A	1	2000	20 000	0.5	5	300	1176.0
B	1	2000	15 000	0.5	5	300	1018.7
C	1	2000	10 000	0.5	5	300	831.7
D	1	2000	8 000	0.5	5	300	743.9
E	1	2000	20 000	0.5	10	300	1176.0
F	1	2000	15 000	0.5	10	300	1018.7
G	1	2000	10 000	0.5	10	300	831.7
H	1	2000	8 000	0.5	10	300	743.9

Fig. 6.1 shows the radial structure of the 4 initial hydrostatic models. The plotted lines in Fig. 6.1 (a) from top to bottom correspond to the model A(E), B(F), C(G) and D(H), respectively. The plotted quantities are

upper diagram: the temperature T and the logarithm of the nucleation rate J_*

middle diagram: the logarithm of the density ρ and the logarithm of the supersaturation ratio S

lower diagram: the logarithm of the growth velocity χ_{gr}

The distinct difference in the model parameters is essentially defined by the luminosity and temperature. High luminosities and low effective temperatures provide high densities, the favorable condition for the dust formation. To compare the extension of the initial models, the quantities are depicted in solar radii in Fig. 6.1 (b), and the plotted lines from left to right correspond to models A, B, C and D. The higher the luminosity is, the more extended is the initial model and the more smooth is its density profile.

The supersaturation ratio $S > 1$ indicates that the partial pressure of monomer of the condensing species is greater than the vapor saturation pressure. Hence, the seed material TiO_2 becomes stable and the dust formation can start. The real onset of the dust formation, however, requires that S exceeds a critical supersaturation ratio, for which we here adopt $S_c = 3$ in our calculations (Drain and Salpeter 1977). In the initial hydrostatic models shown in Fig. 6.1, the supersaturation ratio S of the seed material TiO_2 exceeds the critical supersaturation ratio already at $1.25 R_0$, and the growth velocity χ_{gr} is also positive for all initial models. Therefore, the dust formation can occur even in the initial models. The nucleation rates of each initial model decrease at $2 R_0$, by more than two orders of magnitude with decreasing luminosities, from top to bottom. The growth rates vary by two orders of magnitude

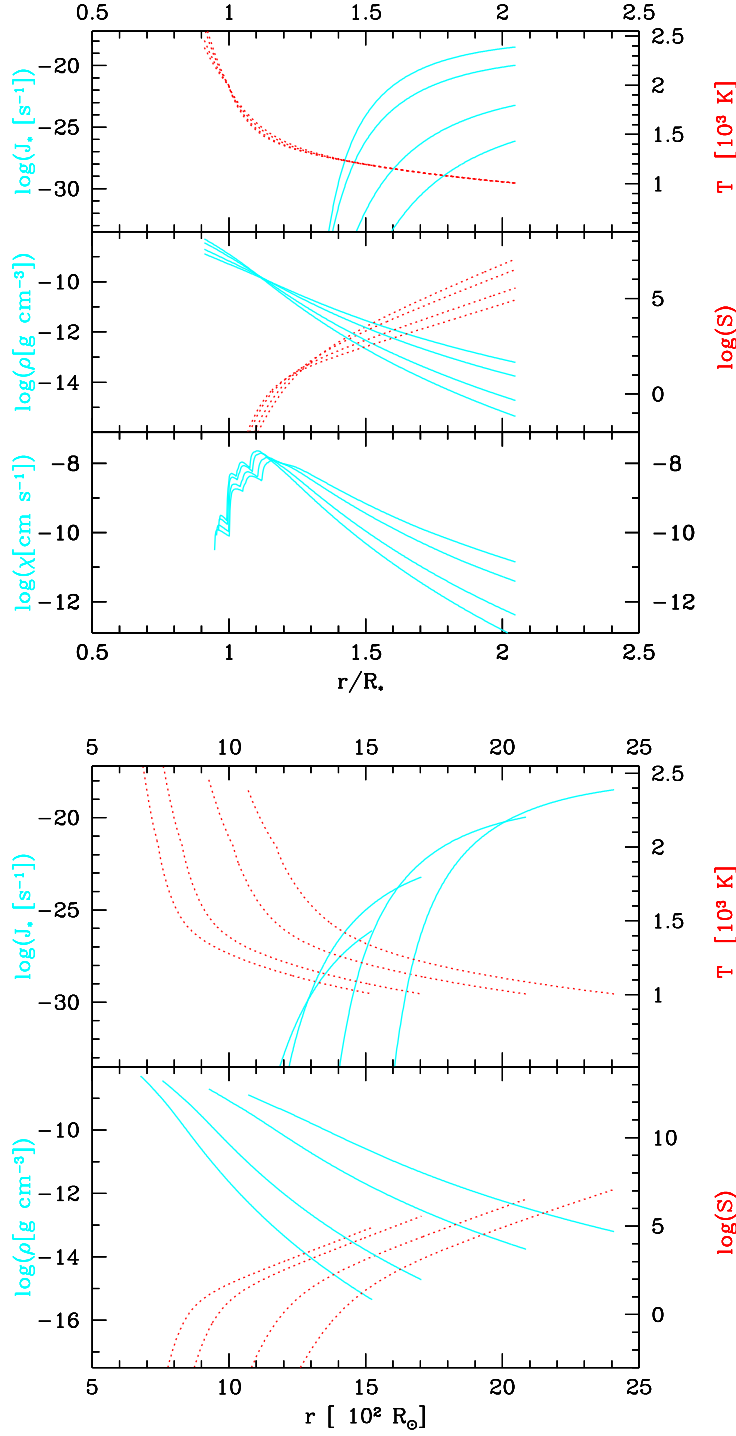


Figure 6.1: Initial hydrostatic models. Model parameters are given in Table 6.1. The plotted lines, from top to bottom correspond to the model A(E), B(F), C(G) and D(H), respectively. **upper diagram:** the logarithm of the nucleation rate J_* (light-blue solid) and the temperature T (red dotted). **middle diagram:** the logarithm of the density ρ (light-blue solid) and the logarithm of the supersaturation ratio S (red dotted). **lower diagram:** the logarithm of the growth velocity χ_{gr} .

at $2 R_0$ between model A and model D. These differences in the dust properties are mainly due to the different density profiles resulting from the different luminosities, whereas the temperature profiles of initial models are more or less similar with each other.

6.2 Comparison of Dynamic Model Calculations

The radial structure of the eight dynamic model calculations is shown in Fig. 6.2 and Fig. 6.3. Figures are plotted at the zero phase of a pulsation cycle. Fig. 6.2 shows the radial structure of the models with a velocity amplitude at the inner boundary of $\Delta u_p = 5 \text{ km s}^{-1}$ (model A, B, C and D from the left column to the right), and Fig. 6.3 shows the radial structure of the models of $\Delta u_p = 10 \text{ km s}^{-1}$ (model E, F, G and H from left to right). A direct comparison of the models shows the general characteristics of a close coupling of dust formation to hydrodynamics and to thermodynamics.

- If the dust formation and growth is efficient, they induce a perturbation in the velocity structure which becomes a shock wave. Shock waves are passing periodically and propagate through the atmospheres of the models.
- The determining influence of the dust formation on the thermodynamical structure can be seen in the temperature structure between $2 R_0$ and $4 R_0$ which coincides with the first maximum of the radiative acceleration α . This temperature jump results from the opacity of the newly formed dust.
- The correlations among the number density of the dust grains per H-atom, the hydrodynamic structure, and the density are clearly to be seen. The radiation acceleration α correlates strongly with the mean radius $\langle r_d \rangle$ of the dust grains.
- The distribution of the dust particles is strikingly inhomogeneous, which can be seen from the number density of dust grains and the mean grain radius. The number density of the dust grains per H-atom $n_d/n_{<H>}$ shows a large variation, by three orders of magnitude, in the radial structure.
- The nucleation rates $J_*/n_{<H>}$ reach a maximum of several 10^{-20} s^{-1} , but due to the constraint on the condensible TiO_2 molecule in the gas phase through the depletion of Ti, the nucleation occurs in several separate regions where the condensible TiO_2 molecules are available.
- The mean radius of the dust grain also reveals the inhomogeneity in the radial structure, and it shows a wide range of values between $0.01 \mu\text{m}$ and several $0.5 \mu\text{m}$.

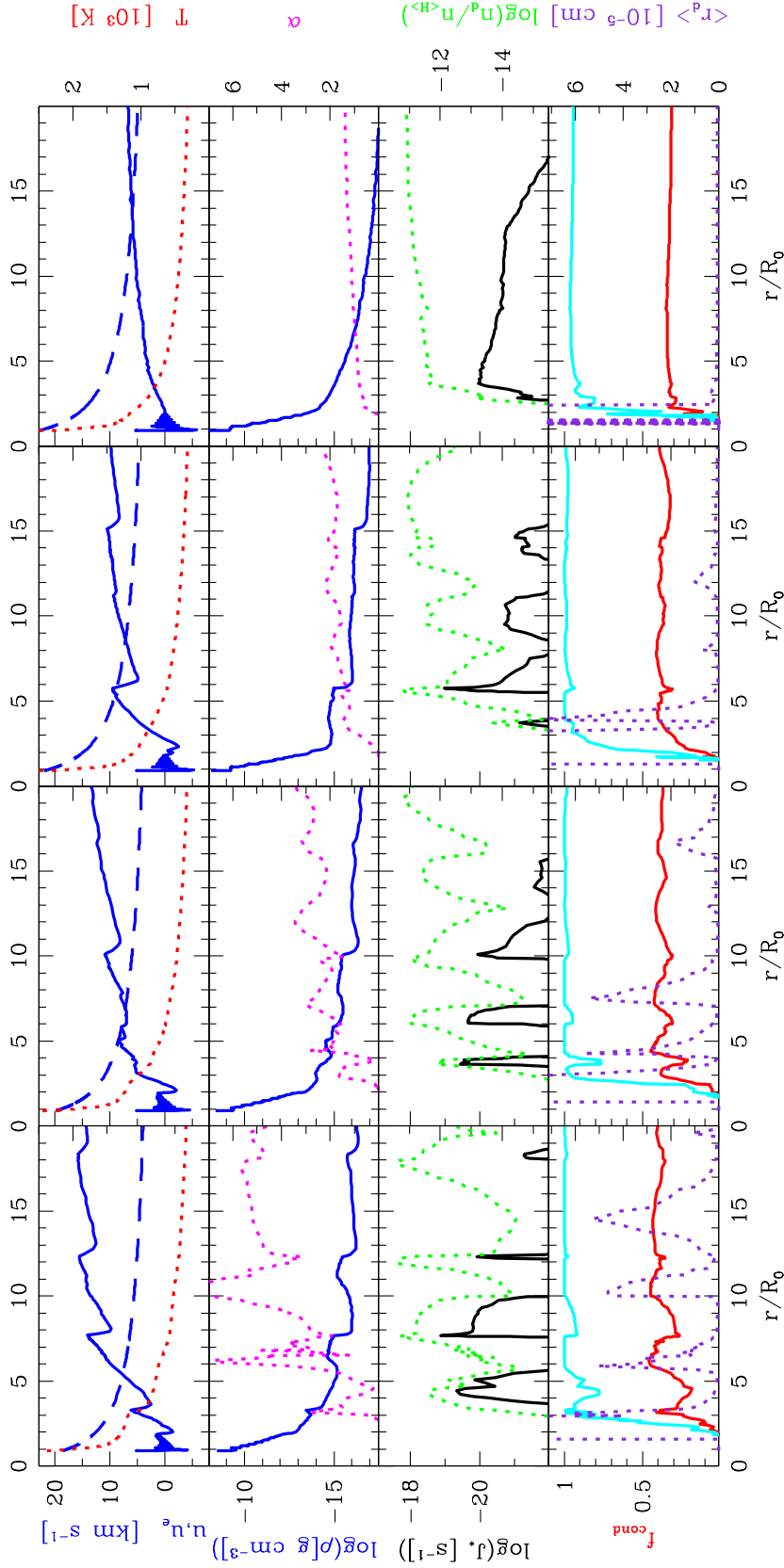


Figure 6.2: Radial structure of models A, B, C and D with $\Delta u_p = 5 \text{ km s}^{-1}$ at the zero phase of a pulsational cycle. **upper diagram:** the velocity u (solid line) the escape velocity u_e (dashed line), both of which belong to the l.h.s. ordinate, and the temperature T (dotted line, r.h.s. ordinate); **2nd diagram:** the logarithm of the density ρ (solid) and the radiative acceleration α in unit of the gravitational acceleration (dotted); **3rd diagram:** the logarithm of the nucleation rate J_* (solid) and the logarithm of the number density of dust grains per H-atom $n_d/n_{<H>}$ (dotted); **lower diagram:** the degree of condensation for O (red solid), and Ti (lilac solid) and the mean grain radius $\langle r \rangle$ (dotted).

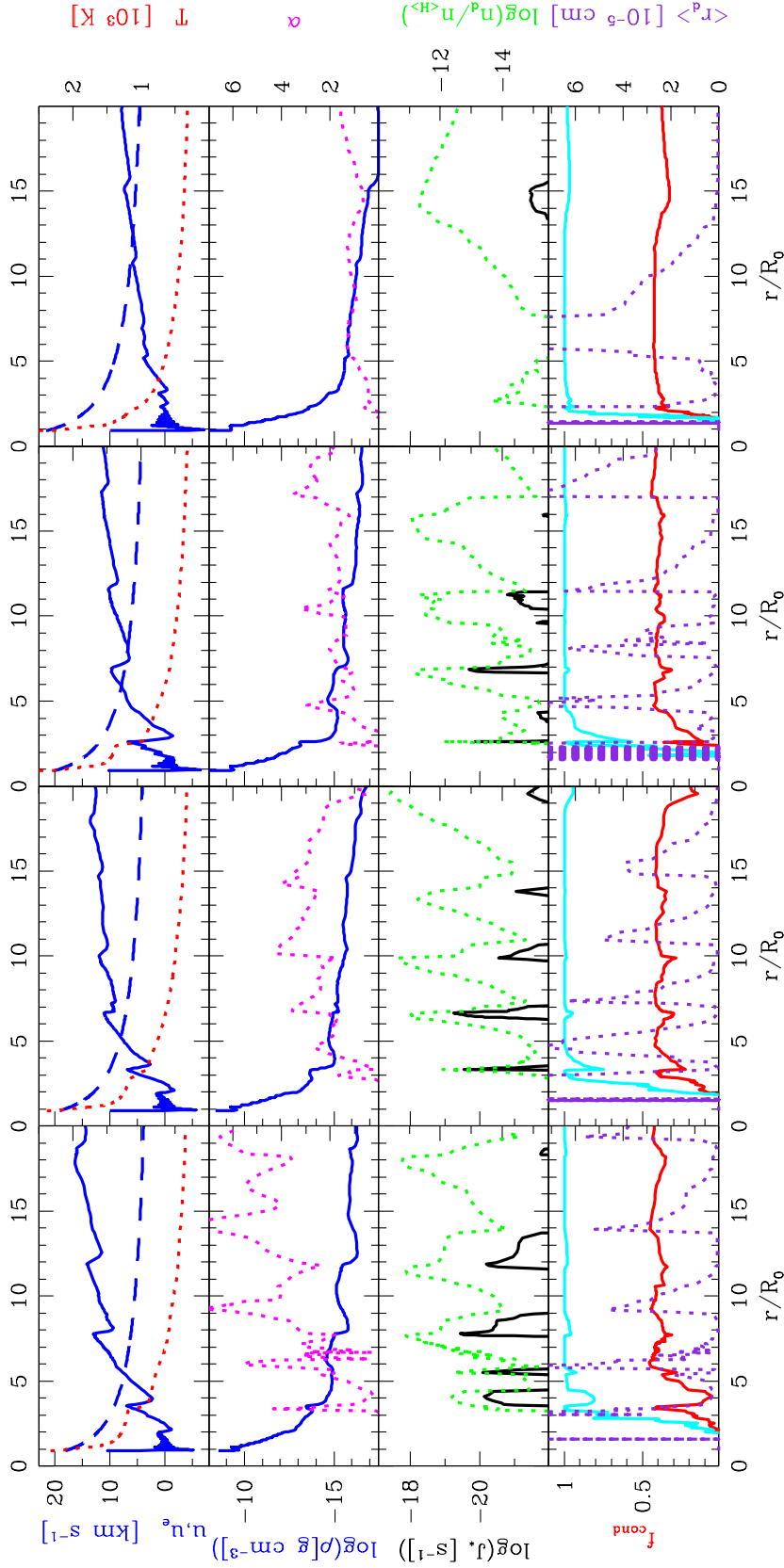


Figure 6.3: Radial structure of models E, F, G and H with $\Delta u_p = 10 \text{ km s}^{-1}$ at the zero phase of a pulsational cycle. Model parameters are given in Table 6.1. **upper diagram:** the velocity u (solid line), the escape velocity u_e (dashed line), both of which belong to the l.h.s. ordinate, and the temperature T (dotted line, r.h.s. ordinate); **2nd diagram:** the logarithm of the density ρ (solid) and the radiative acceleration a_{rad} (dotted); **3rd diagram:** the logarithm of the nucleation rate J_* (solid) and the logarithm of the number density of dust grains per H-atom n_d/n_H (dotted); **lower diagram:** the degree of condensation for O (red solid) and Ti (lilac solid), and the mean grain radius $\langle r \rangle$ (dotted).

The close coupling of dust formation to hydrodynamics can be seen in the radial structure of the velocity. The peak of the velocity between $3 R_0$ and $4 R_0$ coincides with the innermost maximum of the radiative acceleration on the dust grains α which obviously includes a perturbation in the velocity structure, subsequently steepens and becomes a new dominating shock.

All models have in common the levitation of the atmosphere in comparison to an exponentially decreasing density structure of hydrostatic models. This effect is mainly due to the deposition of mechanical energy caused by the pulsation. As already mentioned, the atmospheres of all models are passed periodically by shock waves and develop a wind.

The frequency of the passing shock waves in the atmosphere is decreasing from model A to model D and from model E to model H, respectively. The same tendency is also seen in the outflow velocities. The outflow velocity exceeds the escape velocity between $5 R_*$ and $8 R_*$ and it drives the wind, whereas for model D and H, the outflow velocity exceeds the escape velocity beyond $12 R_*$.

The hydrodynamic structure clearly coincides with the density structure and with the number density of the dust grains per H-atom. Model A and E show the distinct enhancement of the density structure corresponding to the velocity structure. In model B, the perturbation in the velocity structure also has an influence on the density profile, whereas the density profile in model C reveals the stepwise structure.

In general, the nucleation of TiO_2 occurs between $3 R_*$ and $5 R_*$ which corresponds to the nucleation region in the case of the carbon-rich CDS. The beginning zone is slightly outer than in the carbon-rich case and this is mainly due to the different thermodynamical properties of the seed material.

After the onset of the nucleation, the growth process is mainly dependent on the density of the growth material. Therefore, the growth process is effective in the enhanced density region and this leads even to the total consumption of elements in the gas phase through the growth of the species in the mantle of the dust grains. Through the consumption of Ti by the growth of the Ti-bearing species on the dust grains, the nucleation of TiO_2 occurs in several separate regions, where Ti is available to form TiO_2 in the gas phase.

6.2.1 The degree of Condensation f_{cond}

Fig. 6.4 and Fig. 6.5 depict the degree of condensation $n_i/n_{<i>}$ for each element i contained in the dust grains in the radial structure. The degree of condensation is strongly correlated with the density structure, which reflects the dependence of the growth of dust grains on the density structure.

The growth species are mostly oxides of the less abundant elements, of which abundances are in general an order of magnitude smaller than the abundance of oxygen. Therefore, the amount of oxygen contained in dust grains is rather dependent on the amount of the less abundant elements in dust grains and the dust to

gas ratio is essentially related to the total amount of the less abundant elements.

Oxygen has a degree of condensation of $f_{cond} = 0.4$ which means that 40 % of the oxygen in gas is depleted and the rest of oxygen is mostly contained in the H_2O molecules of the gas. Model D has a degree of condensation for oxygen of about 0.3, which is mainly due to the considerably lower density profile than the other models.

The first depleted element from the gas phase is Al, followed by Ti. This is due to the high stability of the aluminium- and titanium-bearing species, e.g. Al_2O_3 , Al_2SiO_4 , Al_6SiO_{13} , Ti_2O_3 and $MgTiO_3$, even at higher temperatures (above 1 000 K). These two elements show complete depletion already at the inner region between $3 R_*$ and $4 R_*$, just after the nucleation.

The degree of condensation for Mg, Si and Fe follows more or less a similar trend. For Mg and Fe, the degree of condensation reaches $f_{cond} = 1$ in several regions of the CDS, whereas Si is not completely depleted from the gas phase. The degree of condensation for Si generally varies between 0.7 and 0.85. The degree of condensation for Fe becomes remarkably larger after the temperature decreases below 1000 K. Sulphur generally has a lower degree of condensation than the other elements, but at temperatures lower than 600 K, its degree of condensation increases with increasing density profiles.

Of specific interest are the degrees of condensation in Model D and H, with $L_* = 8 \cdot 10^3 L_\odot$. In these two models, the density decreases relatively steeper than in the other models. Except for Al and Ti, which have reached already $f_{cond} = 1$ at the inner region of the CDS, the degrees of condensation for the other elements decrease with decreasing density profiles. This again shows the sensitive dependence of the growth process on the density profiles.

6.2.2 The Dust to Gas Ratio ρ_d/ρ_g

The radial structure of the dust to gas ratio ρ_d/ρ_g is shown in Fig. 6.6 and Fig. 6.7 at the zero phase of a pulsational cycle. The dust to gas ratio is given by

$$\frac{\rho_d}{\rho_g} = \sum_i \frac{m_i}{\mu m_H} f_c^i \varepsilon_i \quad (6.1)$$

where i labels elements with mass m_i , f_c^i is the degree of condensation of the respective element with an abundance ε_i and m_H is the mass of hydrogen atom. From the CO blocking, the abundance of available oxygen is taken as $\varepsilon_O^0 = \varepsilon_O - \varepsilon_C$.

It is interesting that the resulting dust to gas ratios ρ_d/ρ_g of all models are confined to a narrow interval between $3 \cdot 10^{-3}$ and $4.2 \cdot 10^{-3}$ which well agree with the observations (Knapp 1985, Sopka *et al.* 1985, Jura 1986, Olofsson *et al.* 1987, Justtanont *et al.* 1994). In the oxygen-rich case this confinement of dust to gas ratio is due to the fact that the dust grains consist of the less abundant elements. The amount of dust is still small compared to the surrounding gas.

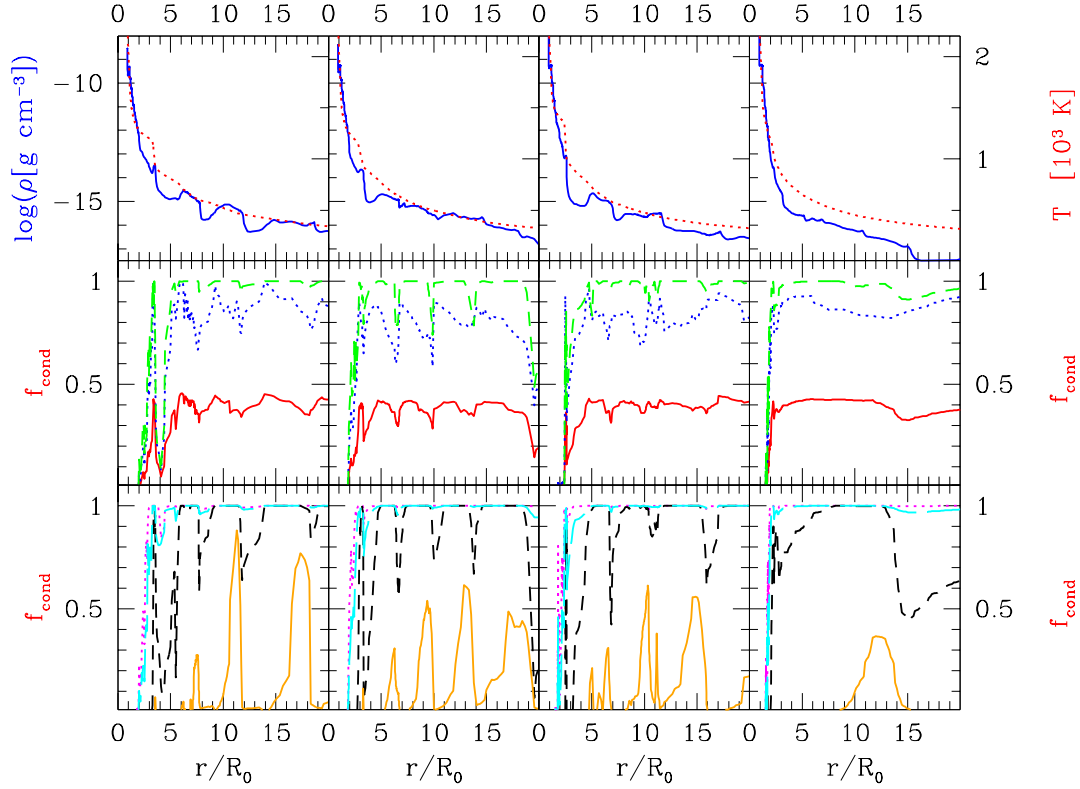


Figure 6.4: Radial structure of degree of condensation of elements for models with $\Delta u_p = 10 \text{ km s}^{-1}$ at the zero phase of a pulsational cycle. The columns correspond to model E, F, G and H from left to right. **Upper diagram:** the logarithm of density ρ (solid) and the temperature T (dotted line); **middle diagram:** the degree of condensation for O (solid), Si (dotted line) and Mg (dashed line); **lower diagram:** the degree condensation of Al (dotted line), Fe (dashed line), S (dash-dotted line), and Ti (solid).

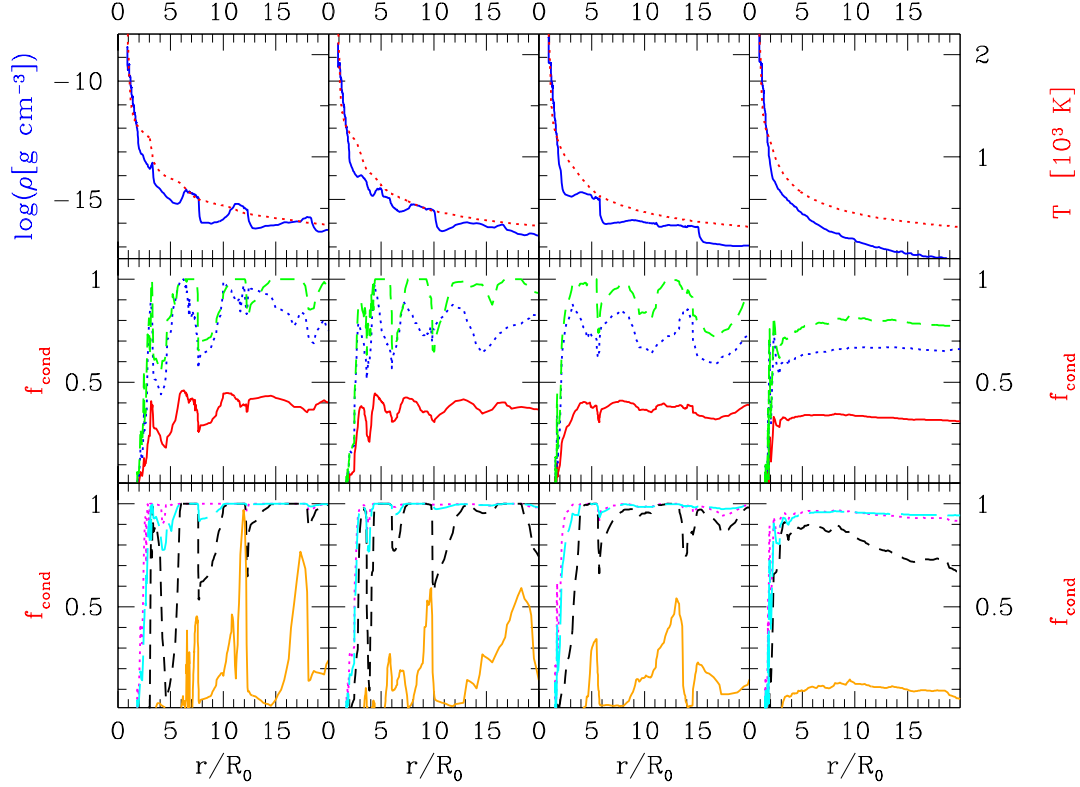


Figure 6.5: Radial structure of degree of condensation of elements for models with $\Delta u_p = 5 \text{ km s}^{-1}$ at the zero phase of a pulsational cycle. The columns correspond to model A, B, C and D from left to right. **Upper diagram:** the logarithm of density ρ (solid) and the temperature T (dotted line); **middle diagram:** the degree of condensation for O (solid), Si (dotted line), and Mg (dashed line); **lower diagram:** the degree condensation of Al (dotted line), Fe (dashed line), S (dash-dotted line), and Ti (solid).

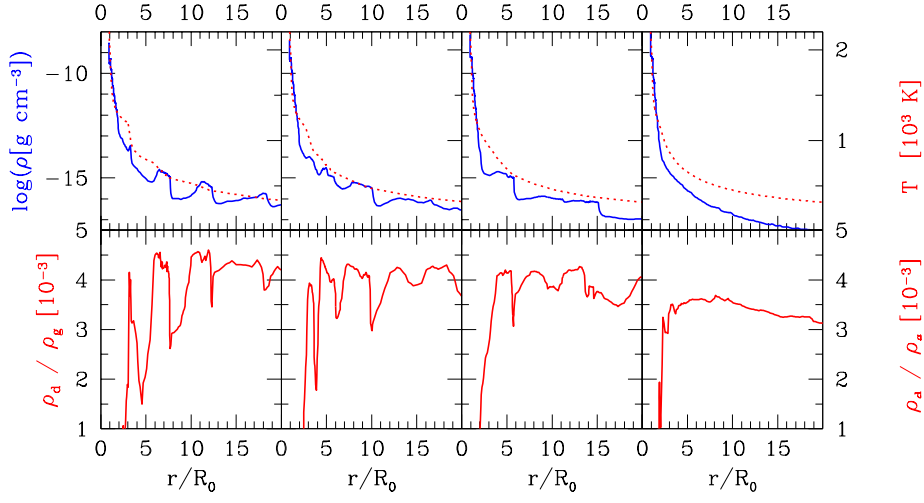


Figure 6.6: Radial structure of dust to gas ratio ρ_d/ρ_g for models with $\Delta u_p = 5 \text{ km s}^{-1}$ at the zero phase of a pulsational cycle. The columns from left to right correspond to Model A, B, C and D, respectively.

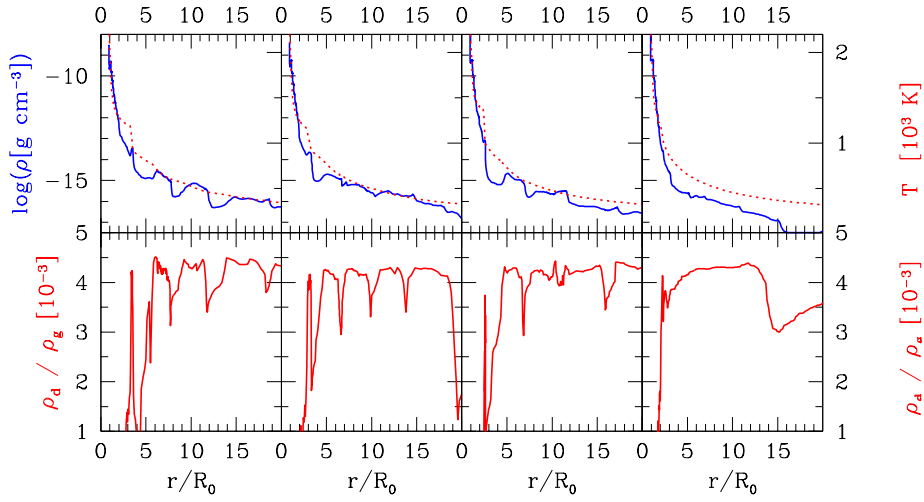


Figure 6.7: Radial structure of dust to gas ratio ρ_d/ρ_g for models with $\Delta u_p = 10 \text{ km s}^{-1}$ at the zero phase of a pulsational cycle. The columns, from left to right, correspond to Model E, F, G, and H, respectively.

In comparison with the carbon-rich CDS, the dust to gas ratio is more or less in the same range, but the absorption by the dust grains is less efficient than by the carbonaceous dust grains. This effect of absorption by oxygen-bearing dust grains can be seen in the radial structure of acceleration ratio α .

6.2.3 The Volume Fraction of Growth Species in Dust Grains

In Fig. 6.8 and 6.9, the typical radial structure of the volume fractions of the growth species (e.g. V_{TiO_2} , $V_{\text{Al}_2\text{O}_3}$) in dust grains are depicted and the different composition of the dust grains are shown for the different region in the CDS.

At the inner wind region $r < 4R_*$, most of the dust grain volume is filled by Al-bearing species. With the increasing volume fraction of Mg-silicate (e.g. MgSiO_3), the volume fractions of Al-bearing species decrease, until in the outer wind region most of the dust grain volume consists of Mg-silicates and iron oxides (e.g. Fe_3O_4). Fe itself has the volume fraction less than 5 % in the whole region.

Noteworthy is the volume fraction of Fe-bearing species in Model E. At several wind regions the volume fraction of the Fe-bearing species and of the Mg-silicate are reciprocal (anti-correlated). The volume fraction of Mg-silicate increases, where the iron-bearing species are virtually not contained in the dust grains.

The volume fractions of the sulphur-bearing species show a sporadic trend and are generally less than 15 %. Most of sulphur is contained in SiS_2 which shows a reciprocal distribution to SiO_2 . The reasons are mainly due to the chemical sputtering and the high instability of SiS_2 , as compared to SiO_2 .

Most of Mg is contained in Mg-silicates, but the volume fraction of MgSO_4 sporadically reaches about 9 % where the volume fraction of Mg-silicates decreases. Most of Ti is contained as oxides, e.g. Ti_2O_3 and Ti_3O_5 .

In Model D, where the density profile is very steep with the increasing distance from the central star, the composition of the growth species are determined by iron oxides and Mg-silicates. Iron usually has a volume fraction less than 1 %, only exceptionally more at $\approx 6R_*$. The reciprocal distribution between iron oxides and Mg-silicates can also be seen. Sulphur-bearing species have less than 3 % of volume fraction in the dust grains.

6.2.4 The Mass Loss Rate

From the radial structures in Fig. 6.11 and Fig. 6.12, it can be seen that the mass loss rates vary according to the distance from the central star. The large variation of mass loss rates in the wind regions of $r \leq 15R_*$ is mainly due to the density change, whereas the velocities in the same region is relative smaller than those in the well extended outer wind region, at around $35 R_*$. The local mass loss rates vary by at least an order of magnitude at an instant of time.

Since the mass loss rate varies in pulsational cycles, the corresponding mean values are averaged over pulsational periods. Table 6.2 shows the resulting quanti-

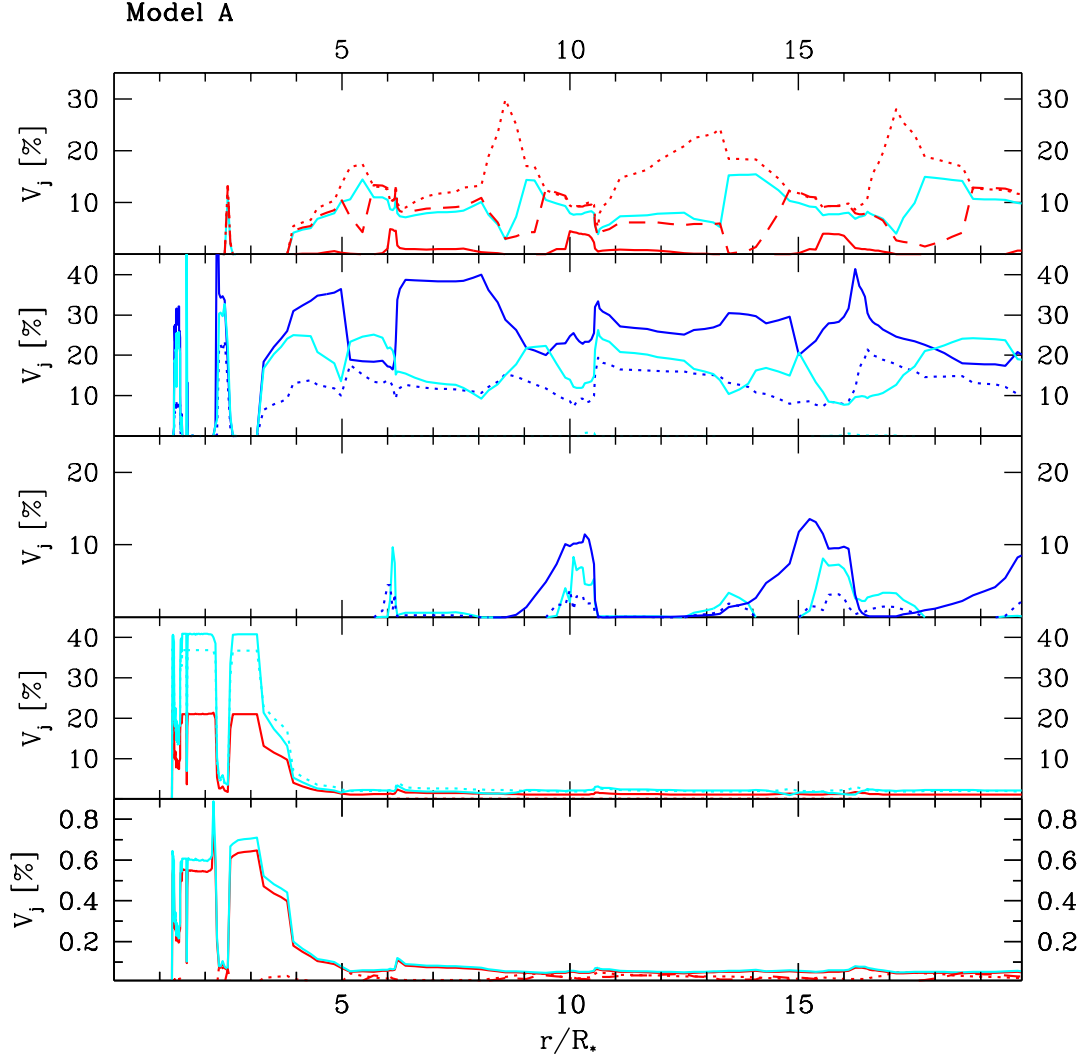


Figure 6.8: Radial structure of the volume fraction of the growth species in dust grains for model A at $t = 165$ P. **Upper diagram:** Fe (red solid), FeO (light-blue solid), Fe_2O_3 (red dashed), and Fe_3O_4 (red dotted). **2nd diagram:** SiO (light-blue dashed), MgO (light-blue dotted), SiO_2 (blue dotted), MgSiO_3 (blue solid), and Mg_2SiO_4 (grey solid). **3rd diagram:** MgS (blue dotted), SiS_2 (blue solid), MgSO_4 (light-blue solid), and Al_2S_3 (light-blue dotted). **4th diagram:** Al_2O_3 (red solid), MgAl_2O_4 (red dotted), Al_2SiO_5 (light-blue solid), and $\text{Al}_6\text{Si}_2\text{O}_{13}$ (light-blue dotted). **Lower diagram:** TiO (light-blue dashed), TiO_2 (red dotted), Ti_2O_3 (red solid), Ti_3O_5 (light-blue solid), and MgTiO_3 (red dashed).

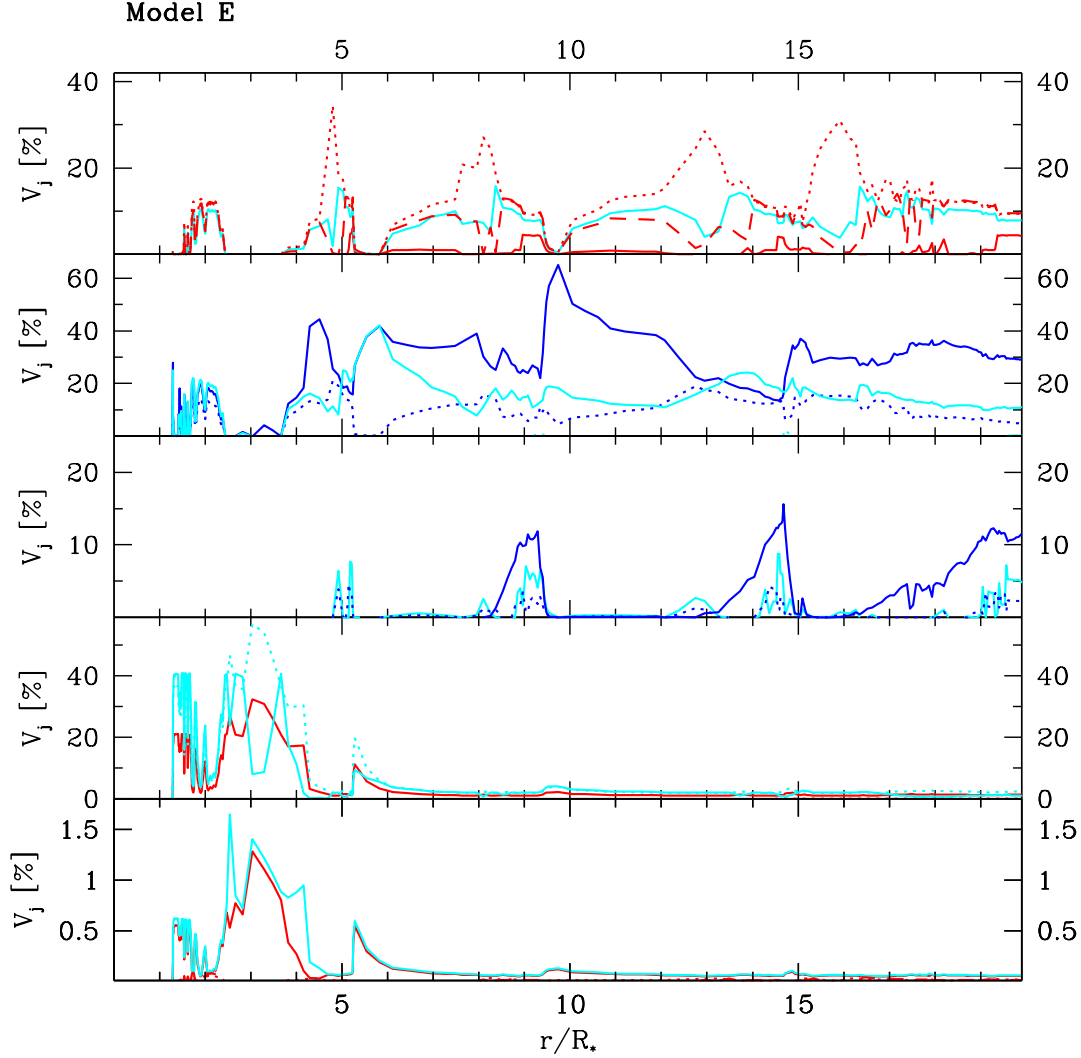


Figure 6.9: Radial structure of the volume fraction of the growth species in dust grains for model E at $t = 150$ P. **Upper diagram:** Fe (red solid), FeO (light-blue solid), Fe_2O_3 (red dashed), and Fe_3O_4 (red dotted). **2nd diagram:** SiO (light-blue dashed), MgO (light-blue dotted), SiO_2 (blue dotted), MgSiO_3 (blue solid) and Mg_2SiO_4 (light-blue solid). **3rd diagram:** MgS (blue dotted), SiS_2 (blue solid), MgSO_4 (light-blue solid), and Al_2S_3 (light-blue dotted). **4th diagram:** Al_2O_3 (red solid), MgAl_2O_4 (red dotted), Al_2SiO_5 (light-blue solid), and $\text{Al}_6\text{Si}_2\text{O}_{13}$ (light-blue dotted). **Lower diagram:** TiO (light-blue dashed), TiO_2 (red dotted), Ti_2O_3 (red solid), Ti_3O_5 (light-blue solid), and MgTiO_3 (red dashed).

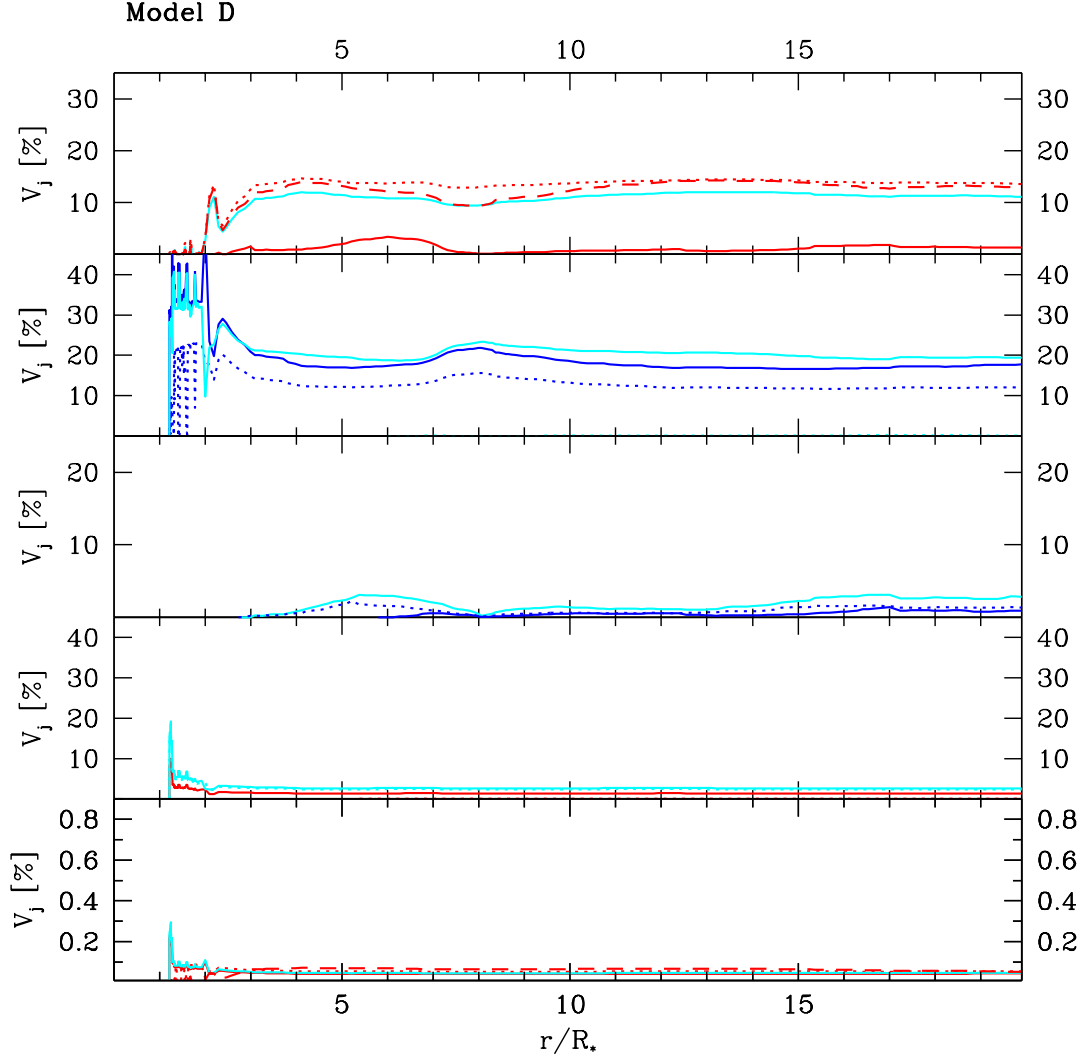


Figure 6.10: Radial structure of the volume fraction of the growth species for model D at $t = 202$ P. **Upper diagram:** Fe (red solid), FeO (light-blue solid), Fe_2O_3 (red dashed), and Fe_3O_4 (red dotted). **2nd diagram:** SiO (light-blue dashed), MgO (light-blue dotted), SiO_2 (blue dotted), MgSiO_3 (blue solid), and Mg_2SiO_4 (light-blue solid). **3rd diagram:** MgS (blue dotted), SiS_2 (blue solid), MgSO_4 (light-blue solid), and Al_2S_3 (light-blue dotted). **4th diagram:** Al_2O_3 (red solid), MgAl_2O_4 (red dotted), Al_2SiO_5 (light-blue solid), and $\text{Al}_6\text{Si}_2\text{O}_{13}$ (light-blue dotted). **Lower diagram:** TiO (light-blue dashed), TiO_2 (red dotted), Ti_2O_3 (red solid), Ti_3O_5 (light-blue solid), and MgTiO_3 (red dashed).

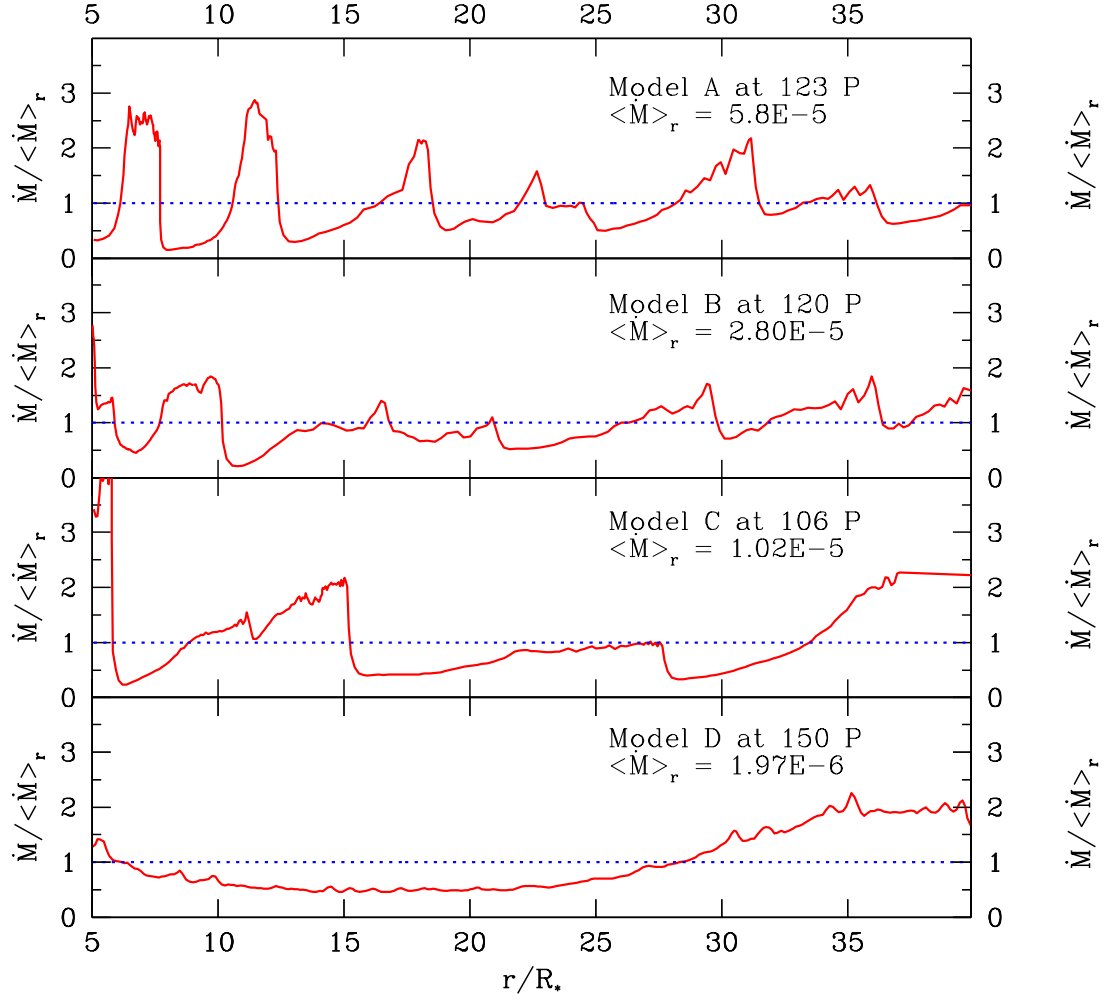


Figure 6.11: Radial structure of the local mass loss rates for models with $\Delta u_p = 5 \text{ km s}^{-1}$ at the zero phase of a pulsational cycle. $\langle \dot{M} \rangle_r$ is the radial mean of the mass loss rate at an instant time.

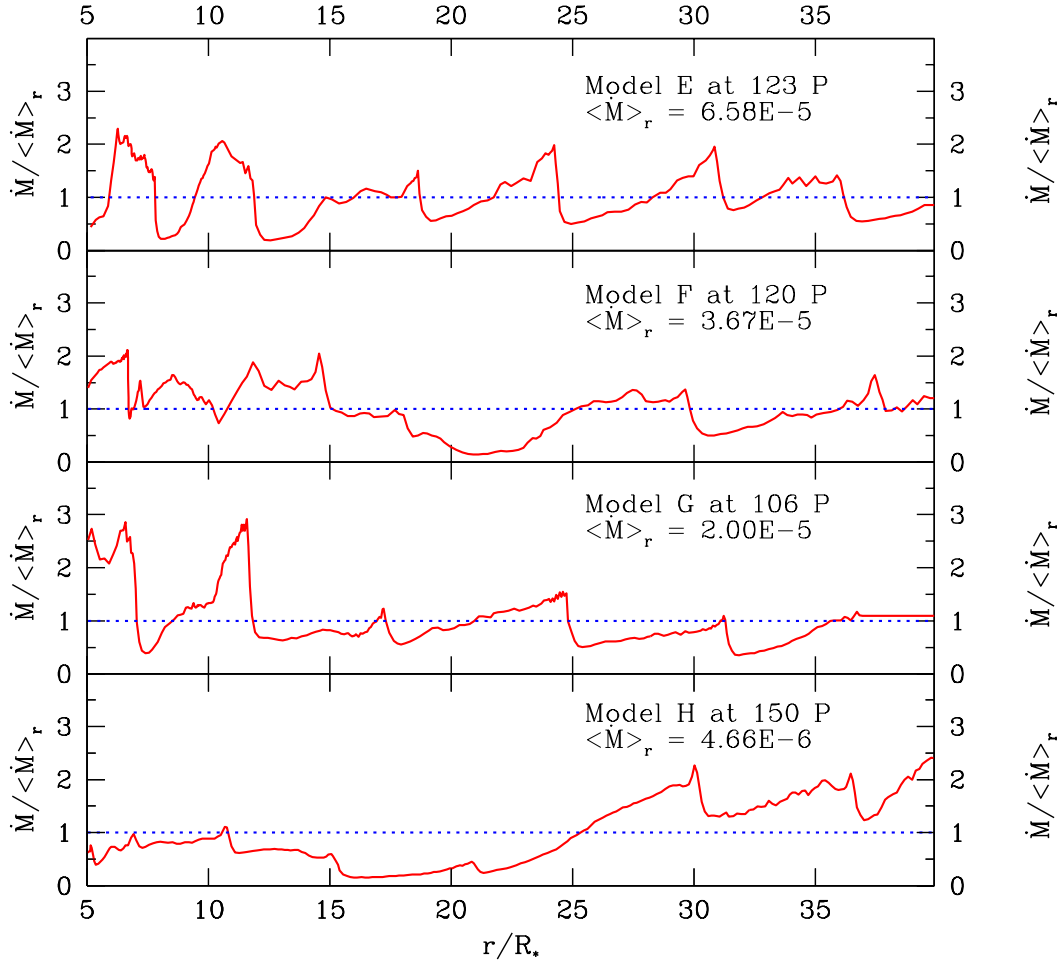


Figure 6.12: Radial structure of the local mass loss rates for models with $\Delta u_p = 10 \text{ km s}^{-1}$ at the zero phase of a pulsational cycle. $\langle \dot{M} \rangle_r$ is the radial mean of the mass loss rate at an instant of time.

Table 6.2: The resulting wind properties from the extended models. These are given as time averaged values at $r = 35 R_*$; mass loss rate $\langle \dot{M} \rangle$, the time averaged outflow velocity $\langle u_\infty \rangle$, the time averaged dust to gas ratio $\langle \rho_d / \rho_g \rangle$, the maximum and minimum luminosity $L_{*,max}$ and $L_{*,min}$ and the maximum velocity difference at the shock front Δu_{max} .

Model	$\langle \dot{M} \rangle$ [$M_\odot \text{ yr}^{-1}$]	$\langle u_\infty \rangle$ [km s^{-1}]	$\langle \rho_d / \rho_g \rangle$ [10^{-3}]	$L_{*,max}$ [$10^4 L_\odot$]	$L_{*,min}$ [$10^4 L_\odot$]
A	$6.2 \cdot 10^{-5}$	16.3	$4.2 \cdot 10^{-3}$	2.11	1.89
B	$2.7 \cdot 10^{-5}$	14.3	$4.1 \cdot 10^{-3}$	1.60	1.41
C	$3.6 \cdot 10^{-6}$	11.3	$3.9 \cdot 10^{-3}$	1.08	0.92
D	$4.2 \cdot 10^{-7}$	7.2	$3.2 \cdot 10^{-3}$	0.87	0.73
E	$7.2 \cdot 10^{-5}$	16.0	$4.2 \cdot 10^{-3}$	2.23	1.79
F	$1.6 \cdot 10^{-5}$	14.4	$3.7 \cdot 10^{-3}$	1.70	1.31
G	$7.6 \cdot 10^{-6}$	12.8	$4.0 \cdot 10^{-3}$	1.16	0.85
H	$1.5 \cdot 10^{-6}$	8.7	$4.2 \cdot 10^{-3}$	0.95	0.67

ties of the model calculations at $r = 35 R_*$: the time averaged values for the mass loss rate $\langle \dot{M} \rangle$, the time averaged final outflow velocity $\langle u_\infty \rangle$, the averaged dust to gas ratio $\langle \rho_d / \rho_g \rangle$, maximum and minimum stellar luminosity $L_{*,max}$, $L_{*,min}$ over one pulsational cycle.

The mean mass loss rates fit reasonably well into the observed range between $10^{-7} M_\odot \text{ yr}^{-1}$ and $10^{-4} M_\odot \text{ yr}^{-1}$ for Miras and LPVs, and the final outflow velocities are in the range of 7 km s^{-1} to 20 km s^{-1} and exhibit relative good agreement with observations (of the order of 10 km s^{-1}) (Danchi *et al.* 1994, Habing 1996).

6.3 Detailed Study: Model A

The radial structures of a shell at various instants of time are described in this section in order to study the time-dependent effect of the dust formation, growth, and evaporation in a CDS and its close coupling to hydrodynamics and thermodynamics. As an example this is carried out here in detail for model A.

6.3.1 The radial structure

For the oxygen-rich CDS, changes of the hydrodynamical quantities and the dust quantities over a period can be neglected. Therefore, any distinct differences of the respective quantities over a period can not be seen in any time sequence of a period. In comparison to the carbon-rich CDS (Fleischer *et al.* 1991, 1992), the temporal change of the radial structure of the oxygen-rich CDS are considerably

slower and hence the further investigation about the temporal development of the radial structure is required.

The temporal change of the radial structure of the oxygen-rich CDS is shown for Model A in Fig. 6.14 and 6.15. the time interval of each column is 2 pulsational periods. The description of the hydrodynamical and the dust quantities corresponds to those in the previous section. The radius is given in units of the stellar radius $R_*(t=0)$ of the initial hydrostatic model.

The respective wind quantities are following:

- upper diagram: the velocity u (solid line), the escape velocity u_e (dashed line), both of which belong to the l.h.s. ordinate, and the temperature T (dotted line, r.h.s. ordinate),
- 2nd diagram: the logarithm of the density ρ (solid) and the radiative acceleration α in units of the gravitational acceleration (dotted)
- 3rd diagram: the logarithm of the nucleation rate J_* (solid) and the logarithm of the number density of dust grains per H-atom $n_d/n_{<H>}$ (dotted). If relevant evaporation occurs, the logarithm of the evaporation rate J_{ev} is shown (dash-dot),
- lower diagram: the degree of condensation f_c (solid) and the mean grain radius $\langle r \rangle$ (dotted). The degree of condensation $n_i/n_{<i>}$ is given for each element i . Plotted are here the seed element Ti and oxygen which is bound to almost all growth species.

The sequence of plots can be conceived as a periodically repeating series, since the situation at $t = nP$ equals to the wind structure at $t = (n + \beta)P$ and β is an arbitrary value in units of pulsational period which differs from Model to model. This value β is *eigenperiod* of the dust formation around the wind system. For Model A, the eigenperiod is $\approx 12P$ as it is shown in Fig. 6.13. The typical eigenperiod for oxygen-rich CDS is between 12 P and 20 P and is generally rather longer than for carbon-rich CDS (e.g. Fleischer 1994). These long term changes in the dynamics provide again the dust formation process in the CDS, and can well explain the gradual change in the spectra of these stars (Monnier *et al.* 1999).

The time sequence of the hydrodynamical time begins, where the shock is newly formed in the innermost region of the CDS. The propagation of the newly formed shock is relative slow as can be seen in the velocity structure. The beginning of dust formation is regarded as the moment in which a new maximum occurs in the number of the dust particles per H-atom, as we can see between 6 P and 8 P of the hydrodynamical cycle.

The discrete shell structure of the radial dust distribution can be understood in terms of an interaction among the dust formation, hydrodynamics and thermodynamics. Between $t = 0P$ and $t = 2P$, a new peak in the nucleation rate develops

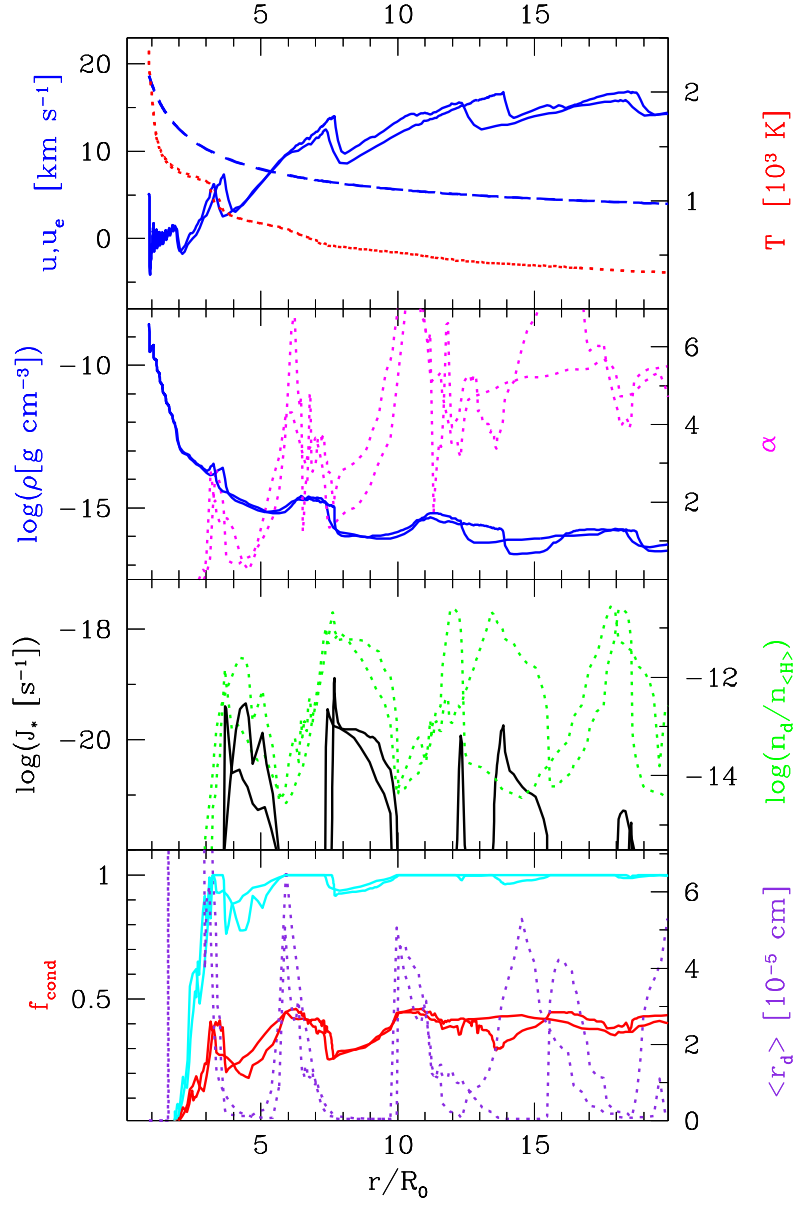


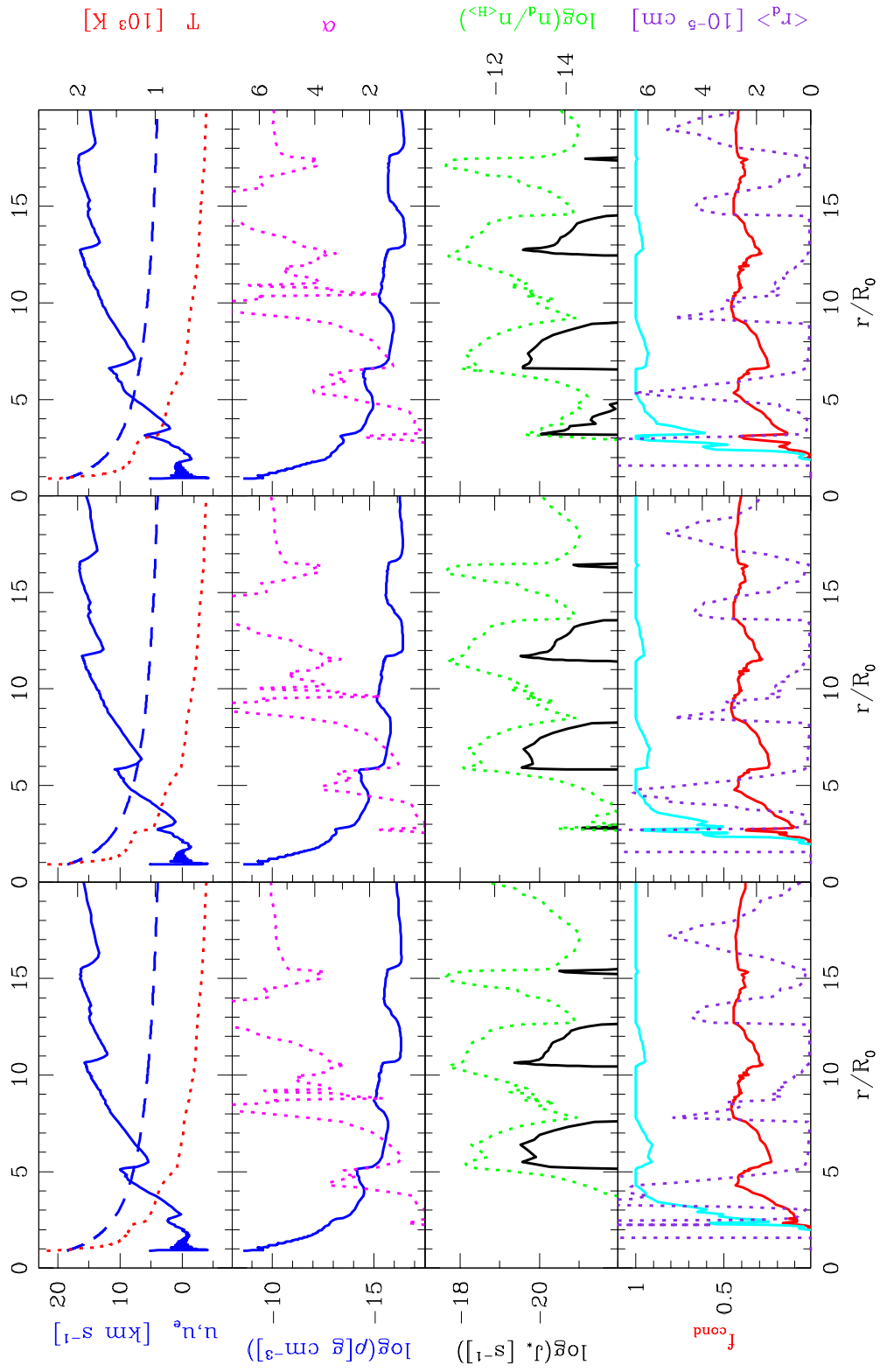
Figure 6.13: Radial structure of Model A at $t = (123 + \beta)P$ with $\beta = 12$.

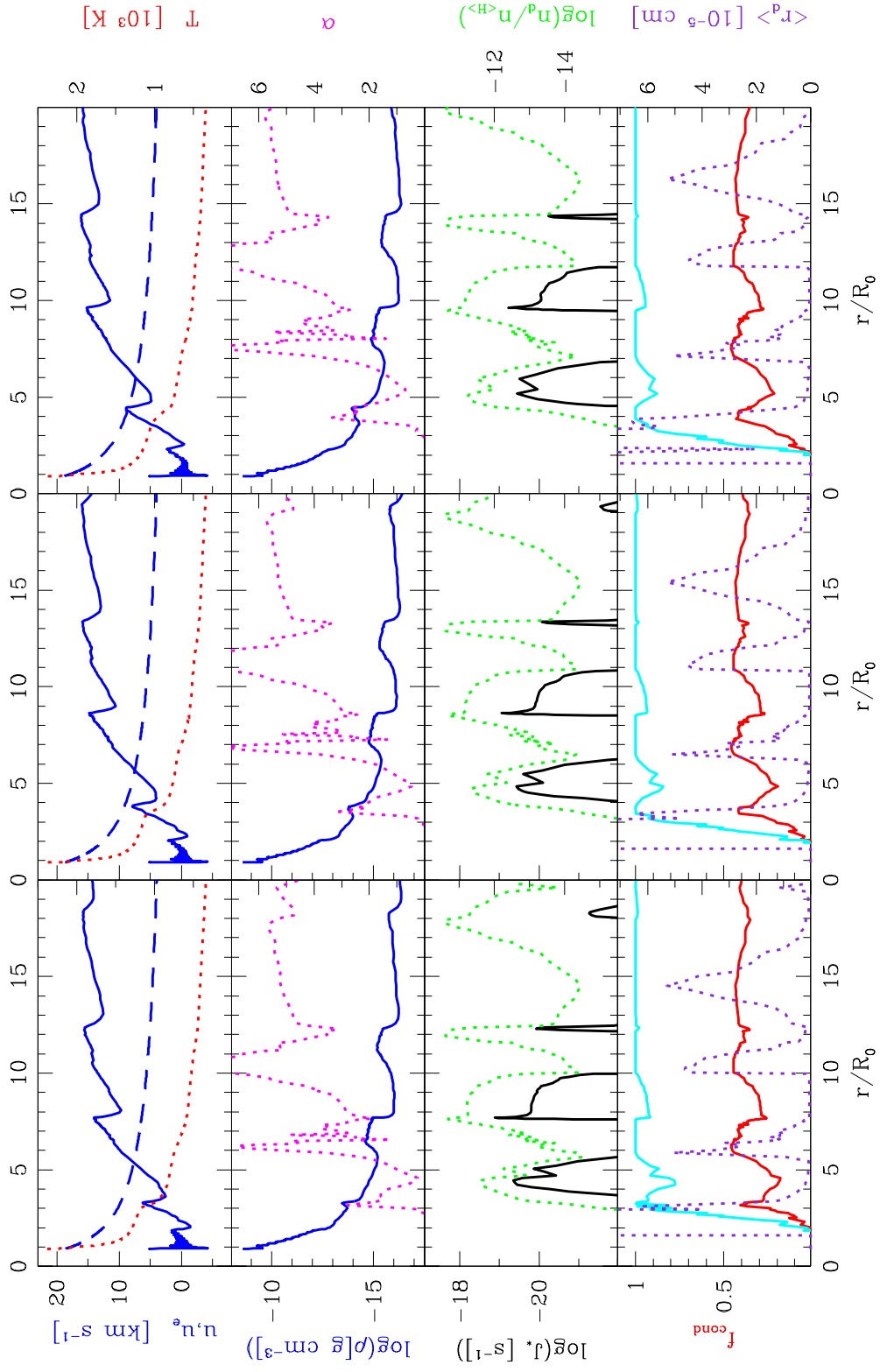
between $2.5 R_*$ and $4 R_*$. Subsequently, the number of dust grains per H-atom increases rapidly in this radius interval. The material pushed outwards by the preceding shock front is decelerated or almost at rest, and the density in the region is enhanced or remains constant which offers favorable conditions for the nucleation in this wind region (cf. time development of the density structure between $t = 0$ P and $t = 2$ P). On the other hand, the temperature decreases substantially; for example, at $2.5 R_*$ it drops from 1300 K at $t = 0$ P down to 1100 K at $t = 2$ P. This is not only due to the inward movement of the inner boundary, which also causes an inward movement of the stellar radius, but it is also due to the vanishing influence of the *back-warming* effect (Fleischer *et al* 1995) of the preceding dust layer.

In the innermost peaks of the degree of condensation, a large amount of dust absorbs the radiation field with great efficiency and consequently its opacity affects the temperature structure. The significant influence of the dust opacity on the temperature profile can be seen in the temperature plots. The steps in the temperature stratification by about 300 K, at $r = 3 R_*$ and $t = 2$ P, move outward along with the newly formed peak in f_{cond} , but they always lag slightly behind (time lag between the temperature stratification and the growth process). This effect is caused by the newly formed dust layer which blocks the outgoing radiation and therefore heats the material behind the shock at the inner region. This *back-warming effect*, however, prevents any new formation of dust particles, through the increase of temperature. The temperature reaches values high enough to even evaporate a considerable amount of particles at the inner edge of the newly formed shell.

The decrease of temperature at the innermost wind region is the most important process in this time interval and it provides conditions that are favorable especially for the nucleation of dust grains, as can be seen by the inward moving peak in the nucleation rate. Subsequently, the number of dust grains per H-atom increases rapidly up to $n_d/n_{<H>} = 1 \cdot 10^{-13}$ at $r = 3 R_*$ and at $t = 2$ P and the mean grain radius $\langle r \rangle$ decrease steeply due to many small newly formed grains. Finally, the growth of the grains causes a tiny, but noticeable peak in the degree of condensation f_{cond} of about 20 % around $3 R_*$.

At $t = 2$ P, the dust particles at the inner edge, between $r = 2.5 R_*$ and $r = 3.0 R_*$, are overrun by the new shock wave which developed in the inner wind below $2.5 R_*$. It is sufficient for this shock wave to compress the mass elements containing the newly formed dust particles, in order to provide favourable conditions for the growth of dust particles by increasing the density of at least two orders of magnitude. This causes a steep increase of the degree of condensation around $r \approx 2.8 R_*$ from $t = 2$ P to $t = 4$ P, which yields values as high as $f_{cond} = 0.98$ of Ti or other elements.

Figure 6.14: Radial structure of Model A at the different phase of $t = 0 \text{ P}$, 2 P , and 4 P .

Figure 6.15: Radial structure of Model A at the different phase of $t = 6P, 8P$, and $10P$.

A steep increase of the radiative acceleration on dust grains is mainly due to such a steep increase of the degree of condensation. This acceleration reverses the infall of the dust particles and induces the perturbation in the velocity field which subsequently steepens and finally becomes a new strong shock wave. This shock is connected to an outward moving shell of material as can be seen in Fig. 6.15 by the outward moving peak of the degree of condensation of oxygen, which reaches values as high as 0.4. The radiative acceleration reaches its maximum value of $\alpha = 8.5$ at $r = 15R_*$ and $t = 4P$.

During this dust forming process, the dust generates a shock between $t = 4P$ and $t = 4P$. New particles are still formed in front of the peak of the degree of condensation, at larger radii (cf. plot of $n_d/n_{<H>}$ at $r \geq 3.0R_*$ and at $t = 4P$), where $n_d/n_{<H>}$ reaches the first peak value of $1.0 \cdot 10^{-13}$. However, these grains are now overrun by the newly formed shock. It sweeps up and compresses the material ahead of it and hence produces an enhanced density where the grains find excellent conditions for growth. By this effect, the radiative acceleration on dust increases monotonically until it has reached its maximum value, followed by the broadening of the peak of α between $t = 6P$ and $t = 8P$. The velocity of the outward shock front increases at the innermost region around $\Delta u_{max} \approx 7 \text{ kms}^{-1}$, but the shock becomes broaden in the outer wind region.

Therefore, by the interior pulsation, the dust formation is triggered in such a sense that the pulsation provides the favorable conditions for the onset of a new dust formation cycle by means of temperature variation, and by an appropriate density for the further growth of the nucleating material. Subsequently, the development of the circumstellar structure is dominated by the dust, which produce a self accelerating mechanism for the dominating shock waves that run through the dust shell.

The existence of dust in a CDS does not only have a significant influence on the hydrodynamics of the system, but it also has the effect of *back-warming*, which affects the thermodynamical conditions for the new dust formation, since process is very sensitive to the local temperature and density. The nucleation process is rather sensitive to temperature, whereas the growth of the dust particles is rather strongly dependent on density. Therefore, a small fluctuation in temperature can cause the onset of the dust formation at the inner region of a CDS.

A comparison of the calculation with the different optical constants of dust grains is shown in Fig. 6.16. Calculations have been performed in Model A with the optical constants of the amorphous dirty silicates tabulated by Draine and Lee (1984) and by Jones and Merrill (1976). This comparison reveals the similar results in hydrodynamic structures and the dust properties. The calculation with the optical constants of dust grains given by Jones and Merrill (1976) results the more frequent shell structures in the outer region of the wind at $15 R_*$ than that by Draine and Lee (1984). The mass loss rates $\langle \dot{M} \rangle$, the final outflow velocity $\langle v \rangle$ and the dust to gas ratio ρ_d/ρ_g at $r = 35R_*$ are given in Tab. 6.3.

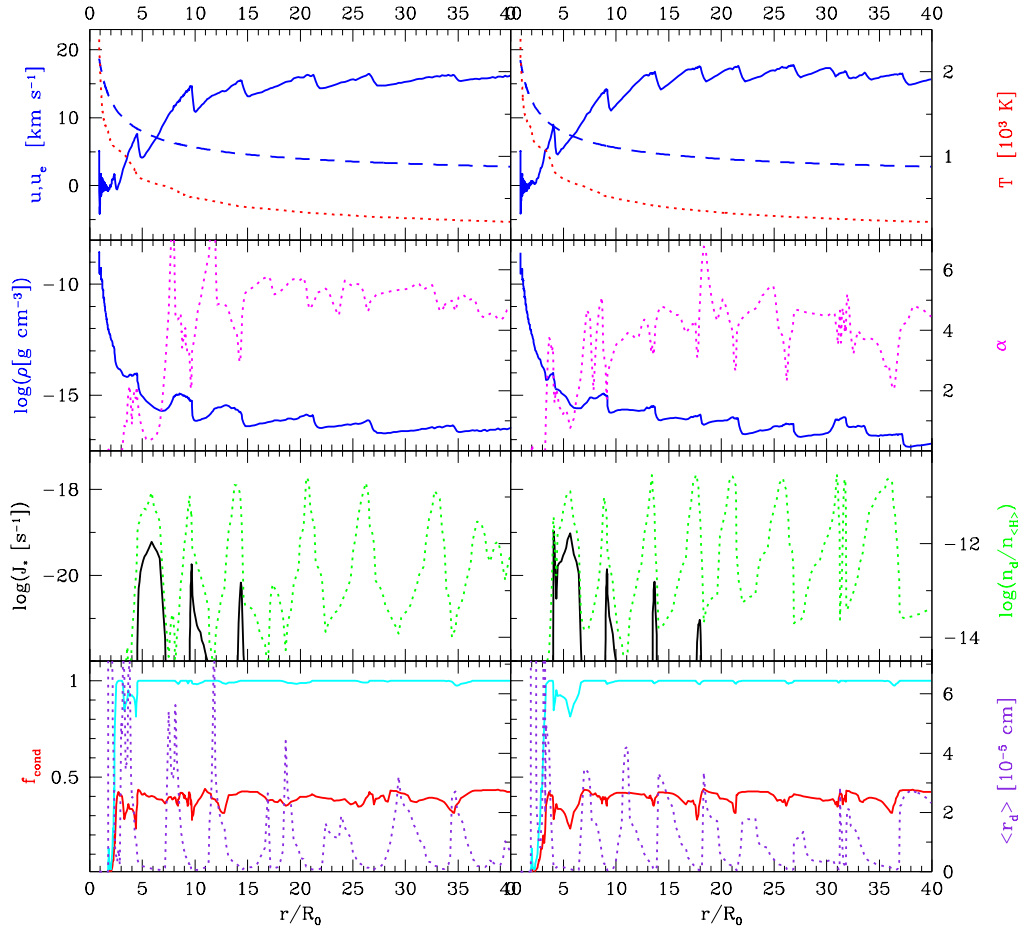


Figure 6.16: The radial structure of Model A with different optical constant of dust grains. The left diagram illustrates the result with the optical constant by Draine and Lee (1984) tabulated in Draine (1985) and the right diagram shows the calculations with the optical constant of Jones and Merrill (1976)

Table 6.3: The resulting wind properties from the calculations with different optical properties of dust grains. These are given at $r = 35 R_*$ and at $t = 125P$; mass loss rate \dot{M} , the outflow velocity u_∞ , the dust to gas ratio ρ_d/ρ_g .

Model	\dot{M} [$M_\odot \text{ yr}^{-1}$]	u_∞ [km s^{-1}]	ρ_d/ρ_g [10^{-3}]
Draine & Lee	$8.4 \cdot 10^{-5}$	16.5	4.3
Jones & Merrill	$3.9 \cdot 10^{-5}$	16.5	4.3

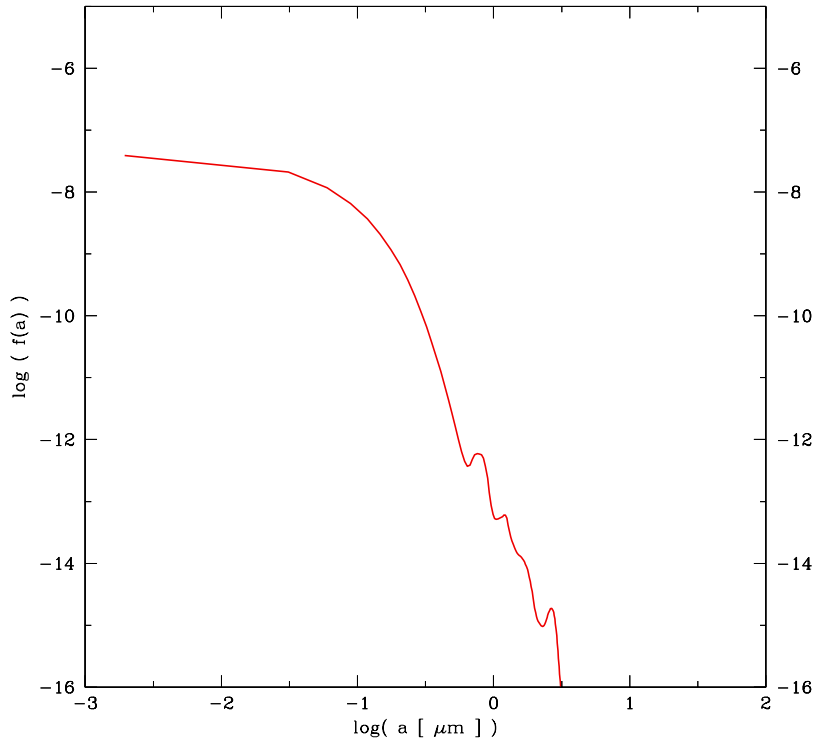


Figure 6.17: Degree of condensation in a radial structure of Model A at $t=0.0P$.

6.3.2 grain size distribution

the grain size distribution depends strongly on the history of the dust particles and the reflects the history of the fluid on the its trajectories throught the atmosphere. Hence no uniform grain size distribution can be expected for the entire CDS. In Fig. 6.17 a grain size distribution is shown in the outer wind region, where the dust formation and growth process are definitely ceased and the spectra have their final shape.

The upper limit of size distribution spectra of the dust particles is so small in comparision with the wavelength of interest. The assumption of small particle limit is well supplied with this result in these models. The most particle has size of $0.5 \mu m$ and remains well below $0.1 \mu m$. Comparison to the stationary dust wind in Domink *et al* (1989) and Dominik (1992) shows a distict contrast in the size distribution. The presence of pulsation limits the time interval, which a fluid element stays in the innermost dense region in which the excellerent growth process can take place. In the stationary dust driven model, this effect is absent and a considerable amount of dust particles reaches rather large sizes up to a few μm .

The final size distribution which is equal to the value at $30 R_*$ is an almost perfect power law in the large size interval from about $0.01 \mu m$ up to the largest grain size present. The index of the the spectrum in this model is equal to -4.5 given as $f(a) = a^{-4.5}$.

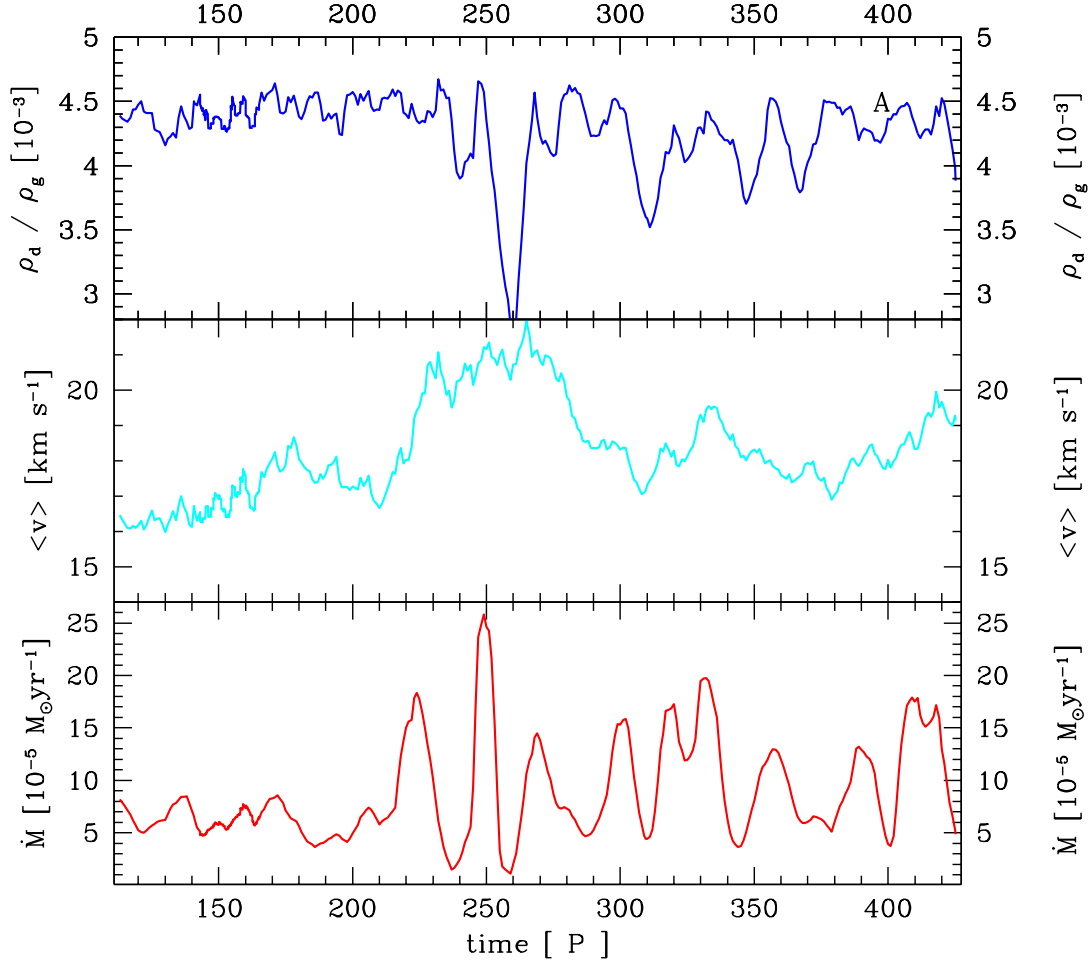


Figure 6.18: Temporal variation of the mass loss rates of Model A. **Upper diagram:** the temporal variation of the dust to gas ratio ρ_d/ρ_g , **middle diagram:** the temporal variation of outflow velocity, **lower diagram:** the temporal variation of the local mass loss rates at $r=35 R_*$.

6.3.3 Temporal variation of the mass loss rates

In Fig. 6.18, the temporal variation of the local mass loss rates at $r=35 R_*$ are represented for model A during about 300 pulsation periods. The local mass loss rates show the regular temporal variation with the time step of about 20 P, which can reflect the passing through time of the layered structure of dust shells at $35 R_*$. The time step of the mass loss rates in Model B and C is longer than in case of Model A, 60 P and shows a distinct pattern of variation of the local mass loss rates as illustrated in Fig. 6.19 and Fig. 6.20.

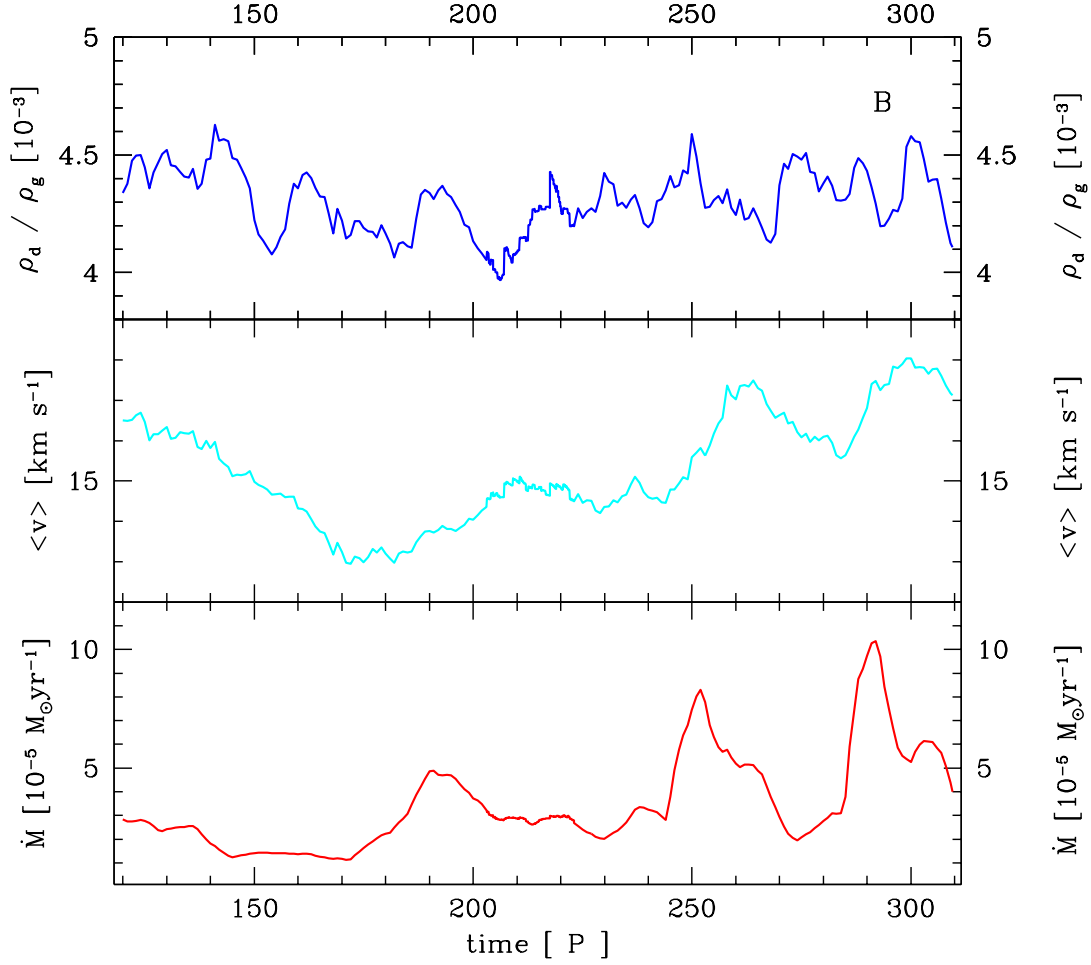


Figure 6.19: Temporal variation of the mass loss rates of Model B. **Upper diagram:** the temporal variation of the dust to gas ratio ρ_d/ρ_g , **middle diagram:** the temporal variation of outflow velocity, **lower diagram:** the temporal variation of the local mass loss rates at $r=35\ R_*$.

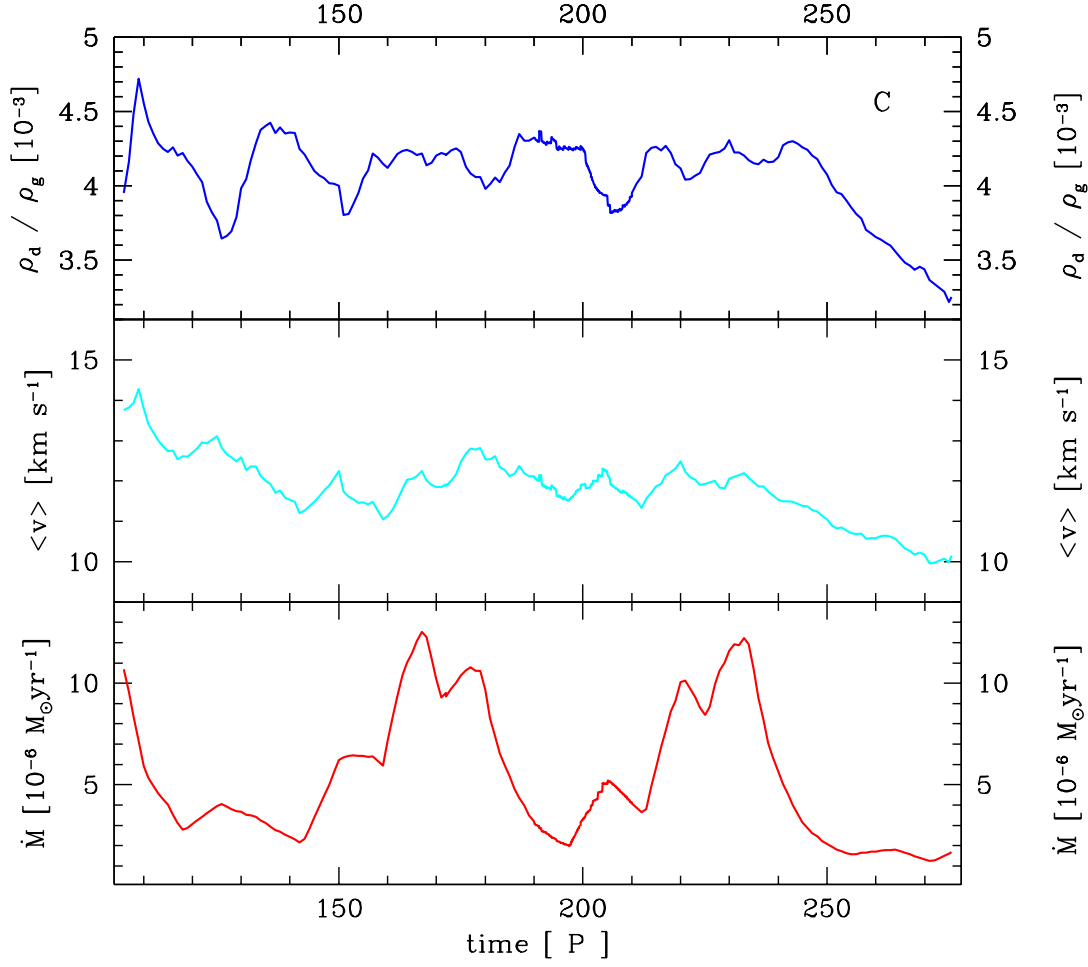


Figure 6.20: Temporal variation of the mass loss rates of Model C. **Upper diagram:** the temporal variation of the dust to gas ratio ρ_d/ρ_g , **middle diagram:** the temporal variation of outflow velocity, **lower diagram:** the temporal variation of the local mass loss rates at $r=35 R_*$.

Der Reiz, seine Erkenntnisse zu erweitern, ist so groß, daß man nur durch einen klaren Widerspruch, auf den man stößt, in seinem Fortschritte aufgehalten werden kann.

Immanuel Kant 1787 Kritik der reinen Vernunft

Chapter 7

Summary and the outlook

This thesis has explored the *oxygen-rich* circumstellar shells around Miras and the long period variables. The investigations have been performed based on the self consistent treatment of hydrodynamics, thermodynamics, radiative transfer, chemistry, and the dust formation. Dust plays the key role in the determination of the structure of the *oxygen-rich* circumstellar shells and the radial structure of the atmosphere of this objects reveals the discrete shell structure as shown in case of the carbon-rich circumstellar shells.

Nucleation, the onset of the dust formation requires the information about the cluster size distribution, which can be calculated from the Gibbs free energy of formation. Often it is the case that the data required are not available for the condensates, e.g. TiO_2 in the cooling outflows of *oxygen-rich* stars. In order to get the thermochemical properties like Gibbs free energy of formation for TiO_2 clusters, the geometric optimisation of the electronic structures has been performed in the quantum mechanical calculations based on the density functional theory. This calculations indicate that TiO_2 clusters are very stable with the binding energy of about 5.7 eV per atom contained in a cluster, compared to the TiO clusters which have the binding energy of 4.4 eV per nucleus. Adopting the modified nucleation theory, in which the Gibbs free energy is approximated in terms of the surface energy of the solid bulk, the Gibbs free energy derived from the approximation in terms of the surface exhibits a well agreement with the Gibbs energy calculated from the density functional theory. Therefore, the modified nucleation theory is further taken for the homogeneous nucleation theory.

In order to determine the most likely *primary* condensation seed, nucleation rates J_* have been calculated for Al_2O_3 , SiO , Fe , TiO and TiO_2 in the p – T plane, covering the typical range for the inner region of a dust forming circumstellar shell. Although solid Al_2O_3 is already stable at very high temperatures, the respective molecule is virtually not present in the gas phase (Chang *et al.* 1998). Therefore, *homogeneous nucleation* of molecular Al_2O_3 from the gas phase seems to be very *unlikely* in a circumstellar environment and is regarded only as the growth species. The SiO molecule is the most abundant candidate for nucleation in oxygen-rich circumstellar

shells, but its nucleation rate peaks around 600 K, which is significantly lower than typical temperatures at the inner edge of the dust shells. Similarly, efficient Fe nucleation occurs at temperatures well below 1000 K. Only the titanium oxides show efficient nucleation rates at temperatures above 1000 K, where TiO_2 nucleation is by far more efficient than TiO due to its higher gas phase concentration in the relevant region of the $p - T$ plane.

Contrary to the carbon-rich circumstellar shells, where the dust formation proceeds mainly *homogeneous*, the dust formation in *oxygen-rich* CDS becomes *heterogeneous*, since grains can only be formed from molecules containing the remaining oxygen and those less abundant heavy elements like Fe, Si, Mg, S, Al, and Ti.

The influence of the dust on the thermodynamics is reflected through the dust opacity as the back-warming effect, an increase of the temperatures behind the shock fronts. This leads to the levitation of the time interval where the dust formation is possible at the inner region of the dust shell.

The interior pulsation also provides a levitation of the atmosphere due to the deposition of mechanical energy by the shock wave dissipations which propagate through the atmosphere. The variation of the mechanical energy input has only a small influence on the multiperiodicity.

The grain size distribution shows that the grains remain rather smaller than $0.1 \mu\text{m}$ and the distribution of the dust in the shell exhibits inhomogeneity. The dust to gas ratio ρ_d/ρ_g is well in agreement with the observation and is confined in the narrow range between $3 \cdot 10^{-3}$ and $4.5 \cdot 10^{-3}$. Although the dust to gas ratio is almost the same as the value of the carbon-rich case, the acceleration ratio α differs from each other. This is mainly due to the less effective absorption of silicates.

The higher luminosities provide the higher density structure which is the favorable condition the dust formation becomes effective and the final outflow velocity and the mass loss rates increase. In case of the less effective dust formation, the dust-driven wind becomes quasi stationary.

The non-linear effect due to the coupling of the whole systems of hydrodynamics, thermodynamics, radiative transfer, chemistry, and the dust formation reflects the multiperiodicity such that the radial structure of the CDS repeats in the time scale of βP with the pulsation period P and integer β . In the time variation of the mass loss rates, this kind of multiperiodicity is also reflected, involving with the different timescales, e.g. the duration time of the successive two layers of the shell.

Since the nucleation is a very steep function of the temperature, the calculations in the *oxygen-rich* circumstellar shells still have the crucial problem of the gas temperature. At the temperature enough low, where the nucleation can occur, the density is often so low that the dust formation can not be effective for generating the wind. This crucial problem could be solved by considering the cooling function in the gas energy equation, which leads to the significant temperature decrease (Woitke and Sedlmayr 1999). Another way of investigation for the solution is to include the frequency dependence of the gas opacity and to investigate the influence of the molecular opacity on the thermodynamic structure of the circumstellar shells.

In grid of model calculation with the basic stellar parameters a fit formula for the *oxygen-rich* Miras and LPVs can be derived, explaining the observed high mass loss rates without introducing artificial fit parameters. This fit formula of mass loss can be used in the evolutionary calculations, as in case of the carbon-rich stars (Arndt *et al.* 1997)

Based on the work presented here, the optical appearance of the models are to be investigated and carried out for the concrete objects.

Um Mitternacht

*Gelassen stieg die Nacht ans Land,
Lehnt träumend an der Berge Wand,
Ihr Auge sieht die goldne Waage nun
Der Zeit in gleichen Schalen stillen ruhn;
Und kecker rauschen die Quellen hervor,
Sie singen der Mutter, der Nacht, ins Ohr
Vom Tage,
Vom heute gewesene Tage.*

*Das uralte alte Schlummerlied,
Sie achtets nicht, sie ist es müd;
Ihr klingt des Himmels Bläue süßer noch,
Der flüchtgen Studen gleichgeschwungnes Joch.
Doch immer behalten die Quellen das Wort,
Es singen die Wasser im Schläfe noch fort
Vom Tage,
Vom heute gewesenen Tage.*

Eduard Mörike

Appendix A

Thermochemical properties of TiO and TiO₂ clusters

The thermochemical properties of (TiO)_n n=1-3 clusters and (TiO₂)_n n=1-6 clusters are here given as thermal functions like entropy S, enthalpy increments [$H^\circ(T) - H^\circ(T_r)$], and Gibbs energy function [$G^\circ(T) - H^\circ(T_r)$]/T and formation functions like enthalpy of formation $\Delta_f H^\circ$ and the Gibbs free energy of formation $\Delta_f G^\circ$.

Table A.1: The calculated thermochemical properties of TiO molecule.

T K	S° J mol ⁻¹ K ⁻¹	-[G°-H°(T _r)]/T J mol ⁻¹ K ⁻¹	H°-H°(T _r) kJ mol ⁻¹	Δ _f H° kJ mol ⁻¹	Δ _f G° kJ mol ⁻¹
0	0.000	infinite	-9.966	85.059	85.059
100	197.858	264.272	-6.641	86.371	76.077
200	219.558	236.124	-3.313	86.327	66.009
298.15	232.047	232.047	0.000	85.854	56.422
300	232.242	232.031	0.063	85.843	56.245
400	241.467	232.579	3.555	85.237	46.793
500	248.861	234.506	7.177	84.588	37.598
600	255.076	236.891	10.911	83.917	28.617
700	260.446	239.401	14.732	83.222	19.817
800	265.172	241.900	18.618	82.515	11.177
900	269.391	244.332	22.553	81.757	2.678
1000	273.199	246.672	26.527	80.878	-5.684
1100	276.667	248.913	30.529	79.811	-13.908
1200	279.849	251.053	34.555	74.568	-21.870
1300	282.788	253.096	38.599	73.840	-29.490
1400	285.518	255.048	42.658	73.034	-37.019
1500	288.066	256.913	46.729	72.134	-44.458
1600	290.454	258.698	50.810	71.126	-51.807
1700	292.702	260.408	54.900	69.997	-59.064
1800	294.824	262.048	58.996	68.733	-66.222
1900	296.834	263.624	63.099	67.317	-73.288
2000	298.742	265.139	67.206	51.052	-79.796
2100	300.559	266.598	71.319	48.547	-85.879
2200	302.292	268.004	75.435	46.035	-91.824
2300	303.950	269.361	79.554	43.516	-97.634
2400	305.538	270.672	83.676	40.988	-103.315
2500	307.061	271.941	87.801	38.451	-108.877
2600	308.526	273.168	91.929	35.907	-114.316
2700	309.935	274.358	96.058	33.355	-119.645
2800	311.294	275.512	100.189	30.793	-124.863
2900	312.605	276.632	104.322	28.223	-129.972
3000	313.872	277.720	108.457	25.645	-134.982
3100	315.098	278.778	112.593	23.060	-139.890
3200	316.286	279.808	116.730	20.466	-144.701
3300	317.436	280.810	120.868	17.865	-149.415
3400	318.553	281.786	125.007	15.256	-154.042
3500	319.638	282.738	129.147	12.642	-158.578
3600	320.692	283.667	133.288	10.019	-163.028
3700	321.717	284.573	137.430	-401.708	-159.605
3800	322.715	285.459	141.573	-403.110	-152.635
3900	323.687	286.324	145.716	-404.571	-145.620

Table A.2: The calculated thermochemical properties of (TiO)₂ molecule.

T K	S° J mol ⁻¹ K ⁻¹	-[G°-H°(T _r)]/T J mol ⁻¹ K ⁻¹	H°-H°(T _r) kJ mol ⁻¹	Δ _f H° kJ mol ⁻¹	Δ _f G° kJ mol ⁻¹
0	0.000	infinite	-13.272	-236.220	-236.220
100	237.046	335.020	-9.797	-236.771	-241.493
200	266.904	294.026	-5.424	-239.143	-245.336
298.15	288.829	288.829	0.000	-241.291	-247.899
300	289.202	288.830	0.112	-241.327	-247.940
400	307.674	291.299	6.550	-243.086	-249.869
500	323.310	296.179	13.566	-244.611	-251.386
600	336.755	301.848	20.944	-246.043	-252.606
700	348.488	307.691	28.558	-247.460	-253.588
800	358.864	313.452	36.330	-248.874	-254.366
900	368.149	319.022	44.214	-250.378	-254.964
1000	376.540	324.361	52.179	-252.117	-255.383
1100	384.189	329.458	60.204	-254.231	-255.611
1200	391.211	334.315	68.275	-264.699	-255.391
1300	397.700	338.945	76.382	-266.135	-254.557
1400	403.728	343.359	84.517	-267.731	-253.606
1500	409.357	347.574	92.675	-269.515	-252.536
1600	414.634	351.602	100.852	-271.515	-251.342
1700	419.601	355.457	109.045	-273.760	-250.016
1800	424.291	359.152	117.250	-276.276	-248.543
1900	428.734	362.698	125.467	-279.095	-246.931
2000	432.953	366.106	133.693	-311.615	-244.249
2100	436.970	369.386	141.927	-316.615	-240.757
2200	440.804	372.546	150.168	-321.630	-237.031
2300	444.470	375.594	158.416	-326.660	-233.071
2400	447.982	378.537	166.668	-331.708	-228.891
2500	451.353	381.383	174.925	-336.774	-224.507
2600	454.593	384.137	183.187	-341.856	-219.912
2700	457.713	386.805	191.452	-346.954	-215.128
2800	460.720	389.391	199.721	-352.072	-210.153
2900	463.622	391.901	207.992	-357.205	-204.991
3000	466.427	394.339	216.266	-362.356	-199.658
3100	469.141	396.708	224.543	-367.521	-194.148
3200	471.770	399.013	232.822	-372.704	-188.473
3300	474.318	401.256	241.102	-377.903	-182.631
3400	476.790	403.442	249.385	-383.116	-176.639
3500	479.192	405.572	257.669	-388.341	-170.490
3600	481.526	407.650	265.955	-393.583	-164.191
3700	483.797	409.677	274.242	-1217.034	-142.171
3800	486.007	411.657	282.531	-1219.833	-113.080
3900	488.160	413.591	290.821	-1222.753	-83.920

Table A.3: The calculated thermochemical properties of (TiO)₃ molecule.

T K	S° J mol ⁻¹ K ⁻¹	-[G°-H°(T _r)]/T J mol ⁻¹ K ⁻¹	H°-H°(T _r) kJ mol ⁻¹	Δ _f H° kJ mol ⁻¹	Δ _f G° kJ mol ⁻¹
0	0.000	infinite	-21.358	-485.117	-485.117
100	273.923	441.948	-16.803	-486.601	-485.519
200	324.512	371.287	-9.355	-489.271	-483.391
298.15	362.353	362.353	0.000	-491.274	-480.050
300	362.990	362.355	0.190	-491.305	-479.981
400	394.096	366.529	11.027	-492.764	-475.973
500	419.981	374.705	22.638	-493.965	-471.634
600	442.010	384.133	34.726	-495.092	-467.062
700	461.112	393.796	47.121	-496.243	-462.301
800	477.936	403.283	59.723	-497.421	-457.371
900	492.947	412.427	72.468	-498.757	-452.288
1000	506.486	421.167	85.319	-500.462	-447.037
1100	518.807	429.492	98.247	-502.743	-441.589
1200	530.108	437.412	111.235	-517.563	-435.550
1300	540.540	444.949	124.269	-518.844	-428.664
1400	550.227	452.127	137.340	-520.369	-421.669
1500	559.265	458.971	150.440	-522.182	-414.558
1600	567.735	465.507	163.565	-524.322	-407.318
1700	575.705	471.757	176.710	-526.834	-399.934
1800	583.228	477.743	189.872	-529.754	-392.379
1900	590.351	483.484	203.048	-533.132	-384.663
2000	597.116	488.998	216.236	-581.063	-375.387
2100	603.556	494.301	229.435	-587.715	-364.939
2200	609.700	499.408	242.643	-594.391	-354.180
2300	615.575	504.332	255.858	-601.091	-343.107
2400	621.202	509.085	269.081	-607.820	-331.742
2500	626.602	513.678	282.309	-614.576	-320.107
2600	631.793	518.122	295.543	-621.358	-308.188
2700	636.789	522.425	308.782	-628.164	-296.019
2800	641.605	526.596	322.025	-635.000	-283.593
2900	646.254	530.643	335.272	-641.861	-270.918
3000	650.746	534.572	348.522	-648.748	-258.015
3100	655.091	538.390	361.776	-655.657	-244.875
3200	659.300	542.103	375.032	-662.594	-231.513
3300	663.380	545.716	388.291	-669.554	-217.928
3400	667.339	549.235	401.552	-676.536	-204.142
3500	671.184	552.665	414.816	-683.536	-190.146
3600	674.921	556.009	428.081	-690.563	-175.949
3700	678.556	559.272	441.349	-1924.903	-138.194
3800	682.094	562.458	454.617	-1928.266	-89.854
3900	685.541	565.570	467.888	-1931.810	-41.43

Table A.4: The calculated thermochemical properties of TiO_2 .

T K	S° $\text{J mol}^{-1} \text{K}^{-1}$	$-\frac{[G^\circ - H^\circ(T_r)]}{T}$ $\text{J mol}^{-1} \text{K}^{-1}$	$H^\circ - H^\circ(T_r)$ kJ mol^{-1}	$\Delta_f H^\circ$ kJ mol^{-1}	$\Delta_f G^\circ$ kJ mol^{-1}
0	0.000	infinite	-10.998	-365.379	-365.379
100	216.299	292.772	-7.647	-365.493	-368.966
200	241.572	261.460	-3.978	-366.652	-372.024
298.15	257.704	257.704	0.000	-367.894	-374.393
300	257.966	257.704	0.078	-367.916	-374.433
400	270.686	259.415	4.509	-369.070	-376.427
500	281.280	262.757	9.261	-370.118	-378.144
600	290.387	266.621	14.260	-371.104	-379.656
700	298.367	270.598	19.439	-372.068	-381.005
800	305.456	274.520	24.748	-373.020	-382.216
900	311.823	278.317	30.155	-374.010	-383.308
1000	317.595	281.961	35.634	-375.114	-384.283
1100	322.870	285.444	41.169	-376.403	-385.139
1200	327.724	288.767	46.747	-381.869	-385.750
1300	332.216	291.939	52.360	-382.819	-386.035
1400	336.396	294.967	58.001	-383.850	-386.243
1500	340.303	297.861	63.664	-384.979	-386.376
1600	343.970	300.629	69.345	-386.220	-386.431
1700	347.423	303.281	75.042	-387.588	-386.404
1800	350.687	305.825	80.752	-389.096	-386.288
1900	353.780	308.268	86.473	-390.763	-386.089
2000	356.719	310.618	92.203	-407.287	-385.342
2100	359.519	312.880	97.942	-410.058	-384.176
2200	362.192	315.062	103.688	-412.844	-382.881
2300	364.749	317.167	109.439	-415.647	-381.455
2400	367.200	319.201	115.197	-418.466	-379.907
2500	369.552	321.168	120.959	-421.303	-378.245
2600	371.814	323.073	126.725	-424.157	-376.464
2700	373.992	324.919	132.495	-427.027	-374.579
2800	376.092	326.710	138.269	-429.915	-372.585
2900	378.120	328.449	144.045	-432.820	-370.486
3000	380.080	330.138	149.825	-435.741	-368.291
3100	381.976	331.781	155.607	-438.678	-365.997
3200	383.814	333.380	161.391	-441.632	-363.610
3300	385.596	334.936	167.177	-444.601	-361.128
3400	387.326	336.454	172.965	-447.585	-358.562
3500	389.006	337.934	178.755	-450.581	-355.907
3600	390.640	339.378	184.546	-453.594	-353.170
3700	392.230	340.788	190.339	-865.717	-342.561
3800	393.779	342.165	196.133	-867.521	-328.408
3900	395.288	343.512	201.928	-869.392	-314.213

Table A.5: The calculated thermochemical properties of (TiO₂)₂.

T K	S° J mol ⁻¹ K ⁻¹	-[G°-H°(T _r)]/T J mol ⁻¹ K ⁻¹	H°-H°(T _r) kJ mol ⁻¹	Δ _f H° kJ mol ⁻¹	Δ _f G° kJ mol ⁻¹
0	0.000	infinite	-19.018	-1248.836	-1248.836
100	257.902	406.909	-14.901	-1251.648	-1241.125
200	302.535	344.196	-8.332	-1254.736	-1229.358
298.15	336.215	336.215	0.000	-1256.844	-1216.415
300	336.789	336.217	0.172	-1256.874	-1216.164
400	365.177	340.009	10.067	-1258.146	-1202.382
500	389.341	347.521	20.910	-1258.903	-1188.347
600	410.253	356.273	32.388	-1259.395	-1174.187
700	428.605	365.323	44.298	-1259.772	-1159.955
800	444.906	374.271	56.508	-1260.083	-1145.672
900	459.541	382.946	68.935	-1260.450	-1131.352
1000	472.800	391.279	81.521	-1261.030	-1116.979
1100	484.910	399.249	94.228	-1261.972	-1102.531
1200	496.047	406.857	107.027	-1271.260	-1087.743
1300	506.350	414.119	119.899	-1271.514	-1072.439
1400	515.932	421.053	132.830	-1271.928	-1057.109
1500	524.885	427.680	145.808	-1272.534	-1041.746
1600	533.286	434.021	158.824	-1273.361	-1026.337
1700	541.197	440.095	171.873	-1274.442	-1010.869
1800	548.671	445.921	184.949	-1275.803	-995.320
1900	555.753	451.517	198.048	-1277.480	-979.698
2000	562.482	456.898	211.166	-1308.869	-963.064
2100	568.890	462.080	224.302	-1312.754	-945.679
2200	575.008	467.075	237.451	-1316.668	-928.112
2300	580.859	471.896	250.614	-1320.613	-910.359
2400	586.465	476.554	263.788	-1324.593	-892.433
2500	591.847	481.058	276.972	-1328.608	-874.351
2600	597.021	485.420	290.164	-1332.655	-856.094
2700	602.003	489.646	303.365	-1336.735	-837.692
2800	606.806	493.745	316.572	-1340.851	-819.134
2900	611.443	497.724	329.786	-1345.000	-800.424
3000	615.925	501.590	343.005	-1349.183	-781.579
3100	620.261	505.348	356.229	-1353.396	-762.589
3200	624.461	509.005	369.458	-1357.643	-743.464
3300	628.533	512.566	382.692	-1361.920	-724.199
3400	632.485	516.035	395.929	-1366.227	-704.814
3500	636.323	519.417	409.169	-1370.558	-685.297
3600	640.054	522.717	422.413	-1374.922	-665.657
3700	643.683	525.937	435.660	-2197.508	-630.318
3800	647.217	529.083	448.910	-2199.454	-587.930
3900	650.659	532.156	462.162	-2201.534	-545.497

Table A.6: The calculated thermochemical properties of $(\text{TiO}_2)_3$.

T K	S° $\text{J mol}^{-1}\text{K}^{-1}$	$-\frac{[G^\circ - H^\circ(T_r)]}{T}$ $\text{J mol}^{-1}\text{K}^{-1}$	$H^\circ - H^\circ(T_r)$ kJ mol^{-1}	$\Delta_f H^\circ$ kJ mol^{-1}	$\Delta_f G^\circ$ kJ mol^{-1}
0	0.000	infinite	-27.549	-2082.817	-2082.817
100	291.243	515.736	-22.449	-2088.113	-2062.767
200	356.555	420.536	-12.796	-2092.944	-2035.427
298.15	408.236	408.236	0.000	-2095.807	-2006.517
300	409.126	408.239	0.266	-2095.844	-2005.962
400	453.372	414.142	15.692	-2097.170	-1975.766
500	491.200	425.865	32.667	-2097.595	-1945.355
600	523.969	439.548	50.653	-2097.564	-1914.905
700	552.725	453.704	69.314	-2097.332	-1884.479
800	578.260	467.708	88.442	-2096.988	-1854.092
900	601.177	481.287	107.901	-2096.719	-1823.750
1000	621.934	494.330	127.604	-2096.765	-1793.421
1100	640.886	506.804	147.490	-2097.351	-1763.064
1200	658.311	518.714	167.517	-2110.456	-1732.269
1300	674.429	530.080	187.655	-2110.008	-1700.772
1400	689.418	540.932	207.880	-2109.798	-1669.298
1500	703.421	551.303	228.177	-2109.877	-1637.835
1600	716.558	561.225	248.533	-2110.288	-1606.358
1700	728.928	570.730	268.937	-2111.079	-1574.844
1800	740.613	579.846	289.382	-2112.288	-1543.258
1900	751.686	588.601	309.861	-2113.972	-1511.608
2000	762.206	597.021	330.370	-2160.226	-1478.485
2100	772.224	605.127	350.904	-2165.221	-1444.275
2200	781.787	612.941	371.460	-2170.261	-1409.833
2300	790.933	620.483	392.035	-2175.348	-1375.150
2400	799.697	627.769	412.628	-2180.487	-1340.244
2500	808.109	634.815	433.235	-2185.677	-1305.137
2600	816.196	641.637	453.855	-2190.917	-1269.803
2700	823.983	648.247	474.487	-2196.205	-1234.281
2800	831.490	654.658	495.129	-2201.548	-1198.558
2900	838.737	660.882	515.781	-2206.940	-1162.635
3000	845.741	666.927	536.441	-2212.382	-1126.539
3100	852.518	672.806	557.109	-2217.872	-1090.253
3200	859.082	678.525	577.784	-2223.411	-1053.792
3300	865.446	684.093	598.465	-2228.995	-1017.145
3400	871.622	689.518	619.152	-2234.624	-980.345
3500	877.620	694.807	639.844	-2240.289	-943.371
3600	883.450	699.967	660.541	-2246.004	-906.237
3700	889.122	705.003	681.243	-3479.051	-845.577
3800	894.644	709.921	701.948	-3481.139	-774.366
3900	900.024	714.727	722.658	-3483.428	-703.108

Table A.7: The calculated thermochemical properties of (TiO₂)₄.

T K	S° J mol ⁻¹ K ⁻¹	-[G°-H°(T _r)]/T J mol ⁻¹ K ⁻¹	H°-H°(T _r) kJ mol ⁻¹	Δ _f H° kJ mol ⁻¹	Δ _f G° kJ mol ⁻¹
0	0.000	infinite	-37.026	-2927.596	-2927.596
100	331.447	635.582	-30.414	-2934.843	-2895.361
200	419.637	506.526	-17.378	-2941.120	-2853.278
298.15	489.809	489.809	0.000	-2944.622	-2809.317
300	491.020	489.812	0.362	-2944.664	-2808.477
400	551.331	497.856	21.390	-2945.972	-2762.834
500	602.938	513.841	44.549	-2946.013	-2717.028
600	647.638	532.500	69.083	-2945.419	-2671.280
700	686.846	551.807	94.527	-2944.547	-2625.659
800	721.650	570.904	120.597	-2943.521	-2580.169
900	752.874	589.418	147.111	-2942.595	-2534.811
1000	781.148	607.200	173.948	-2942.090	-2489.533
1100	806.957	624.203	201.029	-2942.305	-2444.274
1200	830.681	640.435	228.296	-2959.214	-2398.484
1300	852.623	655.923	255.710	-2958.052	-2351.804
1400	873.025	670.711	283.240	-2957.210	-2305.198
1500	892.084	684.841	310.865	-2956.753	-2258.647
1600	909.962	698.358	338.566	-2956.740	-2212.115
1700	926.794	711.305	366.332	-2957.234	-2165.568
1800	942.696	723.722	394.152	-2958.286	-2118.960
1900	957.761	735.647	422.017	-2959.973	-2072.295
2000	972.074	747.114	449.921	-3021.085	-2023.697
2100	985.705	758.153	477.858	-3027.188	-1973.678
2200	998.715	768.794	505.825	-3033.349	-1923.376
2300	1011.157	779.063	533.816	-3039.574	-1872.778
2400	1023.080	788.984	561.830	-3045.868	-1821.906
2500	1034.524	798.578	589.863	-3052.231	-1770.790
2600	1045.525	807.866	617.914	-3058.660	-1719.393
2700	1056.117	816.866	645.980	-3065.154	-1667.767
2800	1066.329	825.594	674.060	-3071.722	-1615.894
2900	1076.187	834.066	702.152	-3078.354	-1563.775
3000	1085.715	842.296	730.255	-3085.055	-1511.443
3100	1094.933	850.298	758.369	-3091.817	-1458.877
3200	1103.862	858.083	786.491	-3098.647	-1406.095
3300	1112.518	865.663	814.622	-3105.536	-1353.084
3400	1120.918	873.047	842.761	-3112.485	-1299.884
3500	1129.077	880.246	870.906	-3119.484	-1246.469
3600	1137.007	887.269	899.058	-3126.548	-1192.856
3700	1144.722	894.124	927.216	-4770.054	-1107.892
3800	1152.233	900.817	955.379	-4772.283	-1008.873
3900	1159.550	907.358	983.547	-4774.779	-909.808

Table A.8: The calculated thermochemical properties of $(\text{TiO}_2)_5$.

T K	S° $\text{J mol}^{-1}\text{K}^{-1}$	$-\frac{[G^\circ - H^\circ(T_r)]}{T}$ $\text{J mol}^{-1}\text{K}^{-1}$	$H^\circ - H^\circ(T_r)$ kJ mol^{-1}	$\Delta_f H^\circ$ kJ mol^{-1}	$\Delta_f G^\circ$ kJ mol^{-1}
0	0.	infinity	-45.783	-3767.249	-3767.249
100	361.867	742.030	-38.016	-3776.808	-3722.210
200	471.096	580.342	-21.849	-3784.781	-3664.288
298.15	559.300	559.300	0.000	-3789.031	-3604.110
300	560.828	559.305	0.457	-3789.079	-3602.962
400	637.005	569.460	27.018	-3790.438	-3540.652
500	702.282	589.659	56.312	-3790.145	-3478.218
600	758.843	613.251	87.356	-3789.026	-3415.930
700	808.460	637.667	119.555	-3787.541	-3353.863
800	852.501	661.821	152.544	-3785.857	-3292.018
900	892.009	685.241	186.092	-3784.294	-3230.389
1000	927.782	707.734	220.048	-3783.253	-3168.906
1100	960.435	729.245	254.310	-3783.111	-3107.486
1200	990.450	749.778	288.806	-3803.835	-3045.441
1300	1018.208	769.372	323.486	-3801.970	-2982.317
1400	1044.017	788.079	358.313	-3800.503	-2919.318
1500	1068.125	805.954	393.257	-3799.519	-2856.417
1600	1090.740	823.054	428.299	-3799.087	-2793.568
1700	1112.033	839.432	463.421	-3799.291	-2730.726
1800	1132.146	855.141	498.610	-3800.191	-2667.831
1900	1151.203	870.226	533.856	-3801.885	-2604.890
2000	1169.306	884.731	569.151	-3877.860	-2539.553
2100	1186.547	898.696	604.488	-3885.073	-2472.460
2200	1203.003	912.157	639.861	-3892.360	-2405.034
2300	1218.741	925.147	675.266	-3899.726	-2337.257
2400	1233.821	937.696	710.698	-3907.178	-2269.155
2500	1248.295	949.833	746.155	-3914.716	-2200.766
2600	1262.210	961.581	781.633	-3922.338	-2132.042
2700	1275.607	972.965	817.131	-3930.040	-2063.048
2800	1288.523	984.006	852.646	-3937.835	-1993.760
2900	1300.991	994.723	888.177	-3945.709	-1924.179
3000	1313.041	1005.134	923.722	-3953.670	-1854.347
3100	1324.700	1015.255	959.279	-3961.707	-1784.236
3200	1335.993	1025.103	994.847	-3969.829	-1713.869
3300	1346.941	1034.690	1030.426	-3978.025	-1643.228
3400	1357.565	1044.031	1066.015	-3986.296	-1572.364
3500	1367.884	1053.137	1101.612	-3994.629	-1501.242
3600	1377.914	1062.020	1137.217	-4003.044	-1429.887
3700	1387.672	1070.690	1172.830	-6057.011	-1319.352
3800	1397.171	1079.158	1208.449	-6059.382	-1191.261
3900	1406.425	1087.431	1244.075	-6062.086	-1063.123

Table A.9: The calculated thermochemical properties of (TiO₂)₆.

T K	S° J mol ⁻¹ K ⁻¹	-[G°-H°(T _r)]/T J mol ⁻¹ K ⁻¹	H°-H°(T _r) kJ mol ⁻¹	Δ _f H° kJ mol ⁻¹	Δ _f G° kJ mol ⁻¹
0	0.	infinity	-56.012	-4600.765	-4600.765
100	414.766	878.582	-46.382	-4611.925	-4544.461
200	548.232	681.400	-26.634	-4621.145	-4473.137
298.15	655.754	655.754	0.000	-4625.831	-4399.332
300	657.615	655.760	0.557	-4625.881	-4397.926
400	750.351	668.126	32.890	-4627.051	-4321.686
500	829.702	692.705	68.499	-4626.243	-4245.413
600	898.378	721.393	106.191	-4624.460	-4169.404
700	958.567	751.065	145.251	-4622.258	-4093.735
800	1011.959	780.404	185.244	-4619.831	-4018.390
900	1059.833	808.838	225.896	-4617.561	-3943.354
1000	1103.165	836.138	267.027	-4615.928	-3868.538
1100	1142.707	862.237	308.517	-4615.382	-3793.835
1200	1179.047	887.144	350.283	-4639.880	-3718.416
1300	1212.648	910.907	392.264	-4637.277	-3641.733
1400	1243.886	933.589	434.416	-4635.157	-3565.227
1500	1273.063	955.258	476.706	-4633.619	-3488.865
1600	1300.429	975.985	519.110	-4632.747	-3412.589
1700	1326.193	995.835	561.609	-4632.639	-3336.343
1800	1350.529	1014.871	604.185	-4633.370	-3260.055
1900	1373.585	1033.149	646.829	-4635.054	-3183.731
2000	1395.488	1050.723	689.529	-4725.878	-3104.549
2100	1416.345	1067.641	732.279	-4734.188	-3023.279
2200	1436.252	1083.947	775.071	-4742.588	-2941.624
2300	1455.290	1099.682	817.900	-4751.084	-2859.564
2400	1473.532	1114.881	860.761	-4759.684	-2777.130
2500	1491.040	1129.580	903.651	-4768.389	-2694.364
2600	1507.872	1143.808	946.566	-4777.193	-2611.210
2700	1524.076	1157.594	989.504	-4786.096	-2527.747
2800	1539.699	1170.963	1032.461	-4795.110	-2443.942
2900	1554.780	1183.940	1075.437	-4804.220	-2359.798
3000	1569.355	1196.545	1118.430	-4813.434	-2275.365
3100	1583.457	1208.800	1161.437	-4822.740	-2190.608
3200	1597.115	1220.723	1204.457	-4832.148	-2105.554
3300	1610.357	1232.330	1247.490	-4841.646	-2020.182
3400	1623.207	1243.638	1290.533	-4851.234	-1934.554
3500	1635.687	1254.662	1333.587	-4860.896	-1848.625
3600	1647.819	1265.416	1376.650	-4870.657	-1762.426
3700	1659.620	1275.911	1419.722	-7335.081	-1629.221
3800	1671.108	1286.160	1462.802	-7337.590	-1474.958
3900	1682.300	1296.175	1505.889	-7340.499	-1320.647

Appendix B

Thermochemical properties of the non-stoichiometric molecules Ti_xO_y

The thermochemical properties of the desultory molecules, TiO_3 , Ti_2O , Ti_2O_3 , Ti_3O_4 , and Ti_3O_5 are here given as thermal functions like entropy S , enthalpy increments $[\text{H}(\text{T}) - \text{H}(\text{T}_r)]$, and Gibbs energy function $[\text{G}(\text{T}) - \text{H}(\text{T}_r)]/\text{T}$ and formation functions like enthalpy of formation $\Delta_f H^\circ$ and the Gibbs free energy of formation $\Delta_f G^\circ$.

Table B.1: The calculated thermochemical properties of TiO_3 molecule.

T K	S° J mol ⁻¹ K ⁻¹	$-[G^\circ - H^\circ(T_r)]/T$ J mol ⁻¹ K ⁻¹	$H^\circ - H^\circ(T_r)$ kJ mol ⁻¹	$\Delta_f H^\circ$ kJ mol ⁻¹	$\Delta_f G^\circ$ kJ mol ⁻¹
0	0.000	infinite	-13.393	-426.048	-426.048
100	233.642	332.331	-9.869	-427.441	-423.983
200	264.698	291.362	-5.333	-429.189	-419.837
298.15	286.281	286.281	0.000	-430.510	-414.947
300	286.643	286.282	0.108	-430.530	-414.850
400	304.437	288.663	6.309	-431.398	-409.481
500	319.506	293.364	13.071	-431.966	-403.932
600	332.534	298.831	20.222	-432.380	-398.285
700	343.969	304.480	27.643	-432.730	-392.575
800	354.130	310.063	35.254	-433.047	-386.815
900	363.256	315.475	43.003	-433.398	-381.017
1000	371.527	320.673	50.854	-433.861	-375.173
1100	379.083	325.644	58.783	-434.511	-369.275
1200	386.033	330.391	66.771	-439.342	-363.189
1300	392.465	334.922	74.806	-439.661	-356.830
1400	398.447	339.248	82.879	-440.067	-350.442
1500	404.038	343.383	90.982	-440.576	-344.024
1600	409.284	347.340	99.111	-441.203	-337.569
1700	414.224	351.130	107.260	-441.965	-331.071
1800	418.892	354.766	115.427	-442.874	-324.519
1900	423.316	358.259	123.609	-443.950	-317.917
2000	427.519	361.618	131.803	-459.890	-310.796
2100	431.523	364.852	140.009	-462.088	-303.288
2200	435.344	367.970	148.223	-464.309	-295.677
2300	438.999	370.979	156.447	-466.555	-287.960
2400	442.502	373.887	164.677	-468.828	-280.145
2500	445.865	376.699	172.914	-471.128	-272.240
2600	449.098	379.422	181.157	-473.453	-264.234
2700	452.210	382.061	189.404	-475.804	-256.145
2800	455.211	384.620	197.657	-478.183	-247.967
2900	458.109	387.104	205.913	-480.586	-239.699
3000	460.909	389.518	214.173	-483.015	-231.354
3100	463.619	391.865	222.436	-485.469	-222.925
3200	466.243	394.148	230.703	-487.948	-214.418
3300	468.787	396.372	238.972	-490.449	-205.827
3400	471.257	398.538	247.243	-492.974	-197.168
3500	473.655	400.650	255.517	-495.517	-188.430
3600	475.987	402.711	263.793	-498.085	-179.621
3700	478.255	404.722	272.071	-909.770	-162.950
3800	480.463	406.686	280.351	-911.143	-142.743
3900	482.614	408.606	288.632	-912.588	-122.504

Table B.2: The calculated thermochemical properties of Ti_2O molecule.

T K	S° $\text{J mol}^{-1} \text{K}^{-1}$	$-\frac{[G^\circ - H^\circ(T_r)]}{T}$ $\text{J mol}^{-1} \text{K}^{-1}$	$H^\circ - H^\circ(T_r)$ kJ mol^{-1}	$\Delta_f H^\circ$ kJ mol^{-1}	$\Delta_f G^\circ$ kJ mol^{-1}
0	0.000	infinite	-11.822	435.608	435.608
100	230.585	314.375	-8.379	436.477	423.736
200	257.966	279.963	-4.399	435.167	411.413
298.15	275.800	275.800	0.000	433.428	400.123
300	276.091	275.800	0.087	433.395	399.916
400	290.166	277.696	4.988	431.584	389.030
500	301.709	281.379	10.165	429.749	378.602
600	311.467	285.602	15.519	427.873	368.548
700	319.897	289.913	20.989	425.940	358.813
800	327.305	294.133	26.538	423.971	349.357
900	333.905	298.192	32.142	421.890	340.153
1000	339.852	302.066	37.786	419.561	331.194
1100	345.260	305.751	43.460	416.851	322.485
1200	350.217	309.253	49.158	405.784	314.278
1300	354.792	312.582	54.873	403.748	306.735
1400	359.038	315.750	60.603	401.553	299.355
1500	362.999	318.770	66.344	399.173	292.137
1600	366.710	321.651	72.095	396.580	285.083
1700	370.201	324.405	77.853	393.746	278.198
1800	373.496	327.042	83.618	390.648	271.494
1900	376.616	329.570	89.388	387.252	264.962
2000	379.579	331.997	95.164	354.162	259.529
2100	382.398	334.330	100.943	348.601	254.935
2200	385.089	336.577	106.726	343.031	250.602
2300	387.660	338.742	112.511	337.456	246.528
2400	390.124	340.832	118.300	331.870	242.697
2500	392.488	342.852	124.091	326.275	239.093
2600	394.760	344.805	129.884	320.672	235.719
2700	396.947	346.696	135.679	315.063	232.555
2800	399.055	348.528	141.475	309.442	229.601
2900	401.090	350.306	147.273	303.814	226.852
3000	403.056	352.032	153.073	298.176	224.290
3100	404.958	353.708	158.873	292.533	221.922
3200	406.800	355.339	164.675	286.880	219.735
3300	408.585	356.925	170.478	281.219	217.728
3400	410.318	358.470	176.281	275.551	215.886
3500	412.000	359.976	182.086	269.878	214.214
3600	413.636	361.444	187.891	264.195	212.705
3700	415.227	362.876	193.697	-559.690	226.928
3800	416.775	364.274	199.503	-562.918	248.234
3900	418.284	365.640	205.311	-566.259	269.620

Table B.3: The calculated thermochemical properties of Ti_2O_3 molecule.

T K	S° $\text{J mol}^{-1} \text{K}^{-1}$	$-\frac{[G^\circ - H^\circ(T_r)]}{T}$ $\text{J mol}^{-1} \text{K}^{-1}$	$H^\circ - H^\circ(T_r)$ kJ mol^{-1}	$\Delta_f H^\circ$ kJ mol^{-1}	$\Delta_f G^\circ$ kJ mol^{-1}
0	0.000	infinite	-17.010	-762.237	-762.237
100	257.644	387.566	-12.992	-763.697	-761.813
200	297.456	333.227	-7.154	-766.059	-759.014
298.15	326.394	326.394	0.000	-767.911	-755.137
300	326.882	326.395	0.146	-767.940	-755.058
400	350.867	329.607	8.504	-769.265	-750.551
500	371.060	335.932	17.564	-770.275	-745.752
600	388.409	343.267	27.085	-771.144	-740.764
700	403.557	350.821	36.915	-771.972	-735.636
800	416.967	358.267	46.960	-772.782	-730.388
900	428.976	365.468	57.157	-773.676	-725.038
1000	439.837	372.371	67.466	-774.802	-719.576
1100	449.742	378.961	77.859	-776.302	-713.984
1200	458.842	385.244	88.317	-786.157	-708.000
1300	467.253	391.233	98.827	-786.983	-701.453
1400	475.071	396.945	109.376	-787.970	-694.836
1500	482.373	402.400	119.959	-789.151	-688.144
1600	489.220	407.614	130.569	-790.551	-681.369
1700	495.665	412.606	141.201	-792.203	-674.498
1800	501.753	417.391	151.852	-794.131	-667.514
1900	507.520	421.984	162.519	-796.370	-660.424
2000	512.999	426.399	173.199	-828.317	-652.294
2100	518.215	430.648	183.891	-832.752	-643.384
2200	523.194	434.743	194.593	-837.209	-634.266
2300	527.955	438.693	205.304	-841.691	-624.938
2400	532.517	442.508	216.023	-846.199	-615.415
2500	536.896	446.196	226.749	-850.734	-605.711
2600	541.105	449.766	237.481	-855.294	-595.815
2700	545.157	453.224	248.218	-859.879	-585.752
2800	549.064	456.578	258.960	-864.492	-575.515
2900	552.835	459.832	269.707	-869.129	-565.109
3000	556.479	462.994	280.457	-873.792	-554.551
3100	560.005	466.066	291.211	-878.478	-543.831
3200	563.421	469.056	301.968	-883.190	-532.962
3300	566.732	471.966	312.728	-887.925	-521.938
3400	569.945	474.800	323.490	-892.682	-510.781
3500	573.065	477.564	334.255	-897.457	-499.478
3600	576.098	480.259	345.023	-902.258	-488.040
3700	579.049	482.889	355.792	-1725.274	-460.891
3800	581.922	485.458	366.563	-1727.644	-426.682
3900	584.720	487.967	377.336	-1730.142	-392.417

Table B.4: The calculated thermochemical properties of Ti_3O_4 molecule.

T K	S° J mol ⁻¹ K ⁻¹	$-[G^\circ - H^\circ(T_r)]/T$ J mol ⁻¹ K ⁻¹	$H^\circ - H^\circ(T_r)$ kJ mol ⁻¹	$\Delta_f H^\circ$ kJ mol ⁻¹	$\Delta_f G^\circ$ kJ mol ⁻¹
0	0.000	infinite	-22.536	-1110.631	-1110.631
100	282.065	461.251	-17.919	-1113.505	-1104.572
200	334.957	385.594	-10.127	-1117.287	-1094.148
298.15	375.865	375.865	0.000	-1119.951	-1082.174
300	376.567	375.867	0.210	-1119.990	-1081.939
400	411.425	380.522	12.361	-1121.620	-1068.986
500	441.034	389.741	25.646	-1122.676	-1055.699
600	466.528	400.464	39.638	-1123.479	-1042.225
700	488.791	411.526	54.085	-1124.206	-1028.626
800	508.490	422.439	68.840	-1124.898	-1014.923
900	526.119	432.997	83.810	-1125.714	-1001.130
1000	542.054	443.119	98.935	-1126.876	-987.229
1100	556.579	452.783	114.176	-1128.598	-973.186
1200	569.917	461.996	129.505	-1142.851	-958.603
1300	582.242	470.778	144.904	-1143.559	-943.221
1400	593.694	479.153	160.357	-1144.508	-927.773
1500	604.386	487.150	175.854	-1145.745	-912.252
1600	614.411	494.793	191.388	-1147.310	-896.640
1700	623.846	502.110	206.951	-1149.250	-880.919
1800	632.756	509.123	222.540	-1151.600	-865.060
1900	641.196	515.854	238.149	-1154.415	-849.073
2000	649.212	522.323	253.777	-1201.787	-831.554
2100	656.844	528.549	269.420	-1207.888	-812.893
2200	664.128	534.547	285.077	-1214.019	-793.946
2300	671.092	540.333	300.746	-1220.182	-774.709
2400	677.765	545.922	316.424	-1226.381	-755.204
2500	684.169	551.324	332.112	-1232.615	-735.451
2600	690.325	556.553	347.808	-1238.883	-715.434
2700	696.252	561.618	363.511	-1245.183	-695.187
2800	701.965	566.529	379.220	-1251.522	-674.702
2900	707.479	571.295	394.935	-1257.893	-653.983
3000	712.809	575.924	410.655	-1264.299	-633.056
3100	717.965	580.423	426.380	-1270.735	-611.907
3200	722.959	584.799	442.109	-1277.206	-590.552
3300	727.800	589.060	457.842	-1283.707	-568.986
3400	732.498	593.210	473.579	-1290.239	-547.235
3500	737.060	597.255	489.318	-1296.794	-525.286
3600	741.495	601.200	505.061	-1303.383	-503.150
3700	745.809	605.051	520.806	-2537.292	-457.467
3800	750.009	608.810	536.554	-2540.230	-401.209
3900	754.100	612.483	552.304	-2543.356	-344.883

Table B.5: The calculated thermochemical properties of Ti_3O_5 molecule.

T K	S° $\text{J mol}^{-1} \text{ K}^{-1}$	$-\text{[G}^\circ\text{-H}^\circ(\text{T}_r)]/\text{T}$ $\text{J mol}^{-1} \text{ K}^{-1}$	$\text{H}^\circ\text{-H}^\circ(\text{T}_r)$ kJ mol^{-1}	$\Delta_f \text{H}^\circ$ kJ mol^{-1}	$\Delta_f \text{G}^\circ$ kJ mol^{-1}
0	0.000	infinite	-25.282	-1596.731	-1596.731
100	292.507	495.569	-20.306	-1600.698	-1584.144
200	352.109	409.680	-11.514	-1604.935	-1565.878
298.15	398.617	398.617	0.000	-1607.647	-1546.070
300	399.416	398.620	0.239	-1607.684	-1545.688
400	439.099	403.917	14.073	-1609.117	-1524.777
500	472.897	414.420	29.239	-1609.821	-1503.602
600	502.081	426.655	45.256	-1610.179	-1482.322
700	527.626	439.293	61.833	-1610.403	-1460.994
800	550.267	451.777	78.792	-1610.559	-1439.637
900	570.558	463.867	96.022	-1610.818	-1418.260
1000	588.916	475.469	113.448	-1611.409	-1396.837
1100	605.665	486.555	131.022	-1612.553	-1375.329
1200	621.054	497.130	148.709	-1626.223	-1353.334
1300	635.282	507.217	166.484	-1626.345	-1330.589
1400	648.507	516.842	184.330	-1626.709	-1307.822
1500	660.858	526.036	202.233	-1627.361	-1285.026
1600	672.443	534.828	220.183	-1628.344	-1262.177
1700	683.348	543.247	238.171	-1629.705	-1239.255
1800	693.648	551.319	256.191	-1631.481	-1216.230
1900	703.406	559.069	274.240	-1633.726	-1193.107
2000	712.675	566.520	292.311	-1680.536	-1168.483
2100	721.502	573.692	310.403	-1686.081	-1142.744
2200	729.927	580.603	328.512	-1691.664	-1116.746
2300	737.983	587.272	346.636	-1697.286	-1090.484
2400	745.703	593.713	364.774	-1702.953	-1063.975
2500	753.112	599.942	382.923	-1708.663	-1037.242
2600	760.234	605.971	401.083	-1714.415	-1010.264
2700	767.091	611.812	419.253	-1720.208	-983.077
2800	773.702	617.477	437.430	-1726.047	-955.670
2900	780.083	622.975	455.615	-1731.927	-928.047
3000	786.250	628.315	473.807	-1737.849	-900.233
3100	792.217	633.506	492.004	-1743.811	-872.213
3200	797.997	638.557	510.208	-1749.815	-844.002
3300	803.600	643.474	528.416	-1755.856	-815.594
3400	809.037	648.264	546.629	-1761.935	-787.016
3500	814.317	652.933	564.846	-1768.045	-758.252
3600	819.450	657.487	583.066	-1774.196	-729.315
3700	824.444	661.933	601.291	-3007.672	-676.841
3800	829.305	666.273	619.518	-3010.185	-613.804
3900	834.040	670.515	637.749	-3012.891	-550.710

Appendix C

The calculated harmonic wave number of Ti_xO_y clusters

In Tab. C.5–C.6 are given the calculated harmonic wave number $\tilde{\nu}_k$ [cm^{-1}], wavelength in $\lambda[\mu\text{m}]$, and the absorption coefficients A_k [$10^{-8}\text{cm}^2\text{s}^{-1}$] for each molecule.

Table C.1: the calculated harmonic wave number $\tilde{\nu}_k$ [cm^{-1}], wavelength λ [μm], and absorption coefficient A_k [$10^{-8}\text{cm}^2\text{s}^{-1}$] of TiO_3 and of Ti_2O with the label k .

	TiO_3			Ti_2O		
k	$\tilde{\nu}_k$	λ	A_k	$\tilde{\nu}_k$	λ	A_k
1	223.6	44.7	9.1	218.4	45.8	3.5
2	247.9	40.4	15.6	692.9	14.4	454.5
3	667.0	15.0	15.7	796.4	12.6	15.9
4	683.2	14.6	20.5			
5	973.6	10.3	52.3			
6	1103.5	9.1	131.4			

Table C.2: The calculated harmonic wave number $\tilde{\nu}_k$ [cm^{-1}], the wavelength λ [μm], and the absorption coefficient A_k [$10^{-8}\text{cm}^2\text{s}^{-1}$] of $(\text{TiO})_n$ $n=1-3$ with the label k .

	TiO			$(\text{TiO})_2$			$(\text{TiO})_3$		
k	$\tilde{\nu}_k$	λ	A_k	$\tilde{\nu}_k$	λ	A_k	$\tilde{\nu}_k$	λ	A_k
1	1151.9	8.7	125.5	202.6	49.4	10.6	62.8	159.2	0.6
2				460.4	21.7	0.0	102.3	97.8	0.0
3				531.1	18.8	0.0	173.8	57.6	9.4
4				730.2	13.7	345.4	245.3	40.8	10.4
5				764.4	13.1	28.5	323.7	30.9	15.4
6				810.5	12.3	0.0	360.2	27.8	0.1
7							413.1	24.2	4.4
8							443.6	22.5	79.2
9							545.6	18.3	24.9
10							748.8	13.4	193.1
11							836.3	11.9	59.5
12							848.8	11.8	174.3

Table C.3: vibrational wave number $\tilde{\nu}_k$ [cm^{-1}], wavelength λ [μm], and absorption coefficient A_k [$10^{-8}\text{cm}^2\text{s}^{-1}$] of Ti_2O_3 , Ti_3O_4 , and Ti_3O_5 with the label k .

	Ti_2O_3			Ti_3O_4			Ti_3O_5		
k	$\tilde{\nu}_k$	λ	A_k	$\tilde{\nu}_k$	λ	A_k	$\tilde{\nu}_k$	λ	A_k
1	88.3	113.3	11.7	90.1	111.0	0.8	58.5	172.3	2.8
2	186.5	53.6	50.6	90.1	111.0	0.8	86.5	115.7	1.7
3	235.2	42.5	4.7	175.6	57.0	0.0	157.2	63.6	13.2
4	408.1	24.5	9.7	218.1	45.9	9.0	164.2	60.9	5.4
5	521.8	19.2	1.4	218.3	45.8	9.0	219.3	45.6	6.2
6	586.7	17.1	19.2	298.8	33.5	0.0	276.4	36.2	0.9
7	789.4	12.7	67.0	496.0	20.2	0.9	288.4	34.7	2.9
8	819.3	12.2	2.8	527.7	19.0	0.2	344.6	29.0	30.0
9	1100.0	9.1	227.2	527.9	19.0	0.1	496.6	20.1	14.3
10				639.7	15.6	0.0	501.7	19.9	0.1
11				695.4	14.4	626.0	533.6	18.7	0.8
12				772.3	13.0	45.0	658.6	15.2	70.6
13				772.5	12.9	44.9	740.9	13.5	550.5
14				802.4	12.5	0.1	748.7	13.4	83.9
15				817.5	12.2	20.7	770.0	13.0	53.4
16							781.6	12.8	94.8
17							813.3	12.3	70.7
18							1100.9	9.1	202.7

Table C.4: vibrational wave number $\tilde{\nu}_k$ [cm^{-1}], wavelength λ [μm], and absorption coefficient A_k [$10^{-8}\text{cm}^2\text{s}^{-1}$] of TiO_2 , $(\text{TiO}_2)_2$, and $(\text{TiO}_2)_3$ with label k .

	TiO_2			$(\text{TiO}_2)_2$			$(\text{TiO}_2)_3$		
k	$\tilde{\nu}_k$	λ	A_k	$\tilde{\nu}_k$	λ	A_k	$\tilde{\nu}_k$	λ	A_k
1	354.5	28.2	6.3	94.9	105.3	20.0	72.5	137.9	2.7
2	1044.1	9.6	196.9	175.9	56.8	11.5	73.7	135.7	0.1
3	1088.4	9.2	20.0	203.6	49.1	0.0	161.5	61.9	2.6
4				302.4	33.1	0.0	172.5	57.9	4.4
5				363.3	27.5	32.1	177.4	56.4	24.9
6				433.5	23.1	0.0	262.6	38.1	4.5
7				523.1	19.1	0.0	275.8	36.3	1.9
8				741.5	13.5	104.9	292.2	34.2	0.3
9				774.7	12.9	295.4	338.8	29.5	21.3
10				776.1	12.9	0.0	359.0	27.9	11.6
11				1080.0	9.3	289.3	497.0	20.1	42.5
12				1100.9	9.1	0.0	509.1	19.6	0.2
13							509.2	19.6	4.2
14							742.4	13.5	405.9
15							745.0	13.4	76.3
16							754.9	13.2	287.6
17							768.1	13.0	2.9
18							777.7	12.9	17.8
19							807.8	12.4	352.0
20							1108.1	9.0	230.1
21							1114.5	8.9	43.7

Table C.5: vibrational wave number $\tilde{\nu}_k$ [cm^{-1}], wavelength λ [μm], and absorption coefficient A_k [$10^{-8}\text{cm}^2\text{s}^{-1}$] of $(\text{TiO}_2)_4$ and of $(\text{TiO}_2)_5$ with label k .

	$(\text{TiO}_2)_4$			$(\text{TiO}_2)_5$		
k	$\tilde{\nu}_k$	λ	A_k	$\tilde{\nu}_k$	λ	A_k
1	38.1	262.9	4.4	35.3	282.9	0.5
2	50.2	199.0	0.0	35.9	277.9	0.1
3	77.2	129.6	0.0	66.9	149.5	0.0
4	105.6	94.7	0.0	69.7	143.5	1.9
5	115.6	86.5	13.4	97.2	102.9	0.8
6	150.4	66.5	30.8	108.9	91.8	4.5
7	158.3	63.2	0.0	129.6	77.2	0.3
8	205.0	48.8	0.0	146.6	68.2	0.0
9	222.5	44.9	0.0	171.8	58.2	31.4
10	260.6	38.4	6.2	180.5	55.4	3.3
11	283.8	35.2	0.0	201.6	49.6	0.2
12	316.8	31.6	2.7	237.1	42.2	2.7
13	329.5	30.4	24.9	273.8	36.5	3.9
14	345.5	28.9	0.0	281.3	35.6	2.7
15	408.3	24.5	67.2	305.9	32.7	7.4
16	499.9	20.0	0.0	311.5	32.1	5.0
17	502.6	19.9	0.0	311.9	32.1	2.5
18	512.8	19.5	1.7	337.9	29.6	10.6
19	528.9	18.9	0.0	358.8	27.9	75.7
20	722.1	13.9	1603.9	458.1	21.8	1.5
21	736.9	13.6	87.2	496.2	20.2	0.3
22	749.2	13.4	0.0	500.9	19.9	0.2
23	760.8	13.2	186.6	511.9	19.5	0.9
24	762.3	13.1	0.0	512.6	19.5	1.0
25	771.9	12.9	0.0	540.6	18.5	47.3
26	772.8	12.9	62.7	691.4	14.5	2857.1
27	788.4	12.7	202.6	739.6	13.5	13.3
28	848.6	11.8	0.0	750.3	13.3	1.4
29	1105.2	9.1	267.5	754.8	13.3	55.4
30	1107.4	9.0	0.0	756.7	13.2	3.9
31				760.7	13.2	111.5
32				767.9	13.0	52.8
33				771.8	12.9	104.9
34				772.4	12.9	109.4
35				773.7	12.9	0.0
36				835.3	11.9	1.9
37				852.1	11.7	7.7
38				1116.5	8.9	223.0
39				1117.8	8.9	47.0

Table C.6: vibrational wave number $\tilde{\nu}_k$ [cm^{-1}], wavelength λ [μm], and absorption coefficient A_k [$10^{-8}\text{cm}^2\text{s}^{-1}$] of $(\text{TiO}_2)_6$ with label k .

k	$\tilde{\nu}_k$	λ	A_k	k	$\tilde{\nu}_k$	λ	A_k
1	15.4	651.2	0.0	25	484.5	20.6	78.2
2	15.9	626.2	0.8	26	484.6	20.6	0.0
3	37.5	266.6	0.0	27	491.5	20.4	0.0
4	43.5	229.8	0.0	28	493.0	20.3	2.0
5	72.5	137.9	5.9	29	502.7	19.9	3.5
6	74.4	134.5	6.6	30	504.2	19.8	0.0
7	81.9	122.1	2.8	31	547.5	18.3	0.0
8	118.9	84.1	0.0	32	650.9	15.4	4165.1
9	119.9	83.4	0.0	33	731.5	13.7	34.7
10	140.2	71.4	0.0	34	736.1	13.6	0.0
11	141.3	70.7	0.0	35	742.7	13.5	19.5
12	159.7	62.6	34.7	36	743.9	13.4	0.0
13	185.0	54.1	0.0	37	748.7	13.4	0.0
14	196.7	50.8	5.2	38	755.1	13.2	15.5
15	237.6	42.1	0.0	39	758.1	13.2	250.0
16	266.2	37.6	7.0	40	760.2	13.2	0.0
17	266.6	37.5	20.1	41	760.7	13.2	11.5
18	271.9	36.8	0.0	42	766.3	13.1	0.0
19	298.6	33.5	8.3	43	767.2	13.0	139.5
20	301.9	33.1	8.2	44	810.5	12.3	0.0
21	303.6	32.9	0.0	45	841.3	11.9	26.5
22	326.8	30.6	0.0	46	844.0	11.9	0.0
23	340.9	29.3	66.1	47	1110.8	9.0	269.7
24	398.6	25.1	0.0	48	1111.5	8.9	0.0

Bibliography

- [Albaret *et al.* 1999] Albaret, T., Finocchi, F., and Noguera, C., 1999. Ab initio Simulation of Titanium Dioxide Clusters. *Appl. Sur. Sci.*, **144–145**, 672–676.
- [Alexander *et al.* 1983] Alexander, D. R., Johnson, H. R., and Rypma, R. L., 1983. Effect of molecules and grains on Rosseland mean opacities. *ApJ*, **272**, 773–780.
- [Allen 1973] Allen, C. W., 1973. *Astrophysical Quantities*. The Athlone Press, London.
- [Arndt *et al.* 1997] Arndt, T. U., Fleischer, A. J., and Sedlmayr, E., 1997. Circumstellar Dust shells around Long-period Variables. VI. An approximative formula for the mass loss rate of C-rich stars. *A&A*, **327**, 614–619.
- [Bakalbassis *et al.* 1996] Bakalbassis, E., Stiakaki, M., Tsipis, A., and Tsipis, C., 1996. . *Chem. Phys.*, **205**, 389.
- [Balducci *et al.* 1985a] Balducci, G., Gigli, G., and Guido, M., 1985. Identification and stability determinations for the gaseous titanium oxide molecules Ti_2O_3 and Ti_2O_4 . *J.Chem.Phys.*, **83**, 1913–1916.
- [Balducci *et al.* 1985b] Balducci, G., Gigli, G., and Guido, M., 1985. Mass spectrometric study of the thermochemistry of gaseous EuTiO_3 and TiO_2 . *J.Chem.Phys.*, **83**, 1909–1912.
- [Barnes *et al.* 1997] Barnes, M., Merer, A., and Metha, G., 1997. . *J. Mol. Spec.*, **181**, 180.
- [Bauschlicher *et al.* 1983] Bauschlicher, C., Bagus, P., and Nelin, C., 1983. . *Chem. Phys. Lett.*, **101**, 229.
- [Beck 1993] Beck, H. K. B., 1993. *Ionization, Chemistry and Dust Formation in the Outflows of Classical Novae and Red Giants*. PhD thesis, Technische Universität, Berlin, FRG.

- [Beck *et al.* 1992] Beck, H. K. B., Gail, H.-P., Henkel, R., and Sedlmayr, E., 1992. Chemistry in circumstellar shells. I. Chromospheric radiation fields and dust formation in optically thin shells of M-giants. *A&A*, **265**, 626–642.
- [Begemann *et al.* 1997] Begemann, B., Dorschner, J., Henning, T., Mutschke, H., Gürtler, J., Kömpe, C., and Nass, R., 1997. Aluminum oxide and the opacity of oxygen-rich circumstellar dust in the 12-17 micron range. *Astrophys. J.*, **476**, 199–208.
- [Bergström *et al.* 1996] Bergström, R., Lunell, S., and Eriksson, L. A., 1996. Comparative Study of DFTMethods Applied to Small Titanium/Oxygen Compounds. *Int. J. Quant. Chem.*, **59**, 427–443.
- [Berruyer and Frisch 1983] Berruyer, N. and Frisch, H., 1983. Dust-driven winds. I. A two-fluid model and its numerical solution. *A&A*, **126**, 269–277.
- [Bowen 1988] Bowen, G. H., 1988. Dynamical modelling of long-period variable star atmospheres. *ApJ*, **329**, 299–317.
- [Castor *et al.* 1975] Castor, J. I., Abbott, C., and Klein, R. I., 1975. Radiation-driven winds in Of stars. *ApJ*, **195**, 157–174.
- [Chang *et al.* 1998] Chang, C., Patzer, A. B. C., Sedlmayr, E., and Sülzle, D., 1998. Ab initio studies of stationary points of the Al_2O_3 molecule. *Eur. Phys. J. D*, **2**, 57–62.
- [Chertihin and Andrews 1995] Chertihin, G. and Andrews, L., 1995. Reactions of Laser Ablated Titanium, Zirconium, and Hafnium Atoms with Oxygen Molecules in Condensing Argon. *J.Phys.Chem.*, **99**, 6356–6366.
- [Danchi *et al.* 1994] Danchi, W. C., Bester, M., Degiacomi, C. G., Greenhill, L. J., and Townes, C. H., 1994. Characteristics of dust shells around 13 late-type stars. *AJ*, **107**, 1469–1513.
- [Deutsch 1956] Deutsch, A. J., 1956. The circumstellar envelope of alpha Herculis. *ApJ*, **123**, 210–227.
- [Dominik 1992] Dominik, C., 1992. *Formation of dust grains in the winds of cool giants*. PhD thesis, Technische Universität, Berlin, FRG.
- [Dominik *et al.* 1990a] Dominik, C., Gail, H.-P., Sedlmayr, E., and Winters, J. M., 1990. Dust driven mass loss during late stages of cool giant evolution. In Mennessier, M. O. and Omont, A., editors, *From Miras to Planetary Nebulae: Which path for stellar evolution?*, pages 201–203, Editions Frontières, Gif sur Yvette Cedex - France.

- [Dominik *et al.* 1990b] Dominik, C., Gail, H.-P., Sedlmayr, E., and Winters, J. M., 1990. HR diagrams for dust driven winds around C-stars. *A&A*, **240**, 365–375.
- [Dominik *et al.* 1993] Dominik, C., Sedlmayr, E., and Gail, H.-P., 1993. Dust formation in stellar winds. VI. Moment equations for the formation of heterogeneous and core-mantle grains. *A&A*, **277**, 578–594.
- [Donn and Nuth 1985] Donn, B. and Nuth, J. A., 1985. Does nucleation theory apply to the formation of refractory circumstellar grains. *ApJ*, **288**, 187–190.
- [Draine 1985] Draine, B. T., 1985. Tabulated optical properties of graphite and silicate grains. *ApJS*, **57**, 587–594.
- [Draine and Lee 1984] Draine, B. T. and Lee, H. M., 1984. Optical properties of interstellar graphite and silicate grains. *ApJ*, **285**, 89–108.
- [Draine and Salpeter 1977] Draine, B. T. and Salpeter, E. E., 1977. Time dependent nucleation theory. *J.Chem.Phys.*, **67**, 2230–2235.
- [Draine and Salpeter 1979] Draine, B. T. and Salpeter, E. E., 1979. On the physics of dust grains in hot gas. *ApJ*, **231**, 77–94.
- [Feder *et al.* 1966] Feder, J., Russell, K. C., Lothe, J., and Pound, G. M., 1966. Homogeneous nucleation and growth of droplets in vapours. *Adv. Phys.*, **15**, 111–178.
- [Fix 1969] Fix, J. D., 1969. The formation and growth of carbon particles in the atmospheres of cool carbon stars. *MNRAS*, **146**, 37–49.
- [Fleischer 1994] Fleischer, A. J., 1994. *Hydrodynamics and Dust Formation in the Circumstellar Shells of Miras and Long-Period Variables*. PhD thesis, Technische Universität, Berlin, FRG.
- [Fleischer *et al.* 1991] Fleischer, A. J., Gauger, A., and Sedlmayr, E., 1991. Generation of shocks by radiation pressure on newly formed circumstellar dust. *A&A*, **242**, L1–L4.
- [Fleischer *et al.* 1992] Fleischer, A. J., Gauger, A., and Sedlmayr, E., 1992. Circumstellar dust shells around long-period variables. I. Dynamical models of C-stars including dust formation, growth and evaporation. *A&A*, **266**, 321–339.
- [Fleischer *et al.* 1995] Fleischer, A. J., Gauger, A., and Sedlmayr, E., 1995. Circumstellar dust shells around long-period variables. III. Instability due to an exterior κ -mechanism caused by dust formation. *A&A*, **297**, 543–555.
- [Foltin *et al.* 1999] Foltin, M., Stueber, J., and Bernstein, E. R., 1999. On the growth dynamic of neutral vanadium oxide and titanium oxide clusters. *J. Chem. Phys.*, **111**, 9577–9586.

- [Frisch *et al.* 1994] Frisch, M. J., Trucks, G. W., Head-Gordon, M., Gill, P. M., Wong, M. W., Foresman, J. B., Johnson, B. G., Schlegel, H. B., Robb, M. A., Repogle, E. S., Gomperts, R., Andres, J. L., Raghavachari, K., Binkley, J. S., Gonzalez, C., Martin, R. L., Fox, D. J., Defrees, B. J., Stewart, J. J. P., and Pople, J. A., 1994. *Gaussian94/DFT*. Gaussian Inc., Pittsburgh, PA.
- [Fulde 1993] Fulde, P., 1993. *Electron Correlations in Molecules and Solids*. Springer-Verlag, Berlin.
- [Gail and Sedlmayr 1985] Gail, H.-P. and Sedlmayr, E., 1985. Dust formation in stellar winds. II. Carbon condensation in stationary, spherically expanding winds. *A&A*, **148**, 183–190.
- [Gail and Sedlmayr 1986] Gail, H.-P. and Sedlmayr, E., 1986. The primary condensation process for dust around late M-type stars. *A&A*, **166**, 225–236.
- [Gail and Sedlmayr 1987] Gail, H.-P. and Sedlmayr, E., 1987. Dust formation in stellar winds. III. Self-consistent models for dust-driven winds around C-stars. *A&A*, **171**, 197–204.
- [Gail and Sedlmayr 1988] Gail, H.-P. and Sedlmayr, E., 1988. Dust formation in stellar winds. IV. Heteromolecular carbon grain formation and growth. *A&A*, **206**, 153–168.
- [Gail and Sedlmayr 1998a] Gail, H.-P. and Sedlmayr, E., 1998. Dust formation in M stars. In Hartquist, T. and Williams, D., editors, *The Molecular Astrophysics of Stars and Galaxies*, page 285, Oxford Science Pub., Oxford, GB.
- [Gail and Sedlmayr 1998b] Gail, H.-P. and Sedlmayr, E., 1998. Inorganic dust formation in astrophysical environments. In Sarre, P., editor, *Chemistry and physics of molecules and grains in space. Faraday Discussion no. 109*, page 303, London, GB.
- [Gail *et al.* 1984] Gail, H.-P., Keller, R., and Sedlmayr, E., 1984. Dust formation in stellar winds. I. A rapid computational method and application to graphite condensation. *A&A*, **133**, 320–332.
- [Gauger *et al.* 1990] Gauger, A., Gail, H.-P., and Sedlmayr, E., 1990. Dust formation, growth and evaporation in a cool pulsating circumstellar shell. *A&A*, **235**, 345–361.
- [Gauger *et al.* 1993] Gauger, A., Fleischer, A. J., Winters, J. M., and Sedlmayr, E., 1993. Dynamical models of dust shells around LPVs: Effects of time-dependent postshock cooling. *AG Abstr. Ser.*, **9**, 127.

- [Gehrz 1989] Gehrz, R. D., 1989. Sources of stardust in the galaxy. In Allamandola, L. J. and Tielens, A. G. G. M., editors, *Interstellar Dust*, pages 445–453, Kluwer Academic Publishers, Dordrecht.
- [Gill 1996] Gill, P. M. W., 1996. . *Mol.Phys.*, **89**, 433.
- [Gillett *et al.* 1971] Gillett, F. C., Merrill, K. M., and Stein, W. A., 1971. Observations of infrared radiation from cool stars. *ApJ*, **164**, 83–90.
- [Gilman 1969] Gilman, R. C., 1969. On the composition of circumstellar grains. *ApJ*, **155**, L185–L187.
- [Goeres 1992] Goeres, A., 1992. *Staubbildung in den Hüllen von Kohlenstoffsternen: R Coronae Borealis*. PhD thesis, Techn. Univ. Berlin, Berlin.
- [Goeres *et al.* 1988] Goeres, A., Henkel, R., Sedlmayr, E., and Gail, H.-P., 1988. Non-equilibrium chemistry in Circumstellar Shells. *Rev. Mod. Astron.*, **1**, 231–248.
- [Guo *et al.* 1992] Guo, B., Kerns, K., and Castleman, A. W., 1992. . *Int. J. Mass Spectrom. Ion Proc.*, **117**, 129.
- [Gustafsson 1989] Gustafsson, B., 1989. Chemical analyses of cool stars. *ARA&A*, **27**, 701–756.
- [Habing 1990] Habing, H. J., 1990. The evolution of Red Giants to White Dwarfs, a review of the observational evidence. In Mennessier, M. O. and Omont, A., editors, *From Miras to Planetary Nebulae: Which path for stellar evolution?*, pages 16–40, Editions Frontières, Gif sur Yvette Cedex - France.
- [Habing 1996] Habing, H., 1996. Circumstellar envelopes and Asymptotic Giant Branch stars. *A&AR*, **7**, 97–207.
- [Hagfeldt and Lunell 1994] Hagfeldt, A. and Lunell, H., S. Siegbahn, 1994. Energy Levels of Small Titanium Oxide Clusters Obtained from SCF Calculations. *Int. J. Quant. Phys.*, **49**, 97–104.
- [Hagfeldt *et al.* 1992] Hagfeldt, A., Siegbahn, H., Lindquist, S.-E., and Lunell, S., 1992. Semiempirical Calculations of TiO₂ (Rutile) Clusters. *Int. J. Quant. Chem.*, **44**, 477–495.
- [Hagfeldt *et al.* 1993] Hagfeldt, A., Bergström, R., Siegbahn, H., and Lunell, S., 1993. Structure and Stability of Small Titanium/Oxygen Clusters Studied by ab initio Quantum Chemical Calculations. *J.Phys.Chem.*, **97**, 12725–12730.

- [Hearn 1990] Hearn, A. G., 1990. The physics of mass loss from AGB stars. In Mennessier, M. O. and Omont, A., editors, *From Miras to Planetary Nebulae: Which path for stellar evolution?*, pages 121–130, Editions Frontières, Gif sur Yvette Cedex - France.
- [Helling 1999] Helling, C., 1999. *Role of molecular opacities in circumstellar dust shells*. PhD thesis, Technische Universität Berlin, FRG.
- [Henrich and Cox 1994] Henrich, V. E. and Cox, P. A., 1994. *The surface science of metal oxides*. Cambridge Univ. Press, New York, NY.
- [Hoffmeister *et al.* 1984] Hoffmeister, C., Richter, G., and Wenzel, W., 1984. *Veränderliche Sterne*. Springer, Berlin, 2nd edition.
- [Holzer and MacGregor 1985] Holzer, T. E. and MacGregor, K. B., 1985. Mass loss mechanisms for cool, low-gravity stars. In Morris, M. and Zuckerman, B., editors, *Mass Loss from red giants*, pages 229–255. D. Reidel Pub. Com.
- [Huber and Herzberg 1979] Huber, K. and Herzberg, G., 1979. *Molecular Spectra and Molecular Structure*, volume VI. Van Nostrand Reinhold, New York.
- [Iben and Renzini 1983] Iben, I. and Renzini, A., 1983. Asyptotic Giant Branch evolution and beyond. *ARA&A*, **21**, 271–342.
- [Jeong *et al.* 1999a] Jeong, K. S., Winters, J. M., and Sedlmayr, E., 1999. Dust formation in oxygen-rich circumstellar shells around long-period variables. In Le Bertre, T., Lèbre, A., and Waelkens, C., editors, *IAU Symp. 191: Asymptotic Giant Branch stars*, pages 233–238.
- [Jeong *et al.* 1999b] Jeong, K. S., Winters, J. M., and Sedlmayr, E., 1999. Dust formation in oxygen-rich circumstellar shells around long-period variables. In Hron, J. and Höfner, S., editors, *Abstracts of the 2nd Austrian ISO Workshop. Atmospheres of M, S and C Giants*, pages 37–38. Institute of Astronomy, University of Vienna.
- [John 1995] John, M., 1995. Bildung von Eisen-Clustern in kühlen Sternwinden. Master’s thesis, Technische Universität, Berlin, FRG.
- [Jones and Merrill 1976] Jones, T. W. and Merrill, K. M., 1976. Model dust envelopes around late-type stars. *ApJ*, **209**, 509–524.
- [Jørgensen and Johnson 1992] Jørgensen, U. G. and Johnson, H. R., 1992. Radiative force on molecules and its possible role for mass loss in evolved AGB stars. *A&A*, **265**, 168–176.
- [Jura 1986a] Jura, M., 1986. Mass loss from carbon stars. *ApJ*, **303**, 327–332.

- [Jura 1986b] Jura, M., 1986. The Role of dust in mass loss from late-type stars. *Irish Astr. J.*, **17**, 322–330.
- [Justtanont *et al.* 1994] Justtanont, K., Skinner, C. J., and Tielens, A. G. G. M., 1994. Molecular rotational line profiles from oxygen-rich red giant winds. *ApJ*, **435**, 852–863.
- [Kaufman *et al.* 1967] Kaufman, M., Muentner, J., and Klemperer, W., 1967. Geometry of Some Refractory Metal Dioxides. *J.Chem.Phys.*, **47**, 3365.
- [Knapp 1985] Knapp, G. R., 1985. Mass Loss from evolved stars. IV. The dust-to-gas ratio in the envelopes of Mira variables and carbon stars. *ApJ*, **293**, 273–280.
- [Knapp and Morris 1985] Knapp, G. R. and Morris, M., 1985. Mass loss from evolved stars. III. Mass loss rates for 50 Stars from CO $J = 1 - 0$ observations. *ApJ*, **292**, 640–669.
- [Köhler *et al.* 1997] Köhler, T. M., Gail, H.-P., and Sedlmayr, E., 1997. MgO dust nucleation in M-stars: Calculation of cluster properties and nucleation rates. *A&A*, **320**, 553–567.
- [Kozasa and Hasegawa 1987] Kozasa, T. and Hasegawa, H., 1987. Grain Formation through Nucleation Process in Astrophysical Environments. II. *Prog. Theor. Phys.*, **77**, 1402–1410.
- [Kozasa and Sogawa 1999] Kozasa, T. and Sogawa, H., 1999. Formation of crystalline silicates around oxygen-rich AGB stars. In Le Bertre, T., Lèbre, A., and Waelkens, C., editors, *IAU Symp. 191: AGB stars*, pages 239–244. ASP Conf. Ser.
- [Kozasa *et al.* 1984] Kozasa, T., Hasegawa, H., and Seki, J., 1984. Grain formation in the expanding gas flow around cool luminous stars. *Ap&SS*, **98**, 61–79.
- [Le Bertre 1993] Le Bertre, T., 1993. Oxygen-rich late-type star lightcurves in the 1-20 μm range. *A&AS*, **97**, 729–753.
- [Le Sidaner and Le Bertre 1993] Le Sidaner, P. and Le Bertre, T., 1993. Optical and infrared observations of two oxygen-rich Miras: dust shell modelling as a function of phase. *A&A*, **278**, 167–178.
- [Le Sidaner and Le Bertre 1996] Le Sidaner, P. and Le Bertre, T., 1996. Optical and infrared observations of 27 oxygen-rich stars: modelling of the circumstellar dust shells. *A&A*, **314**, 896–908.
- [Little *et al.* 1987] Little, S. J., Little-Marenin, I. R., and Bauer, W. H., 1987. Additional late-type stars with technetium. *AJ*, **94**, 981–995.

- [Loock *et al.* 1998] Loock, H.-P., Simard, B., Wallin, S., and Linton, C., 1998. Ionization potentials and bond energies of TiO, ZrO, NbO and MoO. *J.Chem.Phys.*, **109**, 8980–8992.
- [Lucy 1971] Lucy, L. B., 1971. The formation of resonance lines in extended atmospheres. *ApJ*, **163**, 95–110.
- [Lucy 1976] Lucy, L. B., 1976. Mass loss by cool carbon stars. *ApJ*, **205**, 482–491.
- [March 1975] March, N., 1975. *Self-Consistent Fields in Atoms*. Pergamon, Oxford.
- [McIntyre *et al.* 1971] McIntyre, N., Thompson, K., and Weltner, J. W., 1971. Spectroscopy of Titanium Oxide and Titanium Dioxide Molecules in Inert Matrices at 4° K. *J.Phys.Chem.*, **75**, 3243–3249.
- [Menietti and Fix 1978] Menietti, J. D. and Fix, J. D., 1978. Models of mass flows from cool, luminous stars. *ApJ*, **224**, 961–968.
- [Mihalas 1978] Mihalas, D., 1978. *Stellar Atmospheres*. W. H. Freeman and Company, San Francisco, 2nd edition.
- [Molster *et al.* 1999] Molster, F., Waters, L., Trams, N., van Winckel, H., Decin, L., and *et al.*, 1999. The composition and nature of the dust shell surrounding the binary FGL 4106. *A&A*, **350**, 163–180.
- [Monnier *et al.* 1999] Monnier, J. D., Geballe, T. R., and Danchi, W. C., 1999. Mid-infrared Spectra of late-type stars: Long term evolution. *ApJ*, **521**, 261.
- [Nittler *et al.* 1997] Nittler, L. R., Alexander, C. M. O. D., Gao, X., Walker, R. M., and Zinner, E., 1997. Stellar sapphires: The properties and origins of presolar Al₂O₃ in meteorites. *ApJ*, **483**, 475–495.
- [Olofsson 1988] Olofsson, H., 1988. Radio and infrared observations of circumstellar envelopes. *Space Sci. Rev.*, **47**, 145–174.
- [Olofsson *et al.* 1987] Olofsson, H., Eriksson, K., and Gustafsson, B., 1987. CO ($J = 1 - 0$) observations of bright carbon stars. *A&A*, **183**, L13 – L16.
- [Olofsson *et al.* 1993] Olofsson, H., Eriksson, K., Gustafsson, B., and Carlström, U., 1993. A study of circumstellar envelopes around bright carbon stars. I. Structure, kinematics, and mass loss rate. *ApJS*, **87**, 267–304.
- [Onaka *et al.* 1989] Onaka, T., de Jong, T., and Willems, F. J., 1989. A study of M Mira variables based on IRAS LRS observations. I. Dust formation in the circumstellar shell. *A&A*, **218**, 169–178.
- [Parr and Yang 1989] Parr, R. G. and Yang, W., 1989. *Density-Functional Theory of Atoms and Molecules*. Oxford Uni. Press, Oxford.

- [Patzner *et al.* 1998] Patzner, A. B. C., Gauger, A., and Sedlmayr, E., 1998. Dust formation in stellar winds VII. Kinetic nucleation theory for chemical non-equilibrium in the gas phase. *A&A*, **337**, 847–858.
- [Patzner *et al.* 1999] Patzner, A. B. C., Chang, C., Sedlmayr, E., and Sülzle, D., 1999. Ab initio thermodynamic properties for different isomers of the Al_2O_3 molecule. *Eur. Phys. J. D*, **6**, 57–62.
- [Pauldrach *et al.* 1986] Pauldrach, A. W. A., Puls, J., and Kudritzki, R. P., 1986. Radiation-driven winds of hot luminous stars. Improvements of the theory and first results. *A&A*, **164**, 86–100.
- [Perdew 1986] Perdew, J. P., 1986. Density functional approximation for the correlation energy of the inhomogeneous electron gas. *Phys. Rev. B*, **33**, 8822–8824.
- [Pijpers and Hearn 1989] Pijpers, F. P. and Hearn, A. G., 1989. A model for the stellar wind driven by linear acoustic waves. *A&A*, **209**, 198–210.
- [Posch *et al.* 1999] Posch, T., Kerschbaum, F., Mutschke, H., Fabian, D., Dorschner, J., and Hron, J., 1999. On the origin of the $13\mu\text{m}$ feature. A study of ISO-SWS spectra of oxygen-rich AGB stars. *A&A*, **352**, 609–618.
- [Ramana and Phillips 1988] Ramana, M. and Phillips, D., 1988. A Computational study of the TiO_2 molecule. *J. Chem. Phys.*, **88**, 2637–2640.
- [Rassolov *et al.* 1998] Rassolov, V., Pople, J. A., Ratner, M., and Windus, T. L., 1998. 6 – 31 G^* basis set for atoms K through Zn. *J. Chem. Phys.*, **109**, 1223–1229.
- [Rosi *et al.* 1998] Rosi, M., Bauschlicher, C., Chertihin, G., and Andrews, L., 1998. The vibrational frequencies of CaO_2 , ScO_2 , and TiO_2 : a comparison of theoretical methods. *Theor. Chem. Acc.*, **99**, 106–112.
- [Salpeter 1974] Salpeter, E. E., 1974. Formation and flow of dust grains in cool stellar atmospheres. *ApJ*, **193**, 585–592.
- [Saraf *et al.* 1998] Saraf, L., Patil, S., Ogale, S., Sainkar, S., and Kshirsager, S., 1998. Synthesis of Nanophase TiO_2 by Ion Beam Sputtering and Cold Condensation Technique. *Int. J. Mod. Phys. B*, **12**, 2635–2647.
- [Schröder *et al.* 1999] Schröder, K.-P., Winters, J. M., and Sedlmayr, E., 1999. Tip-AGB stellar evolution in the presence of a pulsating, dust-induced “superwind”. *A&A*, **349**, 898–906.
- [Sedlmayr 1989a] Sedlmayr, E., 1989. Dust condensation in stellar outflows. In Allamandola, L. J. and Tielens, A. G. G. M., editors, *Interstellar Dust*, pages 467–477. Kluwer Academic Publishers, Dordrecht.

- [Sedlmayr 1989b] Sedlmayr, E., 1989. Dust formation and stellar wind. In Mennessier, M. O. and Omont, A., editors, *From Miras to Planetary Nebulae: Which Path for Stellar Evolution*, pages 179–185. Edition Frontières, 91192 Gif sur Yvettes Cedex.
- [Sopka *et al.* 1985] Sopka, R. J., Hildebrand, R., Jaffe, D. T., Gatley, I., Roelling, T., Werner, M., Jura, M., and Zuckerman, B., 1985. Submillimeter observations of evolved stars. *ApJ*, **294**, 242–255.
- [Tielens 1983] Tielens, A. G. G. M., 1983. Stationary flows in the circumstellar envelopes of M giants. *ApJ*, **271**, 702–716.
- [Tielens 1990] Tielens, A. G. G. M., 1990. Towards a circumstellar silicate mineralogy. In Mennessier, M. O. and Omont, A., editors, *From Miras to Planetary Nebulae: Which path for stellar evolution?*, pages 186–200, Editions Frontières, Gif sur Yvette Cedex - France.
- [Treffers and Cohen 1974] Treffers, R. and Cohen, M., 1974. High-resolution spectra of cool stars in the 10- and 20-micron regions. *ApJ*, **188**, 545–552.
- [Tsipis and Tsipis 1999] Tsipis, A. and Tsipis, C., 1999. A theoretical study of molecular titanium oxide clusters: structure, bonding, vibrations and stability. *Phys.Chem.Chem.Phys.*, **18**, 4453.
- [Tsuji 1973] Tsuji, T., 1973. Molecular abundances in stellar atmospheres II. *A&A*, **23**, 411–431.
- [Unno and Kondo 1976] Unno, W. and Kondo, M., 1976. The Eddington approximation generalized for radiative transfer in spherically symmetric systems. I. Basic method. *PASJ*, **28**, 347–354.
- [Unno and Kondo 1977] Unno, W. and Kondo, M., 1977. The Eddington approximation generalized for radiative transfer in spherically symmetric systems. II. Nongray extended dust-shell models. *PASJ*, **29**, 693–710.
- [Vassiliadis and Wood 1993] Vassiliadis, E. and Wood, P. R., 1993. Evolution of low- and intermediate- mass stars to the end of the asymptotic giant branch with mass loss. *ApJ*, **413**, 641–657.
- [Veen and Rugers 1989] van der Veen, W. E. C. J. and Rugers, M., 1989. A comparison between CO-, OH- and IR-mass-loss rates of evolved stars. *A&A*, **226**, 183–202.
- [Wallis and Wickramasinghe 1997] Wallis, D. H. and Wickramasinghe, N. C., 1997. Comet P/Shoemaker-Levy 9 Collision with Jupiter: A Model of G-Site Dust Composition. *Astrophys. Space Sci.*, **254**, 25–35.

- [Waters and Molster 1999] Waters, L. B. F. M. and Molster, F. J., 1999. Crystalline silicates in AGB and post-AGB stars. In Le Bertre, T., Lèbre, A., and Waelkens, C., editors, *IAU Symp. 191: AGB stars*, pages 209–219. ASP Conf. Ser.
- [Waters *et al.* 1996] Waters, L. B. F. M., Molster, F. J., de Jong, T., Beintema, D. A., Waelkens, C., Boogart, A., Boxhoorn, D. R., de Graauw, T., Drapatz, S., Feuchtgruber, H., Genzel, R., Helmich, F., Heras, A. M., Huygen, R., Izumiura, H., Justanont, K., Kester, D. J. M., Kunze, D., Lahuis, F., Lamers, H. J. G. L. M., Leech, K. J., Loup, C., Lutz, D., Morris, P. W., Price, S. D., Roelfsema, P. R., Salama, A., Schaeidt, S. G., Tielens, A. G. G. M., Trams, N. R., Valentijn, E. A., Vandenbussche, B., van den Ancker, M. E., van Dishoeck, E. F., Wesselius, P. R., and Young, E., 1996. Mineralogy of Oxygen-rich dust shells. *A&A*, **315**, L361–L364.
- [Weidemann and Schönberner 1990] Weidemann, V. and Schönberner, D., 1990. Stellar evolution theory: Up to and on the AGB. In Mennessier, M. O. and Omont, A., editors, *From Miras to Planetary Nebulae: Which path for stellar evolution?*, pages 3–15, Editions Frontières, Gif sur Yvette Cedex - France.
- [Winters 1994] Winters, J. M., 1994. *Internal structure and optical appearance of circumstellar dust shells around cool carbon giants*. PhD thesis, Technische Universität, Berlin, FRG.
- [Winters *et al.* 1994] Winters, J. M., Fleischer, A. J., Gauger, A., and Sedlmayr, E., 1994. Circumstellar dust shells around long-period variables. II. Theoretical lightcurves of C-stars. *A&A*, **290**, 623–633.
- [Winters *et al.* 1995] Winters, J. M., Fleischer, A. J., Gauger, A., and Sedlmayr, E., 1995. Circumstellar dust shells around long-period variables. IV. Brightness profiles and spatial spectra of C-stars. *A&A*, **302**, 483–496.
- [Winters *et al.* 1996] Winters, J. M., Fleischer, A. J., Le Bertre, T., and Sedlmayr, E., 1996. Optical appearance of dynamical models for circumstellar dust shells around long-period variables: AFGL 3068. In Wing, R. F., editor, *IAU Symp. 177: The Carbon Star Phenomenon*, page in press, Kluwer Academic Publishers, Dordrecht.
- [Winters *et al.* 1997] Winters, J. M., Fleischer, A. J., Gauger, A., and Sedlmayr, E., 1997. Dynamical models of circumstellar dust shells around long-period variables: Spectrum, lightcurves, intensity profiles, and visibilities of IRC +10216. In Latter, W. B., Radford, S. J. E., Jewell, P. R., Mangum, J. G., and Bally, J., editors, *CO: Twenty-five Years of Millimeter-wave Spectroscopy*, pages 477–478. Kluwer Academic Publishers.

- [Woitke 1997] Woitke, P., 1997. *Radiative Heating and Cooling in Circumstellar envelopes*. PhD thesis, Technische Universität, Berlin, FRG.
- [Woitke and Sedlmayr 1999] Woitke, P. and Sedlmayr, E., 1999. Heating and cooling by iron in cool star winds. *A&A*, **347**, 617–629.
- [Wood 1979] Wood, P. R., 1979. Pulsation and mass loss in Mira variables. *ApJ*, **227**, 220–231.
- [Woolf and Ney 1969] Woolf, N. J. and Ney, E. P., 1969. Circumstellar infrared emission from cool stars. *ApJ*, **155**, L181–L184.
- [Yamamoto and Hasegawa 1977] Yamamoto, T. and Hasegawa, H., 1977. Grain formation through nucleation process in astrophysical environment. *Prog. Theor. Phys.*, **58**(3), 816–828.
- [Yu and Freas 1990] Yu, W. and Freas, R., 1990. Formation and Gragmentation of Gas-Phase Titanium/Oxygen Cluster Positive Ions. *J.Am.Chem.Soc.*, **112**, 7126–7133.
- [Zinner 1998] Zinner, E., 1998. Stellar nucleosynthesis and the isotopic composition of presolar grains from primitive meteorites. *Ann. Rev. Earth Planet. Sci.*, **26**, 147–188.
- [Zuckerman *et al.* 1986] Zuckerman, B., Dyck, H. M., and Claussen, M. J., 1986. Carbon Monoxide Emission from Stars in the IRAS and Revised AFGL Catalogs. II. Massive Carbon stars. *ApJ*, **304**, 401–408.

Acknowledgement

It was a long way.

On this way I experienced several tiny moments which seemed unnoticed and common at first, but left impressive changes in my life. Reading the 'notoriously confusing' paper I and IV was the first step to this long journey for searching for the dust in the universe.

I am indebted to Prof. Erwin Sedlmayr, one of authors of these papers and my mentor, for attending the dissertation and for every support with which I could finish my thesis in Institut für Astronomie und Astrophysik, TU Berlin. I would like to thank Prof. Hans Peter Röser in Institute of Space Technology and Planetary Exploration, Deutsches Zentrum für Luft- und Raumfahrt Berlin for the second report on my thesis. I appreciate the presidency of the promotion committee to Prof. Peter Zimmermann.

My thank goes to Dr. Jens-Peter Kaufmann for the calm conversations which encouraged me in the hard time. I am very grateful to Andreas Gauger for the precise introduction at the very beginning of this work. I thank Jan Martin Winters for the fruitful discussions which began with harmless questions, but ended with a controversial dispute and with the excessive consumption of alcohol, which I really enjoyed. My thanks go to Uwe Bolick who gave me uncountable hints and answers to the computer problems, in spite of my explosive reaction on your slow tempo, and to other super-users, Marcus Luettker and Thorsten Arndt. I would like to thank Christian Chang, Detlev Sülzle in Schering AG and Thomas Steinke in ZIB for the collaboration, in which I had a bunch of fun. My warm thanks go to Jan Martin Winters, Christiane Helling, Christian Chang, Detlev Sülzle, Klaus-Peter Schröder, Beate Patzer for careful reading of script and valuable comments on this work and to Peter Voitke for the last correction of abstract in German. I am grateful to Sonja Friedrich for the literature and data research. I would like to express my thanks to Karin Sedlmayr for the heart-warming consideration. Thank you, all in the Bierrunde and the Kinorunde !

The calculations in this work were performed on the Cray computers of the Konrad-Zuse-Zentrum für Informationstechnik Berlin (ZIB). This work has been partly performed in Institute of Space Technology and Planetary Exploration, Deutsches Zentrum für Luft- und Raumfahrt Berlin (DLR) and partly supported by Deutsche Forschungsgemeinschaft. I am very grateful to the FAZIT Stiftung for the financial support.

I would like to thank my parents for their understanding and support by all means. Their silent encouragement was the inexhaustible source of my energy, with which I could take a step, forward. I have a fortune to have so nice siblings who give me the happiness and share the life with me. Very often I have suffered from the long separation from the people who have my heart. Perhaps you have more suffered than I can imagine. I am deeply grateful to you for your love and patience with me, which I owe in my whole life.

Schließlich ritten sie über die Höhen und schlugen die Ostenstraße ein, und dann ritten Merry und Pippin weiter nach Bockland; und unterwegs sangen sie schon wieder. Aber Sam bog nach Wasserau ein und kam so zum Bühl zurück, als sich der Tag wiederum neigte...

Tolkien Herr der Ringe

Lebenslauf

Persönliche Daten

Name	Kyung Sook Jeong
Geburtsdatum	12. Juli 1965
Geburtsort	Seoul, Korea
Eltern	Byung Soo Jeong Tae Chun Lee
Staatsangehörigkeit	koreanisch
Familienstand	ledig

Schule und Studium

1971 – 1977	Grundschule Sungrye in Seoul, Korea
1977 – 1980	Mittelschule Sungshin in Seoul, Korea
1980 – 1983	Oberschule Ehwa (Gymnasium) in Seoul, Korea
Feb. 1983	Abschluß: Abitur
1983 – 1989	Studium an der Fakultät für Astrophysik und Meteorologie an der Universität Yonsei in Seoul, Korea Thema der Diplomarbeit: <i>On the Dynamical Structure of Jet Systems</i>
1983 – 1987	Stipendiatin an der Universität Yonsei in Seoul, Korea
1987 – 1989	Studentische Hilfskraft mit Lehraufgaben am Institut für Astronomie und Meteorologie an der Universität Yonsei in Seoul, Korea

Beruflicher Werdegang

1989 – 1990	Wissenschaftliche Mitarbeiterin am Institut für Naturwissenschaften der Yonsei Universität in Seoul, Korea
1995 – 1996	Wissenschaftliche Mitarbeiterin in einem DFG Projekt mit dem Thema LPV-Diagnostik im Institut für Astronomie und Astrophysik, TU Berlin
1996 – 1999	Stipendiatin der FAZIT Stiftung am Institut für Astronomie und Astrophysik, TU Berlin
seit 1994	am Institut für Astronomie und Astrophysik, TU Berlin in der Arbeitsgruppe von Prof. Dr. E. Sedlmayr